

DISSERTATION

TIMING, KINEMATICS, AND TECTONIC SIGNIFICANCE OF STRIKE-SLIP FAULT
SYSTEMS IN THE ATACAMA DESERT OF NORTHERN CHILE AND THE LOWER
COLORADO RIVER CORRIDOR, U.S.A.

Submitted by

Skyler Mavor

Department of Geosciences

In partial fulfillment of the requirements

For the Degree of Doctor of Philosophy

Colorado State University

Fort Collins, Colorado

Fall 2021

Doctoral Committee:

Advisor: John Singleton

Sean Gallen

John Ridley

Melinda Laituri

Copyright by Skyler Mavor 2021
All Rights Reserved

ABSTRACT

TIMING, KINEMATICS, AND TECTONIC SIGNIFICANCE OF STRIKE-SLIP FAULT SYSTEMS IN THE ATACAMA DESERT OF NORTHERN CHILE AND THE LOWER COLORADO RIVER CORRIDOR, U.S.A.

Strike-slip fault systems are ubiquitous features of plate-boundary deformation worldwide and play a fundamental role in accommodating margin-oblique shear. In this dissertation I present case studies of strike-slip fault systems in two geographic areas: the Coastal Cordillera of northern Chile, and the lower Colorado River corridor in the southwestern United States. I use geologic mapping, brittle and ductile structural analysis, and multiple geochronology methods to resolve the spatial, kinematic, and temporal details of these strike-slip systems and interpret how they may relate to changing plate-boundary dynamics.

Previous studies have found that the Atacama fault system (AFS) localized into the contemporaneous magmatic arc where the thermal and hydrothermal influence of magmatism weakened the crust and facilitated ductile shear. However, outstanding questions and uncertainties remain regarding the driving factors that led to localization and abandonment of the AFS. I present new geologic mapping of the Atacama and Taltal fault systems that illustrates the spatial distribution, geometry, and timing, of deformation since the late Paleozoic. Refined spatial patterns of mylonitic fabric indicate that only two spatially-extensive mylonitic zones are present in the map area and both are restricted to thermal aureoles of Mesozoic plutons; an older shear zone is connected to the Middle Jurassic Matancilla granodiorite, and the other is located at the margin of the Early Cretaceous Cerro Del Pingo pluton along the AFS. In contrast to

previous interpretations, the Matancilla shear zone is spatially, geometrically, and temporally incompatible with the Early Cretaceous AFS and is instead related to Middle Jurassic intrusion of that pluton. Mylonitic fabric is present both within the pluton and in the thermal aureole, and the most highly strained rocks are in the Paleozoic Chañaral Complex quartzite and phyllite surrounding the pluton. Textural and spatial patterns of ductile shear satisfy criteria for determining that the shear zone surrounding the pluton reflects the regional strain field and not localized stresses due to pluton emplacement, suggesting that plate convergence imparted a sinistral obliquity during Middle Jurassic subduction that was partitioned to the magmatic arc. The geometry and location of the Early Cretaceous AFS is independent of the Matancilla shear zone, indicating that inherited anisotropy was not a contributing factor to localization of the intra-arc AFS.

The NW-striking sinistral Taltal fault, and a system of parallel faults that together compose the Taltal fault system (TFS), cross-cut the AFS in the late Early Cretaceous with 10.6 km cumulative sinistral shear across a ~15 km-wide zone. Timing constraints from U-Pb zircon and calcite geochronology restrict the switch between fault systems to 114–107 Ma, which is 5–12 Myr after the youngest synkinematic plutonism that localized AFS ductile shear. A kinematic switch from the AFS to the TFS corresponds temporally to eastward migration of the magmatic arc, development of a widespread unconformity across the South American plate, and inversion of rift basins, and likely stems from a global plate reorganization at the end of the Early Cretaceous. Abrupt thickness changes of Jurassic strata, collocation with a sharp aeromagnetic anomaly, and Late Jurassic to Early Cretaceous ages of dikes and veins that intrude the Taltal fault suggest that the fault system reactivated a pre-existing crustal weakness.

A second case study concerns a distributed fault system in the southwestern United States near Blythe, California, where NW-striking faults span two tectonic provinces: the Colorado River extensional corridor, which has experienced high-magnitude Miocene extension via detachment faults, and the Eastern California Shear Zone and San Andreas fault systems, which record Neogene to Quaternary dextral faulting. Previously the timing of this fault system in this area was poorly constrained, and the tectonic significance faults was unclear. We present kinematic data and new geochronology to further constrain the structural evolution of faulting in this region and find evidence that these faults record a shift between late Miocene strain regimes. A kinematic shift from normal to dextral faulting is compatible with a documented regional transition from early to middle Miocene NE-directed extension during detachment fault slip to distributed E-W extension and strike-slip faulting. We estimate 10–38 km of cumulative dextral slip occurred across a ~55 km wide zone from the Palen to Riverside mountains, which may partly alleviate discrepancies of cumulative dextral shear estimated by palinspastic reconstructions in the region.

Together, these case studies provide findings relevant to global understandings of strike-slip systems connected to plate-boundary oblique motion. Our observations suggest that intra-arc faults may be transient rather than long-lived features and form independent of pre-existing crustal anisotropy. Ductile shear in intra-arc systems near the brittle-plastic transition is dependent on several spatial and lithologic criteria which leads to heterogeneity and lack of along-strike continuity. When the thermal influence of magmatism wanes, or plate boundary dynamics change the regional stress field, strain may favor reoccupation of previously formed crustal weaknesses. Distributed strike-slip systems are an important part of accommodating such

brittle strain, and cumulative shear magnitudes may be much greater across a system of connected faults than for the single greatest structure in a strike-slip system.

ACKNOWLEDGEMENTS

I owe an enormous debt to my advisor for this project, Dr. John Singleton. John's enduring optimism, support, and encouragement carried me through the past four and a half years.

This research benefited immeasurably from my interactions with collaborators from Colorado State University, Pontificia Universidad Católica de Chile, US Geological Survey, Northern Arizona, and others. Beyond just our academic interactions, I've shared wonderful experiences and am lucky to have such excellent people as both colleagues and as friends.

Funding for this project was provided by research grants from the National Science Foundation and Geological Society of America. I am deeply grateful for scholarships from the Warner College of Natural Resources and American Institute of Professional Geologists that provided support during my graduate studies.

Lastly I am deeply grateful for the support from my family and my wonderful partner Karina. I couldn't have done this without you.

TABLE OF CONTENTS

ABSTRACT	ii
ACKNOWLEDGEMENTS.....	vi
LIST OF SUPPLEMENTARY DATA INCLUDED SEPARATELY	xi
1. INTRODUCTION	1
2. TIMING, KINEMATICS, AND DISPLACEMENT OF THE TALTAL FAULT SYSTEM, NORTHERN CHILE: IMPLICATIONS FOR THE CRETACEOUS TECTONIC EVOLUTION OF THE ANDEAN MARGIN	5
2.1. Introduction.....	5
2.2. Geologic Setting	7
2.3. Previous Work	9
2.4. Methods	10
2.4.1. Zircon U-Pb Geochronology and (U-Th)/He Thermochronology.....	11
2.4.2. Calcite U-Pb Geochronology	12
2.5. Distribution, Geometry, and Offset of TFS Faults.....	13
2.5.1. Map Relationships.....	13
2.5.2. Correlation of Units Across the Taltal Fault	15
2.5.3. Kinematics	19
2.5.4. Cross-Cutting Relationships and Geochronology Results.....	21
2.6. Discussion.....	26
2.6.1. Structural Inheritance of the TFS	26
2.6.2. Timing of the TFS.....	29
2.6.3. Relationship of TFS Kinematics to Cretaceous Plate Tectonics	32
2.7. Conclusions.....	33
3. SINISTRAL SHEAR DURING MIDDLE JURASSIC EMPLACEMENT OF THE MATANCILLA PLUTONIC COMPLEX IN NORTHERN CHILE (25.4° S) AS EVIDENCE OF OBLIQUE PLATE CONVERGENCE DURING THE EARLY ANDEAN OROGENY	52
3.1. Introduction.....	52
3.2. Geologic setting.....	54
3.3. Methods	57
3.4. Pre-mylonitic Deformation recorded in the Paleozoic Chañaral Complex	58
3.5. Geometry, kinematics, and microstructures of mylonitic fabrics associated with the Matancilla plutonic complex.....	59
3.5.1. Field relations.....	59
3.5.2. Mylonite in Chañaral Complex metasedimentary rocks in the Matancilla pluton aureole.....	61
3.5.3. Matancilla protomylonite	62
3.5.4. Discrete shear zones in the Matancilla plutonic complex	63

3.6. Development of mylonitic fabrics.....	65
3.6.1. Rheology and shear zone deformation conditions.....	65
3.6.2. Shear zone kinematics.....	69
3.6.3. Timing.....	70
3.7. Discussion.....	72
3.7.1. Mylonite as a record of regional tectonic stresses.....	72
3.7.2. Localization of the AFS.....	72
3.7.3. Implications for plate tectonics.....	74
3.8. Conclusions.....	75
4. GEOLOGIC MAP OF THE ATACAMA AND TALTAL FAULT SYSTEMS NEAR TALTAL, CHILE: NEW CONSTRAINTS FOR THE EVOLUTION OF THE ANDEAN MARGIN.....	87
4.1. Introduction.....	87
4.2. Geologic setting.....	89
4.3. Methods.....	91
4.3.1. Geologic mapping and structural data collection.....	91
4.3.2. Zircon U-Pb geochronology.....	92
4.4. Deformation of the Paleozoic Chañaral Complex and early Mesozoic magmatism.....	92
4.5. Atacama fault system.....	93
4.5.1. Field relations.....	94
4.5.2. Ductile deformation and relation to igneous units.....	95
4.5.3. AFS brittle deformation.....	98
4.6. Taltal Fault system.....	99
4.6.1. Field relations.....	99
4.6.2. Distribution of brittle deformation.....	100
4.7. Age and structure of Mesozoic volcanic and sedimentary rocks.....	100
4.7.1. Ages of volcanic rocks.....	100
4.7.2. Folds in Jurassic-Cretaceous volcanic rocks.....	103
4.8. Cenozoic sedimentation hiatus and alluvial lineaments.....	105
4.9. conclusions.....	106
5. MIOCENE NORMAL AND DEXTRAL FAULTING IN THE LOWER COLORADO RIVER CORRIDOR NEAR BLYTHE, CALIFORNIA.....	116
5.1. Introduction.....	116
5.2. Geology of the Blythe region.....	117
5.3. Methods.....	119
5.3.1. Fault kinematic data collection.....	119
5.3.2. Calcite U/Pb geochronology.....	120
5.3.3. Sanidine ⁴⁰ Ar/ ³⁹ Ar geochronology.....	121
5.4. Faults in the Big Maria Mountains.....	122

5.4.1. Eagle’s Nest, Maria Wilderness, and Slaughter Tree Wash faults	122
5.4.2. Maria fault.....	129
5.4.3. Blythe graben	131
5.5. Faults in the Little Maria Mountains.....	132
5.5.1. Valley fault.....	132
5.6. Packard Well fault zone	134
5.7. Faults in the Palen and McCoy Mountains	137
5.8. Northwest-striking faults southeast of Blythe.....	139
5.9. Discussion.....	142
5.9.1. Overall fault kinematic patterns	142
5.9.2. Fault timing	145
5.9.3. Structural inheritance	149
5.9.4. Cumulative dextral shear of NW-striking faults	150
5.9.5. Fault connections to other regional structures.....	153
5.9.6. Connections to regional tectonics	154
5.10. Conclusions.....	156
6. CONCLUSIONS	176
6.1. Localization of intra-arc faults.....	176
6.2. Significance of distributed deformation.....	179
6.3. Methodology for studying strike-slip faults.....	180
6.3.1. Estimating offset	180
6.3.2. Methods to constrain deformation timing	181
REFERENCES	182
APPENDIX A: FRICTIONAL SLIDING ANALYSIS OF THE ATACAMA AND TALTAL FAULT SYSTEMS	209
Reduced friction coefficient.....	212
Elevated pore fluid pressures	213
Orientation of the principal stress axes	213
Transitions between faults and fault strength.....	213
APPENDIX B: DESCRIPTION OF MAP UNITS	219
Paleozoic.....	219
PZms(c) – Metasedimentary rocks of the Chañaral Complex (Paleozoic).....	219
Triassic.....	220
Trg(c) – Capitana syenogranite (~215–207 Ma).....	220
Jurassic.....	220
Jgd(cc) – Cerro Concha granodiorite (~195 Ma)	220
EJgd – Early Jurassic Granodiorite (~189 Ma)	221

Jv – La Negra Formation volcanic and volcanoclastic rocks (Jurassic).....	221
Jgd(m) – Matancilla plutonic complex granodiorite (~169 Ma)	222
Jpg(sr) and Jfg(sr) – Quebrada San Ramón intrusive complex	223
Jgd(q) – Quezada intrusive complex (153 Ma)	224
JKgd(lf) – La Finca pluton granodiorite (149–139 Ma).....	224
Cretaceous.....	224
JKv(r) – Rhyolite (145–146 Ma).....	224
JKv – Aeropuerto Formation volcanic and volcanoclastic rocks (~146–122 Ma).....	226
Km – Marine limestone and carbonate-cemented clastic strata (Early Cretaceous)	226
Kcg(g), Kmg(g), Kfg(g), Kr(g) – Goyenchea intrusive complex (142–130 Ma).....	227
Kqd – Quartz diorite near Cerro del Pingo (Early Cretaceous).....	228
Kgd – Cretaceous granodiorite (~140 Ma).....	229
Kgd(lt)– Las Tipias granodiorite (~130 Ma).....	229
Kt(cp1) and Kt(cp2) – Cerro del Pingo plutonic complex older (134–132 Ma) and younger (120–119 Ma) intrusions.....	230
Kt(bs) – Barreal Seco tonalite (125-121 Ma).....	231
Kc(u) – Undivided cataclasite (Early Cretaceous)	231
K(d) – Early Cretaceous andesite dike (~110 Ma).....	232
Neogene	233
Qoa – Older alluvium (Miocene to Pleistocene)	233
Qa – Alluvium (Pleistocene to Holocene).....	233
ml – modified land (Holocene)	234

LIST OF SUPPLEMENTARY DATA INCLUDED SEPARATELY

Plate 1: Chapter 4 Geologic map of the Atacama and Taltal fault systems - North

Plate 2: Chapter 4 Geologic map of the Atacama and Taltal fault systems - Central

Plate 3: Chapter 4 Geologic map of the Atacama and Taltal fault systems - South

Dataset 1: Chapter 3 Zircon U-Pb analytical data

Dataset 2: Chapter 4 Zircon U-Pb analytical data

Dataset 3: Chapter 5 Tabulated structural data for stereoplots

Dataset 4: Chapter 5 Cumulative shear magnitude estimates

Dataset 5: Chapter 5 Calcite U-Pb analytical data

Dataset 6: Chapter 5 Sanidine $^{40}\text{Ar}/^{39}\text{Ar}$ analytical data

1. INTRODUCTION

Strike-slip faults are important structures in accommodating shear both oblique and parallel to plate boundaries and are present in both convergent and divergent settings. Most convergent plate boundaries have oblique motion (Woodcock, 1986; Philippon and Corti, 2016), and strike-slip faults can accommodate significant deformation via plate margin-parallel translation (e.g., Umhoefer and Dorsey, 1997). Strain may be distributed across many faults within a translational or vertical-axis block rotation system (Nur et al., 1986; Garfunkel, 1989). Strain in oblique margins can be partitioned between margin-parallel strike-slip faults and dip-slip faults or folds that accommodate margin-normal deformation; partitioning has been recognized at plate boundaries around the world (e.g., Lettis and Hanson, 1991; Lallemand and Oldow, 2000; McCaffrey et al., 2000; Calais et al., 2002). Crustal anisotropy can have a profound effect on the localization of strike-slip faults (e.g., Curren and Bird, 2014); pre-existing faults, lithologic interfaces, and thermally- and/or hydrothermally-weakened zones can all influence the location of major structures.

Of particular interest to plate-boundary strike-slip systems are intra-arc fault systems, which localize along the axis of a magmatic arc in the upper plate of a subduction system. Association of intra-arc fault systems with the magmatic arc axis suggests that the thermal and hydrothermal influence of magmatism weakens the crust and reduces the depth of the brittle-plastic transition, where rheologic strength is greatest. While the existence of modern and fossil intra-arc strike-slip systems has been well documented, fundamental questions remain about their rheologic controls, longevity, and the effect of structural inheritance on these fault systems. Research questions concerning intra-arc strike-slip systems addressed herein include:

- What is the spatial and temporal distribution of brittle and ductile deformation in an intra-arc system and how does this distribution relate to magmatism?
- How are intra-arc fault systems influenced by pre-existing crustal weaknesses?
- What factors contribute to abandonment of intra-arc fault systems?
- Are intra-arc strike-slip systems long-lived features of an evolving plate margin?

Of additional interest to understanding strike-slip fault systems is those with distributed or diffuse deformation. Many strike-slip systems do not have strain coalesced into major regional-scale faults but instead have deformation spread across numerous kinematically compatible faults, sometimes across zones tens to hundreds of kilometers wide. The cumulative shear magnitude across such systems may be significant but difficult to recognize. Rigid block-model palinspastic reconstructions that do not account for shear on smaller faults within distributed systems will have inherent inaccuracies and overestimate the magnitude of slip on the largest faults in the system, potentially leading to flawed estimates of slip rate or seismic hazard. Research questions concerning distributed fault systems include:

- How does slip across a distributed strike-slip system relate to slip on the largest faults?
- How do pre-existing weaknesses and changing stress/strain regimes affect development of distributed fault systems?

The research goals presented here are addressed using two case studies. Chapters 2, 3, and 4 are centered on a field area in the Atacama Desert of northern Chile, where the Early Cretaceous intra-arc Atacama fault system (AFS) is well exposed with both brittle and ductile structures. Chapter 2 documents the timing, kinematics, and displacement of the brittle Taltal fault system (TFS), which cuts the AFS, and investigates the role of inherited crustal weaknesses

on this distributed fault system. Chapter 3 examines the Matancilla shear zone, which is spatially associated with the Middle Jurassic Matancilla pluton rather than the Early Cretaceous AFS, and explores implications for Jurassic plate convergence directions and the role of inherited fabrics on the AFS. Chapter 4 presents geologic mapping of a ~75 km swath of the Atacama and Taltal fault systems to document patterns of brittle and ductile deformation and the deformation history of the region since the Paleozoic. Chapter 5 is centered on a separate field area in SE California, where a distributed fault system with poorly-constrained timing and kinematics may have accommodated significant strike-slip displacement and affected deposition patterns of the ancestral Colorado River. This chapter documents the timing, changing kinematics, and cumulative slip magnitude of this distributed fault system and how it relates to plate-boundary dynamics.

This research is unified in part by methodological themes, with emphasis on using geologic mapping, structural analysis, and geochronology to better constrain the timing and kinematic significance of strike-slip systems. Geologic mapping is particularly effective for reconstructing deformation associated with larger strike-slip fault systems, as displacement markers can be evaluated in map-view, which is often not possible for dip-slip structures. For large strike-slip fault systems, slight obliquities of slip vectors can lead to significant magnitudes of vertical separation. Fault kinematic data can be used to evaluate slip vectors in areas where ideal piercing points are not available. Unlike dip-slip systems, strike-slip faults commonly do not preserve a sedimentary record of their activity, so field relationships coupled with geochronology are essential for determining the timing of slip. Cross-cutting relationships are often unable to tightly constrain the ages of some faults, and novel methods such as calcite U-Pb geochronology provide an opportunity to date mineralization that can constrain deformation

timing. Interplay between strike-slip faults and geometric complexities such as stepovers, splays, and bends allow fault systems to transfer deformation between structures, and these can create pathways for focused fluid flow and mineralization (e.g., Cox, 2005) as well as generate significant vertical displacement. Potential fields geophysical datasets are useful to assess the extent of faulting in the subsurface and can be an indispensable aid to assess concealed fault connections, geophysical offset markers, and inherited structures (e.g., Johnson et al., 2004; Langenheim et al., 2010a, 2010b; Langenheim and Miller, 2017).

2. TIMING, KINEMATICS, AND DISPLACEMENT OF THE TALTAL FAULT SYSTEM, NORTHERN CHILE: IMPLICATIONS FOR THE CRETACEOUS TECTONIC EVOLUTION OF THE ANDEAN MARGIN¹

2.1. INTRODUCTION

Tectonic activity in northern Chile has been dominated by subduction and arc magmatism since at least the Early Jurassic (e.g., Coira et al., 1982; Parada et al., 2007). In the Coastal Cordillera, plutons and volcanic deposits of the Jurassic to Early Cretaceous arc are dissected by an extensive system of NW striking sinistral faults from 25.4° to 27.2°S (Figure 2.1). Timing constraints suggest that some of these faults were active only in the Jurassic (Bonson, 1998; Contreras et al., 2013), whereas others clearly displace Early Cretaceous units. The largest magnitude sinistral displacement on an individual NW striking fault (7.5 km) occurs at the Taltal fault (Figures 2.1 and 2.2). The Taltal fault and nearby parallel faults (herein referred to as the Taltal fault system, TFS) displace the Atacama fault system (AFS), a major tectonic feature that traces more than 1,000 km north-south in the Coastal Cordillera and accommodated brittle-ductile sinistral shear in response to oblique convergence in the Early Cretaceous (Scheuber and Andriessen, 1990). The shift from slip on the AFS to TFS marks a notable change in deformation geometry and style near the active margin. While AFS deformation timing is well documented, the timing of slip on the TFS is largely unconstrained beyond its relative timing with the AFS. Evidence that AFS brittle deformation continued as late as ~110 Ma (Seymour et al., 2020)

¹Chapter published as Mavor, S.P., Singleton, J.S., Gomila, R., Heuser, G., Seymour, N.M., Williams, S.A., Arancibia, G., Johnston, S.M., Kylander-Clark, A.R.C., and Stockli, D.F., 2020, Timing, Kinematics, and Displacement of the Taltal Fault System, Northern Chile: Implications for the Cretaceous Tectonic Evolution of the Andean Margin: *Tectonics*, doi:10.1029/2019TC005832.

Supporting information tables and analytical data referenced in this chapter are available from: <https://agupubs.onlinelibrary.wiley.com/doi/abs/10.1029/2019TC005832>

suggests that the most recently published 125–110 Ma age estimates for the younger Taltal fault (Espinoza et al., 2014) require revision.

The paleomagnetic studies suggest that NW striking faults in the Coastal Cordillera accommodated vertical axis clockwise block rotation that cannot be fully explained by the development of the Bolivian orocline (Randall et al., 1996) and reveal that the Taltal fault is an important structural boundary that separates domains with a marked difference in tectonic rotations (Contreras, 2018). One kinematic model for clockwise rotation links NW striking faults to the transpressional Chivato fault system to form a crustal sinistral strike-slip duplex in the Late Cretaceous after AFS abandonment (e.g., Grocott and Taylor, 2002; Randall et al., 1996; Taylor et al., 1998). According to this model, oblique convergence was largely partitioned between margin-parallel sinistral shear east of the AFS and margin orthogonal shortening along NW striking faults in the Coastal Cordillera. Another tectonic model relies on kilometer-scale displacement of the Taltal fault during dextral transpression and rotation of large-scale domino blocks in the middle-late Eocene (Abels and Bischoff, 1999), yet it is unclear if the fault was active at that time.

Regionally, some NW striking faults are interpreted to wholly predate the AFS, whereas others postdate or evolved contemporaneously with the AFS (Bonson, 1998). Mapped relationships in the Jurassic La Negra Formation suggest that slip on NW striking sinistral faults near Cifuncho ceased in the Late Jurassic (Contreras et al., 2013). NW striking faults near Antofagasta are well documented as secondary faults that splay from and developed contemporaneously with AFS fault strands in a transtensional duplex arrangement (Cembrano et al., 2005; Jensen et al., 2011; Veloso et al., 2015). Northwest striking faults in the Precordillera

have well documented sinistral offset in the Eocene; however, an along-strike connection of these faults to the Taltal fault has been hypothesized but not demonstrated (Abels and Bischoff, 1999). While some TFS slip clearly postdates the AFS, the origin of the TFS and genetic relationship to parallel Jurassic faults are unclear. In addition, detailed kinematic data from the TFS and related NW striking faults in the Coastal Cordillera have not been published, so it is unclear to what extent this fault system records transpression or transtension. Here we present new geologic mapping and geochronology of units with prekinematic and synkinematic relationships to the TFS that constrain the slip history of the fault system, and we present brittle fault data that record the changing kinematic regime of the Cretaceous Chilean Coastal Cordillera.

2.2. GEOLOGIC SETTING

The oldest rocks exposed in the Coastal Cordillera of northern Chile are late Paleozoic metasedimentary rocks of the Chañaral epimetamorphic complex. These rocks recorded multiple episodes of deformation during late Paleozoic subduction and terrane accretion (Bell, 1982; Fuentes et al., 2016). Triassic clastic strata overlying the Chañaral epimetamorphic complex record syndepositional extension and sedimentation patterns that suggest structural control by NW striking half-graben basins in northern Chile (Suarez and Bell, 1992; Tankard et al., 1995). Additional structurally controlled Triassic depocenters are widespread across central Chile and eastern Argentina (Charrier et al., 2007). The Andean orogenic cycle began by the Early Jurassic and in the early stages was characterized by arc-normal extension recorded by dikes and back-arc basin sedimentation (Charrier et al., 2007; Scheuber, 1994; Scheuber and Gonzalez, 1999). Southeast directed subduction oblique to the N-S trench imparted a sinistral margin-parallel shear component with some deformation recorded in the Early-Middle Jurassic and clearly recorded by the trench-linked AFS in the Early Cretaceous (Scheuber and Andriessen, 1990;

Scheuber and Gonzalez, 1999). The AFS localized in the rheologically weak magmatic arc (Brown et al., 1993; Grocott et al., 1994), where elevated geothermal gradients near synkinematic plutons enabled ductile deformation at ~5–10 km crustal depths (Bonson, 1998; Seymour et al., 2020). Several ~139–119 Ma syntectonic plutons record the timing of ductile strain (e.g., Brown et al., 1993; Espinoza et al., 2014; Seymour et al., 2020; Wilson et al., 2000), which is overprinted by continued deformation in the brittle regime. Near the end of the Early Cretaceous, AFS deformation waned as arc magmatism migrated eastward from the Coastal Cordillera toward the present location in the high Andes (Dallmeyer et al., 1996; Scheuber et al., 1994), with a magmatic hiatus at ~90–80 Ma (Haschke et al., 2002). Recent work by Seymour et al. (2020) indicates that brittle slip on the AFS near Taltal was in its final stages at ~110 Ma. The AFS was subsequently cut and displaced by the TFS. Migration of the magmatic arc and residual cooling of the Coastal Cordillera coincides with the cessation of slip along the AFS (Brown et al., 1993; Seymour et al., 2020).

Late Cretaceous and Paleogene deposits are not preserved in the Taltal region. East of the Coastal Cordillera, Late Cretaceous volcanic rocks unconformably overlie folded Early Cretaceous deposits. Deformation and erosion associated with this angular unconformity is tied to the Peruvian phase of the Andean orogeny with regional crustal shortening and uplift (Scheuber et al., 1994), and basin deposits in the Precordillera record Peruvian phase deformation beginning as early as 107 Ma (Bascuñán et al., 2016). Additional margin-normal shortening events in the Cenozoic and development of the Bolivian orocline imparted a clockwise vertical axis rotation to the Taltal region (Contreras, 2018).

Previous studies suggest that NW striking faults in the Coastal Cordillera occupy preexisting weaknesses inherited from Paleozoic contraction or Triassic rifting, both of which

imparted a NW-SE structural grain. Collocation of these faults with linear magnetic anomalies suggests that they are situated on deep-seated weaknesses, and some studies suggest these faults are part of major crustal boundaries that extend as far as western Argentina (Abels and Bischoff, 1999; Bonson, 1998). NW striking sinistral faults near Cifuncho cut the lower but not upper members of the La Negra Formation, suggesting they were active in the early Late Jurassic (Contreras et al., 2013). The parallelism between these faults and the Taltal fault raises the possibility that parts of the TFS initiated in the Jurassic or earlier and were reactivated in the Cretaceous. However, parallelism of fault generations is considered equivocal criteria to establish fault reactivation (Holdsworth et al., 1997). Improved timing and kinematic constraints for the TFS are needed to determine how development of the TFS relates to the pre-Cretaceous structural grain, the end of AFS slip and migration of the magmatic locus, and Late Cretaceous to Cenozoic shortening events.

2.3. PREVIOUS WORK

Reconnaissance geologic mapping by Arabasz (1968) recognized that the Taltal fault cuts and displaces the eastern strand of the AFS by ~10 km near the town of Taltal, and more recent estimates revise this displacement to ~8 km (Escribano et al., 2013). Limited fault plane orientation data collected by Arabasz (1971) indicate that TFS strands are near vertical to steeply northeast dipping. From the observation that the Taltal fault juxtaposes deeper-level Paleozoic metasedimentary rocks and plutons on the northeast side against shallow level volcanic and volcanoclastic rocks to the southwest, previous workers have suggested a northeast-up reverse oblique component of slip on the Taltal fault (Escribano et al., 2013; Espinoza et al., 2014). However, detailed kinematic analyses including slickenline orientations that support this hypothesis have not been presented for the TFS.

Recent 1:100,000-scale mapping depicts the Taltal fault cross cutting the 106–101 Ma Librillo plutonic complex and also apparently cut by the older ~110 Ma Tropezón plutonic complex (Espinoza et al., 2014). This inconsistency also conflicts with the reported 125–110 Ma age range of the Taltal fault (Espinoza et al., 2014), bracketed between the end of AFS ductile deformation and intrusion of the Tropezón pluton. Descriptions of mine workings in the Tropezón and Librillo plutonic complexes suggest that both plutons are cut by faults (Escribano et al., 2013; Tornos et al., 2010), though these faults have not been tied to the TFS. Escribano et al. (2013) describe a small body of rhyolite along the Taltal fault that they interpret as Late Cretaceous and either postkinematic or synkinematic with the fault, though no direct geochronology of the rhyolite has been presented to test this hypothesis.

2.4. METHODS

We mapped the TFS near its intersection with the AFS to clarify the timing and kinematic relationships between the TFS, AFS, and Cretaceous igneous units. Mapping was performed at 1:20,000 scale with key areas mapped at 1:10,000 scale and compiled and digitized using Esri ArcGIS 10.5.1 to align with the Esri world imagery basemap. We collected new high-resolution aerial imagery for key areas using a DJI Phantom 4 pro drone flown at altitudes <300 m above ground level. Photosets were processed in Agisoft Photoscan Pro to generate georeferenced orthomosaic images to support our field observations.

We collected fault-slip data from the Taltal fault and parallel strands, noting location, fault rock and mineralization, and confidence of slip-sense interpretation (Table S1 in the supporting information). Where offset markers were not directly visible in outcrop, sense of slip was determined using R- and T- fracture criteria (Petit, 1987), slickenfiber steps, asymmetric

folding, or oblique foliation in fault gouge. Slip sense was assumed for some measurements either along strike from, or with similar geometry to, faults of known slip sense.

Structural data were analyzed using Stereonet 10.1.1 (Allmendinger et al., 2011; Cardozo and Allmendinger, 2013) and FaultKin 7.7.4 (Allmendinger et al., 2011; Marrett and Allmendinger, 1990) software. Orientation averages reported in the text are calculated using the maximum eigenvector. We determined incremental shortening and extension axes (P and T axes) for paired fault plane and slickenline lineation measurements (e.g., Marrett and Allmendinger, 1990), and cumulatively the mean axes reflect overall finite strain patterns.

2.4.1. Zircon U-Pb Geochronology and (U-Th)/He Thermochronology

We processed samples for zircon separation using standard magnetic and heavy liquid separation methods. Isotopic analytical data were collected with UTChron facilities at the University of Texas at Austin. Zircon U-Pb data were collected using laser ablation-inductively coupled plasma-mass spectrometry. Zircon grains were mounted parallel to the c axis on a tape mount and analyzed by a depth-profiling method. Data collection and reduction were performed following UTChron laboratory procedures outlined in Marsh and Stockli (2015) and Seymour et al. (2016), and errors propagated through data reduction. Unless stated otherwise, U-Pb dates referred to in the text are reported as mean $^{206}\text{Pb}/^{238}\text{U}$ dates $\pm 2\sigma$ uncertainty with grains filtered for $<10\%$ $(^{206}\text{Pb}/^{238}\text{U})/(^{207}\text{Pb}/^{235}\text{U})$ discordance calculated using the weighted mean calculation of Isoplot (Ludwig, 2003). Kernel density estimator plots are prepared using DensityPlotter software (Vermeesch, 2012) using the default optimal bandwidth calculated by the program. We employed single-grain zircon (U-Th)/He analysis following the methods of Wolfe and Stockli (2010) for one sample with insufficient zircon for a robust U-Pb analysis and probable xenocrystic zircon grains. Dates from such analyses represent the time at which the grains passed

below the zircon He closure temperature of ~180–190 °C (Reiners et al., 2002, 2004; Wolfe and Stockli, 2010). Based on laboratory reproducibility of standards, an 8% analytical uncertainty is reported for each aliquot.

2.4.2. Calcite U-Pb Geochronology

The calcite-bearing fault surfaces with clear slip-sense indicators were sampled to directly date fault displacement using U-Pb calcite geochronology. Approximately 120 µm thick sections were prepared from samples cut perpendicular to the fault plane and parallel to the slip direction. Isotope analyses were performed on the thick sections using the University of California, Santa Barbara Dual laser ablation inductively coupled plasma-mass spectrometry facility following the analytical procedures of Kylander-Clark et al. (2013) and Nuriel et al. (2017). For each investigated sample, calcite from a variety of textural settings within the mineralized portion of the fault was microsampled using an 85 µm spot run at 10 Hz for 15 s. Unknown analyses were corrected for instrument drift and mass bias using a combination of analyses from NIST614 glass and calcite standard WC-1 (254 Ma; Roberts et al., 2017) that were measured periodically throughout the analytical session. Given the variation in U-Pb ratios observed in most calcite samples, initial Pb compositions and dates can be calculated by regression of individual spot analyses on a Terra-Wasserburg diagram and reported dates with 95% confidence errors are lower-intercept dates calculated using Isoplot (Ludwig, 2003). Low-U analyses with $^{238}\text{U}/^{206}\text{Pb} < 0.53$ that are inversely discordant have been removed from our preferred age calculations to avoid regression errors associated with potentially inherited or contaminant Pb, although inclusion of low-U analyses still yields ages that overlap within error of our preferred ages. Analyses of calcite standards ASH 15D (3.001 ± 0.012 Ma [2σ], Mason et al., 2013; Vaks et al., 2013) and Duff Brown (64.0 ± 0.7 Ma [2σ], Hill et al., 2016) analyzed

throughout the analytical session yielded dates with 95% confidence errors of 3.14 ± 0.13 Ma and 66.4 ± 4.0 Ma, respectively, and that overlap within uncertainty of their accepted ages.

2.5. DISTRIBUTION, GEOMETRY, AND OFFSET OF TFS FAULTS

2.5.1. Map Relationships

All map-scale faults in the study area pertain to the NNW striking AFS or the younger NW striking TFS. The AFS is composed of two main NNW tracing faults ~5 km apart with intervening parallel subsidiary fault strands (Figure 2.3). The eastern strand of the AFS separates Paleozoic metasedimentary rocks and Mesozoic plutons east of the fault from Cretaceous andesites and volcanoclastic rocks west of the fault. The AFS eastern strand is near vertical and provides an excellent marker of horizontal offset across TFS faults. Mylonite zones up to 1.2 km thick and cataclasite zones up to 300 m thick are found only along the eastern strand, suggesting that this fault accommodated the most deformation and is the most significant strand of the fault zone. The western branch of the AFS juxtaposes Jurassic andesites against Cretaceous volcanic and clastic rocks with a gouge core and lacks mylonite or extensive cataclasite.

A prominent NNW to NW striking fault called El Muelle fault locally parallels both the AFS and TFS. The strike of the El Muelle fault changes from 344° near the intersection with the western branch of the AFS to 327° as it approaches parallelism with the Taltal fault, which likewise curves gently from strike 310° near the intersection with the AFS to 320° near Taltal. Alluvium conceals the intersection zone of the El Muelle fault and AFS fault strands to the north with the AFS western branch, so it is unclear if the El Muelle fault splays from or is the direct continuation of the AFS western branch; we follow the nomenclature of Espinoza et al. (2014) to treat these faults separately. The El Muelle fault cuts Early Cretaceous volcanic rocks, but no

postkinematic units have been identified. In contrast to other AFS fault strands, the El Muelle fault is not clearly displaced by the TFS.

Our geologic mapping identifies all exposed NW striking faults of the TFS that displace the Atacama fault by >10 m between 25.37°S and 25.70°S (Figure 2.3). Faults in the TFS are characterized by entirely brittle deformation with no evidence for associated mylonitic deformation. TFS fault damage zones exhibit brecciation but little cataclasite. Fault cores are instead composed of incohesive gouge and breccia, typically 5–10 m thick, which in several areas have eroded out to form fault-trace topographic lineaments (Figure 2.4). Immediately south of the Taltal fault, several closely spaced parallel faults displace the eastern strand of the AFS with tens to hundreds of meters of sinistral separation (Figure 2.5). South of Quebrada de la Peineta, numerous smaller faults offset the eastern strand of the Atacama fault with tens of meters of separation. We revise the mapping of Arabasz (1971) and Espinoza et al. (2014) to extend the NW striking fault at Quebrada de la Peineta into outcrop south of the Panamerican highway (Figures 2.3 and 2.6). This fault offsets the eastern strand of the AFS by ~990 m across the Quebrada de la Peineta. North of the Taltal fault, two major parallel faults displace the AFS (Figure 2.7). The Quebrada Tipias fault displaces the eastern strand of the AFS by 940 m and has a foliated fault gouge core that in places is up to 26 m thick (Figure 2.4). Near the intersection of the Quebrada Tipias fault and the AFS eastern strand, numerous centimeter-scale thickness calcite veins parallel the Quebrada Tipias fault and cross-cut AFS cataclasite. The northernmost TFS fault to displace the AFS is the El Loro fault, with 360 m sinistral separation of the AFS eastern strand (Figure 2.7). Using the near-vertical eastern strand of the AFS as a marker, we determine 7.5 km of offset on the main Taltal fault and 10.6 km of cumulative offset for all TFS faults across a width of ~15 km (Figure 2.8).

2.5.2. Correlation of Units Across the Taltal Fault

2.5.2.1. Matancilla Pluton

At the intersection with the Taltal fault, the eastern strand of the AFS separates andesite on the west from granodiorite on the east (Figures 2.5 and 2.7). Previous mapping (Espinoza et al., 2014) depicted the thin strip of granodiorite east of the AFS and south of the Taltal fault as the La Finca pluton. However, when displacement across the TFS is restored, these outcrops are isolated from other outcrops of the La Finca pluton. We instead correlate this body with the Matancilla pluton, exposed east of the AFS north of Taltal. Restoration of the TFS aligns the outcrop east of Cerro Breadal to Matancilla granodiorite that intersects the Taltal fault from the north (Figures 2.3 and 2.7). Our new zircon U-Pb date of 169.0 ± 1.6 Ma from the southern strip of hornblende granodiorite (sample 188S61, Figures 2.5 and 2.9, and Table S2) falls within the reported 175–158 Ma U-Pb zircon age range of the Matancilla pluton north of the Taltal fault (Escribano et al., 2013) and contrasts with the 149–139 Ma age range of the La Finca plutonic complex (Espinoza et al., 2014). This date supports the correlation across the Taltal fault indicated by field relationships and lithologic similarity.

2.5.2.2. Spherulitic rhyolite

Following the hypothesis of Arabasz (1968), we correlate the pink spherulitic flow-banded rhyolite south of the Taltal fault (unit *Ksh* of Escribano et al., 2013) to the rhyolite exposed north of the Taltal fault just east of the town of Taltal (unit *Jmh(r)* of Escribano et al. (2013), Figures 2.2 and 2.7). Both units have a conspicuous pink color on fresh faces, millimeter-scale flow banding, and are markedly distinct from the red-brown andesite and gray sandstone that are the dominant lithologies of the Mesozoic volcanic and sedimentary rocks in the region. Thin sections show well-developed radiating spherulites up to 3 mm in diameter with polygonal

boundaries (Figure 2.10). Phenocrysts (4–15%) are dominantly alkali feldspar (3–7%, 1–3 mm), quartz (1–4%, 0.5–2 mm), red-brown euhedral biotite (1–2%, <1 mm), euhedral plagioclase (1–2%, <1 mm), and disseminated opaque grains (<0.5 mm). Quartz in samples from both outcrops has irregular embayment textures (Figure 2.10). The comparable proportions and sizes of phenocrysts, spherulitic texture, millimeter-scale flow banding, and marked lithologic difference with Jurassic and Cretaceous volcanic rocks typical of the region suggest that the rhyolite is a suitable offset marker across the Taltal fault.

North of the Taltal fault, the rhyolite forms resistant outcrops on a N-S ridge from Caleta el Hueso to the Taltal fault. Field relationships indicate that this rhyolite is a flow conformable in the surrounding sequence of andesite flows and volcanoclastic rocks, instead of a dike that intruded these rocks (e.g., Arabasz, 1971; Escribano et al., 2013). The upper and lower contacts of the rhyolite dip westward, concordant with bedding orientations in the surrounding volcanoclastic strata (Figure 2.7). Flow banding within the rhyolites is most commonly parallel to the contacts, but folded flow banding is visible in several outcrops, and measurements not parallel to the contacts have a seemingly random distribution (Figure 2.7). The lower contact of the flow is sharp against the underlying andesite, while the upper contact is marked by several meters of monomict rhyolite breccia that we interpret as flowtop autobreccia. Andesite flows and conglomerates overlying the rhyolite include rhyolitic clasts, clearly demonstrating that these strata postdate extrusion of the underlying rhyolite (Figure 2.10).

The southern rhyolite outcrops trace along the southern side of the Taltal fault for ~2.3 km, with the thickest exposure in the northwest end and a thinning tail extending southeast from this body (Figure 2.7). At the northeastern margin, the rhyolite is truncated by the Taltal fault and juxtaposed against Paleozoic metasedimentary rocks with ~10 m of fault gouge. The

southwestern contact is not well exposed but traces roughly parallel to the Taltal fault and dips steeply. Flow banding measurements in these outcrops are most commonly subparallel with the Taltal fault (Figure 2.7), but folding is also visible at the outcrop scale. Volcaniclastic interbeds between andesite flows surrounding the rhyolite intrusion are shallowly dipping and are not rotated to parallelism with the Taltal fault. Foliation in Paleozoic metasedimentary rocks to the north consistently strikes northeast at a high angle to the Taltal fault, even within 3 m of the fault, suggesting that major fault-proximal rotation has not occurred. Where visible to the southwest of the Taltal fault, stratification in Mesozoic volcanic rocks is gently dipping. From these observations and the elongate outcrop pattern of rhyolite parallel to the Taltal fault, we interpret this rhyolite body to have intruded volcanic rocks on the southeastern side of the fault using the fault as a preferential pathway for magma flow. This intrusive rhyolite likely fed the surficial flows exposed north of the Taltal fault. Our interpretation follows that of Escribano et al. (2013) that intrusion of the southern rhyolite must have followed the Taltal fault or a precursor structure.

Sample 181-S159 was collected from a body of spherulitic rhyolite bound to the north by the Taltal fault (Figure 2.7). Of 55 grains analyzed for zircon U-Pb, a weighted mean average gives a date of 146.3 ± 0.8 Ma at <10% discordance (Mean Square of Weighted Deviates [MSWD] = 4.3) and 146.4 ± 1.7 Ma at <3% discordance (MSWD = 7.6, Figure 2.9 and Table S2). Sample 188-S139 was collected from coastal outcrops of flow-banded rhyolite at Caleta el Hueso (Figure 2.3). U-Pb zircon analyses of 50 grains give a weighted mean average of 143.6 ± 1.2 Ma at <10% discordance (MSWD = 10.7) and 144.7 ± 1.4 Ma at <3% discordance (MSWD = 8.0, Figure 2.9 and Table S2). The two sample dates overlap at 146.1–144.7 Ma when filtered to 3% discordance but do not overlap with a 10% discordance filter (Table S2). These dates

contrast with a published date of 152.0 ± 2.8 Ma (zircon U-Pb SHRIMP; sample TPE-068 of Escribano et al., 2013) for the northern rhyolite body from a sample collected near the Taltal fault (Figure 2.7). However, each of the three dates has a relatively large spread of individual grain dates and high MSWD values for igneous samples, and the weighted mean date may not be the best representation of the true emplacement age of the rhyolite. Kernel density estimate plots of the three samples show overlapping spectra with one distinct peak for each sample (Figure 2.9).

Given the large spread of individual zircon dates in these rhyolite samples, we performed a K-S test comparison (Guynn and Gehrels, 2010) of the three samples following methods for detrital zircon analyses. These tests indicate that samples 181-S159 ($n = 55$) and 188-S139 ($n = 50$) are not statistically differentiable ($p = 0.069$ at $<10\%$ discordance and $p = 0.183$ at $<5\%$ discordance). With caveats noted that the K-S test is considered appropriate only for samples with ≥ 20 analyses and designed to compare samples with similar numbers of analyses (Guynn and Gehrels, 2010), we compared published zircon U-Pb analyses of sample TPE-068 ($n = 19$ via SHRIMP; Escribano et al., 2013) to the two rhyolite samples analyzed in this study. Both comparisons reject the null hypothesis and determine that sample TPE-068 (no discordance filter) is statistically different from samples 181-S159 (at $<10\%$ discordance, $p = 0.0005$) and 188-S139 (at $<10\%$ discordance $p = 0.00009$). Aside from a possible hiatus between individual flows, we have no compelling geologic reason why sample TPE-068 should have an age several million years different than its seemingly along-strike equivalent sample 188-S139 (Figure 2.3). The statistical difference between samples may instead reflect the discrepancy in the number of analyses or comparison across different analytical methods. Based on the lithologic similarity of all rhyolite outcrops and the results of the K-S test that show that the two rhyolite samples dated

in this study via the same analytical method are not statistically dissimilar, we interpret the rhyolite as a satisfactory offset marker across the Taltal fault.

While field relationships suggest the southeastern rhyolite outcrops intruded at deeper levels than the northwestern counterpart outcrops, the magnitude of vertical separation cannot be resolved. The amount of horizontal offset required to juxtapose rhyolite outcrops across the Taltal fault is a minimum of 7.5 km and a maximum of 10.0 km. The eastern strand of the AFS is offset 7.5 km across the main strand of the Taltal fault and offset 0.9 km by the Quebrada Tipias fault. The northwestern extent of the Quebrada Tipias fault is concealed by alluvium, but it most likely merges with the Taltal fault (Figure 2.7). If the 8.4 km cumulative sinistral separation on these two faults is restored, the rhyolite north of the Taltal fault will align with the thickest part of the rhyolite exposure to the south; this reconstruction appears to be the most reasonable pre-TFS configuration. If the interpretation that the southern outcrop represents a deeper exposure level of the rhyolite is correct, it would indicate a component of NE down slip across these faults.

2.5.3. Kinematics

Measurements of the principal slip surface of the Taltal fault are vertical or dip steeply northeast (average principal slip plane is oriented 327, 80 NE; Figure 2.11). Slickenline lineations are generally shallowly raking, though sparse dip-slip lineations are observed. From measurements of all faults belonging to the TFS, the average fault plane is slightly steeper (309, 84 NE) and the average slickenline lineation plunges shallowly northwest (309/11). Kinematic indicators such as Riedel shears, T-fractures, and oblique gouge foliations (Figure 2.4) consistently indicate sinistral kinematics. We calculated a slip lineation perpendicular to the intersection of the average principal slip surface (315, 80°NE) and average gouge foliation (339,

74°E) following Moore (1978); this slip vector (319/17) has a slightly steeper northwest plunge than the average of slickenline lineation measurements (Figure 2.11). P- and T-kinematic axes for fault planes with slickenline lineations are oriented in shallow E-W and N-S clusters, respectively, with the average P axis shallowly west plunging (261/10). A fault plane solution from linked Bingham vector statistics gives a steeply northeast dipping nodal plane (309, 87°NE) and a shallowly northwest plunging slip lineation (309/08). These kinematic data indicate that TFS is a nearly pure strike-slip fault system with a slight NE down extensional component. These kinematics refute the interpretation that a reverse component of oblique slip on the Taltal fault exhumed metasedimentary rocks of deeper crustal levels in the hanging wall (Escribano et al., 2013; Espinoza et al., 2014). Instead, we emphasize that this apparent difference of exposure levels is seen across the eastern strand of the AFS and was merely displaced by the Taltal fault (Figure 2.3).

Using the linked Bingham solution plane and slip lineation for the TFS and 7.5 km of measured sinistral horizontal separation, the Taltal fault records 990 m of NE down throw and 50 m of extensional heave. Using the linked Bingham solution plane and slip vector and 10.6 km of cumulative horizontal separation across all map-scale TFS faults, the cumulative NE-down throw is 1,390 m and the cumulative extensional heave is 70 m. Similar calculations made using the less steeply dipping average measured TFS fault plane and more steeply plunging average measured slickenline lineation give 2,040 m throw and 220 m heave for the entire fault system, and 1,450 m throw and 150 m heave for the Taltal fault alone.

While no suitable marker horizons exist to test these hypothesized dip-slip offset amounts, the component of NE down slip is consistent with the deeper exposure levels we interpret for the footwall rhyolite body. Furthermore, we note that the NW dipping contact

between Chañaral Complex metasedimentary rocks and the Matancilla pluton gives smaller amounts of horizontal separation across the Taltal and Quebrada Tipias faults than the amount of separation on the same faults using the AFS as a separation marker (Figure 2.7); this separation discrepancy can be accounted for by a component of NE down slip, resulting in deeper exposure level in the footwall.

2.5.4. Cross-Cutting Relationships and Geochronology Results

2.5.4.1. Dikes

In Quebrada de La Peineta southeast of Taltal a 7–12 m-wide porphyritic andesite dike cross cuts both the eastern strand of the AFS and a 175 m-wide zone of cataclasite bordering the eastern strand but is sinistrally displaced 148 m along an AFS strand 300 m further west (Figure 2.6, see also Seymour et al., 2020). These crosscutting relationships indicate that the dike intruded in the waning stages of AFS brittle deformation after slip had ceased on the easternmost branches and shifted to an AFS strand further west. Both the dike and the AFS fault strands are offset by NW striking, steeply NE dipping faults with shallowly northwest raking slickenlines. From the similar geometry, kinematics, and cross-cutting relationships with the AFS we interpret this younger fault as part of the TFS. Seymour et al. (2020) present a 109.9 ± 4.0 Ma zircon U-Pb crystallization age of this dike, which serves to mark a transition between the latest stages of AFS deformation and later TFS faulting.

Near the intersection of the eastern strand of the AFS and the Taltal fault, a 1–2 m wide dacitic dike cross cuts the AFS eastern strand cataclasite but is cut and displaced by several strands of the TFS (Figure 2.6). The magnitude of sinistral displacement of the dike is comparable to displacement of the eastern strand of the AFS across these faults (372 m across three map-scale faults). In addition, the dike is offset by numerous small faults with centimeter-

to meter-scale offset; many of these faults are parallel to the Taltal fault and have subhorizontal slickenlines and sinistral shear-sense indicators. Mineral separation for the dacitic dike sample 181-S145 yielded only six zircon grains. Given the likelihood that several or all of these grains are xenocrystic, producing a statistically sound U-Pb zircon crystallization age would be unlikely for this sample. Instead, we performed zircon (U-Th)/He analysis of this sample, which gives a date of 106.7 ± 8.5 Ma (Figure 2.9 and Table S3). This date is an average cooling age of five grains and records the time at which zircons cooled below $\sim 180\text{--}190$ °C, the closure temperature for the (U-Th)/He system (Reiners et al., 2002, 2004; Wolfe and Stockli, 2010). Since the dike is at most 2 m wide it can be assumed to have rapidly cooled to ambient temperatures after emplacement, and the cooling age approximates the crystallization age of the dike. Alternatively, cooling below the zircon (U-Th)/He closure temperature may have lagged millions of years after dike emplacement if the country rocks were ≥ 180 °C. In this case, the date would record regional cooling as the magmatic arc migrated eastward in the Early Cretaceous, providing a minimum intrusion age of the dike. Regionally, zircon (U-Th)/He cooling dates in Jurassic plutons along the AFS are $\sim 117\text{--}103$ Ma (Ruthven et al., 2020; Seymour et al., 2020), so the dike cooling age is consistent with regional cooling. It is possible that heating via hydrothermal fluid flow fully or partially reset the zircon (U-Th)/He system post-emplacement. However, given the similarity of the 106.7 ± 8.5 Ma cooling age to the ~ 110 Ma crystallization age of the late-AFS dike dated by Seymour et al. (2020), we favor the interpretation that the cooling age records intrusion of the dike during late stages of brittle deformation on the AFS.

2.5.4.2. *Calcite Veining*

Regionally, calcite veins represent late-stage mineralization with paragenetic textures indicating that calcite overprints or is coeval with hematite-chalcopyrite mineralization restricted

to NW striking faults (Bonson, 1998). Along the AFS near its intersection with the TFS, we have observed several outcrops where calcite veins cut foliated gouge in the core of the eastern strand of the AFS. Calcite is also commonly associated with the TFS, supporting the interpretation that calcite mineralization is late stage with respect to the Early Cretaceous magmatic arc. Given that no bedrock map units are demonstrably younger than the Taltal fault, and that all dikes identified in this study are cut by the TFS, we employ U-Pb geochronology of calcite mineralization to constrain the timing of slip along the TFS.

2.5.4.2.1. Sample 188-S122

Near the Matancilla pluton, a subsidiary strand of the TFS cuts Chañaral Complex metasedimentary rocks 90 m north of the Taltal fault (Figure 2.5). A pronounced NW-SE topographic lineament follows the gouge core of this fault strand, and fault planes within brecciated quartzite of the Chañaral epimetamorphic complex are exposed on either side. At sample locality 188-S122, calcite veins cut fault breccia (Figure 2.12). However, veins are themselves brecciated and in places offset by small faults with centimeter-scale sinistral separation. These relationships suggest that calcite veining was coeval with TFS brittle deformation. Petrographically, sample 188-S122 has calcite crystals >1 cm without pressure solution boundaries or slip surfaces on grain margins (Figure 2.12).

U-Pb isotopic analyses from distinct textural domains both adjacent to, and separated from, the wall rock yield a range of U concentrations that do not display any systematic correlation with their textural domain (Table S4). When high-U analyses from all textural domains are plotted on a regression line, they define a single population (MSWD = 1.02) with a lower-intercept age of 114.1 ± 7.0 Ma (113.2 ± 6.3 Ma including low-U analyses) that we infer represents the age of calcite precipitation (Figure 2.12 and Table S4).

2.5.4.2.2. Sample 161-34

Sample 161-34 was collected in the core of the Taltal fault along a subparallel secondary fault plane ~10 cm from the Taltal fault principal slip plane (Figure 2.12). Here the Taltal fault separates Paleozoic metasedimentary rocks from Mesozoic volcanic units to the south. Calcite in this sample has undergone brittle grain size reduction along with scattered quartz grains and opaque minerals. Calcite mineralization has a deformation fabric defined by pressure solution boundaries and brecciated bands visible in thin section; this fabric wraps around a clast of metasedimentary wall rock (Figure 2.12). The pervasive grain-scale deformation in this sample indicates that this calcite mineralization records much, if not all, of the Taltal fault deformation and was early synkinematic to the fault.

U-Pb isotopic analyses from individual textural domains from this sample yielded a range of apparent calcite crystallization ages from 186 ± 52 Ma to 131 ± 10 Ma. The youngest and most radiogenic analyses from this sample are located within a 1 mm wide vein of calcite oriented parallel to but physically separated from the main calcite mineralization by a thin septum of wall rock. However, ages from all textural zones overlap within error, and when high-U analyses from all zones are combined on single regression line, the data define a single population (MSWD of 1.4) with an age of 141 ± 11 Ma (148 ± 11 Ma including low-U analyses) that is our preferred age for the timing of calcite precipitation in this sample (Figure 2.12 and Table S3).

2.5.4.3. Relationship of the TFS to the Tropezón and Librillo Plutonic complexes

Based on the apparent lack of kilometer-scale offset of the Tropezón plutonic complex, Espinoza et al. (2014) suggest that Taltal fault slip had ceased by the time of that intrusion, dated to 110.0 ± 2.1 Ma (Tornos et al., 2010). However, this interpretation is inconsistent with

mapping that depicts the Taltal fault displacing the 106–101 Ma Librillo plutonic complex (Espinoza et al., 2014). Google Earth imagery shows abundant NW-SE (and NE-SW) lineaments within the pluton south of the Tropezón mine (Figure 2.13); field-checked lineaments in this study are steep NW striking faults, some with calcite veining and shallowly plunging slickenlines. Abandoned mine workings 2.3 km southwest of the Tropezón mine expose NW-SE striking fault surfaces with Cu-oxide and calcite mineralization. Although this fault does not juxtapose lithologically different map units, it is along strike with the trace of the Taltal fault located ~2.5 km northwest and could be a southeastern extension of the fault. Northwest striking lineaments that cut the southernmost outcrops of the Tropezón intrusive complex are visible in Google Earth imagery and reflected in reduced to pole aeromagnetic data (Figures 2.13 and 2.14; Vivallos and Donoso, 2014a, 2014b, 2014c). Similarly, NW striking faults (parallel to the Taltal fault) with shallow slickenline lineations cut the Librillo intrusive complex in other areas such as Mina San Juan (Bonson, 1998), where a nearby U-Pb zircon date gives a pluton crystallization age of 103.7 ± 1.9 Ma (Escribano et al., 2013). Farther north, the Librillo intrusive complex is cut by the map-scale NW striking Raul Luis and Chanchas Norte faults with vertical or steep northeast dips near a sample with a 102.6 ± 2.4 Ma U-Pb zircon date (Figure 2.2, Escribano et al., 2013).

West of Mina Chuchufleta and south of Quebrada de la Peineta, the surface trace of the Taltal fault appears to bend, with the fault trace azimuth changing from 310° north of Quebrada de la Peineta to a more east-west trace as low as 285° . Near this bend in the fault trace, surface lineaments appear to splay from the Taltal fault and fan southward away from the arcuate trace of the Taltal fault (Figures 2.2 and 2.13). Similarly, other faults appear to splay northward from the Taltal fault; a fault splay depicted on several geologic maps (Arabasz, 1971; Naranjo and

Puig, 1984; Ulriksen, 1979) branches to the north from the Taltal fault at Quebrada de la Peineta and traces into volcanic outcrops. Another fault splay traces from the Taltal fault north into mine workings at Mina Chuchufleta, where mineralization is described along fractures parallel to the Taltal fault (Bonson, 1998). Poor outcrop near the bend in the Taltal fault and a lack of contacts or marker horizons precludes determination of the amount of offset along these splays. However, each splay fault presumably accommodates strain that would otherwise be partitioned onto the main Taltal fault surface, and we hypothesize that offset along the main Taltal fault decreases southeastward. We propose that strain on the southeastward extension of the Taltal fault is shared by this distributed network of faults and splays rather than a single through-going fault, and that map-scale displacement of pluton boundaries on any single fault is small enough to be hidden within the alluvial valleys that conceal outcrops of intrusive contacts. Thus, the Tropezón intrusive complex does not give a map-scale appearance of offset along the Taltal fault but on closer inspection does appear to be cut by numerous NW-SE faults. Although the magnitude of shear in these plutonic complexes cannot be summed, it appears unlikely that the full offset of TFS displacement observed to the west is recorded by these plutons. If this interpretation is correct, it follows that the Tropezón and Librillo intrusive complexes intruded during TFS deformation and are offset by the TFS by lesser amounts than earlier-formed units.

2.6. DISCUSSION

2.6.1. Structural Inheritance of the TFS

If the pre-TFS crust were isotropic, an equal distribution of conjugate sinistral and dextral faults (or thrust faults) might be expected to form in response to E-W shortening. Instead, post-AFS Cretaceous deformation is accommodated only by NW striking sinistral faults; the near absence of dextral faults and thrust faults coeval with the TFS suggests a component of pre-

Cretaceous structural inheritance that favored NW striking faults. Multiple deformation episodes in the pre- or early-Andean tectonic history of the region created anisotropy that could serve as loci for later fault localization. The Chañaral epimetamorphic complex and Chañaral mélangé are characterized by a NW-SE trending structural grain most likely associated with NE directed subduction during the late Paleozoic (Bell, 1984, 1987). The mélangé facies south of Cifuncho have NW trending chevron folds, and the adjacent Paleozoic metasedimentary rocks to the east have a NW-SE structural fabric defined by SE vergent thrusts and thrust-related folds (Fuentes et al., 2016). NW striking extensional faults appear to have controlled sedimentation as early as the Triassic (Suarez and Bell, 1992; Tankard et al., 1995). Such structures could have produced a preexisting anisotropy favorable for reactivation by the TFS.

Contreras (2018) demonstrates that paleomagnetic clockwise rotations are greater in rocks south of the Taltal fault with pre-Late Jurassic magnetization than in rocks with Early Cretaceous magnetization and suggests that a Late Jurassic-Early Cretaceous clockwise rotation event was accommodated by domino fault-block rotation of NW striking faults southeast of Taltal, perhaps kinematically linked with early activity of the AFS. Bonson (1998) described the Taltal fault as collocated with a strong gradient in reduced to pole aeromagnetic data. We note that more recent aeromagnetic data (Vivallos and Donoso, 2014a) support the observation that the Taltal fault is sited along a sharply linear aeromagnetic gradient, even in areas where the same map unit is juxtaposed across the fault at the surface (Figure 2.14). This observation suggests that the geophysical lineament reflects a deep-seated structure. South of Taltal, aeromagnetic and topographic data show a dominant NW-SE grain. Contreras et al. (2013) describe a system of NW-SE faults in this area with Middle Jurassic ages. The similar orientations of these structures to TFS faults and alignment with strong aeromagnetic lineaments

(Figure 2.14) support the interpretation that TFS faults occupy pre-Cretaceous weaknesses of earlier-formed structures. Prinz et al. (1994) describe an abrupt change in the thicknesses of Bathonian and Oxfordian strata across a NW-SE lineament that appears to align with the southeastern projection of the Taltal fault. They interpret this relationship to record fault activity on this lineament since at least the Jurassic and note that other changes in Triassic to Late Jurassic sediment thickness align with the major NW-SE lineaments across northern Chile and northwestern Argentina described by Salfity (1985). We consider this relationship strong evidence for significant pre-AFS displacement along NW striking structures that served as precursors for TFS faulting.

The 141 ± 11 Ma age of calcite mineralization along the Taltal fault (sample 161-34) indicates the presence of a fluid pathway at that time. Deformation of calcite visible in thin section is likely a result of later sinistral slip on the Taltal fault. We propose that the rhyolite intrusion exposed for ~ 2 km on the southeast margin of the Taltal fault utilized the proto-Taltal fault structure as a conduit for magma flow. If true, the ~ 146 Ma age of this rhyolite corroborates the calcite data to show the presence of a preexisting NW striking structure in the Late Jurassic to Early Cretaceous.

While the above lines of evidence argue that the TFS faults occupy preexisting weaknesses, we do not find compelling evidence for measurable pre-AFS strike-slip displacement across the Taltal fault. The intrusive contacts of the 175–158 Ma Matancilla pluton and the 149–139 Ma La Finca pluton into the surrounding metasedimentary rocks do not record lateral offset greater than the offset measured on the eastern strand of the mid-Early Cretaceous AFS. This observation suggests that either there was no displacement on the proto-Taltal fault within that timeframe, or that there may have been dip-slip displacement that cannot be resolved

by using these near-vertical offset markers. The latter interpretation is more consistent with the changes in sedimentary thickness described by Prinz et al. (1994).

TFS faults with the greatest offset are centered near the Taltal fault. NW striking faults are not present north of the El Loro fault, and south of Quebrada de la Peineta TFS faults have relatively minor magnitudes of displacement. NW striking faults are ubiquitous south of Taltal to at least 27°S (Bonson, 1998), but no single fault offsets the AFS with displacement rivaling the 7.5 km of the Taltal fault. We propose that the distribution of TFS faulting is a result of suitably oriented and mechanically weak preexisting zone centered on the Taltal fault, such that post-AFS fault displacement was preferentially localized on this inherited structure zone. See Appendix A for a frictional sliding analysis of the AFS and TFS under different deformation conditions.

2.6.2. Timing of the TFS

The two Cretaceous dikes observed in this study are cut by the TFS, including two dikes that were emplaced following or at the very end of AFS slip. These dikes, with dates of 106.7 ± 8.5 Ma (zircon (U-Th)/He) and 109.9 ± 4.0 Ma (zircon U-Pb, Seymour et al., 2020), confirm the hypothesis that the brittle AFS was active until at least ~114 Ma and perhaps as late as ~106 Ma (the limits of uncertainty of the latter dike), and the requisite stress regime to shift slip to TFS faults had not yet been established. The amount of offset of dike 181-S145 across strands of the TFS is comparable to the amount of offset of the AFS eastern strand along the same faults, suggesting that the TFS was not active when this dike intruded. However, while the 106.7 ± 8.5 Ma zircon (U-Th)/He cooling age may represent the time of dike emplacement, it could also reflect regional cooling and thus gives only a conclusive minimum age.

While we have no direct offset measurements of TFS faults that cut the Tropezón plutonic complex (110.0 ± 2.1 Ma, Tornos et al., 2010), it appears likely that the amount of the

cumulative offset on these faults is less than the 7.5 km of offset on the Taltal fault further east. This interpretation is consistent with the 114.1 ± 7.0 Ma U-Pb calcite date that demonstrates that TFS faults had already accumulated slip and developed gouge fault cores by the time the Tropezón plutonic complex intruded (Figure 2.15). We thus propose that the transition between AFS and TFS slip occurred between 114 and 107 Ma, the overlap in ages between prekinematic dikes and synkinematic calcite and plutonism (Figure 2.15). Both the Tropezón and the Librillo intrusive complexes are cut by faults pertaining to the TFS, which demonstrates that slip along these faults must have continued later than the 106–101 Ma intrusive age of the Librillo intrusive complex.

Bonson (1998) provides a model of mineralization evolution from high-temperature (300–500 °C) magnetite-dominated deposits to moderate-temperature (130–390 °C) hematite-chalcopyrite (+calcite) mineralization. This switch in mineralization style is linked to a switch in structural control, such that the earlier mineralization is controlled by N striking AFS ductile and brittle structures, and the later mineralization is controlled by NW striking brittle faults. Many TFS faults in the area are mineralized with hematite and/or calcite; we use this observation in the context of the Bonson (1998) model to support our interpretation that there was not a protracted hiatus between AFS and TFS brittle deformation.

Cross-cutting relationships reveal that the El Muelle fault cuts Early Cretaceous volcanic rocks, but a younger age limit cannot be determined for this fault. The andesite dike mapped in Figure 2.6 cuts the easternmost strands of the AFS but is displaced by an AFS fault to the west (Figure 2.6). Valley alluvium prevents tracing this dike to the El Muelle fault, but we take the exposed relationship to tentatively suggest that brittle faulting transitioned westward across faults in the waning stages of AFS deformation, and the El Muelle fault may be the youngest

AFS-connected fault. Curvature of the El Muelle fault toward parallelism with the Taltal fault is consistent with a coeval kinematic relationship. Moreover, the El Muelle fault is not displaced by TFS faults, including the Quebrada de la Peineta fault that offsets the eastern strand nearly 1 km. Following typical fault displacement-length scaling relationships for strike-slip faults (e.g., Clark and Cox, 1996; Kim and Sanderson, 2005), faults with ~1 km of displacement should be ~10–100 km long; we propose that the ~1 km offset on of the AFS eastern strand by the Quebrada de la Peineta fault is unlikely to have dissipated along strike at the intersection with the El Muelle fault, and instead, these faults appear to have evolved contemporaneously. We interpret the apparent younging-westward pattern of AFS faults in conjunction with the curving trace of the El Muelle fault to indicate that slip on the TFS and El Muelle branch of the AFS temporally overlapped. With the possible exception of the El Muelle fault, we do not find evidence that TFS faults formed as secondary splay faults in duplex relationships to AFS faults, as documented with NW striking faults near Antofagasta (Cembrano et al., 2005; Jensen et al., 2011; Veloso et al., 2015). Instead, the TFS everywhere cross cuts and postdates the eastern strand and related strands of the AFS with no deflection of TFS fault traces near AFS fault intersections. In contrast with the El Muelle fault, field evidence does not suggest any slip of the AFS eastern branch after TFS activity began.

As there are no Late Cretaceous nor Paleogene map units in the region, and we have not identified any units that clearly postdate the entirety of displacement on the Taltal fault, the lower age limit of slip on the TFS is not well constrained. Arabasz (1971) described canyon incision and deposition of gravels in Quebrada Taltal after displacement on the Taltal fault had ceased; biotite K/Ar analyses of ash layers interbedded with these gravels give mid-Miocene dates (Escribano et al., 2013).

2.6.3. Relationship of TFS Kinematics to Cretaceous Plate Tectonics

Timing constraints presented above place TFS deformation after ~114–107 Ma and at least some of the deformation after 106–101 Ma, which shows that the main episode of TFS deformation followed abandonment of the AFS main strand as the region cooled and underwent a kinematic switch from NW-SE to E-W shortening. This timing shortly precedes or is contemporaneous with the mid-Cretaceous eastward migration of the magmatic arc (Dallmeyer et al., 1996), and no plutonism is recorded in the study area after ~101 Ma. This shift likewise appears contemporaneous with regional shortening and uplift; Late Cretaceous NW-SE or E-W shortening is described inland of the AFS at latitude 27°S (Mpodozis and Allmendinger, 1993), E-W crustal shortening of the Chilean Coastal Cordillera has been reported at latitude 32°S at ~100 Ma (Arancibia, 2004), and a widespread Albian-Cenomanian unconformity across the northern Andes is interpreted to reflect compression during plate reorganization (Jaimes and Freitas, 2006). The middle member of the Cretaceous Tonel Formation in the Salar de Atacama basin records pulses of sedimentation derived from the west interpreted to reflect uplift of the Coastal Cordillera beginning around 107 Ma (Bascuñán et al., 2016); internal unconformities and growth strata show deposition in a compressional tectonic regime alongside an east vergent thrust (Arriagada et al., 2006; Mpodozis et al., 2005). Strain localization onto a NW-striking, steeply dipping pre-existing weakness to accommodate E-W shortening could explain why strike-slip faults are the dominant post-AFS structures in the region surrounding Taltal, while thrust and reverse faults seem to be the dominant structures to accommodate similar shortening directions further east. Following the greatest pulse of arc magmatism in the mid-Early Cretaceous, the Coastal Cordillera may have been substantially thickened, which may have

driven the TFS to develop with N-S extensional strain, rather than the vertical extension seen by reverse faults further east.

The similar timing of the switch between AFS and TFS fault systems and an increase of retroarc foredeep sedimentation suggests a widespread shift in the location and style of deformation. This transition could reflect a margin-wide tectonic shift attributed to the southward passage of the Farallon-Phoenix-South America spreading center along the Andean margin (Scheuber et al., 1994), slab flattening followed by breakoff (Haschke et al., 2002), or a 105–100 Ma global plate reorganization and change in seafloor spreading rates (Matthews et al., 2012). Alternatively, this transition may reflect a change in the loci of strain partitioning such that margin-orthogonal component of oblique convergence was accommodated in the study area while the margin-parallel component shifted east of the Coastal Cordillera. While data presented in this study cannot distinguish between these factors, they demonstrate that deformation of the TFS was contemporaneous with these changes. Regardless of the tectonic drivers of this transition, transfer of slip from the AFS to the TFS in the late Early Cretaceous represented a major shift in the structural evolution of the Coastal Cordillera. While some TFS slip postdates the late Early Cretaceous Tropezón and Librillo plutonic complexes, models that invoke Eocene slip on TFS faults must reconcile with the relationships described in this study that show most slip occurring before intrusion of those plutons.

2.7. CONCLUSIONS

The TFS consists of vertical to steeply NE dipping faults with 10.6 km total sinistral separation across a 15-km wide zone and 7.5 km sinistral slip on the largest fault. Collocation of TFS faults with aeromagnetic lineaments and abrupt changes in the thickness of Jurassic sedimentary strata suggest that they reactivated crustal anisotropies inherited from Paleozoic or

earlier Mesozoic tectonism. Dates of a calcite vein (141 ± 11 Ma) and rhyolite dike ~ 146 Ma emplaced along the Taltal fault indicate that the TFS controlled fluid flow and magmatism as early as the Late Jurassic, prior to displacement on the AFS and subsequent TFS. However, geologic mapping indicates the TFS records little to no pre- or syn-AFS sinistral slip.

Geochronology of dikes and veins with prekinematic and synkinematic relationships to the TFS demonstrates that the transition between AFS and TFS brittle deformation occurred between ~ 114 and 107 Ma (Figure 2.15). The ~ 110 Ma Tropezón plutonic complex records distributed sinistral shear along the splaying eastward termination of the Taltal fault. The 106 – 101 Ma Librillo plutonic complex is likewise cut by TFS faults, demonstrating that at least some slip on the TFS occurred after that time. The transition between these fault systems records a switch from a NW-SE to E-W shortening regime, which most likely reflects either a margin-wide shift in convergence direction or a shift in strain partitioning such that margin-parallel deformation was accommodated further east, and margin-orthogonal shortening along preexisting NW striking weak zones was accommodated in the Coastal Cordillera.

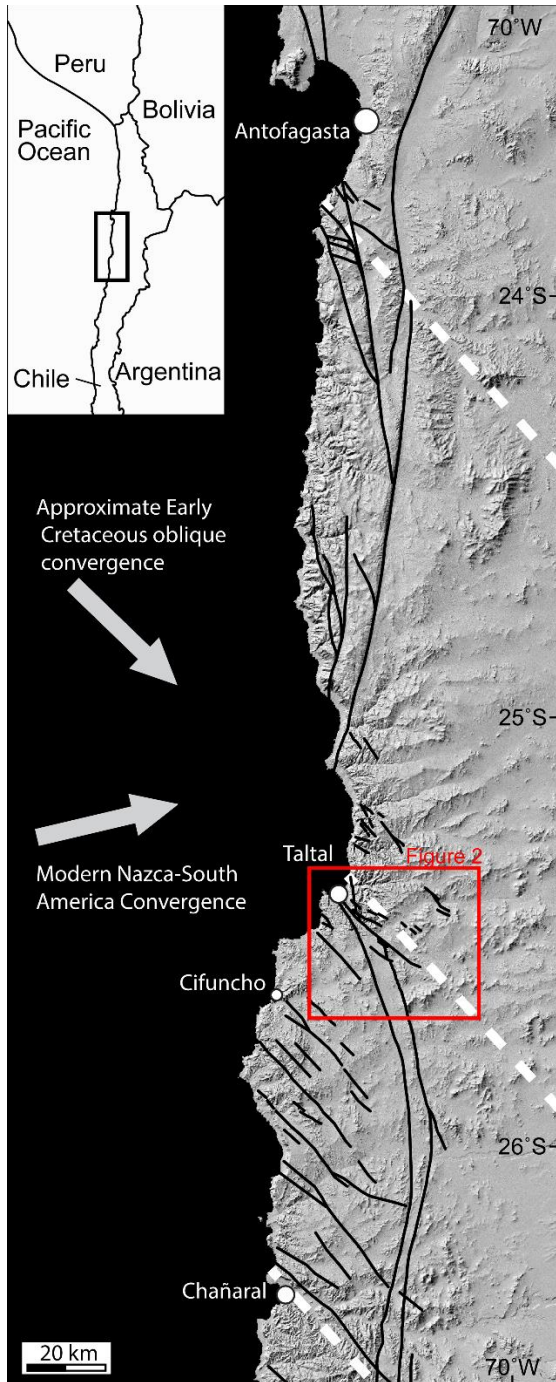


Figure 2.1. Digital elevation map of the Coastal Cordillera between 23° and 27°S, showing major regional faults (black). Structures not pertaining to the AFS or system of NW striking faults are omitted for clarity. Locations of faults are simplified from Álvarez et al. (2016), Cembrano et al. (2005), Escribano et al. (2013), and Grocott and Taylor (2002). The long-lived crustal weaknesses hypothesized by Abels and Bischoff (1999) are shown as dashed white lines. The modern Nazca-South America convergence direction is from Angermann et al. (1999), and an approximate Phoenix-South America oblique convergence direction is after Scheuber and Andriessen (1990).

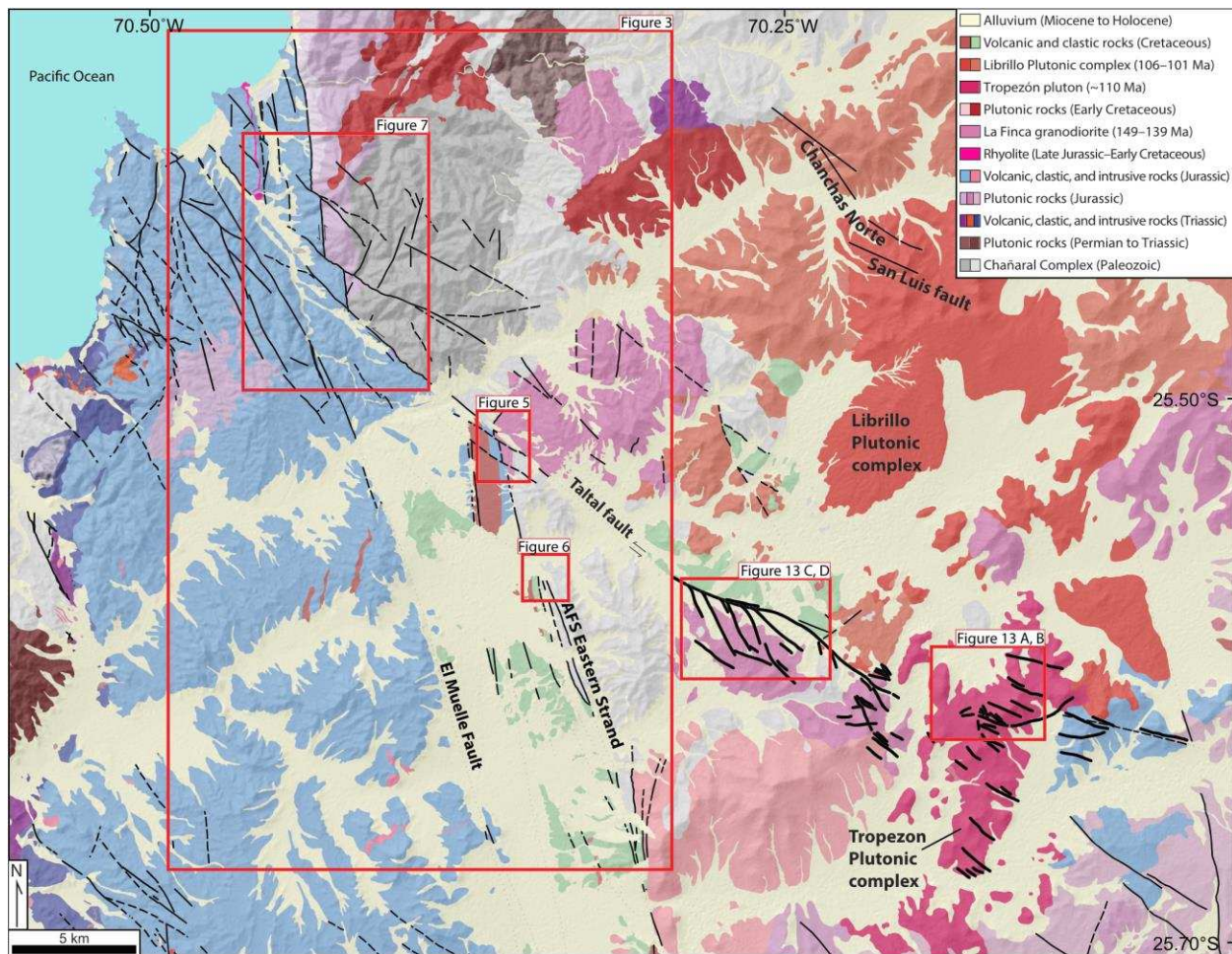


Figure 2.2. Compiled geologic mapping for the region near Taltal, Chile. Geology was compiled and simplified from 1:100,000 scale geologic maps (Contreras et al., 2013; Escribano et al., 2013; Espinoza et al., 2014). Bold black lines show our interpretation of distributed splay faults branching from the southeast end of the Taltal fault and cutting the ~110 Ma Tropezón pluton (magenta). These lineaments are mapped from aerial imagery, field reconnaissance, and lineaments in reduced to pole aeromagnetic data.

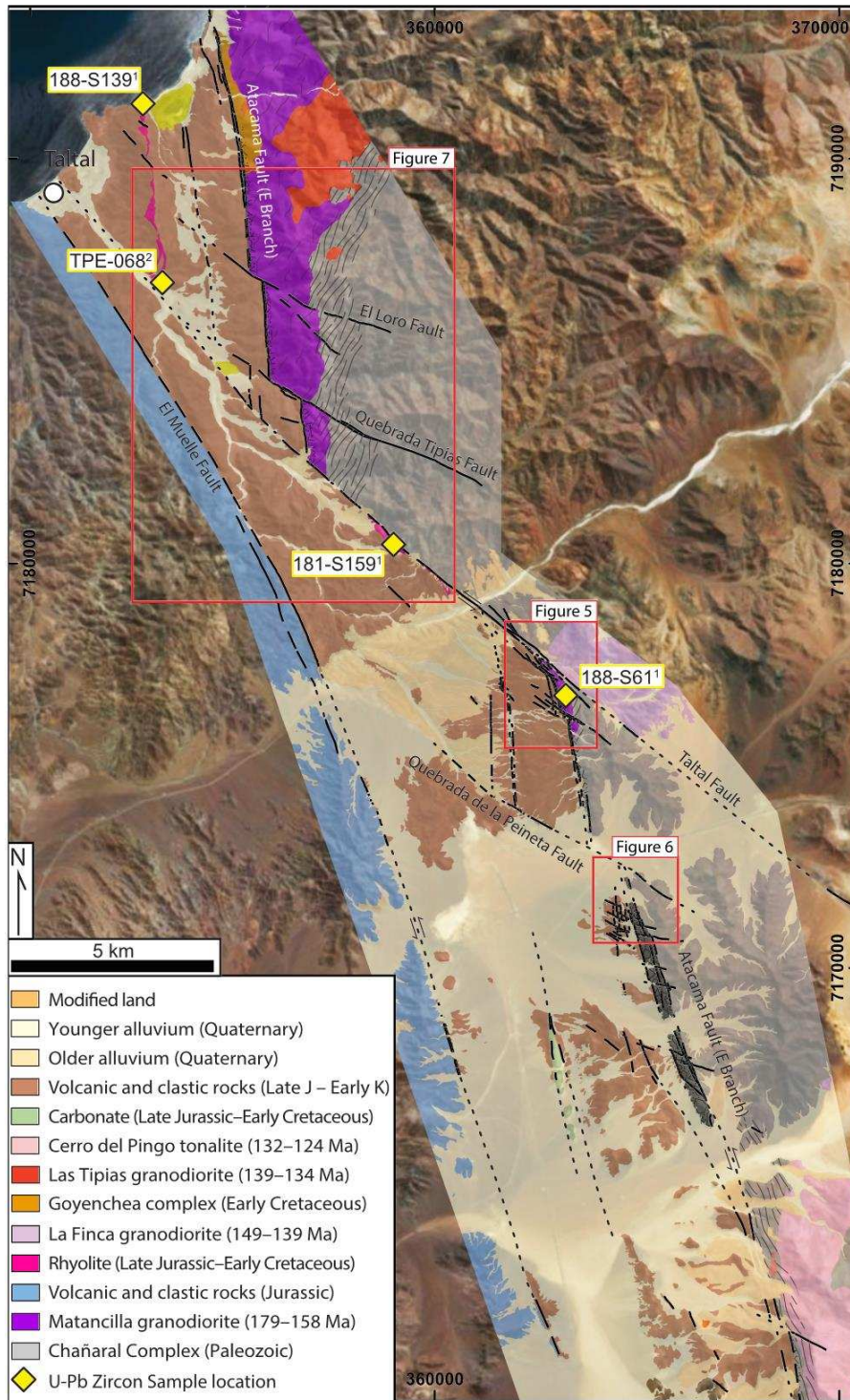


Figure 2.3. New geologic mapping of the Atacama and Taltal fault systems near Taltal, Chile. U-Pb zircon sample locations are marked with yellow diamonds. The rhyolite (pink) and Matancilla pluton (purple) offset markers across TFS faults are discussed in the text. Reference coordinates are given as WGS 1984 UTM zone 19S. Inset boxes give the locations of inset maps in Figures 5–7. U-Pb samples are from ¹this study and ²Escribano et al. (2014).



Figure 2.4. (a) Principal slip plane of the Taltal fault, separating Paleozoic metasedimentary rocks (right) from foliated fault gouge derived from spherulitic rhyolite. Photo taken ~600 m southeast of sample locality 181-S159, view to the northwest. (b) Detail view of the principal slip plane of the Taltal fault seen in 7A. Subsidiary fault surfaces with shallowly raking slickenlines are present on a sinistral Riedel shear adjacent to the principal slip plane (arrows). View from above, parallel to the NW-SE Taltal fault trace. Note pencil for scale. (c) Gouge core of the Taltal fault, with ~8 m of foliated gouge forming the less resistant fault trace valley. Gouge foliation (dashed lines) is oblique clockwise to the fault trace, indicating sinistral slip. Photo taken ~150 m northwest of sample locality 161-34, view to the southeast. (d) Foliated gouge in the core of the Quebrada Tipias fault. Gouge foliation (dashed lines) visible right of the rock hammer is oblique clockwise to the fault principal slip plane (solid line), indicating sinistral slip. View to the southeast.

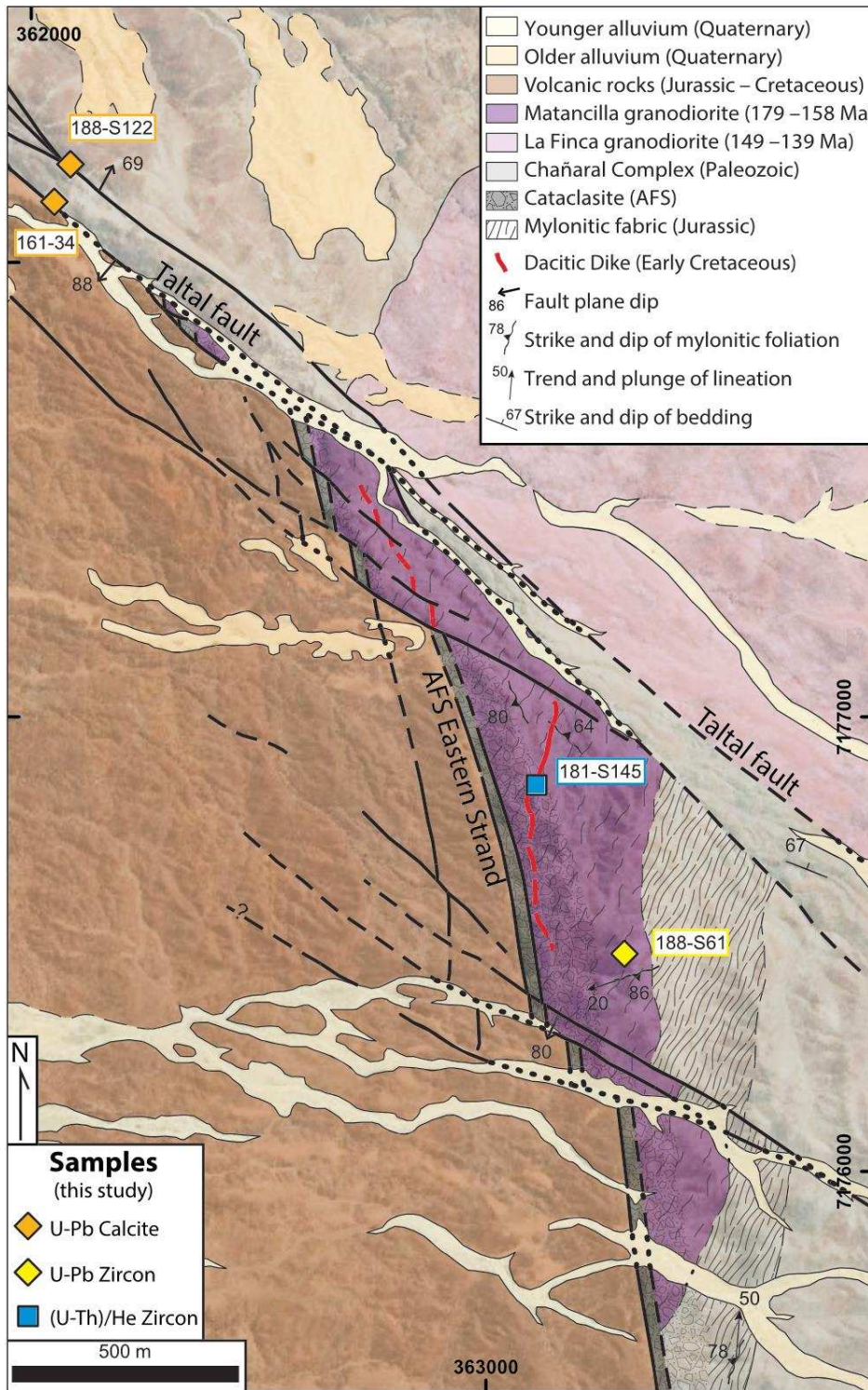


Figure 2.5. Geologic map of the intersection zone between the NNW-SSE striking AFS with the NW-SE striking Taltal fault showing the locations of samples analyzed in this study. Samples are symbolized by analytical method: yellow diamond, zircon U-Pb; orange diamond, calcite U-Pb; and blue square, zircon (U-Th)/He. Reference coordinates are given as WGS 1984 UTM zone 19S.

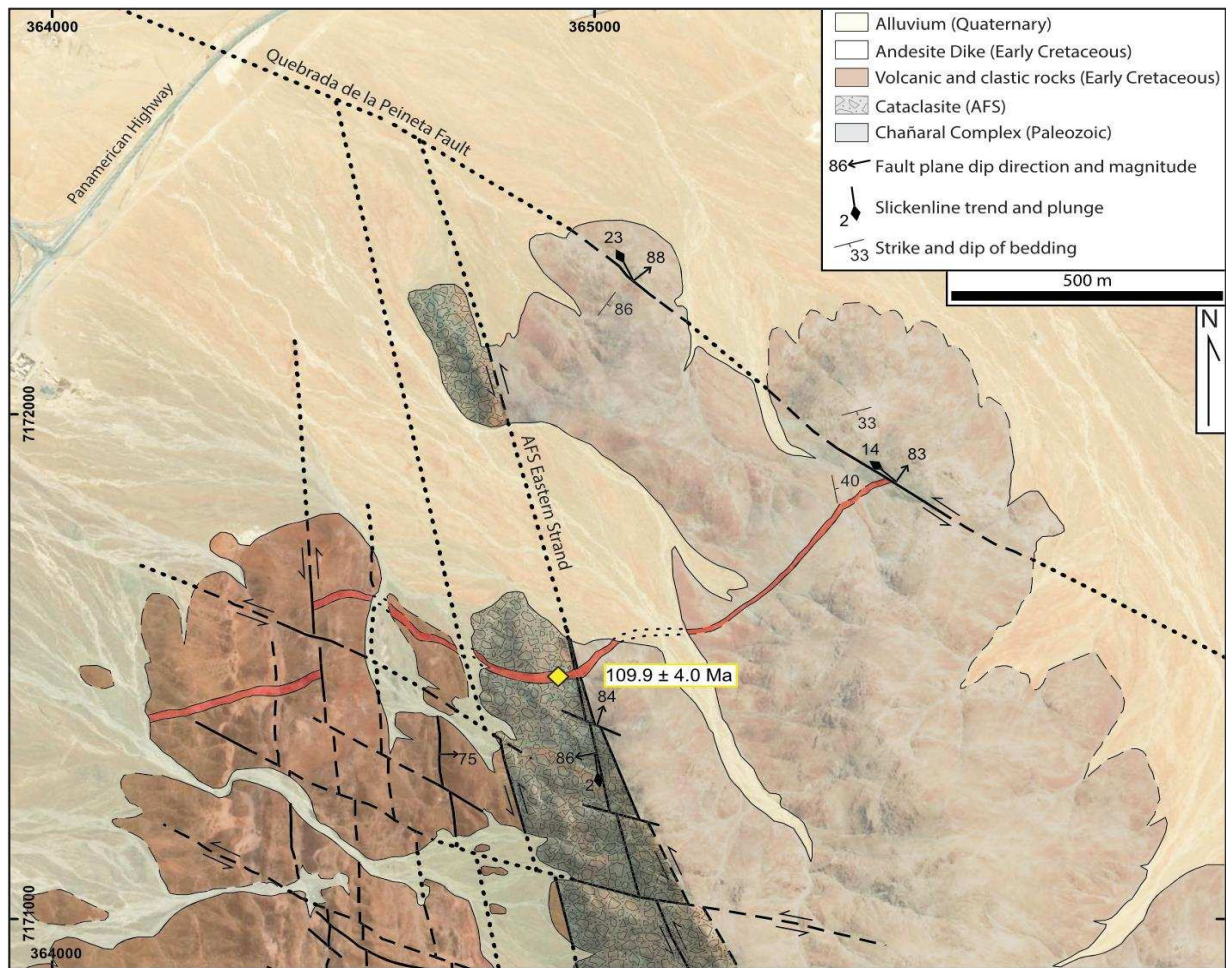


Figure 2.6. Geologic mapping of the andesitic dike in Quebrada de la Peineta (see also Seymour et al., 2020). The dike cuts the four strands of the AFS, including the easternmost (main) strand of the fault system, and is offset 148 m by a left-lateral AFS fault, indicating that slip shifted to westward strands as slip waned on the fault system. All AFS fault strands and the andesitic dike are cut and displaced ~990 m by the Quebrada de la Peineta fault. Yellow diamond marks the position of the zircon U-Pb sample presented by Seymour et al. (2020), dated to 109.9 ± 4.0 Ma. Reference coordinates are given as WGS 1984 UTM zone 19S.

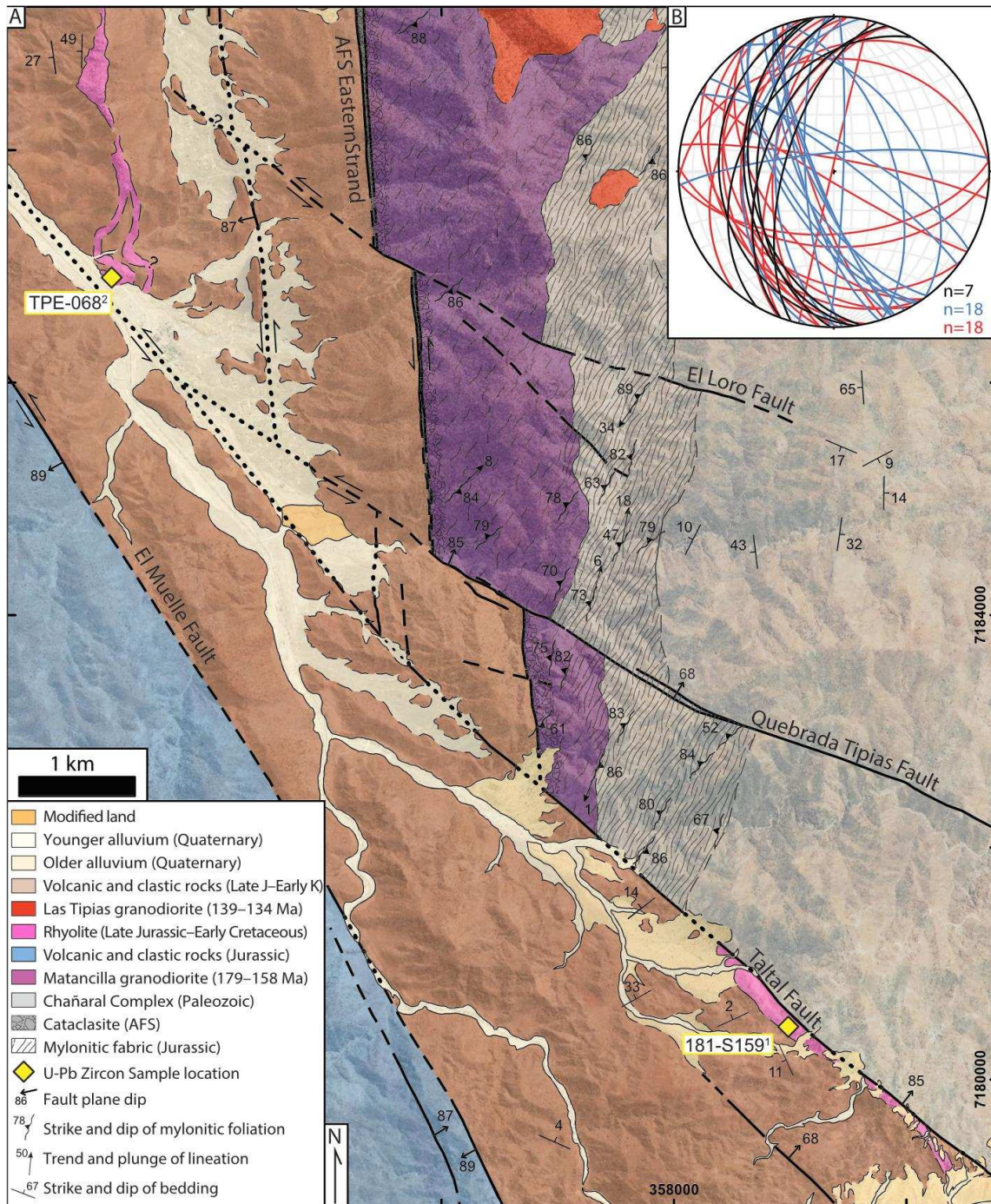


Figure 2.7. (a) Geologic mapping of the Taltal, Quebrada Tipias, and El Loro faults. The spherulitic rhyolite (pink) is an offset marker across the Taltal and Quebrada Tipias faults. Reference coordinates are given as WGS 1984 UTM zone 19S. U-Pb samples are from 1this study and 2Escribano et al. (2013). (b) Stereonet of flow banding in rhyolite. Flow banding north of the Taltal fault (red, $n = 18$) has many measurements parallel to bedding measured in overlying or underlying strata (black, $n = 7$). Flow banding measured in rhyolite outcrops south of the Taltal fault (blue, $n = 18$) is steeper and dominantly strikes NW-SE, roughly parallel to the Taltal fault.

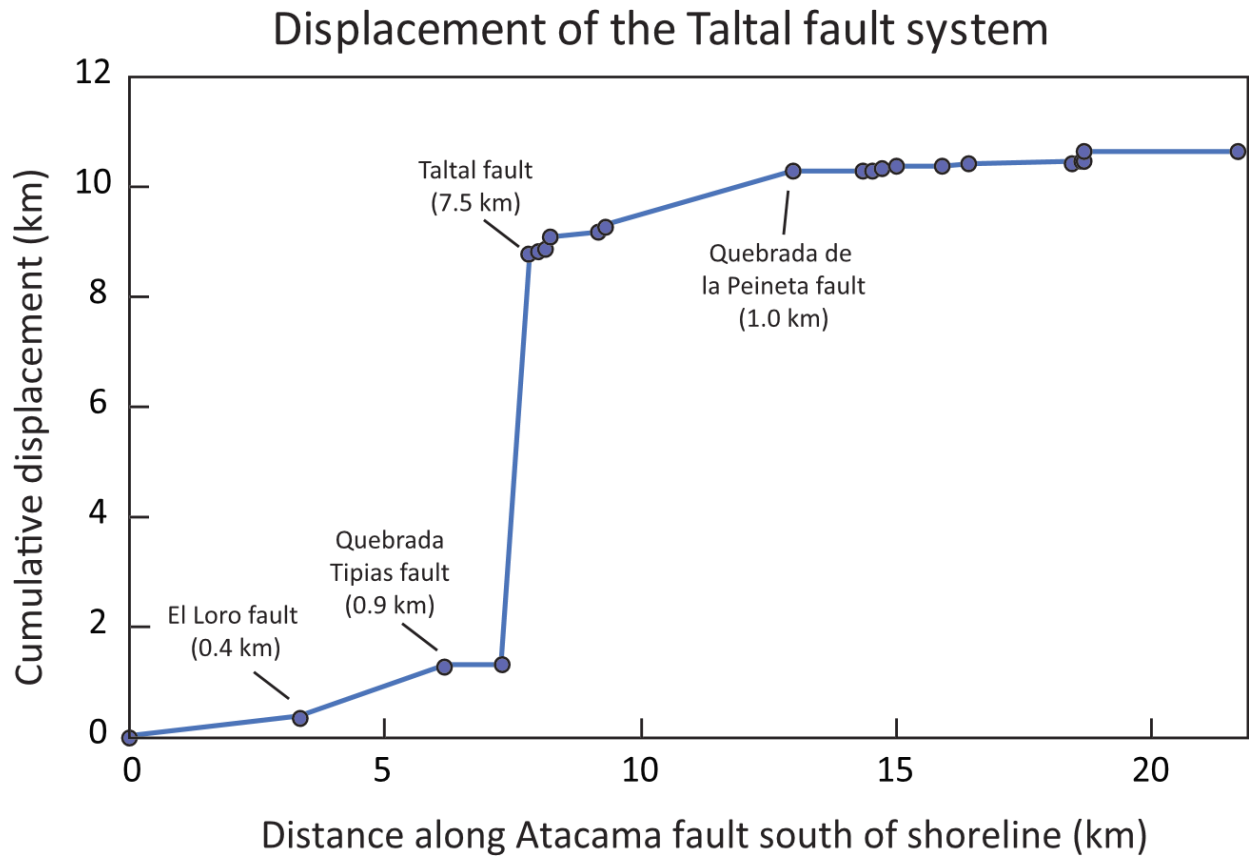


Figure 2.8. Cumulative sinistral offset of the Taltal fault system. Measurements use the near-vertical eastern strand of the AFS as an offset marker for horizontal separation. Faults are plotted as a function of the distance south from the shoreline north of Taltal along the AFS eastern strand. Individual displacements are marked for the largest faults.

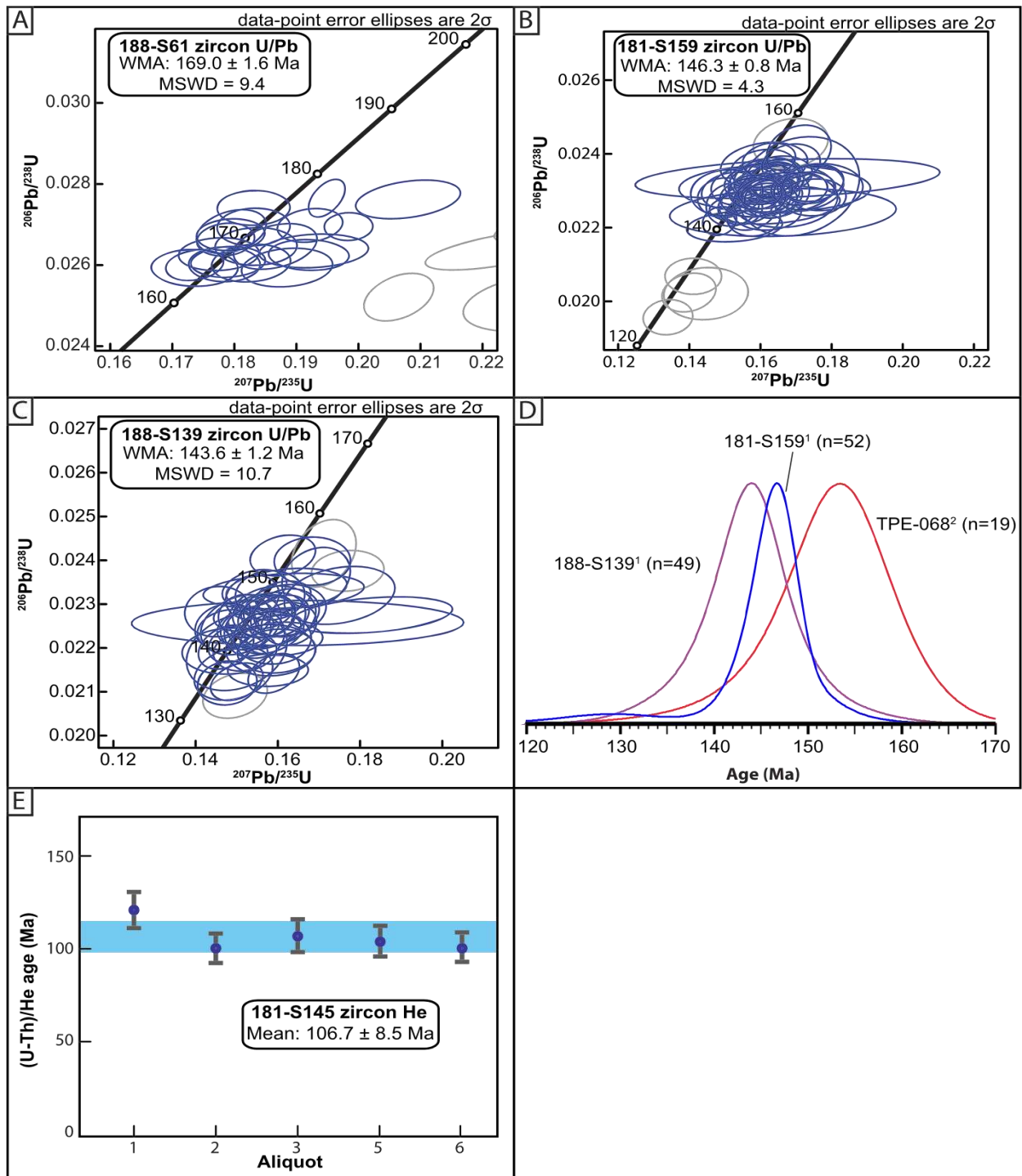


Figure 2.9. Geochronology analytical results. (a) U-Pb Concordia diagram of Matancilla granodiorite sample 188-S61, showing a weighted mean age (WMA) of 169.0 ± 1.6 Ma from 27 total analyses. Seven grains of $>10\%$ discordance (shown in gray) are excluded from the weighted mean. This date is within the 175-158 age range of the Matancilla pluton (Escribano et al., 2013) and corroborates the lithologic correlation to that unit. (b) Zircon U-Pb concordia diagram of rhyolite sample 181-S159 (55 analyses), showing a weighted mean age of 146.3 ± 0.8

Ma. Three grains are >10% discordant, and five grains are rejected from the WMA calculation (gray). While several younger grains (~125–132 Ma) are present in the sample, they are rejected as outliers from the weighted mean calculation algorithm. (c) Zircon U-Pb concordia diagram of rhyolite sample 188-S139, showing a weighted mean age of 143.6 ± 1.2 Ma from 50 analyses, one grain >10% discordant is excluded, and three analyses are rejected from the WMA calculation (gray). (d) KDE plot of the three rhyolite U-Pb zircon samples, with overlapping age spectra. Sample analytical data are from: 1 this study (Table S2, filtered to <10% discordance) and 2 Escibano et al., 2013, not filtered for discordance). Peak heights are normalized to 100% of analyses. (e) Zircon (U-Th)/He cooling age of dike sample 181-S145 with a mean cooling age of 106.7 ± 8.5 Ma (blue highlight). Aliquot 4 gave a date older than the host pluton and is excluded.

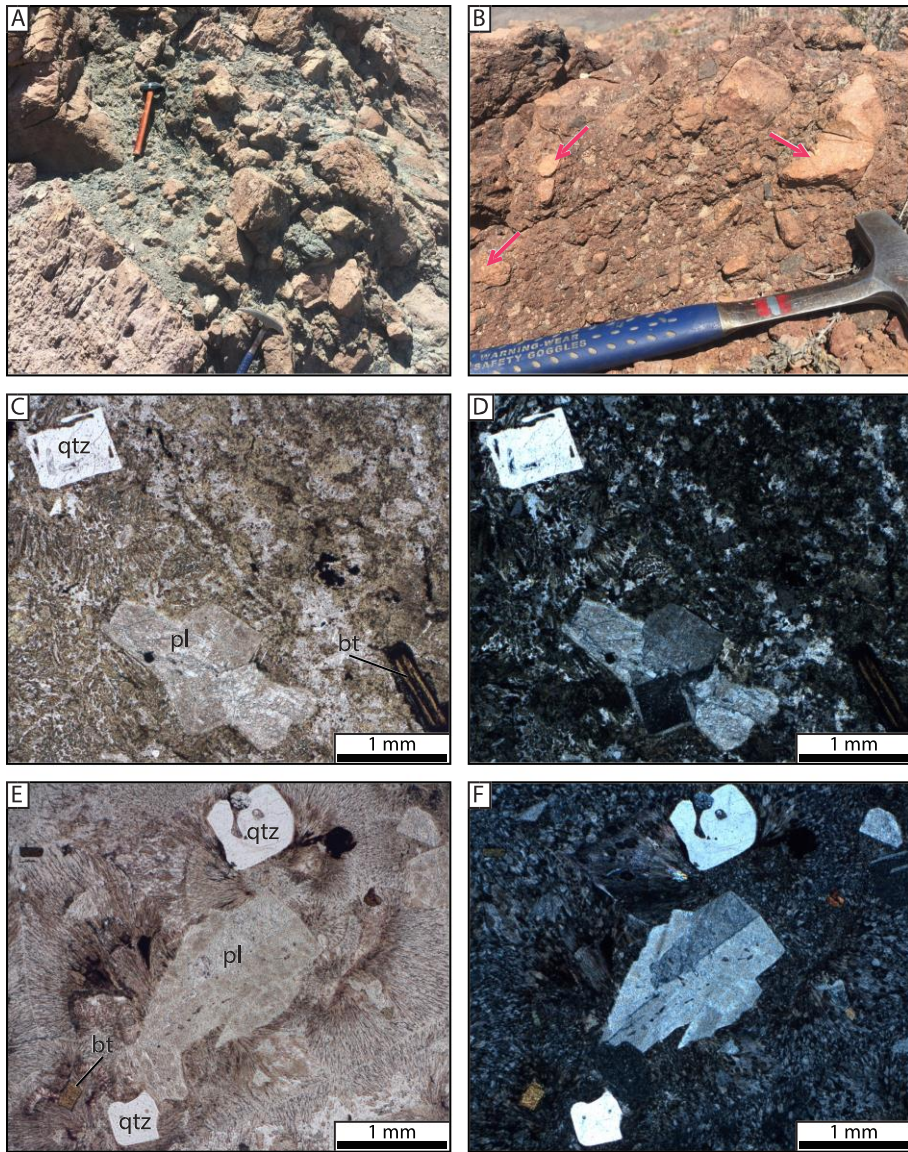


Figure 2.10. Figure 10. (a) Upper contact of the rhyolite unit near sample locality 188-S139. Rhyolite boulders are clasts in conglomerate with a dark green fine-grained clastic matrix. The boulder conglomerate interfingers along strike with sandstone and pebble conglomerate at the upper contact of the rhyolite flow. (b) Polymict conglomerate including clasts of spherulitic rhyolite (pink arrows) among clasts of porphyritic andesite and reworked sandstones. Photo taken 10 m upsection of the rhyolite flow upper contact. Rounded grains demonstrate surficial reworking of the rhyolite in the above strata. (c) Plane-polarized light photomicrograph of sample 181-S159. The spherulitic groundmass is largely composed of K-feldspar (yellow stain). Quartz (qtz), plagioclase (pl), and biotite (bt) phenocrysts are present. Quartz has irregular embayed grain shapes. (d) Cross-polarized light photomicrograph of sample 181-S159. (e) Plane-polarized light photomicrograph of sample 188-S139. Similar phenocryst assemblages and sizes, well-developed spherulitic texture, and embayed quartz texture demonstrate the lithologic similarity to sample 181-S159. Sample is unstained. (f) Cross-polarized light photomicrograph of sample 188-S139.

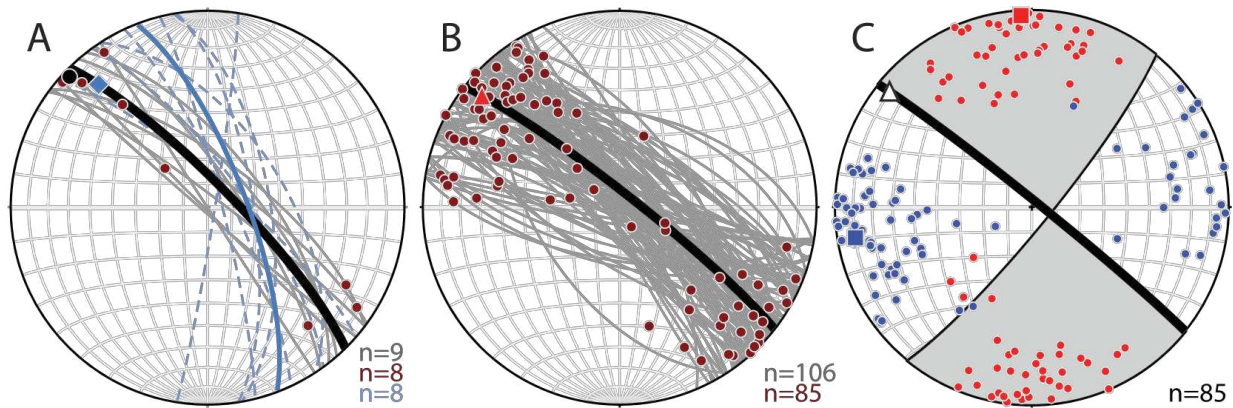


Figure 2.11. (a) Principal slip surface (gray) and slickenline lineation measurements (maroon circles) of TFS faults with >0.5 km sinistral displacement ($n = 9$). Measurements of foliated gouge ($n = 8$) in fault cores (dashed blue) are parallel or slightly oblique clockwise to principal slip surfaces and serve as a sinistral kinematic indicator. The average principal slip plane is oriented $315, 80^\circ\text{NE}$ (black) and the average slickenline lineation is $314/04$ (black circle). The blue diamond shows a calculated slip vector on the average principal slip surface plane perpendicular to the intersection with the average gouge foliation plane. (b) All TFS fault plane ($n = 106$) and slickenline lineation ($n = 85$) measurements. The average fault plane is in bold ($308, 84^\circ\text{NE}$; maximum eigenvalue of poles to fault planes = 0.891), and the red triangle shows the average slickenline lineation plunging shallowly to the northwest ($309/11$, maximum eigenvalue = 0.751). (c) P axes (blue) and T axes (red) are shown for TFS fault planes with a measured slickenline lineation. The solution fault plane ($309, 87^\circ\text{NE}$) dips steeply northeast and the slip vector (hollow triangle) plunges shallowly northwest ($309/08$). The average P axis ($261/10$, blue square) reflects an overall E-W shortening direction.

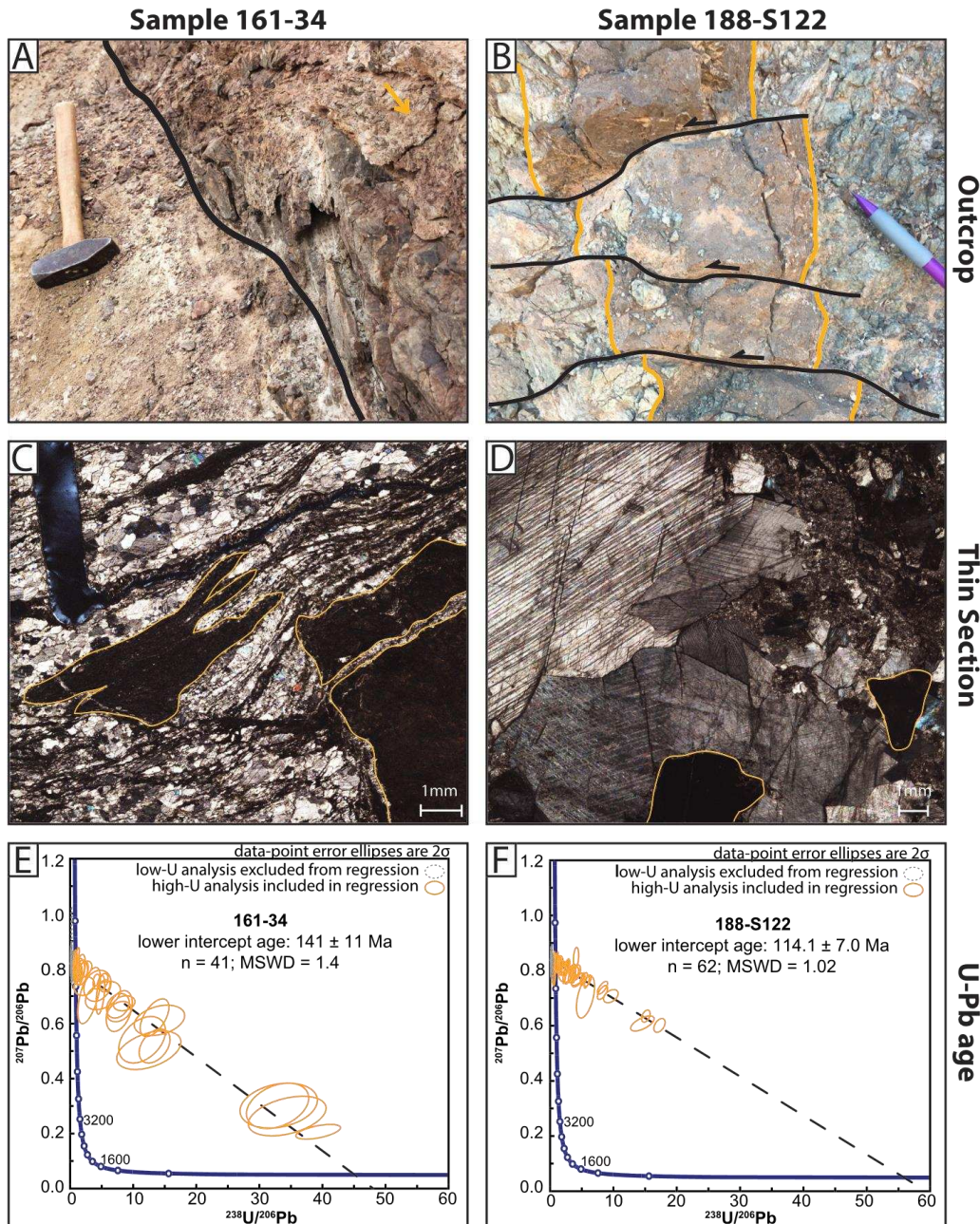


Figure 2.12. (a) Principal slip plane (bold line) of the Taltal fault at calcite sample location 161-34, separating incohesive fault gouge (left) from Paleozoic metasedimentary rocks (right). Calcite mineralization incorporating brecciated wall rock clasts is visible on subsidiary faults adjacent to the principal slip plane (orange arrow). View to the northwest. (b) 13 cm wide calcite vein (orange outline) at sample locality 188-S122. Calcite veining cuts fault breccia of a TFS fault but the vein displaced by sinistral faults with 1–3 cm offset. (c) Thin section (cross-polarized light) of calcite sample 161-34 showing grain boundary slip and pressure solution between calcite grains. Calcite deformation deflects around clasts of wall rock to the fault (orange outline). (d) Thin section of sample 188-S122, showing large (>1 cm) calcite grains without intragrain deformation and clasts of wall rock (orange outline). (e) U-Pb calcite concordia plot for sample 161-34. (f) U-Pb calcite concordia plot for sample 188-S122.

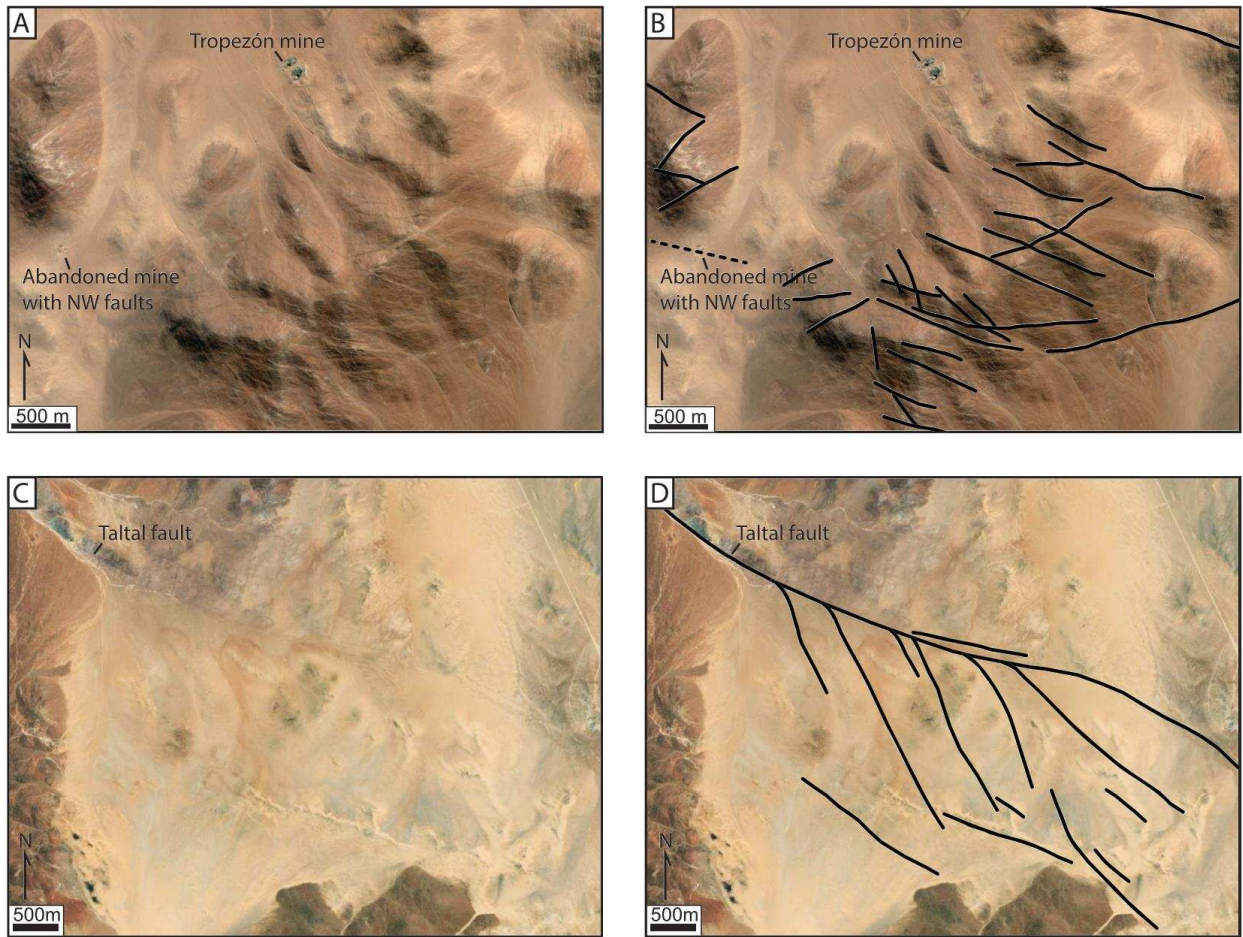


Figure 2.13. (a) Google Earth satellite imagery of the Tropezón pluton showing outcrops cut by abundant NW-SE and NE-SW striking lineaments. The abandoned mine discussed in the text exposes a mineralized NW-SE striking fault zone along strike with the Taltal fault and a lineament to the SE. (b) Esri aerial imagery of faults splaying from the southeastern extent of the Taltal fault. The Taltal fault is marked by a well-defined lineament in the northwest and curves gently eastward to a more E-W trace. NW-SE lineaments splay from the main fault trace. Poor outcrop and eolian cover prevent bedrock observations of the potential fault splays.

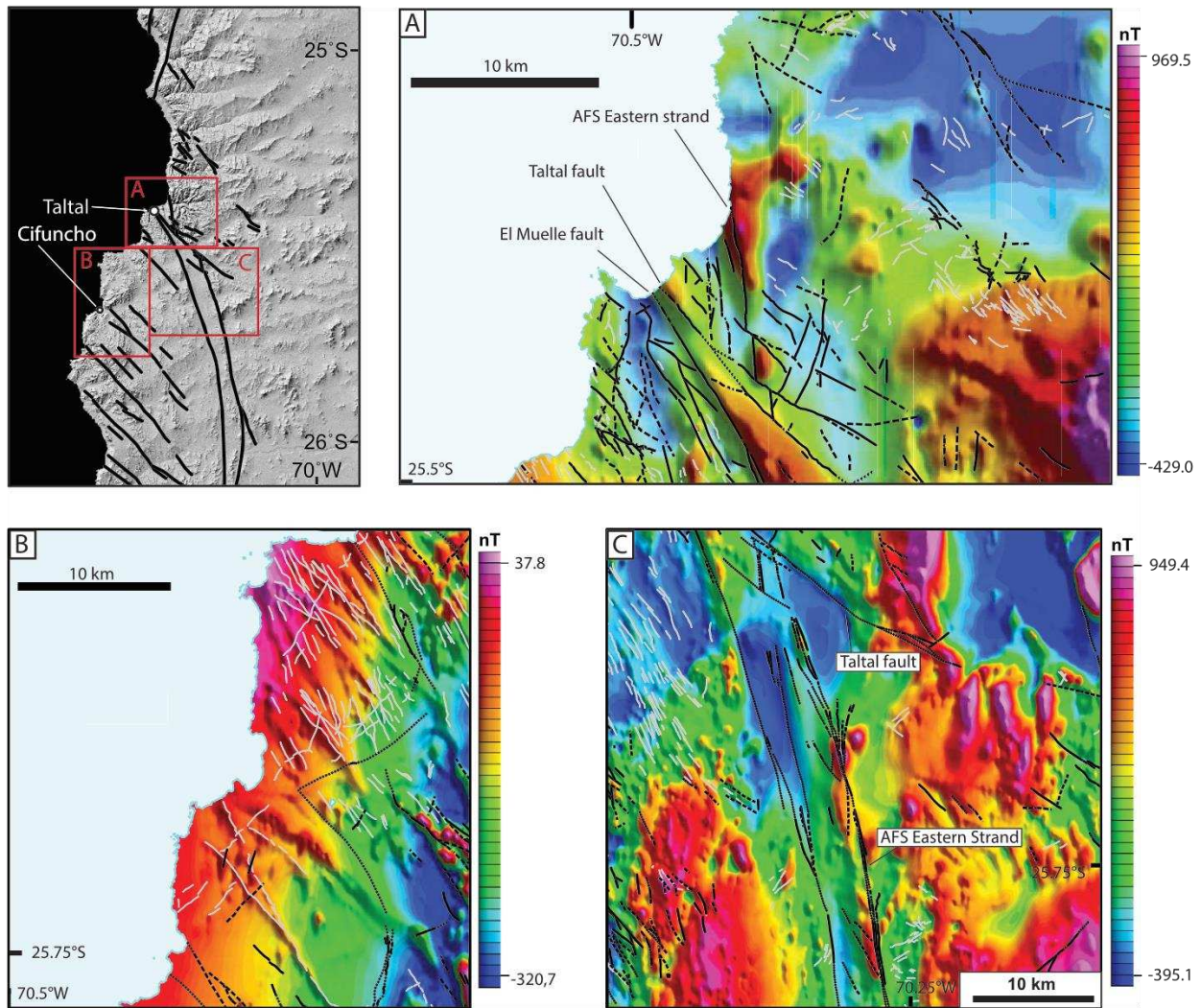


Figure 2.14. Reduced to pole aeromagnetic data in the Taltal region (modified from Vivallos and Donoso, 2014a, 2014b, 2014c). Faults (black) and dikes (gray) are compiled from 1:100,000 scale geologic mapping (Contreras et al., 2013; Escribano et al., 2013; Espinoza et al., 2014). (a) The Taltal and El Muelle faults show association with strong NW-SE linear magnetic gradients. (b) In the Cifuncho area, NW-SE tracing magnetic anomalies are collocated with mapped dikes and faults, both of Jurassic age (Contreras et al., 2013). This juxtaposition suggests that the nearby anomaly aligned with the Taltal fault could have an inherited component from Jurassic deformation and magmatism. (c) The magnetic anomaly associated with the NNW-SSE AFS appears to disrupt a more widespread NW-SE magnetic fabric, with a strong anomaly along the Taltal fault.

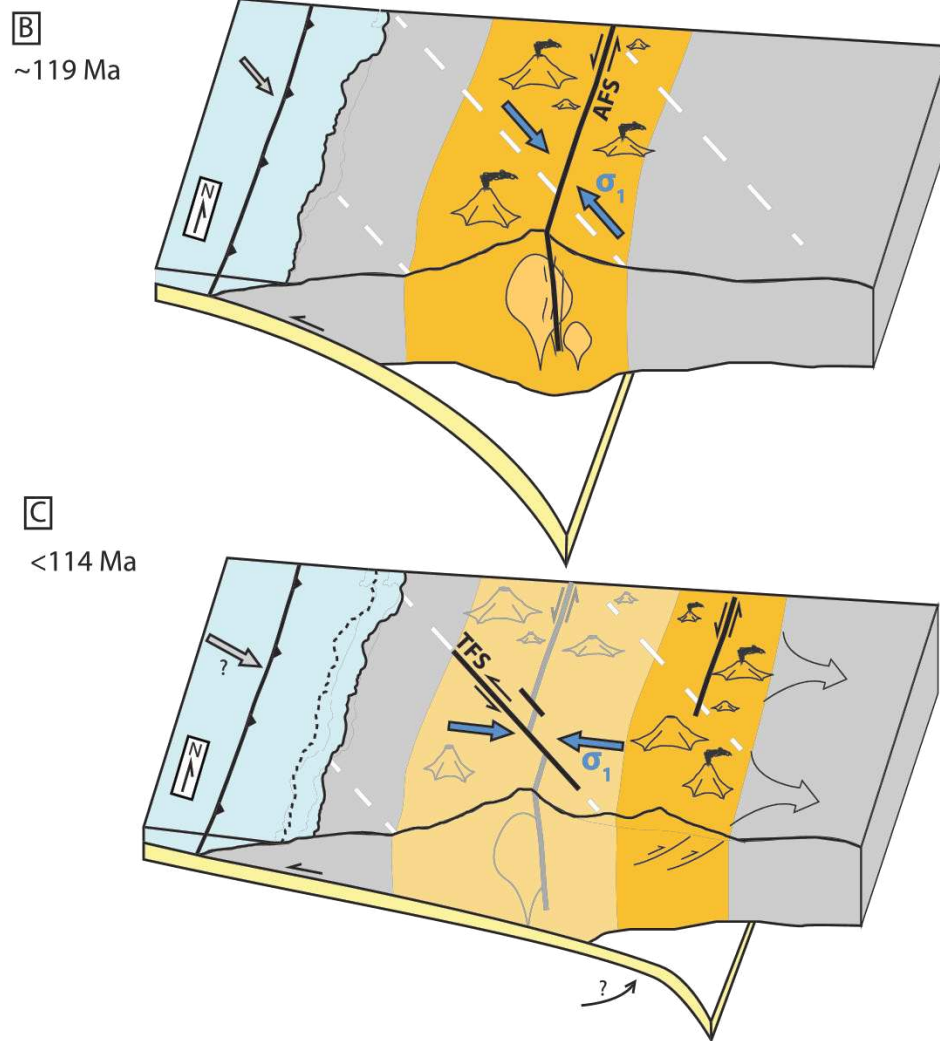
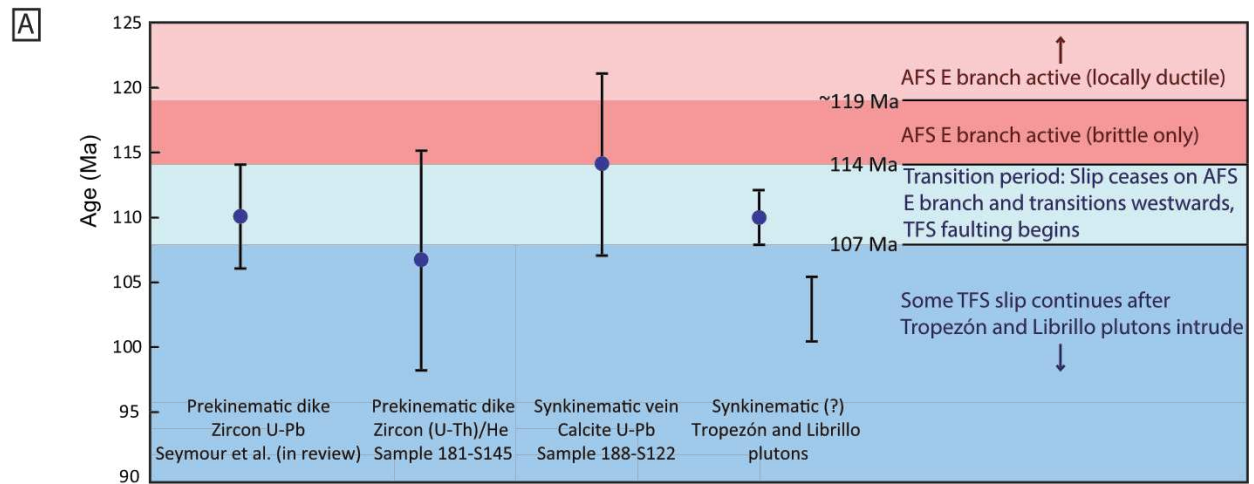


Figure 2.15. (a) Summary of timing constraints for the transition between AFS and TFS slip. The two dikes dated in this study are prekinematic to the TFS and late kinematic to the AFS.

Calcite sample 188-S122 is along a TFS fault that postdates the AFS, and calcite mineralization is late kinematic to that fault. While the Tropezón and Librillo plutons (ages from Tornos et al., 2010 and Espinoza et al., 2014, respectively) are cut by TFS faults, they may have less sinistral offset than older units and are most likely synkinematic to the TFS. We bracket the AFS-TFS transition between the older limit of the andesitic dike date and the younger limit of the Tropezón pluton, similar to the younger limit of the calcite date. (b) Schematic model (not to scale) showing major tectonic features of northern Chile in the mid-Early Cretaceous. Margin-parallel shear is accommodated by the AFS in the rheologically weak Early Cretaceous arc (orange), with localized ductile deformation surrounding synkinematic plutons. Northwest striking inherited weaknesses (dashed white lines) are misoriented for reactivation by the NW-SE shortening regime in the study area (blue). (c) Schematic model showing abandonment and eastward migration of the arc beginning in the late Early Cretaceous. Northwest striking inherited weaknesses are favorably oriented for reactivation by the E-W shortening regime within the study area and offset the inactive arc and AFS (gray). Continued margin-parallel shear may be accommodated by strike-slip faults at the new arc axis (e.g., the transpressional Chivato fault system). Margin-orthogonal shortening away from northwest striking weaknesses could be accommodated by thrust faulting and basin inversion, uplifting the Coastal Cordillera, and providing the sediment pulse (arrows) of the early Peruvian phase as described by Bascuñán et al. (2016). Possible changes to subduction dynamics such as slab shallowing, a change of subduction obliquity or rate, or a change in the margin position from subduction erosion are depicted schematically; additional factors such as a change in slab density or passage of a spreading center could explain the shift between major fault systems.

3. SINISTRAL SHEAR DURING MIDDLE JURASSIC EMPLACEMENT OF THE MATANCILLA PLUTONIC COMPLEX IN NORTHERN CHILE (25.4° S) AS EVIDENCE OF OBLIQUE PLATE CONVERGENCE DURING THE EARLY ANDEAN OROGENY²

3.1. INTRODUCTION

The Andean margin in northern Chile has long stood as a classic example of convergent margin tectonics. Subduction and arc magmatism of the Andean margin has been ongoing since at least the Late Triassic (e.g., Del Rey et al., 2016; Jara et al., 2021b) and spans several kinematic shifts in plate margin obliquity. Plate reconstruction models depict a shift from Early Cretaceous sinistral-oblique convergence to the Late Cretaceous dextral-oblique convergence that has persisted to the present. However, reconstructions of the earlier margin history spanning into the Jurassic are limited by the preservation of seafloor isochrons, and plate margin convergence vectors are less constrained. The Farallon-Phoenix spreading center intersected the South American convergent margin in the northern Andes in the Late Triassic, migrated southwards along the margin to central Chile in the Early Jurassic, and returned northwards by the early Late Jurassic (Seton et al., 2012; Matthews et al., 2016; Young et al., 2019; Figure 3.1). Subduction convergence vectors at the margin may have changed rapidly as the ridge passed, affecting the kinematics of upper plate deformation, but uncertainty in the details of Jurassic plate reconstructions preclude a firm understanding of when such kinematic switches may have occurred.

Steady accumulation of marine back-arc basin deposits suggest that the upper plate of the Andean arc was largely extensional through the Jurassic (Scheuber et al., 1994; Charrier et al.,

² Chapter in preparation for submission to *Journal of South American Earth Sciences*.

2007), and this interpretation is supported by normal faults that accommodate E-W extension in arc volcanoclastic strata (Dallmeyer et al., 1996) and arc geochemistry with low crustal contribution consistent with extensional tectonics and thinning of the upper plate (Oliveros et al., 2020; Jara et al., 2021b). In the Coastal Cordillera, systematic dike orientations appear to record a transition from E-W extension to NNE-SSW extension and sinistral plate margin obliquity from the Late Jurassic to Early Cretaceous (Taylor and Randall, 2000). However, that interpretation is complicated by Late Jurassic dikes with NW-SE dilation that could suggest dextral obliquity or decoupling of onshore deformation from the down-going slab (Scheuber and Gonzalez, 1999). Other attempts to infer plate margin obliquity use ductile shear zones synkinematic with plutonism. Across the Mesozoic Andean margin, ductile deformation may be spatially and temporally restricted to areas adjacent to plutonic bodies, where thermal weakening elevated the geothermal gradient above the brittle-plastic transition and enabled mylonitic strain (e.g., Brown et al., 1993; Seymour et al., 2020). Such ductile deformation is recorded in a connected system of the Early Cretaceous Atacama fault system (AFS; Scheuber and Andriessen, 1990; Seymour et al., 2020), where the margin-parallel component of oblique subduction was partitioned into the arc as sinistral shear. The main phase of AFS sinistral shear began at ~139 Ma on the southern Papos segment (Ruthven et al., 2020) and ~132 Ma on the El Salado segment (Grocott and Taylor, 2002; Seymour et al., 2020), but some studies have suggested that Jurassic ductile shear was a precursor to the AFS (Scheuber and Andriessen, 1990; Scheuber and Gonzalez, 1999; Rodríguez et al., 2021). Ductile shear is not consistently associated with Jurassic plutonism; some Jurassic plutons lack any associated penetrative strain (Seymour et al., 2020), while others such as the Late Jurassic Las Animas pluton have syn-

magmatic shear zones with down-dip lineations that are interpreted to reflect progressive stages of pluton emplacement in an E-W extensional environment (Grocott and Taylor, 2002).

Ductile deformation synkinematic with Jurassic plutonism provides an opportunity to constrain plate-boundary kinematics of the early Andean orogeny. The reported absence of strike-slip shear in plutonism-associated deformation envelopes led Dallmeyer et al. (1996) to suggest that the plate convergence vector was perpendicular to the margin through the Jurassic with a rapid switch to a sinistral oblique regime recorded by sinistral shear in the mid- Early Cretaceous Las Tazas pluton. This assertion is challenged by more recent work that finds evidence for sinistral ductile shear in the Early Jurassic (Scheuber and Gonzalez, 1999; Rodríguez et al., 2021), even associated with intrusions that were previously considered to record only extensional deformation. However, no constraints have been presented for the Middle Jurassic strain regime, and dip-slip extensional (Grocott and Taylor, 2002), sinistral strike-slip (Scheuber and Andriessen, 1990), and sinistral transpressional (Rodríguez et al., 2021) ductile shear zones are recognized for mylonitic Early Jurassic plutons. Here we document a previously unreported sinistral strike-slip shear zone that developed synchronously with the intrusion of the ~169 Ma Matancilla plutonic complex. This shear zone (herein referred to as the Matancilla shear zone) provides a new constraint on the Middle Jurassic strain regime of the Andean orogeny and may record partitioning of the margin-parallel component of SE-directed oblique subduction into the contemporaneous magmatic arc.

3.2. GEOLOGIC SETTING

The geology of the Coastal Cordillera in northern Chile is dominated by voluminous arc magmatism of the early Andean orogeny (Figure 3.1B). The plutonic upper crustal roots of the arc and volcanoclastic equivalents intrude and overlap Paleozoic

metaturbidites of the Chañaral Complex, with the oldest Permian plutons crosscutting lower greenschist-facies metamorphic fabrics (Bell, 1982). Tectonic *mélange* in the Chañaral Complex near Chañaral with SW-vergent chevron folds likely records underthrusting of an accretionary prism during late Paleozoic NE-directed subduction on the western margin of Gondwana (Bell, 1984; Fuentes et al., 2016). Outside of the *mélange* zone, reported Paleozoic deformation is limited to NNE-plunging folds near Taltal (Escribano et al., 2013) and polyphase folding that includes S- to SW-vergent folds near Chañaral that postdate *mélange* development (Bell, 1984). Near Taltal, the Chañaral Complex is typified by alternating quartzite and phyllite intervals and lacks the basaltic flows, dacitic tuffs, and rhyolites observed further south (Bell, 1984; Fuentes et al., 2017).

Sparse Triassic magmatism is present in the Coastal Cordillera near Taltal, but the main phase of arc-related Andean magmatism began in the Late Jurassic and peaked in the Early Cretaceous (Seymour et al., 2020). Volcanic-dominated and plutonic-dominated domains are separated by the AFS, with the deepest structural levels exposed east of the AFS eastern branch. Near Taltal, the Chañaral Complex was intruded by the Middle Jurassic (~169 Ma; Mavor et al., 2020) Matancilla plutonic complex (Arabasz, 1971; Escribano et al., 2013; Figure 3.2) during a lull of plutonism in the Coastal Cordillera (Jara et al., 2021a; Seymour et al., 2020), with medium-grained hypidomorphic granular hornblende biotite granodiorite as the dominant plutonic lithology.

Early Cretaceous synplutonic ductile shear on the northern part of the El Salado segment of the Atacama fault system was active between 132–119 Ma, and brittle AFS deformation continued until 114–110 Ma, when the AFS was cut by the NW-striking Taltal fault system as plutonism ended in the area (Mavor et al., 2020; Seymour et al., 2020). The largest faults of the

Taltal fault system, including the Taltal fault, Quebrada Tipias fault, and El Loro fault, displace the AFS and the Matancilla pluton with kilometer-scale sinistral separation, and kinematic data indicate a slight normal-sense obliquity to sinistral slip on the steeply NE-dipping fault planes. Cumulative sinistral displacement across this part of the AFS is $\sim 54 \pm 6$ km (Seymour et al., 2021), and post-AFS displacement across the Taltal fault system is ~ 10.6 km (Mavor et al., 2020).

Where the spatial patterns, geometry, and timing of AFS-related mylonitic deformation are well documented along the northern El Salado segment (e.g., near the Cerro del Pingo tonalite; Seymour et al., 2020, 2021; Chapter 4) mylonitic fabrics with subhorizontal lineations and sinistral shear sense indicators parallel or are slightly clockwise to the vertical N-S fault system. The highest strain fabrics, locally ultramylonitic, are in screens of Chañaral Complex metasedimentary rocks adjacent Early Cretaceous plutons, and plutonic rocks are locally protomylonitic at distances < 800 m from the AFS trace. Gradients of decreasing fabric strain intensity both away from the AFS trace and along strike of the AFS away from synkinematic plutonism indicate that proximity to both the fault system and the magmatic thermal source was required for mylonitic shear, and pluton intrusion further than ~ 1.3 km from the AFS is marked by contact metamorphism without shear. AFS shear zones were progressively overprinted by brittle deformation as the thermal influence of plutonism waned, but sinistral shear continued, as evidenced by cataclastic overprint of mylonitic fabrics along the eastern (main) branch of the AFS and abundant \sim N-S striking sinistral faults.

Regional-scale (1:100,000) geologic mapping near Taltal depicts mylonitic fabric along the eastern branch of the AFS east of Taltal, where a ~ 500 m wide shear zone affects the Matancilla pluton and the Jurassic La Negra Formation (Escribano et al., 2013). As mapped, this

shear zone contradicts the models of magmatism-connected ductile deformation and suggests either that the AFS was active as early as the Middle Jurassic or that localized ductile deformation occurred in the Early Cretaceous independent of thermal weakening from an adjacent pluton. Outcrops of the Las Tiplas granodiorite with a 139 ± 3 Ma K-Ar date (Las Cenizas, 2007 *in* Escribano et al., 2013) are mapped near the mylonite zone, and it is possible that the mapped mylonitic zone is associated with this Early Cretaceous pluton instead of the Jurassic Matancilla plutonic complex. We use geologic mapping, structural measurements, and microstructural observations to revise the spatial extent of the Matancilla shear zone and show that mylonitic deformation is more extensive than previously mapped and tied to intrusive contact of the Middle Jurassic Matancilla pluton rather than the Early Cretaceous AFS.

3.3. METHODS

To constrain the spatial relations, kinematics, and timing of the Matancilla shear zone, we employ 1:25,000-scale geologic mapping, petrographic analysis of ductile fabrics, and U-Pb zircon geochronology. Aureole mineral assemblages are determined using petrography and a TerraSpec Halo handheld spectrometer. Structural measurements are plotted using Stereonet 10.2 (Allmendinger et al., 2011; Cardozo and Allmendinger, 2013), and length-weighted rose diagrams of mapped contacts are generated using the OAtools plugin for ArcGIS (Kociánová and Melichar, 2016). We utilize petrographic and outcrop kinematic indicators such as asymmetric folds, S-C fabrics, and oblique recrystallized grain shape fabric (e.g., Passchier and Trouw, 2005) for determining shear sense. U-Pb zircon analyses of a cross-cutting pluton were conducted using laser ablation inductively-coupled mass spectrometry (LA-ICP-MS) instrumentation at the UTChron laboratory at the University of Texas at Austin following methods outlined in Seymour et al. (2020). Concordia diagrams and weighted mean average

(WMA) calculations are generated with IsoplotR software (Vermeesch, 2018), using the 95% confidence method for WMA uncertainty calculation and filtered for $\leq 10\%$ discordance.

3.4. PRE-MYLONITIC DEFORMATION RECORDED IN THE PALEOZOIC CHAÑARAL COMPLEX

Chañaral Complex metasedimentary rocks are typified by interlayered lower-greenschist facies quartzite and phyllite. Sedimentary compositional layering is often distinguishable in nonmylonitic rocks as alternating metasilstone and metasandstone layers at mm to meter scales. Phyllitic foliation defined by aligned fine-grained micas and pressure solution seams (Figure 3.3) is most strongly developed in finer-grained protoliths and most commonly parallel to bedding. Outcrop-scale folds deform the foliation and record deformation that is absent in surrounding Mesozoic rocks. Isoclinal folds are not observed which suggests that the foliation represents burial metamorphism rather than transposition. Bedding most commonly dips shallowly, but meter-scale folds are sparsely present in outcrop, with at least two styles and orientations of folding recognized. A stereoplot of poles to bedding (Figure 3.4) shows a broad scattering of orientations not easily explained by a single deformation event. One outcrop exposes open, upright, folds with shallowly west-plunging fold axes (Figure 3.3C, blue colors on Figure 3.4B), while another outcrop 670 m to the south is characterized by close, gently-inclined folds with S-plunging fold hinges (Figure 3.3D, red colors on Figure 3.4B), Fold hinges from these two outcrops are nearly orthogonal and cannot be explained by a single cylindrical folding event. Neither fold has an associated axial planar cleavage, and field exposure did not permit a determination of the relative timing of these fold events.

Crenulation lineation is sparsely visible on foliation surfaces in phyllitic intervals. Crenulation lineation measurements, along with fold axes measured in outcrop and calculated

stereographically are dominantly oriented NE-SW to N-S with shallow plunges (Figure 3.4C). However, variation between measurements indicates that these lineations are either from multiple deformation events or are from the same event but have been rotated about a subvertical axis by subsequent deformation. In either case, structural data in this study provides evidence for at least two deformation events in the Chañaral Complex prior to the intrusion of the Matancilla pluton.

3.5. GEOMETRY, KINEMATICS, AND MICROSTRUCTURES OF MYLONITIC FABRICS ASSOCIATED WITH THE MATANCILLA PLUTONIC COMPLEX

3.5.1. Field relations

Our geologic mapping refines the spatial extent of ductile shear zones east of Taltal and revises the patterns of AFS-connected deformation. Mylonitic fabrics are most developed in the Paleozoic Chañaral Complex near the contact where it is intruded by Matancilla granodiorite (Figures 3.2, 3.5A, 3.6A-C). The map pattern of the boundary between mylonitic and nonmylonitic Chañaral Complex metasedimentary rocks roughly parallels the contact of that unit with the Matancilla pluton to the west. Near the Quebrada Tipias fault, the northwestern boundary of the Matancilla mylonitic zone is ~630 m away from the intrusive contact, though further south weak mylonitic fabrics are found as far as 1.4 km from the contact. In areas far from the pluton with weak mylonitic deformation, the mylonitic fabric is generally only visible in finer-grained phyllitic intervals, while quartzose metasandstone is unstrained. This relation is disrupted by the Las Tipias pluton, which cuts the Matancilla intrusive contact and the mylonitic fabrics in the aureole of the older pluton (Figure 3.7). East of the gradational mylonitic zone boundary, a weak cleavage is visible in fine-grained intervals of the Chañaral Complex at a high angle to bedding and parallels the mylonitic fabrics exposed further west.

At the intrusive contact with Paleozoic rocks, granodiorite of the Matancilla plutonic complex is locally sheared (Figures 3.5B, 3.6D-F). Protomylonitic fabrics in the granodiorite are markedly less strained and encompass zones significantly thinner than the mylonitic fabrics in the surrounding metasedimentary rocks. The thickness of the protomylonitic zone is commonly 2–3 m adjacent to the contact with Chañaral complex metasedimentary rocks but locally reaches >350 m of structural thickness south of the Quebrada Tipias fault (Figure 3.2).

Away from the intrusive contact, discrete centimeter- to meter-scale mylonitic zones exist throughout the Matancilla plutonic complex (Figures 3.5C-D, 3.6G-I). These discrete mylonitic zones are subplanar, undulating, or anastomosing and accommodate localized strain in otherwise unstrained granodiorite. In outcrop, unstrained granodiorite grades into mylonite within the span of centimeters. Discrete zones are almost always marked by localized mineral alteration and are exposed in outcrop with a bleached or pinstriped appearance (Figure 3.5C-D).

We describe details of ductile strain in three categories based upon spatial relations, protolith, and style of ductile deformation: (i) pervasive mylonitic fabric in the Paleozoic metasedimentary rocks spatially associated with the Matancilla plutonic complex intrusive contact (Figures 3.5A, 3.6A-C); (ii) pervasive protomylonitic fabric within Matancilla granodiorite associated with the same intrusive contact (Figures 3.5B, 3.6D-F); and (iii) discrete cm-scale thickness, anastomosing mylonitic zones throughout the Matancilla plutonic complex (Figures 3.5C-D, 3.6G-I). In contrast to previous geologic mapping, we identify a thick zone of cataclasite along the eastern margin of the AFS eastern branch but find no spatial relation of any ductile fabrics with respect to the fault.

3.5.2. Mylonite in Chañaral Complex metasedimentary rocks in the Matancilla pluton aureole

The most extensive and most pervasively strained ductile deformation is within Chañaral Complex rocks surrounding the Matancilla granodiorite (Figures 3.2, 3.5A, 3.6A-C). Pervasive mylonitic foliation in Chañaral Complex strikes SSW and dips steeply NW on average (212, 78 NW). Where the intrusive eastern contact of the Matancilla pluton deflects across topography near Quebrada Tipias the contact dips steeply northwestwards; this map pattern suggests that the mylonitic fabric is subparallel to the contact in three dimensions. Stretching lineations plunge shallowly NE or SW (average 028/05; Figure 3.8A). Many outcrops have strong foliation with faint or no lineation; a lineation was measured at 41% of localities with a foliation measurement, and outcrops with lineation are commonly S>L tectonites. Foliation measurements are slightly variable and correlate with the orientation of the Matancilla intrusive contact. Folded bedding in the Chañaral Complex is transposed into parallelism with the mylonitic fabric and there is no girdle distribution of poles to mylonitic foliation or evidence for post-mylonitic refolding. Strain degree is variable across Chañaral Complex protolith lithologies in the distal areas of the mylonitic aureole, where quartz-rich protoliths are unstrained and retain rounded detrital textures while finer-grained lithologies have protomylonitic shear fabric that was apparently focused into these domains rich in aligned mica grains. In more highly-strained samples, quartz-rich horizons are dynamically recrystallized with textures indicative of subgrain rotation and bulging recrystallization mechanisms.

Asymmetric folds, S-C fabric, C' shear bands, and oblique recrystallized quartz grain shape fabric most commonly indicate sinistral shear, though dextral shear sense indicators are also observed. In the metasedimentary mylonite, petrographic shear sense determinations are sinistral in all nine oriented X:Z thin sections, though outcrop-scale shear sense indicators from

locations without petrographic samples (mostly near the Quebrada Tipias fault) more commonly suggest dextral shear. Poikiloblastic andalusite is present within and slightly beyond the mylonitic envelope surrounding the Matancilla pluton, and absent in Chañaral Complex rocks away from the Matancilla aureole. Porphyroblasts are commonly replaced by sericite-rich fine-grained mixtures and highly strained, with increasing strain in samples closer to the intrusive contact (Figure 3.9). Where strained, asymmetric σ - and δ - type pseudomorphs of andalusite porphyroclasts with quartz and white mica in pressure shadows indicate sinistral shear consistent with shear sense indicators in other phases. Elongate lenses dominated by fine-grained white mica with aspect ratios of $>30:1$ likely represent highly strained pseudomorphs of andalusite (Figure 3.9C). Relict mylonitic foliation is preserved as aligned inclusions within andalusite and rotated within porphyroclasts to angles discordant with the surrounding ductile shear fabric (Figure 3.9D). In conjunction with the spatial restriction of andalusite to the Matancilla granodiorite aureole, preservation of the early-formed mylonitic fabric suggests porphyroblast development was synkinematic with shear zone development and occurred during emplacement of the Matancilla granodiorite. Quartz, adularia, and chlorite veins cut mylonitic fabrics but are commonly folded, often with fold vergence consistent with other kinematic indicators, indicating veining was synkinematic or late synkinematic with ductile shear. Several samples have petrographic evidence for quartz annealing indicative of postmylonitic static recrystallization, with equant grains and straight boundaries, $\sim 120^\circ$ intergrain angles, and little to no undulatory extinction.

3.5.3. Matancilla protomylonite

Pervasive protomylonitic fabric within the Matancilla granodiorite has limited spatial extent and is restricted to the eastern margin of the plutonic complex where it intrudes the

Chañaral Complex. Most exposures with this deformation style have weak planar fabric defined by aligned biotite and hornblende and recrystallized but not continuous quartz ribbons.

Protomylonitic fabric in granodiorite strikes NNW to NNE and dips 83°W on average. Where the intrusive contact is exposed, protomylonitic foliation parallels the adjacent contact trace. Only a single locality has a weak but measurable linear fabric as a S>L tectonite, where the stretching lineation rakes shallowly north.

In thin section, aligned mafic minerals (biotite, hornblende) and discontinuous zones of recrystallized quartz or polyphase quartz-feldspar mixtures define the protomylonitic fabric. Subgrain rotation is the most commonly observed recrystallization mechanism in quartz-rich zones. Plagioclase with partially sericitized zones forms an interconnected strong phase and lacks dynamic recrystallization textures (Figure 3.6D). Microfaults demonstrate brittle behavior of feldspar and are commonly synthetic to sinistral shear sense from other kinematic indicators. Fine-grained recrystallized quartz-feldspar mixtures record the most strain, but feldspar clasts lack plastic deformation in most samples, and larger grains instead have brittle fractures. Petrographic shear sense indicators including C' shear bands, folded chlorite and epidote veins, and oblique quartz recrystallized fabric indicate sinistral shear in 3 of 4 protomylonite oriented thin sections with shear sense determination, and one sample has C' shear band indicators for dextral shear (Figure 3.6E). Secondary actinolite is locally sheared into low-strain σ -shape porphyroclasts, indicating late synkinematic fluid mobility. Late calcite veins cut the mylonitic foliation and are unstrained.

3.5.4. Discrete shear zones in the Matancilla plutonic complex

The Matancilla shear zone is largely unstrained, but irregularly spaced centimeter- to meter-thick, decimeter to decameter-long discrete shear zones record localized ductile shear.

Discrete mylonitic foliation within the Matancilla pluton has variable orientations but are most commonly N- to NE- striking and steeply dipping, and the average foliation is NE-striking (208, 85 NW). Eigenvalue statistics of foliation poles (Vollmer, 1990) indicate that $P \approx G > R$, signifying that the distribution of mylonitic fabric is systematically scattered from a point distribution. This distribution is consistent with field observations of anastomosing discrete shear zones. A slightly bimodal distribution of discrete shear zone foliations could alternatively reflect a scattered conjugate relation, but the lack of systematic difference of measurements with sinistral or dextral shear sense does not lend support to this interpretation. Lineations are shallowly raking (206/08 average). Only 30% of discrete mylonite foliation measurement localities have a measured lineation, though good exposures of the foliation surface are not present at every outcrop where foliation was measured and therefore the presence of lineations may be underrepresented. Kinematic indicators for discrete shear zones are variable. Of four oriented thin sections, three indicate sinistral shear and one has mixed shear sense. Hand sample kinematic indicators are dominantly sinistral, though dextral shear sense indicators were also observed.

Discrete shear zones are gradational from unstrained granodiorite into highly strained zones over centimeters to millimeters with locally intense ultramylonitic strain (Figures 3.5C-D, 3.6G-I). The dominant interconnected weak matrix is fine-grained quartz + feldspar \pm mica mixtures. Brittle shear fractures locally displace quartz and plagioclase porphyroclasts, indicating strong behavior of those phases relative to the weaker matrix assemblage. In higher-strain samples, zones of pure quartz matrix have pervasive subgrain recrystallization textures with local bulging recrystallization. Sericitized feldspar locally has minor recrystallization textures. Fine-grained mica and epidote grains are disseminated throughout the polyphase matrix in the highest strain samples.

In contrast to the pervasive mylonitic fabrics near the margin of the Matancilla pluton, discrete shear zones within the pluton have significant alteration and mineral replacement textures, and a pinstriped or bleached appearance in outcrop (Figures 3.5C-D, 3.6G-I). Feldspar is pervasively altered to sericite, and mafic minerals are completely chloritized. Clots of secondary actinolite form resistant boudins with biotite in boudin necks (Figure 3.6H), and fine-grained actinolite is locally present along C' shear bands, indicating alteration was coeval with mylonitization. Fe-oxides, adularia, and patchy calcite are likewise involved in ductile shear fabrics, and additional generations of adularia, calcite, and chlorite veins cut the mylonitic foliation. Secondary fluid inclusions mottle quartz grains.

3.6. DEVELOPMENT OF MYLONITIC FABRICS

3.6.1. Rheology and shear zone deformation conditions

The degree of mylonitic strain in the Matancilla shear zone is influenced by protolith lithology, proximity to the pluton thermal source, and hydrothermal alteration. The least intensely strained fabric belongs to the domain of pervasive protomylonitic granodiorite at the margin of the Matancilla plutonic complex, where interconnected zones of recrystallized material are uncommon. Hydrothermal alteration in this domain is generally minor, with incompletely chloritized mafic minerals and only partial sericitization of feldspar grains. Quartz has subgrain rotation recrystallization textures, but the 20–25% modal quartz is not sufficiently strained to form a throughgoing fabric, and more abundant feldspars record entirely brittle deformation in most strained samples.

Strain intensity within the Chañaral Complex metasedimentary rocks is dependent on both lithology and proximity to the plutonic complex. In distal parts of the Matancilla shear zone, quartzose sandstone protoliths retain equant grain shapes while adjacent metasilstone is

more highly strained, and in the proximal shear zone, both protolith lithologies record plastic strain (Figure 3.9). Sinistral shear in very fine-grained lithologies is likely accommodated by diffusion creep mechanisms such as grain boundary sliding and dissolution-precipitation creep, while mica-rich domains likely record slip on basal planes. Ultramylonite in the aureole is only present in the finer-grained lithology, where micaceous horizons had lower resistance to deformation.

Inclusion trails of quartz and aligned micas preserve relict mylonitic foliation within andalusite, and the restricted spatial nature of both the mylonitic fabric and of andalusite porphyroblasts to the aureole of the Matancilla pluton provide a confident interpretation that andalusite was synkinematic with mylonitic shear. Andalusite porphyroblast growth can increase viscosity of metapelitic rocks, even to the point such that they can be stronger than metapsammitic interbeds (with sufficiently low initial effective viscosity contrast; Groome et al., 2006). However, replacement of andalusite by sericite-rich alteration products is observed in more highly-strained samples (Figure 3.9), and this alteration counteracted the porphyroblast strengthening effect. Highly-strained andalusite pseudomorphs in pelitic horizons of a sample with low-strain metasandstone horizons indicates the viscosity contrast focused strain into the weaker finer-grained protoliths even where andalusite porphyroblasts are present.

The kilometer-thick zone of mylonitic fabric in Chañaral Complex metasedimentary rocks is both the most extensive and has the highest strain fabrics in the Matancilla shear zone, excluding the spatially-limited discrete shear zones within the pluton. The limited ability of the unaltered granodiorite protolith to undergo significant plastic strain reflects the much greater strength of this feldspar-rich lithology relative to the quartzose and pelitic protolith mylonitic envelope that surrounds the pluton and demonstrates that, like AFS shear zones, pelitic horizons

in the thermal aureole of Middle Jurassic synkinematic plutonism were the weak link in the rheologic system and accommodated the greatest strain.

Across all mylonite protolith domains, subgrain rotation is the dominant quartz recrystallization mechanism with lesser bulging recrystallization, and these textures are consistent with mid- to upper- greenschist facies recrystallization temperatures at typical shear zone strain rates and water contents (e.g., Stipp et al., 2002; Law, 2014). Biotite and actinolite synkinematic with plastic deformation are further supportive of greenschist-facies deformation. Spectral and petrographic analysis indicates biotite and muscovite are present in Chañaral Complex rocks outside of the Matancilla aureole, but that pyrophyllite is absent. Aureole reactions that form andalusite without garnet or staurolite suggest relatively low reaction pressures of $< \sim 3$ kbar and upper-greenschist facies temperatures (e.g., Pattison and Spear, 2018), which is broadly consistent with Al-in-hornblende barometry estimates of 1.9–2.4 kbar intrusion pressures for plutons in the Coastal Cordillera (Dallmeyer et al., 1996). In pure quartz domains in three samples (two metasedimentary mylonites and one Matancilla granodiorite mylonite), we estimate root mean square dynamically recrystallized quartz grain is ~ 18 – 20 μm , suggesting differential stress of ~ 60 – 70 MPa according to the Stipp and Tullis (2003) piezometer.

Quartz static recrystallization textures overprint some Chañaral complex mylonite samples, including a metasilstone with aligned biotite and relict S-C fabrics located between the Las Tiplas and Matancilla plutons (Figure 3.3F). Early Cretaceous intrusion of the Last Tiplas granodiorite is likely responsible for static recrystallization in samples adjacent to that pluton, but quartz static recrystallization textures present in samples > 5 km from the Las Tiplas granodiorite suggest that deformation waned before elevated temperatures from Matancilla magmatism relaxed below quartz plasticity thresholds. In other samples, quartz veins that cut

mylonitic fabrics are asymmetrically folded and recrystallized with grain boundary migration textures, consistent with high temperature and/or low strain rate deformation. A sample of pervasively-strained Matancilla granodiorite near the intrusive contact has grain boundary migration dynamic recrystallization textures with 100–200 μm quartz grains that envelop or terminate against platy biotite (Figure 3.6F), with a weak oblique quartz grain-shape fabric that indicates sinistral shear. Quartz grain boundary migration textures could record low strain rates in the late stages of deformation in the Matancilla thermal aureole.

Strongly heterogeneous deformation in the Matancilla mylonite indicates that strain preferentially localized in weakened zones. The most highly strained domains are discrete shear zones with fine-grained feldspar + quartz-rich mixtures with pre- to synkinematic alteration phases (chlorite, actinolite, adularia, Fe-oxides, calcite, and secondary micas), and fine-grained polyphase mixtures can have the weakest rheology in quartzofeldspathic ultramylonites (Stenvall et al., 2019). Fractured quartz porphyroclasts with undulatory extinction in samples with fine-grained quartz-feldspar mixtures indicate relatively strong behavior of quartz compared to the polyphase matrix (Figure 3.6B). Alteration associated with high-strain ultramylonites in the otherwise rheologically-strong granodiorite suggests that reaction softening and hydrolytic weakening allowed breakdown of strong feldspars and enhanced plastic deformation. The degree of feldspar sericitization and chloritization of mafic minerals is notably greater in high-strain discrete shear zones than in the domain of pervasive protomylonite, despite the same granodiorite protolith. Mobile fluids were likely derived either from mineral reactions (e.g., andalusite formation) or fluids associated with magmatism, and synchronous development of the discrete shear zones with pluton emplacement suggests the latter at least partly enhanced ductile strain.

3.6.2. *Shear zone kinematics*

Across all protoliths, 17 thin sections yield a confident shear sense determination, and 15 of these have sinistral shear sense indicators. However, 7 of 11 shear sense indicators from outcrops without petrographic samples are dextral, indicating possible heterogeneous shear. No geometric pattern is evident that separates mylonitic foliation and lineation measurements with sinistral and dextral shear sense indicators; both are NNE- to NE-striking on average with shallowly raking lineations. Sinistral shear sense indicators are the most widespread across the shear zone, while dextral kinematic indicators are most common in the aureole between the Taltal and Quebrada Tipias faults and could reflect a localized strain anomaly or change of pluton margin geometry. Some localities have seemingly conflicting indicators for sinistral and dextral shear in outcrops separated by only tens of meters, without deflection of the mylonitic foliation. Variable shear sense indications may reflect heterogeneous rheology at meso- and micro-scales controlled by alternating quartzose and micaceous protoliths in the Chañaral complex metaturbidites and by localized discrete shear along possible fluid pathways in the Matancilla granodiorite. From the dominance of clear sinistral shear sense indicators, especially in samples where multiple phases and microstructures indicate the same shear sense, we interpret the Matancilla shear zone to record overall sinistral shear. This interpretation is also supported by the geometry of mylonitic fabrics with respect to the shear zone margin. The intrusive contact of the Matancilla granodiorite largely defines the margin of the main shear zone and strikes N- to NNE- with a distance-weighted trace azimuth of 14° (Figure 3.8D). On average, fabric in the Chañaral Complex mylonite aureole strikes NNE $\sim 18^{\circ}$ clockwise of the intrusive contact, consistent with sinistral shear. The presence of S>L and S-tectonite fabrics and evidence for coaxial or antithetic (dextral) shear in parts of the shear zone suggests an overall transpressional

regime with a component of shortening across the shear zone (e.g., Sanderson and Marchini, 1984).

3.6.3. Timing

The spatial pattern of the mylonitic zone in the Chañaral Complex following the intrusive contact strongly indicates that the shear fabric formed in the thermal aureole of the Matancilla pluton. Protomylonitic fabric within granodiorite at the margins of the plutonic complex largely parallels the intrusive contact and is oriented similar to mylonitic foliation in the surrounding metasedimentary rocks, indicating that ductile shear in both domains was related to Middle Jurassic pluton emplacement.

Some discrete mylonitic fabric measurements strike roughly parallel to the AFS and have shallowly-raking lineations and sinistral shear sense indicators, which is kinematically compatible with the documented Early Cretaceous shear on the N-striking AFS (e.g., Seymour et al., 2021). However, the discrete mylonitic zones seem evenly distributed within the Matancilla pluton and do not reflect any clear pattern of abundance or thickness with proximity to the eastern (main) branch of the AFS, and some of the discrete mylonitic foliation planes near the AFS are nearly perpendicular to the AFS strike. We find no evidence that the discrete mylonitic zones in the Matancilla pluton are spatially or temporally connected to the AFS, and the presence of both mylonitic and nonmylonitic Matancilla granodiorite clasts in AFS cataclasite show a clear overprinting relation of AFS brittle deformation on ductile shear fabrics. Likewise, discrete shear zones are found only within the Matancilla pluton and do not show a spatial pattern with relation to the intrusive contact of the unstrained Early Cretaceous Las Tipias granodiorite, which clearly cross cuts the mylonitic fabric developed in the aureole of the Matancilla pluton. Despite the higher orientation variability, discrete shear zones in granodiorite are, on average,

similarly oriented to the mylonitic fabric in the Matancilla aureole. The average foliation measurements of discrete shear zones and mylonite in the metasedimentary aureole are only 8° different, and the average lineations are within 13° . From the similarity in orientation and kinematics and lack of discrete shear zones overprinting pervasive mylonite, we here infer that all three mylonitic domains are temporally and kinematically connected.

As depicted on regional-scale maps, the Matancilla plutonic complex includes multiple lithologies including granodiorite, diorite, quartz diorite, and monzogranite, with a range of ages from 178–154 Ma (Escribano et al., 2013; Álvarez et al., 2016), though detailed mapping and recent zircon U-Pb geochronology indicates some of these subunits may instead be separate Late Jurassic to Early Cretaceous intrusions (Mavor et al., 2020; Ruthven et al., 2020). The Matancilla shear zone studied here tracks along the intrusive contact of a granodiorite facies of the Matancilla plutonic complex with a zircon U-Pb date of 169.0 ± 1.6 Ma (Mavor et al., 2020), which we interpret as the best estimate for timing of shear zone formation. Further constraints are found from plutons that cut ductile shear fabrics. Two dates of fine- to medium-grained San Ramon granite that cross cut discrete shear zones overlap at ~ 160 Ma (Seymour et al., 2021). A new U-Pb zircon date of Last Tipias granodiorite, which cuts metasedimentary mylonite and lacks internal discrete shear zones, has an overall weighted mean age of 130.6 ± 1.6 (MSWD = 6.7, Figure 3.7B). A grouping of 135–137 Ma grains is seemingly discontinuous with the age spread of other grains in the sample and may represent an older population of ante- or xenocrystic grains that contribute to the high MSWD value. Excluding these grains gives a calculated WMA of 129.5 ± 1.1 (MSWD = 2.1); this is our preferred age, as the lower MSWD indicates a higher likelihood that the analyses are from a single population. In either case, the zircon data indicate the Las Tipias pluton is ~ 10 Myr younger than suggested by K-Ar methods

(Escribano et al., 2013) and that Matancilla fabrics had clearly formed prior to the mid- Early Cretaceous.

3.7. DISCUSSION

3.7.1. Mylonite as a record of regional tectonic stresses

The spatial association of mylonitic fabrics with the Matancilla intrusive contact indicates that ductile deformation occurred only where the thermal influence of plutonism weakened the surrounding quartz- and mica-rich rocks, which were weaker than feldspar-rich plutonic lithologies, but this relation alone does not determine if strain fabric reflects regional tectonism or localized transient stresses due to pluton emplacement. Matancilla shear zone fabrics satisfy two of the three strongest lines of evidence put forward by Paterson et al. (1989) to determine syntectonic pluton intrusion: (1) solid-state deformation fabric within the pluton and in the surrounding aureole parallels the intrusive contact, and (2) porphyroblasts restricted to the contact metamorphic aureole are synkinematic with this fabric. The third criteria, requiring parallelism of magmatic flow fabrics with solid-state deformation, cannot be evaluated as a magmatic or submagmatic foliation is not observed in the Matancilla granodiorite, and the pluton is texturally isotropic where unaffected by mylonitic shear. These criteria, along with the overall consistency of NNE-striking mylonitic foliation without any major deflections and kilometer-scale shear zone thickness suggests that ductile fabrics record regional tectonism rather than a localized strain field.

3.7.2. Localization of the AFS

Observation of Early Jurassic ductile shear zones with sinistral shear sense have led some studies to posit that the main Early Cretaceous phase of AFS deformation was preceded by sinistral and extensional shear in the Jurassic (Scheuber and Andriessen, 1990; Scheuber and

Reutter, 1992). The refined spatial extent and cross-cutting relations of ductile shear zones presented here show that AFS deformation near the Matancilla pluton is exclusively brittle with cataclastic overprint of ductile fabrics. The 20–25° counterclockwise oblique angle of the AFS with the Matancilla intrusive contact and even greater obliquity to the average mylonitic foliation, along with the lack of any deflection in the straight AFS fault trace, demonstrates that Matancilla fabrics had no influence on fault localization during Early Cretaceous deformation. Instead, the trace of the AFS was controlled by thermally-weakened shear zones associated with synkinematic plutonism that were linked via brittle faults to form the throughgoing fault system (Seymour et al., 2020, 2021). Intrusion of the Las Tipias pluton at 130 Ma is ~6 Myr later than most of the mylonitic deformation on the southern Páposo segment (Ruthven et al., 2020) and ~3 Myr later than the initiation of mylonitic deformation on the northern El Salado segment at the Cerro del Pingo pluton (Seymour et al., 2021). The AFS might have already been established as a weak brittle fault near Taltal by the time of Las Tipias intrusion, and it was likely rheologically favorable for strain to localize in the existing fault zone rather than in the pluton ≥ 1 km to the east.

While Jurassic magmatism facilitated plastic strain in the same way as Early Cretaceous plutons, and Matancilla sinistral shear may reflect similar plate boundary slip partitioning as models of the Early Cretaceous AFS, evidence presented here does not support the notion that Jurassic plutons formed a throughgoing proto-AFS precursor structure that guided later strain localization. Instead, the AFS connected the thermally-weakened zones between synkinematic Early Cretaceous plutonism (e.g., between the Cerro del Pingo pluton and southern Páposo segment), independent of Jurassic shear zone geometry.

3.7.3. *Implications for plate tectonics*

Steady sedimentation in the back-arc, syndepositional normal faults in arc clastic strata, and synplutonic extensional shear zones suggest that the overall strain regime of the Jurassic Andean arc was dominantly extensional (e.g., Grocott et al., 1994b; Scheuber and Gonzalez, 1999; Charrier et al., 2007). However, sinistral shear of Matancilla mylonite suggests that upper plate deformation was oblique with a strike-slip component. Steep foliation and subhorizontal lineations in the Matancilla shear zone contrasts with the patterns of pluton emplacement into extensional roof-uplift shear zones in the Late and Early Jurassic and contradicts suggestions that pluton emplacement only occurred when extensional fault systems were active (Grocott et al., 1994; Grocott and Taylor, 2002). Despite the dominant record of margin-perpendicular extension, some additional lines of evidence record sinistral shear in the Jurassic Coastal Cordillera that could also be consistent with sinistral oblique plate convergence (Figure 3.10). NE- striking folds and thrusts, along with discrete shear zones in the Bolfin Complex near 24°S, are compatible with NW-SE shortening and sinistral subduction obliquity between 155–150 Ma (Scheuber and Gonzalez, 1999). The Tigrillo fault system, which records either Early Jurassic extension (Grocott and Taylor, 2002) and/or Early Jurassic sinistral transpression (Contreras et al., 2013) is cut by a system of NW-striking sinistral faults near Cifuncho (~25.7–25.9°S). These faults appear to die out into the upper La Negra Formation, constraining faulting to before the early Late Jurassic (Contreras et al., 2013), apparently contemporaneous with intrusion of the Matancilla pluton. Sinistral shear on NW-striking faults is potentially compatible with the Matancilla shear zone if the regional σ_1 trended between 118° (perpendicular to the average Matancilla mylonite strike) and 138° (approximate strike of NW-striking faults), which would be required to impart sinistral shear on both structures simultaneously. While such interpretations

can be complicated by stress refraction and strain partitioning, these structures provide an opportunity to fill the Middle Jurassic gap of plate-margin kinematic constraints, and contrast with suggestions that Jurassic plate convergence was perpendicular to the plate boundary (Dallmeyer et al., 1996) or that onshore deformation was purely margin-normal (Scheuber and Gonzalez, 1999). Future work to better constrain the kinematics of the Tigrillo fault system and the NW-striking faults that displace it are warranted for further understanding of Coastal Cordillera tectonics in the Middle Jurassic.

Middle Jurassic sinistral plate margin obliquity may provide a constraint for plate margin configurations at that time. If the sinistral shear recorded by Matancilla mylonites does indeed record partitioning of oblique subduction shear into the contemporaneous magmatic arc, it would suggest that the Phoenix-Farallon-South American plate triple point was north of $\sim 25^\circ$ S at 169 Ma (Figure 3.10). Reconstructions showing NE-directed plate motion of the Farallon plate against the stalled South American plate in the Middle Jurassic (Matthews et al., 2016) would impart a dextral shear sense to the margin-parallel component of partitioned strain, while the SE-directed vector of the Phoenix plate is consistent with sinistral shear. With indications for sinistral shear in the Early, Middle, and Late Jurassic, it is possible that the Phoenix-Farallon spreading center was never south of latitude 25° S through the entirety of the Jurassic, and perhaps not south of 24° S if Early and Late Jurassic margin-parallel sinistral shear in the Bolfin Complex reflects subduction obliquity (Scheuber and Gonzalez, 1999; Figure 3.10).

3.8. CONCLUSIONS

Mylonitic deformation associated with intrusion of the Matancilla plutonic complex provides a rare opportunity to constrain the Middle Jurassic tectonics of the Chilean Coastal Cordillera and challenges the paradigm that strain in the upper plate of the Andean Orogeny was

exclusively extensional for most of the Jurassic. The spatial and textural characteristics of mylonitic fabrics demonstrate that ductile shear was guided by the thermal influence of the ~169 Ma Matancilla granodiorite and meets the requisite criteria to interpret regional strain fields from an intrusion-associated shear zone. Sinistral shear with a component of flattening strain in the NNE-striking Matancilla shear zone contrasts with the dominantly E-W extensional strain regime indicated by most Early and Late Jurassic structures. Like ductile fabrics documented for the Early Cretaceous AFS, the Matancilla shear zone may record partitioning of the strike-slip component of plate margin obliquity into rheologic weak zones in the Andean arc, but the Matancilla shear zone did not serve as precursor structure to the AFS that localized Early Cretaceous strain, suggesting that intra-arc shear zones are transient rather than long-lived structural features. Sinistral shear is compatible with the Phoenix-Farallon spreading center intersecting the Andean trench north of latitude 25° S in the Middle Jurassic.

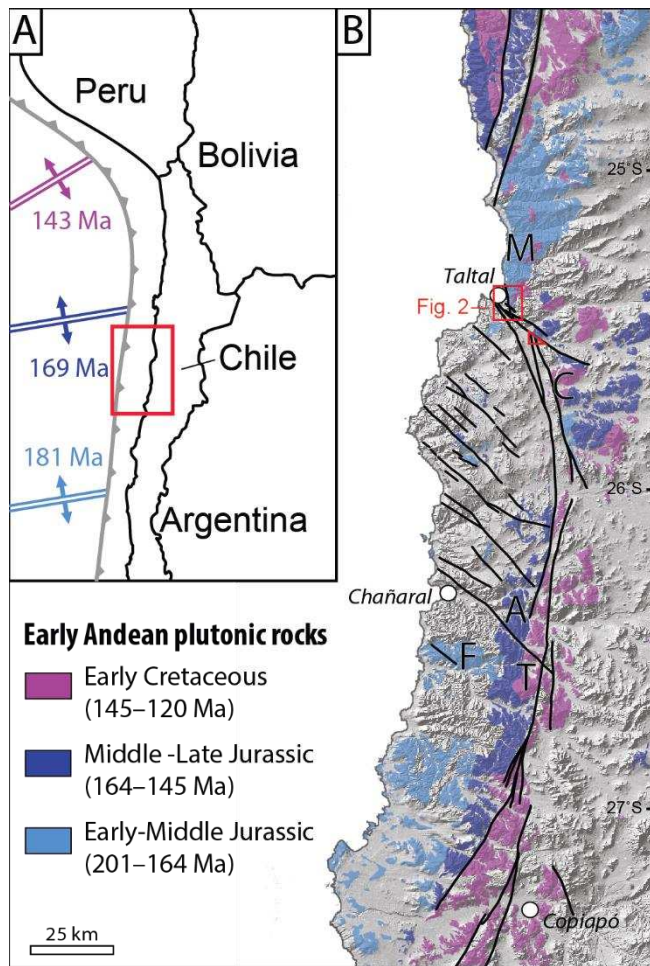


Figure 3.1. A) Approximate locations of the mid-ocean ridge between the Farallon (south) and Phoenix (north) plates through the Jurassic and Early Cretaceous (from Matthews et al., 2016). B) Plutonic provinces of the early Andean arc. Notable plutonic complexes with syn-emplacement ductile shear zones are marked: A – Animas, C – Cerro del Pingo, F – Flamenco, M – Matancilla, T – Las Tazas. Figure modified from Seymour et al. (2020) with data sourced from Álvarez et al. (2016), Arévalo, (2005), Contreras et al. (2013), Escribano et al. (2013), Espinoza et al. (2014), Godoy et al. (2003), Godoy and Lara (1998), Godoy and Lara (1999), and Lara and Godoy (1998).

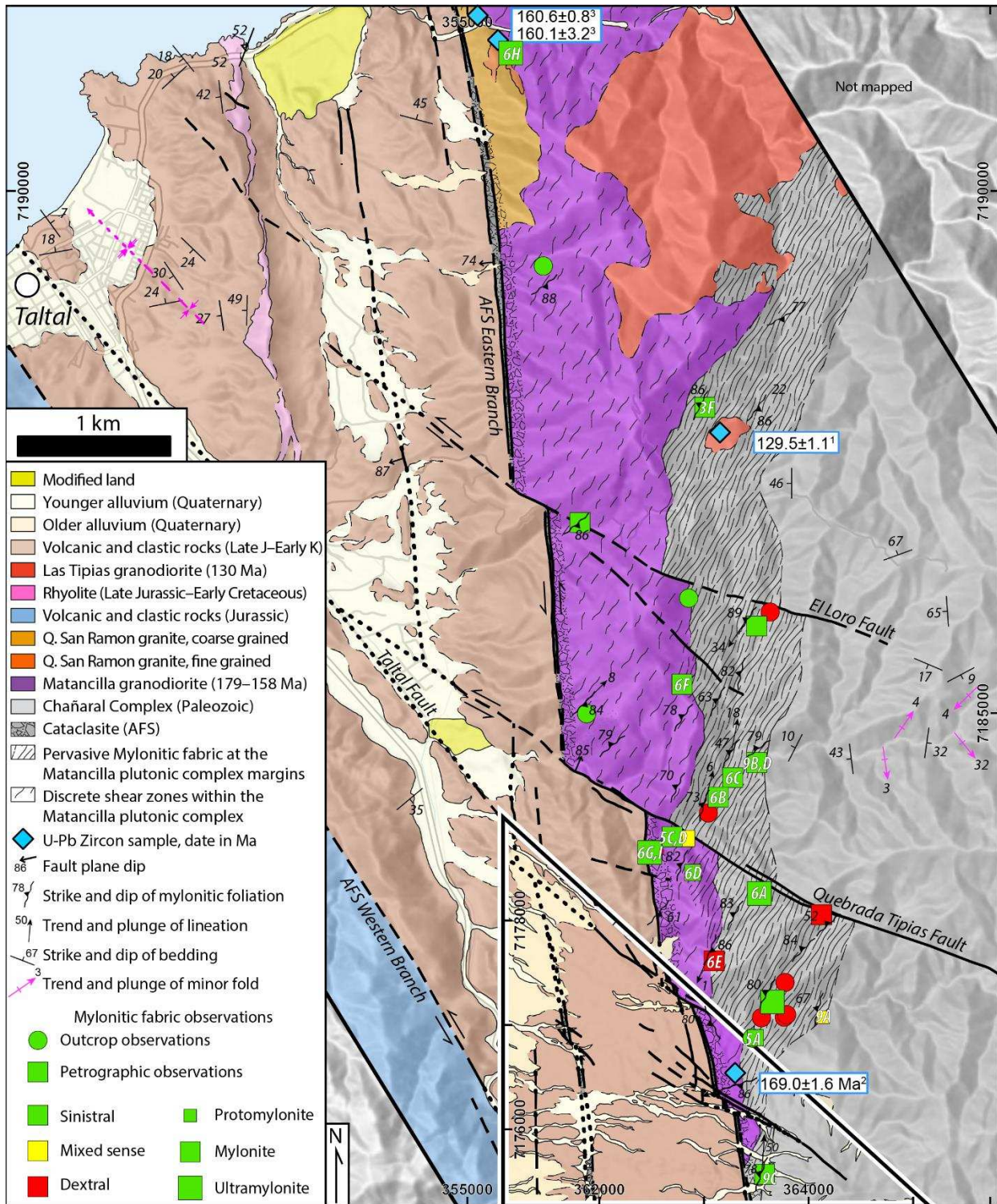


Figure 3.2. Geologic mapping of the Matancilla intrusive complex near Taltal. An inset map with a separate coordinate grid outlined in the white triangle shows the offset sliver of the pluton south of the Taltal fault in a restored position. Slip on other NW-striking faults of the Cretaceous Taltal fault system have not been restored. U/Pb dates are from: ¹This study; ²Mavor et al., 2020; ³Seymour et al., 2021. Coordinate system: WGS1984 19S.

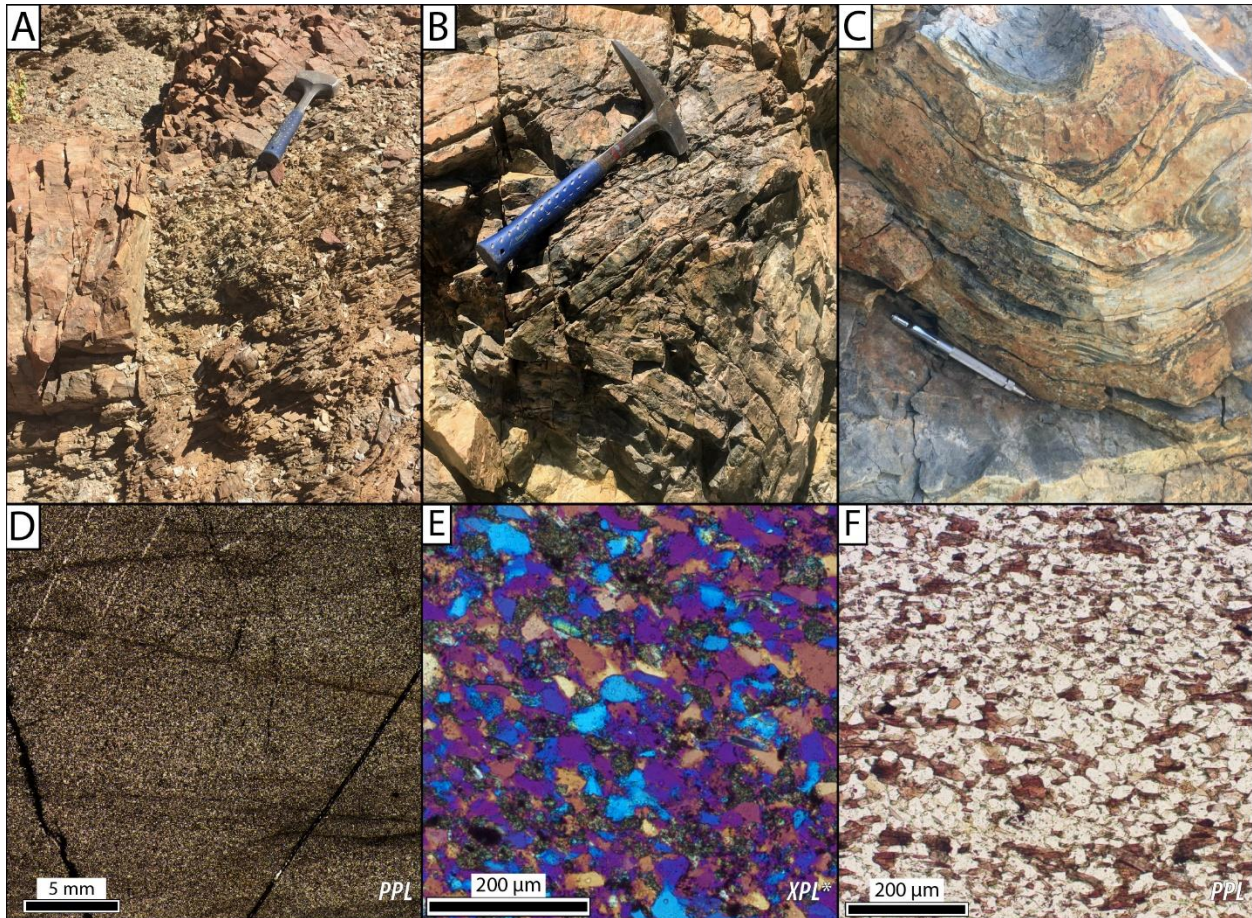


Figure 3.3. Metasedimentary rocks of the Late Paleozoic Chañaral Complex. A) Nonmylonitic metasandstone and metasilstone displaced by a sinistral N-striking fault associated with the Atacama fault system. Foliation is parallel to sedimentary compositional layering. B) Tight recumbent folding of quartzose metasandstone. C) Plunging upright open folds in quartzose metasandstone. D) Thin section scan of nonmylonitic Chañaral Complex metasandstone >5 km from the Matancilla pluton. Faint foliation in this sample is parallel to compositional layering. E) Detail view of the sample in 3F, showing foliation defined by aligned biotite. F) Metasilstone with quartz static recrystallization indicated by straight 120° grain boundaries and lack of undulatory extinction. Foliation oriented parallel to Matancilla mylonitic fabrics is preserved by aligned biotite. * = gypsum plate inserted.

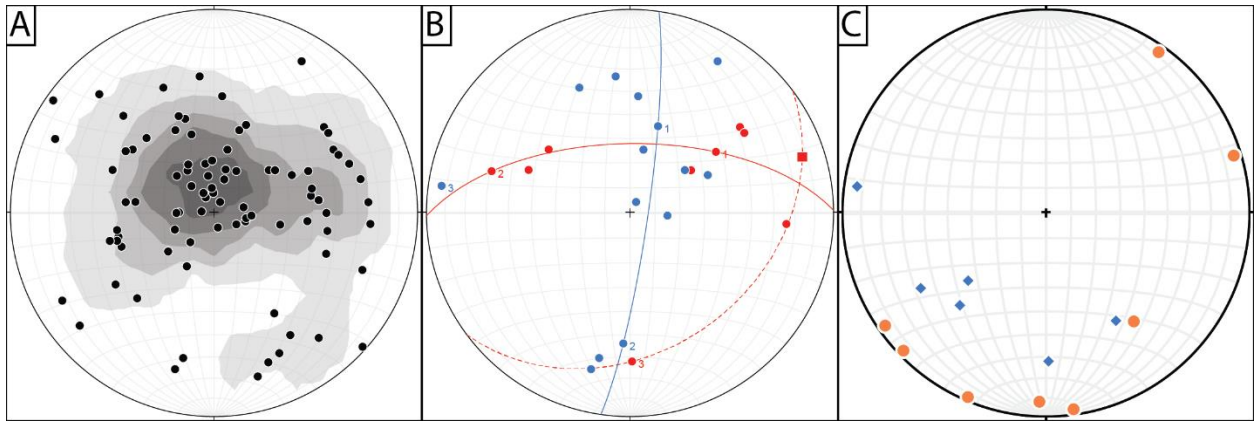


Figure 3.4. A) Poles to bedding (n=88) in Chañaral Complex metasedimentary rocks. Scattered poles reflect the multiple folding events observed in outcrop without a unifying girdle distribution that would characterize a single folding event. Bedding most commonly dips shallowly but in places has near vertical dips. B) Measurements of two outcrop-scale folds in the Chañaral Complex ~670 m apart. The folds show nearly orthogonal calculated fold hinges (278/07, bedding poles in blue and 179/28, bedding poles in red). Using a linear measurement of the axial trace for the latter fold (red square) and the calculated fold axis, the axial plane for the gently inclined fold is calculated as 053, 33 SE (dashed red line). C) Linear structural elements in Chañaral Complex metasedimentary rocks. Crenulation lineation measurements (orange circles) are measured where a crenulation lineation is visible in the bedding-parallel cleavage. Fold axes (blue diamonds) were measured in outcrop or calculated from bedding measurements across outcrop-scale folds. A broad trend of NE-SW to N-S shallowly plunging lineations is present, but significant variation indicates polyphase deformation.

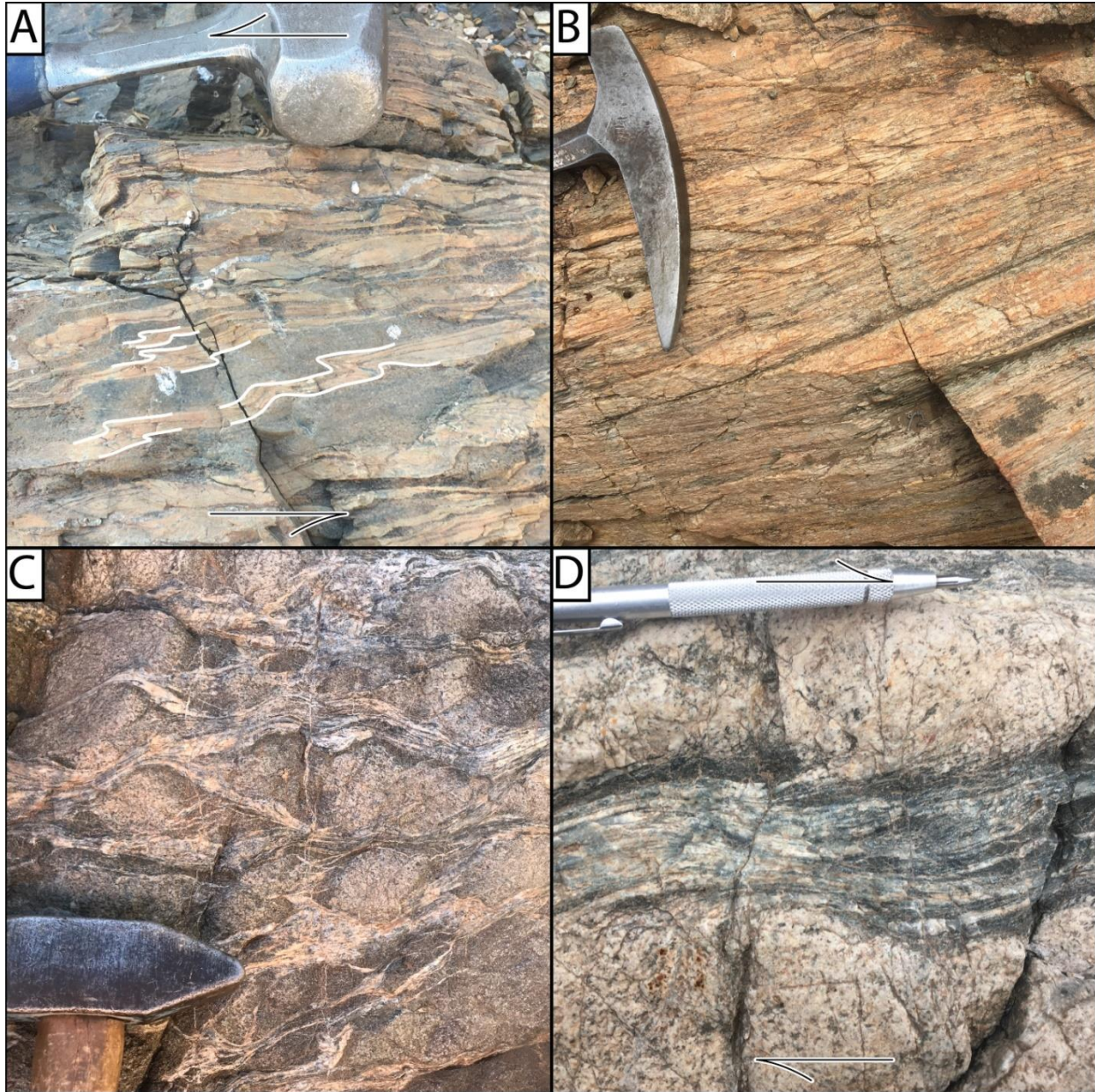


Figure 3.5. Outcrop photos of the three domains of Matancilla mylonite: A) Weakly mylonitic quartzite and phyllite of the Chañaral complex ~400 m from the contact with the Matancilla pluton. Asymmetric folds (white highlight) show sinistral shear. B) Pervasive protomylonitic foliation within Matancilla plutonic complex granodiorite. C) Anastomosing discrete shear zones in Matancilla granodiorite in a zone with unusually high density. D) Gradation from high strain ultramylonitic zone into unstrained Matancilla mylonite. Curvature of the strain fabric indicates dextral shear.

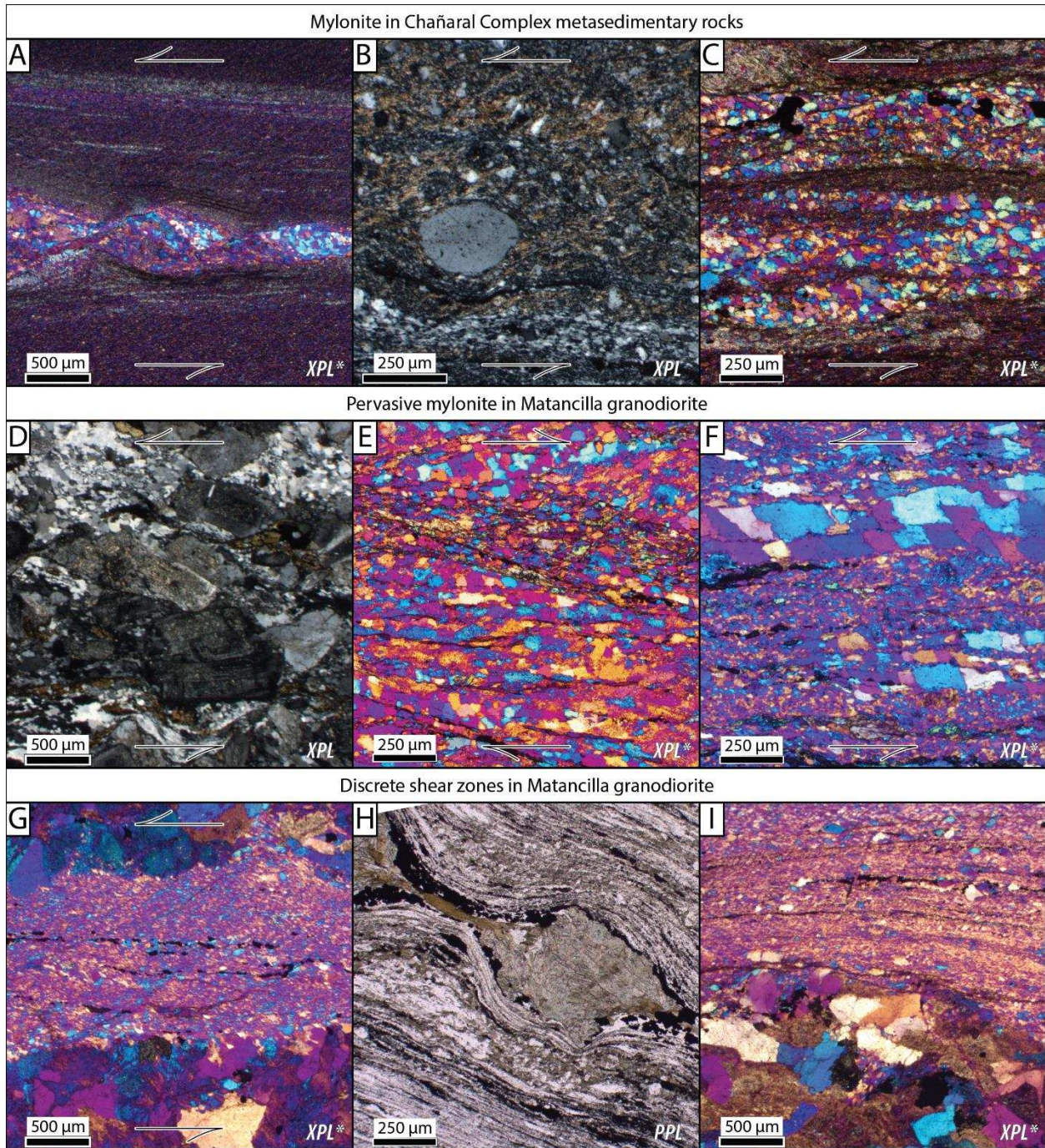


Figure 3.6. Photomicrographs from Matancilla shear zone mylonites with shear sense interpreted from C' shear bands (A-E and G) and/or recrystallized quartz oblique grain shape (A, C-D, and F). A) High strain mylonite in fine grained metasedimentary protolith of the Chañaral complex, with a boudinaged quartzose layer displaced by shear bands. B) Heterogeneously-strained mylonite in a Chañaral complex metasedimentary protolith. C) Subgrain rotation as the dynamic recrystallization mechanism in quartzose layers of a thinly-bedded protolith. D) Protomylonite in Matancilla granodiorite. E) Sample of pervasive mylonite near the Matancilla intrusive contact with shear bands indicating dextral shear. F) Matancilla protomylonite with grain boundary

migration recrystallization mechanism textures. Large, recrystallized quartz grains envelop or are pinned against biotite. G) Sharp transition from unstrained Matancilla granodiorite into an ultramylonitic quartz-feldspar discrete shear zone. H) Boudinaged actinolite (and Fe-oxides (opaque) in ultramylonite of a discrete shear zone. I) Strongly heterogenous strain in discrete mylonite. * = gypsum plate inserted.

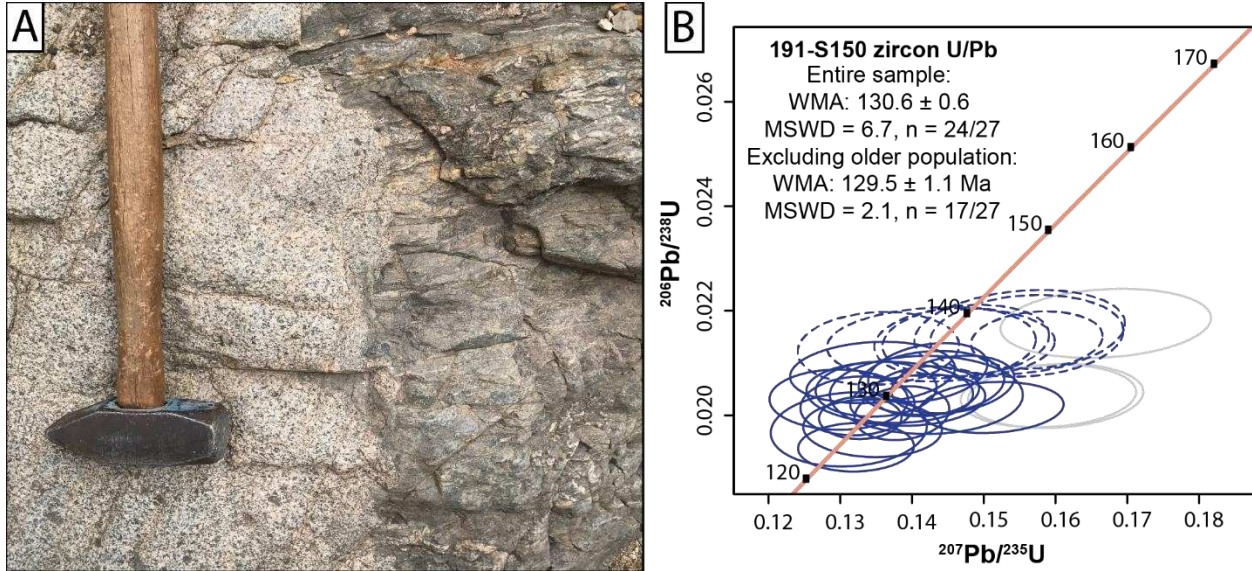


Figure 3.7. A) Intrusive relation of the Las Tiplas granodiorite cross-cutting the mylonitic fabric in metasedimentary rocks in the aureole of the Matancilla pluton near sample locality 191-SM50. The Las Tiplas granodiorite is unstrained at the contact. B) U-Pb concordia diagram for igneous sample 191-SM50 from the Las Tiplas granodiorite. Data-point error ellipses are 2σ . Gray ellipses show analyses with $>10\%$ discordance excluded from calculations. Dashed ellipses mark concordant analyses that possibly represent an older zircon population.

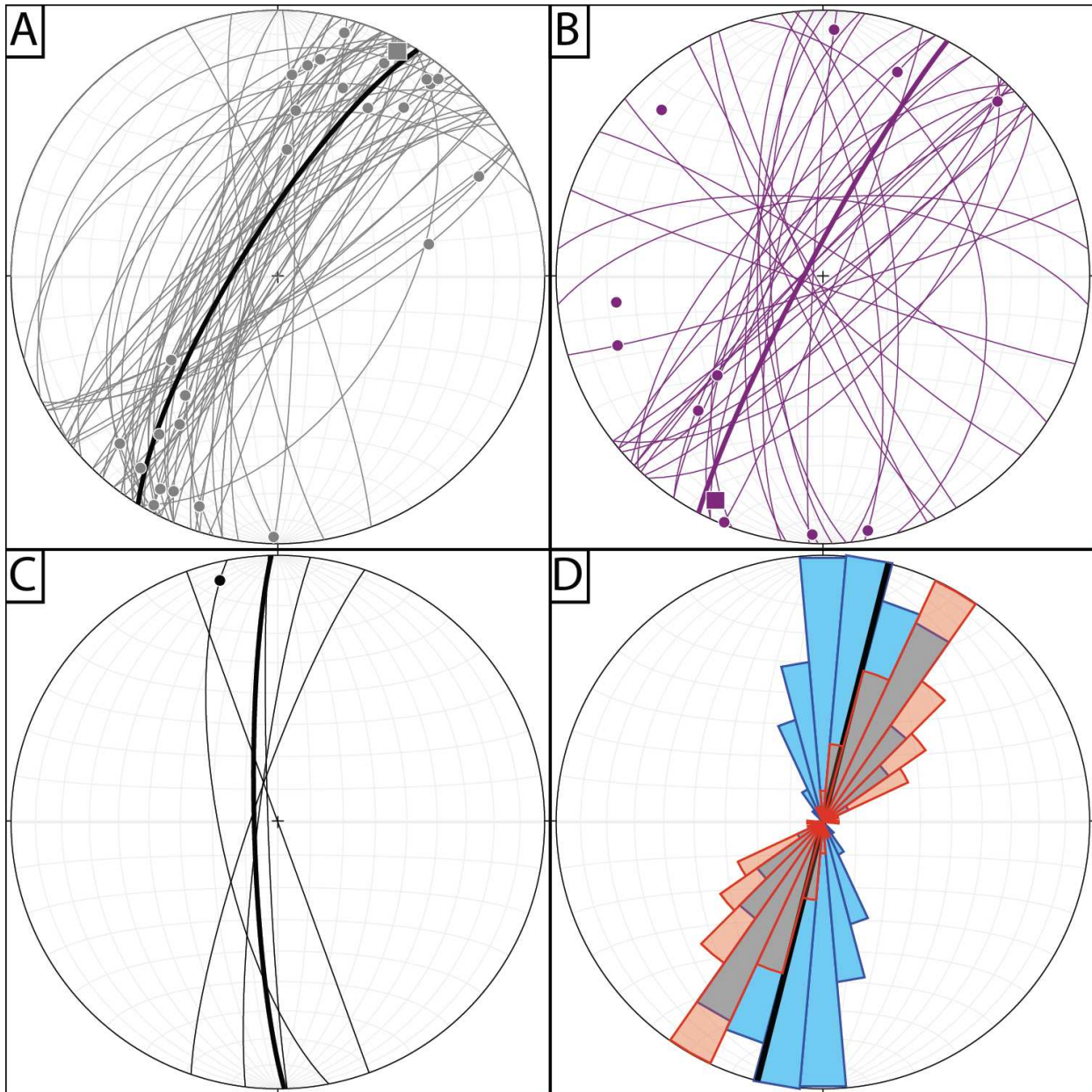


Figure 3.8. Geometry of the Matancilla shear zone, with average foliation and lineation for each population plotted in bold. A) Stereoplot of mylonitic foliation and lineation in metasedimentary rocks surrounding the Matancilla pluton. B) Discrete mylonitic shear zones from within the Matancilla plutonic complex. C) Stereoplot of mylonitic foliation and lineation measured in sparse zones of pervasive protomylonite along the eastern margin of the Matancilla pluton. D) Rose diagram showing the distance-weighted azimuthal distribution of the Matancilla granodiorite intrusive contact (blue) over the 9 km mapped length in 10° bins. The linear directional mean azimuth of 14° is shown with a bold line. Measured strikes of Chañaral Complex mylonitic fabric (red) are on average 18° clockwise of the intrusive contact.

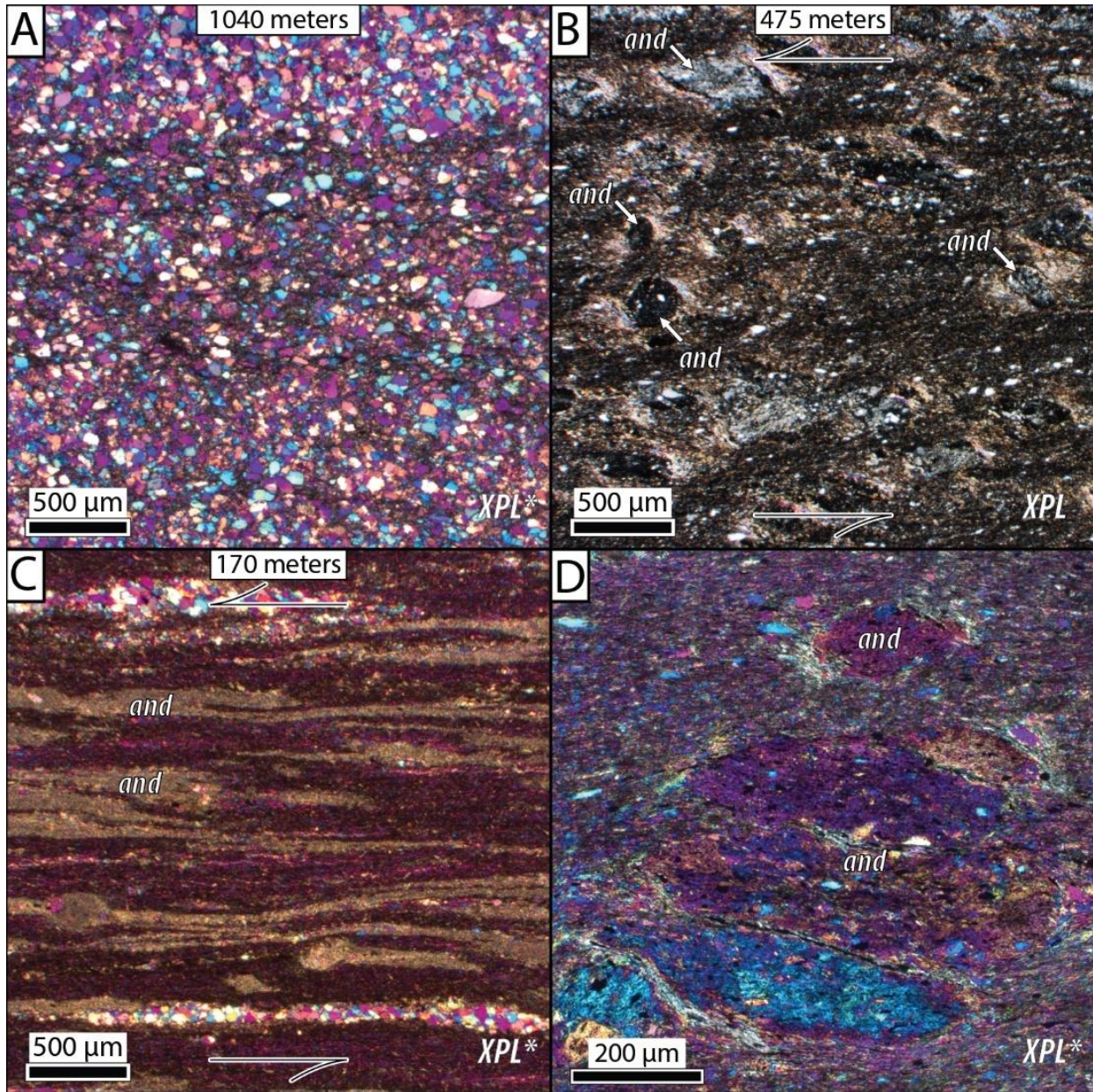


Figure 3.9. A-C) Photomicrographs of Chañaral Complex metasedimentary rocks with increasing proximity to the Matancilla plutonic complex (distance to intrusive contact labeled). A: Nonmylonitic metasandstone outside of the mylonitic aureole lacking andalusite porphyroblasts. Bedding-parallel foliation defined primarily by dark pressure solution seams and roughly aligned fine-grained mica. Quartz has undulatory extinction and minor static grain growth but lacks dynamic recrystallization. B: Mylonitic metasiltstone with synkinematic andalusite porphyroblasts. Both σ - and δ - type andalusite porphyroclasts indicate sinistral shear. C: More highly strained metasedimentary mylonite with dynamic recrystallization of quartz and highly strained lenses of sericite-rich pseudomorphs of andalusite porphyroclasts. Oblique grain shape fabric of recrystallized quartz and σ -type andalusite pseudomorphs indicate sinistral shear. D: Detail view of poikiloblastic andalusite porphyroclasts (same sample as B), showing relict mylonitic fabric as inclusions within andalusite. * = gypsum plate inserted.

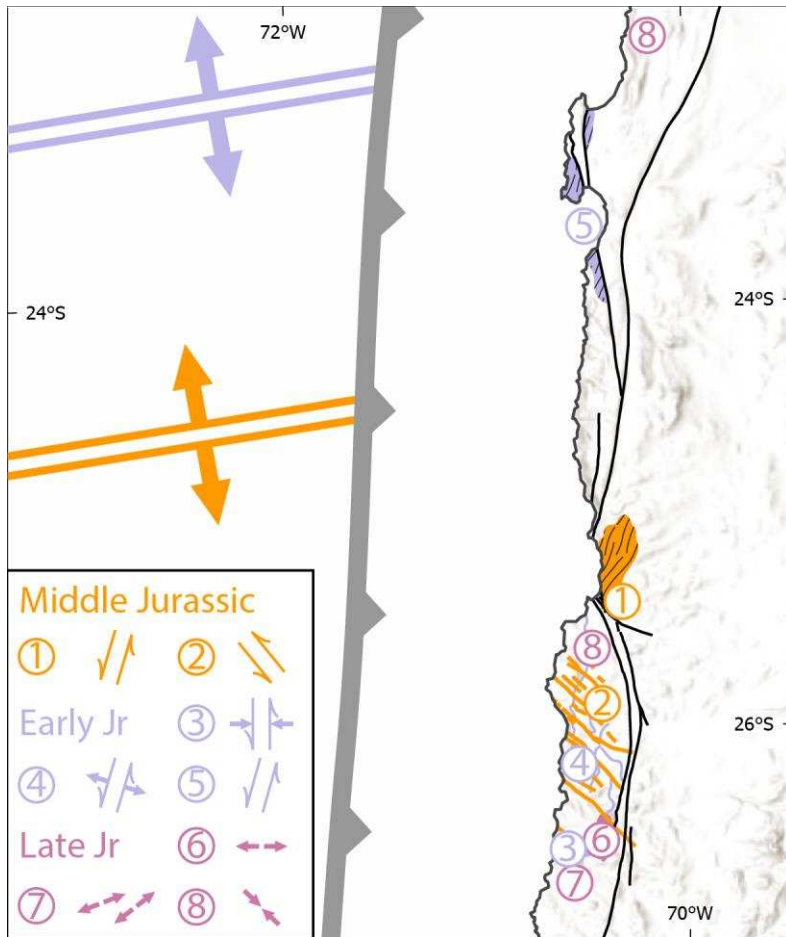


Figure 3.10. Compiled lines of structural evidence for Jurassic upper plate sinistral and extensional shear in the Coastal Cordillera of northern Chile. Structures are shown schematically with inferred shear sense or shortening/extension directions and colored according to deformation timing. Positions of the Phoenix-Farallon spreading center are shown at the furthest southward positions that would impart sinistral obliquity to the northernmost onshore contemporaneous structures and would be north of the area shown in the Late Jurassic and Early Cretaceous. Numbered structures are: 1) The Middle Jurassic sinistral Matancilla shear zone (this study); 2) Middle or early Late Jurassic NW-striking faults near Cifuncho (Contreras et al., 2013); 3) Sinistral shear during emplacement of the Early Jurassic Flamenco pluton (Rodríguez et al., 2021); 4) The Early Jurassic Tigrillo fault zone, recording either extensional (Grocott and Taylor, 2002) or sinistral transpressive (Contreras et al., 2013) strain; 5) Amphibolite-facies mylonitic fabric with sinistral shear sense indicators in the Bolfin Complex (Scheuber et al., 1995; Scheuber and Gonzalez, 1999); 6) Extension during the Late Jurassic intrusion of the Las Animas pluton (Dallmeyer et al., 1996; Grocott and Taylor, 2002); 7) Late Jurassic extension directions from dikes in the Remolino plutonic complex (Taylor and Randall, 2000) at (left) 155 Ma and (right) 144 Ma; 8) Thrust faults and folds that developed between 155–150 Ma (Scheuber and Gonzalez, 1999).

4. GEOLOGIC MAP OF THE ATACAMA AND TALTAL FAULT SYSTEMS NEAR TALTAL, CHILE: NEW CONSTRAINTS FOR THE EVOLUTION OF THE ANDEAN MARGIN³

4.1. INTRODUCTION

The Atacama fault system (AFS) is the largest structural feature associated with Early Cretaceous magmatism and deformation of the Andean margin in northern Chile (Figure 4.1). Previous workers have connected Mesozoic sinistral motion along the AFS to oblique subduction (e.g., Scheuber and Andriessen, 1990; Dallmeyer et al., 1996), with the N-S striking AFS accommodating the margin-parallel component of convergence within the contemporaneous magmatic arc. Mylonitic fabrics are present along parts of the AFS, and the spatial connection between mylonite and synkinematic Early Cretaceous plutons indicates that plutonism localized ductile deformation while the AFS was elsewhere brittle (Bonson, 1998; Grocott and Taylor, 2002; Seymour et al., 2020). However, existing 1:100,000-scale mapping lacks sufficient detail for characterizing the distribution and geometry of ductile and brittle deformation, and some ductile shear zones assumed to be AFS-connected may instead be geometrically and temporally incompatible. The AFS was cut by the brittle-only Taltal fault system (TFS) shortly after AFS brittle deformation ceased, contemporaneous with a regional shift in deformation kinematics and potentially connected to a punctuated change in plate boundary dynamics (Mavor et al., 2020). We use geologic mapping, detailed structural analysis, and geochronology to document the deformation history and kinematics of the Atacama and Taltal fault systems and the relation between magmatism and ductile deformation.

³Chapter in preparation for submission to *Journal of Maps*.

The region surrounding the town of Taltal is ideally situated for addressing unresolved questions regarding the timing and kinematics of both syn- and post- AFS deformation. Faults that displace the AFS are uncommon, and the TFS may have both the largest magnitude of displacement and the most continuous exposure of any single post-AFS fault. TFS deformation represents a fundamental shift in the regional strain field and likely relates to changes in plate margin dynamics that drove widespread uplift, deformation, and erosion (Mavor et al., 2020, Chapter 2). Mesozoic volcanoclastic rocks are reportedly folded near Taltal (Arabasz, 1971; Espinoza et al., 2014), but the ages of folded strata, geometry of folding, and the tectonic significance of folding are not well known. Previous geologic mapping near Taltal include 1:100,000-scale (Arabasz, 1971; Ulriksen, 1979; Escribano et al., 2013; Espinoza et al., 2014), 1:150,000-scale (Kurth, 2000), and 1:250,000-scale (Naranjo and Puig, 1984; Bonson, 1998) investigations. While these studies depict regional geologic relations, they lack the resolution needed to accurately characterize deformation important to understanding the evolution of the Mesozoic Andean margin.

We present a new 1:25,000-scale geologic mapping of the Atacama and Taltal fault systems between latitudes 25.4° and 26.0°S that provides new constraints of the style, timing, kinematics, and spatial relations of rocks deformed by these fault systems (Plates 1–3). This map serves as a basis for new understandings of the evolution of the Andean margin presented in other recent publications, including early Andean subduction obliquity in the Middle Jurassic (Chapter 3), the magnitude, slip rate, and kinematics of the Early Cretaceous Atacama fault system (Seymour et al., 2021), the effects of magmatism on crustal rheology and localization of AFS strain (Seymour et al., 2020), and subsequent displacement of the AFS by the Taltal fault system (Mavor et al., 2020, Chapter 2). The work presented here integrates the findings of these

targeted structural studies with four seasons of collaborative geologic mapping to present a unified view of the Atacama and Taltal fault systems at a scale that depicts relations critical for understanding the tectonic evolution of the Chilean Coastal Cordillera. This report summarizes key findings from geologic mapping and provides a tectonic synthesis of major deformation events.

4.2. GEOLOGIC SETTING

The Andean margin of northern Chile records a long history of tectonic deformation. The oldest exposed rocks in the studied region are late Paleozoic metasedimentary rocks of the Chañaral Complex, deformed in an accretionary wedge during late Paleozoic subduction (Bell, 1982; Fuentes et al., 2017). Most studies suggest a hiatus in subduction during Triassic rift-basin sedimentation and subduction re-initiation in the Early Jurassic (e.g., Coira et al., 1982; Charrier et al., 2007), though some studies contend that subduction has been continuous since the Paleozoic (e.g., del Rey et al., 2016; Oliveros et al., 2020). Triassic clastic strata overlying the Chañaral Complex record syndepositional extension and sedimentation patterns that suggest structural control by NW-striking half-graben basins (Suarez and Bell, 1992; Tankard et al., 1995).

The Andean orogenic cycle began by the Early Jurassic and, in the early stages, was characterized by arc-normal extension recorded by dikes and back-arc basin sedimentation (Scheuber et al., 1994b; Scheuber and Gonzalez, 1999; Charrier et al., 2007). Thick Jurassic arc volcanic deposits record marine conditions and syndepositional subsidence through the Kimmeridgian (Prinz et al., 1994), when continental clastic rocks first appear (Scheuber et al., 1994a). Extension to transtension through much of the Jurassic and into the Early Cretaceous is recorded by dike orientations (Scheuber et al., 1994a; Scheuber and Gonzalez, 1999; Taylor and

Randall, 2000), listric normal faults (Dallmeyer et al., 1996), and the presence of the La Negra Formation back-arc basin (Grocott and Taylor, 2002). A kinematic switch to arc-parallel sinistral deformation and the initiation of the Atacama fault system is thought to have occurred ~140–130 Ma (Dallmeyer et al., 1996; Scheuber and Gonzalez, 1999; Ruthven et al., 2020; Seymour et al., 2020), and many economic deposits in the region were emplaced syn-kinematic with the AFS (Bonson, 1998).

Structural studies have tied Jurassic and Cretaceous sinistral deformation in the Coastal Cordillera to partitioning of the margin-parallel component of oblique subduction from of the Phoenix (Aluk) plate under the South American plate (e.g., Scheuber and Andriessen, 1990; Seymour et al., 2020, 2021). By the Late Cretaceous, arc magmatism migrated eastwards from the Coastal Cordillera, broadly corresponding with the cessation of slip on the AFS (Brown et al., 1993; Dallmeyer et al., 1996; Mavor et al., 2020). A magmatic hiatus at ~90–80 Ma is contemporaneous with a widespread unconformity in the Precordillera interpreted as a regional shortening event (the Peruvian phase of the Andean orogeny; Scheuber et al., 1994; Haschke et al., 2002). A switch from sinistral to dextral oblique subduction may have occurred in the Late Cretaceous (Scheuber et al., 1994a). Additional shortening events marked by thrusts, folding, and unconformities occur through the Paleogene, though sedimentation is generally not preserved in the Coastal Cordillera during this timeframe. Terrestrial clastic deposition beginning in the Miocene covers the Mesozoic bedrock exposures and records slow sedimentation rates in arid environments. Rejuvenation of the Atacama fault in the Neogene with dip-slip kinematics has resulted in 300 m of east-side down displacement of the Paposos segment (Herve, 1987), including Holocene faulting events (Cortés Aranda, 2012), but the El Salado segment near Taltal has not been clearly reactivated, as evidenced by Cretaceous dikes that cross cut the AFS that

were not later displaced (Mavor et al., 2020). Lineaments in Neogene alluvium follow the traces of concealed bedrock faults with asymmetric M-shaped topographic profiles, but the genesis of these features is not well understood (Arabasz, 1971).

4.3. METHODS

4.3.1. Geologic mapping and structural data collection

We mapped a 75 km-long, 5–16 km-wide swath across the northern El Salado segment of the AFS at 1:25,000 scale from the Pacific Ocean at 25.36°S to the C-119 highway at 26.00°S. Geologic mapping conducted in the field was compiled and digitized using ESRI ArcGIS 10.5.1 to align with the ESRI world imagery basemap. We collected new high-resolution aerial imagery for key areas using a DJI Phantom 4 pro drone flown at altitudes <300 m above ground level. Photosets were processed in Agisoft Photoscan Pro to generate georeferenced orthomosaic images to support our field observations. Structural data were analyzed using Stereonet 11 (Allmendinger et al., 2011; Cardozo and Allmendinger, 2013). Mean orientations are determined using maximum eigenvectors, and contours are plotted using a smoothed Kamb method with interval = 2 and significance level = 3. Some geologic measurements of bedding in volcanic rocks (n = 103 on map plates, n=162 total on stereoplots) and mylonitic foliations in metasedimentary rocks (n=3) are digitized from existing geologic maps (Arabasz, 1971; Escribano et al., 2013; Espinoza et al., 2014); all other attitude measurements were collected in the field between 2016 and 2020. Geologic map units are described in Appendix B. Mapping personnel include: Skyler Mavor, Nikki Seymour, John Singleton, Rodrigo Gomila, Gert Heuser, Stewart Williams, Gloria Arancibia, Rachel Ruthven, Evan Strickland, Mica Hernandez, and Gabriela Bórquez.

4.3.2. Zircon U-Pb geochronology

We use laser ablation inductively-coupled mass spectrometry (LA-ICP-MS) U-Pb analysis of detrital zircon samples from clastic intervals of the Aeropuerto Formation to constrain the depositional age of this unit. Analyses were performed at the UTChron laboratory at the University of Texas at Austin following methodology detailed in Seymour et al. (2020). Detrital zircon data are visualized as kernel density estimation (KDE) curves using DensityPlotter 8.5 software (Vermeesch, 2012), using adaptive bandwidth. Zircon dates are presented as $^{206}\text{Pb}/^{238}\text{U}$ dates $\pm 2\sigma$ uncertainty and filtered for $\leq 20\%$ $(^{206}\text{Pb}/^{238}\text{U})/(^{207}\text{Pb}/^{235}\text{U})$ discordance. Maximum depositional ages (MDA) for samples in this study are reported as the maximum likelihood age (Vermeesch, 2021), with additional calculation methods (Coutts et al., 2019) available in supplementary Dataset 2. Geochronology data compiled from previous studies are presented on the map plates.

4.4. DEFORMATION OF THE PALEOZOIC CHAÑARAL COMPLEX AND EARLY MESOZOIC MAGMATISM

Late Paleozoic quartzite and phyllite of the Chañaral Complex are discontinuously exposed as country rock and roof pendants to Mesozoic arc plutons. Lower greenschist-facies metamorphism is recorded by bedding-parallel foliation defined by aligned mica grains and pressure solution surfaces. Multiple folding events deform this foliation (Chapter 3) and probably occurred in the late Paleozoic, as Permian plutonism near Chañaral cuts folded foliation (Bell, 1982). The 215–207 Ma Triassic Capitana syenogranite exposed at the southern end of the map area (Plate 3) overlaps with estimates for the earliest phase of Andean arc magmatism in the Coastal Cordillera (Jara et al., 2021). The first major pulse of Andean magmatism in the region

was between 200–185 Ma and in the map area is marked by the Cerro Concha and adjacent Early Jurassic granodiorite plutons (Plate 3).

Voluminous Jurassic arc volcanism is recorded by andesitic flows of the La Negra Formation, which spans a broad temporal range between the Pliensbachian and Tithonian and is probably composed of two subunits with an Aalenian-Bajocian eruptive hiatus (Espinoza et al., 2014). Granodiorite of the Matancilla plutonic complex intruded east of Taltal at ~169 Ma (Mavor et al. 2020), during a lull in plutonism and La Negra volcanism. The Matancilla pluton is bordered by a shear zone that extends up to 1.4 km from the intrusive contact into Chañaral Complex metasedimentary rocks and overprints earlier folding of phyllitic foliation (Plate 1, see Chapter 3). The shear zone is characterized by NNE-striking, steeply NW-dipping foliation planes with shallowly raking stretching lineation and dominantly sinistral shear sense indicators (Figure 4.2A-C). Pelitic intervals in the contact aureole of the Matancilla granodiorite commonly have synkinematic andalusite, and mylonitic fabrics in this zone are cut by the Early Cretaceous Tipias granodiorite (Plate 1, Chapter 3). Centimeter to meter-scale discrete shear zones associated with mineral breakdown and alteration textures are found throughout the Matancilla pluton with variable orientations and no spatial relation to the AFS. From the spatial patterns of mylonitic fabric and the prevalence of sinistral shear sense indicators the Matancilla shear zone is interpreted to record sinistral-oblique convergence during emplacement of the Middle Jurassic Matancilla pluton (Chapter 3).

4.5. ATACAMA FAULT SYSTEM

Recent investigations have improved timing constraints on AFS brittle and ductile deformation, demonstrating that sinistral mylonitic shear zones localized around the synkinematic Cerro del Pingo pluton at 134–132 Ma and again at 120–119 Ma (Seymour et al.,

2020, 2021). AFS brittle deformation with similar sinistral kinematics overprints these mylonitic fabrics. Post- to late kinematic dikes along the eastern branch of the AFS (Seymour et al., 2020; Mavor et al., 2020; Plate 1) demonstrate that between 114–107 Ma the AFS was abandoned as strain localized on the Taltal fault system (Mavor et al., 2020). Based on mapping synthesized in Seymour et al. (2021) and Plates 1–3, the cumulative AFS sinistral slip across the fault system as a whole is 54 ± 6 km (Seymour et al., 2021). Here, we refine the spatial patterns and map relations of AFS ductile and brittle deformation and clarify the relation of ductile fabrics to Early Cretaceous magmatism.

4.5.1. Field relations

The northern El Salado segment of the Atacama fault system is composed of two well-defined, well-exposed, and regionally-continuous faults (the eastern and western branches) that bound the system, as well as multiple subsidiary strands and splays. For much of the fault system trace, the easternmost and westernmost bounding faults juxtapose differently-aged rocks and have the largest displacements, while internal strands displace strata of Mesozoic volcanic and clastic units. The easternmost strand of the AFS is the most continuous along strike and can be traced for ~75 km from the southern boundary of the map area to the shoreline north of Taltal. The eastern branch separates Mesozoic volcanic and clastic deposits from Paleozoic quartzite and phyllite of the Chañaral Complex on the eastern side of the fault and appears to have accommodated the most displacement of any AFS fault, with as much as 38 km sinistral separation of the Early Cretaceous Cerro del Pingo plutonic complex (Seymour et al., 2021; Plates 2–3). The western branch of the AFS is located ~4–5 km west of the eastern branch and juxtaposes Jurassic andesites against Jurassic-Cretaceous andesite flows and volcanoclastic strata. Based on apparent separation of a chain of hypabyssal Early Cretaceous granite intrusions (the

Goyenchea granite), the western branch has an estimated 16–20 km sinistral displacement (Seymour et al., 2021, Plates 2–3). Jurassic and Early Cretaceous plutons of the Coastal Cordilleran arc primarily crop out east of the eastern branch. The El Muelle fault, a gently arcuate fault that curves from a N-S to NNW-SSE strike near the town of Taltal, may be either continuous with or splay from the AFS western branch at 25.77° S, 70.32° W (Espinoza et al., 2014; Mavor et al., 2020; Plates 1–2). The AFS eastern branch and internal fault strands are offset by faults of the Taltal fault system, but the El Muelle fault is not, suggesting this fault is younger than the rest of the AFS and was contemporaneous with the TFS (Mavor et al., 2020).

4.5.2. Ductile deformation and relation to igneous units

Excluding the Matancilla shear zone discussed above, only two other aerielly-extensive mylonitic zones are present in the map area, and in both cases, mylonitic deformation is restricted to the margins of the Cerro del Pingo plutonic complex and surrounding Chañaral Complex rocks along the eastern branch of the AFS. The Cerro del Pingo tonalite is only strained where it is closest to the eastern branch, where low-strain protomylonitic fabric extends <400 m into the pluton. Higher-strain fabrics are focused in Chañaral Complex rocks, and mylonitic to locally ultramylonitic fabric parallels the trace of the AFS with sinistral shear sense indicators (Figure 4.2D-F). Mylonitic strain in the Chañaral Complex increases with both proximity to the AFS and proximity to the Cerro del Pingo tonalite. These spatial relations indicate that the fault system localized where the thermal influence of plutonism elevated the brittle-plastic transition to allow mylonitic shear and weakened the crust (Seymour et al., 2020).

While this pattern is well documented for the Cerro del Pingo pluton, other Early Cretaceous plutons of similar age that intruded near the AFS do not have associated mylonitic deformation. The western contact of the Barreal Seco pluton (unit *Kt(bs)*), which intruded

between 125–121 Ma (Espinoza et al., 2014), has been previously depicted as an AFS-connected ductile shear zone (the El Carmen fault). The contact between the pluton and volcanic rocks it intrudes is NW-striking and marked by a foliated zone that extends ~330 m into the andesite and a weak fabric within the tonalite (Plate 3). However, our mapping finds that the pluton intrudes the andesite without subsequent mylonitic shear (Figure 4.2G). Foliation in the andesite parallels the intrusive contact and is defined by aligned biotite (Figure 4.2H-I). Quartz has textural evidence for static recrystallization with 120° intergrain angles, a lack of undulatory extinction, and grain boundaries that are locally pinned against biotite. These textures indicate that quartz recrystallization was not accompanied by plastic shear. The weak foliation within the tonalite is defined by aligned biotite and tabular plagioclase that lacks recrystallization, whereas quartz lacks a shape-preferred orientation and is largely unstrained, suggesting the fabric is magmatic. We interpret the foliated zone along the intrusive contact to record flattening that likely formed in response to pluton emplacement rather than a mylonitic shear zone connected with sinistral shear along the AFS.

Similarly, we find that other locations that have been previously depicted as ductile shear zones are nonmylonitic. The contact between the western margin of the La Finca pluton and Chañaral Complex metasedimentary rocks north of the Taltal fault is intrusive rather than mylonitic as depicted by Espinoza et al. (2014), which agrees with other mapping along the same contact further north that depicts a contact metamorphic aureole in the quartzite surrounding the pluton (Arabasz, 1971; Escribano et al., 2013). Areas previously depicted as mylonitic Mesozoic volcanic rocks, such as east of Cerro Perales (Escribano et al., 2013) or southwest of the Taltal airport (Espinoza et al., 2014), were found to exhibit flow banding in andesite but only brittle

deformation near AFS fault strands. No evidence for mylonitic deformation in volcanic rocks is found in this study.

Other Early Cretaceous plutons in the map area, including those that intruded near the AFS trace, have no associated ductile shear. The Las Tipias pluton east of Taltal cuts the Jurassic Matancilla shear zone and has no associated shear fabric, despite intruding as close as 720 m from the eastern branch. The Las Tipias pluton intruded at ~130 Ma (Chapter 3) in between episodes of ductile shear at the Cerro del Pingo pluton (Seymour et al., 2020). We propose that intrusion of the Las Tipias pluton did not enable ductile shear since the Matancilla granodiorite it intruded was rheologically stronger than the quartzose and micaceous Chañaral Complex rocks intruded by the Cerro del Pingo pluton where AFS ductile shear did occur. The Goyenchea granitic complex (~145–140 Ma) intrudes andesite flows and volcanoclastic sandstones with distances as close as 1.2 km from the AFS eastern strand but has no associated mylonitic fabric. The lack of mylonite associated with these intrusions could have several possible explanations: the intrusion distance could be too far from the AFS to accommodate strain; these intrusions are smaller volume than the Cerro del Pingo plutonic complex, which would have led to a smaller thermal aureole; the intrusions were likely emplaced at a much shallower depths and into cooler rocks than other Early Cretaceous plutons (as evidenced by miarolitic cavities in the pluton and the lack of metamorphism in the clastic rocks it intrudes); or the ~141 Ma age of these intrusions could predate the stress field that drove sinistral AFS shear.

Our findings that AFS-connected ductile shear is only observed surrounding the Cerro del Pingo plutonic complex suggest that plutonism alone is insufficient to localize an intra-arc shear zone even where emplacement depths are near the brittle-plastic transition; as ductile shear zones were not formed along plutons that intrude rheologically strong country rock (such as the Las

Tipias pluton), or along plutons that intruded at distances >5 km from the trace of the AFS eastern branch (such as the La Finca or Barreal Seco plutons). Mylonitic deformation is present along only ~29% of the AFS trace, and ~59% of the AFS eastern branch is adjacent to Chañaral Complex rocks, while only ~1% is in direct contact with Early Cretaceous intrusives (as measured on the east side of the AFS eastern branch). Brittle-only deformation for the AFS western branch and internal fault strands is likely due to the shallower exposure levels of these faults relative to the eastern branch but could also suggest these faults were active only during the later stages of AFS deformation (Mavor et al., 2020).

4.5.3. AFS brittle deformation

The AFS eastern branch typically consists of two closely spaced faults separated by cataclasite and fault breccia. The core of the eastern fault, where exposed, is marked by a 2–3 m thick gouge zone. Gouge foliation oriented clockwise to the fault principal slip surface and gouge S-C fabrics serve as sinistral kinematic indicators (Figure 4.3A-B). T-fractures and Riedel shears on subsidiary fault surfaces further support sinistral strike-slip kinematics for AFS brittle deformation. The eastern branch is commonly marked by a subvertical to ENE-dipping resistant band of black cataclasite. North of Cerro del Pingo, the cataclasite is derived almost entirely from a quartzite protolith, with mono- and polycrystalline quartz grains recognizable ranging from centimeter to microscopic scales (Figure 4.3C). A zone of pervasive brittle deformation between the two easternmost fault strands is up to 300 m wide and narrows as these fault strands converge northwards. Fault rock thickness is greatest away from mylonitic zones in the map area and decreases to <2 m in the southern portion of the Cerro del Pingo pluton, where mylonitic deformation was ongoing at ~119 Ma (Seymour et al., 2020).

Between Cerro del Pingo and the Quebrada de la Peineta fault of the TFS, AFS cataclasite changes along strike from primarily volcanic-derived just north of Cerro del Pingo, to primarily metasedimentary-derived north of 25.61°S and includes a plutonic component north of 25.59°S (Plate 1). Clasts of plutonic rock in cataclasite are altered, with chlorite replacing mafic minerals and filling grain fractures. Due to alteration and deformation, it is difficult to assign an association of this pluton with less altered plutonic map units.

Unlike the eastern branch, all other AFS faults, including the western branch, El Muelle fault, and internal AFS faults and splays, are characterized by brittle-only deformation. The thickest fault core of an AFS internal strand is exposed north of the Quebrada de la Peineta fault along a fault that separates andesitic rocks with notably different phenocryst sizes. Here, the fault core in places exceeds 50 m and is composed mostly of gouge with minor cataclasite. The fault core of the El Muelle fault is well exposed in an excavation near Aguada Chépica that reveals a ~3 m wide foliated gouge core (Figure 4.3D). Brittle fault kinematics are consistent across multiple strands of the AFS with sinistral slip and subhorizontal lineations on average, kinematically compatible with mylonitic sinistral shear near the Cerro del Pingo pluton (Seymour et al., 2020, 2021; Figure 4.3).

4.6. TALTAL FAULT SYSTEM

4.6.1. Field relations

The Taltal fault system is a series of NW-striking, steeply (>80°) NE-dipping brittle faults with sinistral displacement. Mavor et al. (2020) document that the system has ~10.6 km of left separation across a ~15 km wide zone. Our geologic mapping indicates that NW-striking faults with sinistral offset of the AFS are sparsely present as far south as ~25.75°S, though the southernmost faults have decameter scale offsets and are relatively insignificant to the total

cumulative offset of the Taltal fault system. With ~7.5 km of strike separation, the Taltal fault has the greatest displacement of any fault in the system, but 30% of the slip in the fault system is along smaller faults. The El Loro fault and Quebrada de la Peineta each have 0.9–1.0 km of displacement, and the remaining faults with slip magnitudes ≤ 360 m accommodate ~12% of the displacement in the system. Slickenlines are near horizontal but rake shallowly NW on average (Mavor et al., 2020, Chapter 2), imparting a slight NE-down extensional oblique component to the dominantly sinistral slip.

4.6.2. Distribution of brittle deformation

Fault rock of the Taltal fault system is largely restricted to foliated gouge in fault cores, with some gouge exposures as much as 24 m thick with anastomosing lozenges of wall rocks. Brecciation extends up to a few tens of meters into surrounding rocks, but map-scale zones of cohesive cataclasite are not present surrounding the Taltal fault system. Foliation of mylonite in the aureole of the Matancilla pluton is deflected adjacent to faults of the Taltal fault system, most notably near the Quebrada Tipias fault where the mylonitic foliation is deflected counterclockwise within a few meters of the fault.

4.7. AGE AND STRUCTURE OF MESOZOIC VOLCANIC AND SEDIMENTARY ROCKS

4.7.1. Ages of volcanic rocks

Mesozoic volcanic and clastic deposits in the map area span from the Early Jurassic to the Early Cretaceous. The oldest rocks are a thick package of repeated andesite flows west of the AFS western branch. These rocks have been dated directly at 173 ± 4 Ma (Espinoza et al., 2014) and are intruded by a 174.7 ± 5.7 Ma granodiorite. Ulriksen (1979) informally defined the package of volcanic and clastic rocks that crop out between AFS strands as the lower member of the Aeropuerto Formation and described an upper member with outcrops east of the eastern

branch. The lower member lacks a suitable type section with identified upper and lower stratigraphic contacts and instead is truncated by the bounding AFS faults. Discontinuous outcrop, few marker horizons, and disruption by numerous faults of the Atacama and Taltal fault systems prevent construction of a coherent stratigraphic column for the package. As such, the nature of the lower and upper contacts and ages of the youngest and oldest members of the unit are unclear. The lower contact of the younger member of the Aeropuerto Formation is likewise not exposed, and those rocks are intruded by Early Cretaceous plutons. Previously published dates from dacitic outcrops located between AFS strands and mapped as Aeropuerto Formation are between 141–138 Ma (Espinoza et al., 2014). West of Cerro del Pingo, clastic rocks are intruded by a ~141 Ma granite (Seymour et al., 2021), establishing a minimum age for deposition of stratified rock in the central part of the map area. Near Taltal, rocks between the AFS eastern branch and the El Muelle fault have older ages and have been variably mapped as the Aeropuerto (Naranjo and Puig, 1984; Kurth, 2000) or La Negra (Escribano et al., 2013) formations. Two 144–146 Ma zircon U-Pb dates of rhyolite unit *JKvr* (Mavor et al., 2020), which is interbedded with andesite flows and lithic sandstone north of the Taltal fault, indicates an age near the Jurassic-Cretaceous boundary. The offset equivalent of this rhyolite south of the Taltal fault intrudes and cross-cut the surrounding shallowly-dipping rocks, indicating that the surrounding andesite and intercalated lithic sandstone (unit *JKv*) in this area is not younger than latest Jurassic (Mavor et al., 2020). Outcrops of the upper member Aeropuerto Formation east of the AFS have younger dates of 124–128 Ma and are intruded by the ~125–121 Ma Barreal Seco pluton (Espinoza et al., 2014). This member is described as a separate and younger pulse of volcanism and sedimentation from the lower member of the Aeropuerto Formation (Espinoza et al., 2014).

We present U-Pb detrital zircon data from two samples from lithic arenite in unit *JKv* (Figure 4.4). Sample 191-N36 is from an interval of SE-dipping sandstone and siltstone from hills east of the El Muelle fault. Zircon analyses ($n = 129$ analyses, $n = 123$ filtered for $< 20\%$ discordance) yield a maximum likelihood age of 122.2 ± 2.6 Ma and multi-grain methods of MDA estimation (Coutts et al., 2019) overlapping between 123.8–127.2 Ma. Sample 191-N34 was collected from a volcanoclastic interval from outcrops previously mapped as the La Negra Formation. Mineral separates from this sample are zircon-poor, with $n = 44$ analyses after filtering for U-poor analyses with ages > 4 Ga that were likely phases other than zircon, and $n = 33$ analyses with discordance $< 20\%$. The maximum likelihood age is 125.5 ± 3.3 Ma and multi-grain methods of MDA calculation overlap between 134.7–135.5 Ma. While a higher number of analyses would be preferable for robust statistical confidence in the calculations for sample 191-N34, MDA calculations for these samples suggest that these rocks are significantly younger than other reported dates from volcanic and clastic rocks of the Aeropuerto Formation that crop out between the eastern and western branches of the AFS. From the southeast dips of clastic horizons at sample locality 191-N36, we infer that the outcrops of unit *Km* are up-section and entirely Early Cretaceous. While unrecognized unconformities are probable, the geochronology synthesized here indicates that Aeropuerto Formation outcrops bounded by the AFS are as old as ~ 146 Ma and as young as ~ 121 Ma, a much wider temporal range than had been previously considered for this unit. Our data find that the lower and upper members, as described by Ulriksen (1979), have significant temporal overlap, and careful re-evaluation of Aeropuerto Formation stratigraphy is warranted. Aeropuerto Formation deposition was at least in part contemporaneous with AFS deformation, and structural control of sedimentation could explain the spatial restriction of much of the Aeropuerto Formation between the eastern and western

branch, supporting suggestions of graben-like subsidence between AFS strands (e.g., Espinoza et al., 2014). Both detrital samples presented here have histogram age peaks between 135–140 Ma, which coincides with a peak of magmatic ages along the El Salado segment of the AFS (Seymour et al., 2020) and with magmatic ages for older parts of the Aeropuerto Formation; these peaks likely reflect erosion and re-sedimentation of those units into the younger clastic deposits. Unit *Jv* west of the western branch is significantly older than the 164–150 Ma dates of the La Negra type section near Antofagasta (Oliveros et al., 2006), and unit *Jv* may instead be a closer temporal match to older rocks such as the Oficina Viz Formation near Iquique. The stratigraphically lowest outcrops of unit *JKv* near Taltal may better correlate with the type section of the La Negra Formation, though most of the exposed outcrop is younger.

4.7.2. Folds in Jurassic-Cretaceous volcanic rocks

Mesozoic volcanic and clastic rocks have variably-inclined bedding and, in some places, outcrop-scale folds (Figure 4.5). While some gently-inclined strata could be preservation of original nonhorizontality, especially for viscous lava flows and proximal coarse clastic deposits, finer-grained clastic rocks and marine limestones certainly record postdepositional tilting. A stereonet of poles to all bedding measurements from stratified Mesozoic rocks (Figure 4.6A) shows that bedding most commonly is subhorizontal or shallowly SE-dipping with local domains where beds dip steeply in variable directions. When bedding measurements across the map area are plotted together, poles have a scattered point distribution (based on the Vollmer, 1990 classification), and the lack of any clear trend suggests that folding in these rocks cannot be explained by a single regional event. To better identify trends in these data, we consider subsets based on geographic domains bounded by major faults.

West of the AFS, unit *JKv* crops out as a thick package of SE-dipping andesite flows. Bedding measurements from unit *JKv* west of the El Muelle fault show that these rocks are largely dip homoclinally southeast (Figure 4.6A). North of the Taltal fault, volcanic rocks east of the AFS are folded into a gently NE-plunging syncline. South of the Taltal fault, bedding close to the El Muelle fault dip away from that structure and shallow towards the eastern branch of the AFS. Near cross section B-B' bedding is shallow or dips SW away from the Taltal fault, forming a gentle syncline between the major faults (Plate 1). A stereoplot of poles to bedding measurements between the El Muelle fault and the AFS eastern branch north of cross section B-B' shows a scattered point distribution (Figure 4.6B). While the data do not conform well to a girdle distribution, the overall calculated fold axis is NNW plunging, roughly similar to the mapped fold axis trend for beds north of the Taltal fault (Figure 4.6B).

A N-S-trending chain of thickly-bedded limestone outcrops (unit *Km*) at 25.60°S 70.36°W is bounded by faults that separate it from pebbly sandstone and andesite flows of unit *JKv*. The bounding faults converge northwards, and no carbonates are present north of the Quebrada de la Peineta fault. Bedding in unit *Km* is folded about a shallowly S-plunging hinge line with a shallowly SE-dipping eastern limb and a steeply W-dipping to near-vertical western limb (Figure 4.6C, green symbols; cross section C-C'). Three-dimensional exposure (Figure 4.5A) of the fold geometry shows a moderately-inclined E-dipping axial surface that indicates E-W shortening and possible west vergence, though the true limb lengths are not known. The nearby volcanic rocks of unit *JKv* are folded into an upright syncline (Figure 4.6C, brown symbols). Poles to bedding planes in volcanic rocks (excluding carbonates) along cross section C-C' define a girdle distribution with a shallowly S-plunging calculated fold axis. Similarity of the calculated fold axes between the volcanic rocks and the folded carbonates suggests that this

folding is not restricted to localized contraction where the two faults converge north of Mina Unión, but instead reflect more widespread deformation that affects the stratified rocks between AFS strands.

A second outcrop chain of limestone is present east of the AFS in the southeast corner of the map area. Bedding measurements roughly define a N-plunging syncline, though poles to bedding planes only loosely conform to a girdle distribution. These outcrops also have centimeter to meter-scale folds (Figure 4.5B). While several of the fold axes measured in outcrop are moderately NE plunging and could be parasitic to the larger fold, other measured fold axes plunge west and deviate significantly from the overall calculated fold axis for this domain (Figure 4.6D). Noncollinearity of measured and calculated fold axes, along with significant scatter from a girdle distribution of bedding poles, suggests multiple deformation episodes or noncylindrical folding.

Fold timing can be bracketed to post-date deposition of Aeropuerto Formation limestone, which is stratigraphically above sample 191-N36 and thus younger than the 121–127 Ma MDA estimates of that sample. Domains with NNW-plunging fold axes are oblique counterclockwise to the AFS and do not match the expected clockwise obliquity for folds developed concurrently with AFS sinistral slip. These fold axes are slightly clockwise to the 309° average strike of TFS faults and have better kinematic compatibility with this fault system. Folds with N-S trending fold axes are compatible with regional late-Early Cretaceous E-W shortening directions interpreted for the TFS (Mavor et al., 2020).

4.8. CENOZOIC SEDIMENTATION HIATUS AND ALLUVIAL LINEAMENTS

Neogene alluvial deposits unconformably overlie Mesozoic and Paleozoic bedrock in the map area, and this depositional hiatus marks the migration of the arc axis eastwards towards the

present high Andes and uplift of the Coastal Cordillera. Along the trace of the AFS in the study area, alluvial surfaces are displaced by lineaments. Where alluvial lineaments can be traced to bedrock exposure, they almost all align with the traces of mapped Mesozoic faults. Scarp morphology in the alluvium is most commonly M-shaped, with 1–4 m high ridges bounding a central depression (see also Arabasz, 1971). Widths of the alluvial lineaments approach ~50 m but are variable, and lineaments on older alluvial surfaces have greater width, greater amplitude, and broader and more rounded ridge morphology compared to lineaments in younger alluvium (Figure 4.7).

In contrast to some previous studies (e.g., Espinoza et al., 2014), we do not interpret these lineaments to reflect Neogene reactivation of older structures as active seismogenic faults, since post-AFS features (e.g., the unit *Kd* dike or faults of the TFS) have no map-scale displacement even where they are intersected by alluvial lineaments. Both the presence of lineaments in Neogene alluvium, including surfaces that may be Holocene, and the changes in lineament morphology across alluvial surfaces of different ages suggest the lineaments are not created from a single event but may instead be the result of ongoing processes and are perhaps related to the subduction zone seismic cycle as has been interpreted for surface cracks in other hyperarid regions of northern Chile (Loveless et al., 2005, 2009).

4.9. CONCLUSIONS

Our new geologic mapping informs the tectonic history of northern Chile and the evolution of the Mesozoic Andean margin. Arc magmatism was preceded by low-grade metamorphism and polyphase folding of late Paleozoic clastic rocks. The earliest Andean orogeny deformation recorded near Taltal is the Matancilla shear zone, which suggests a sinistral obliquity of Middle Jurassic convergence (Chapter 3), while the main structural feature is the

Early Cretaceous AFS. Our mapping finds that the only AFS-connected ductile deformation near Taltal is at the margin of the Cerro del Pingo plutonic complex, and other areas where AFS ductile deformation has been previously reported are either nonmylonitic (e.g., the Barreal Seco and La Finca pluton aureoles and AFS-adjacent volcanic rocks) or are temporally incompatible with the AFS (e.g., the Middle Jurassic Matancilla shear zone). Brittle deformation is characterized by cataclasite and gouge development and is most extensive away from ductile shear zones. Late Jurassic to Early Cretaceous volcanic and clastic rocks between AFS strands span as much as 25 Myr, were at least in part deposited during slip on the AFS, and were likely folded either during the late stages of AFS slip and/or during E-W shortening coeval with TFS slip. Lineaments in Miocene to Quaternary alluvium follow traces of Mesozoic faults and define an M-shaped topographic pattern that suggests complicated motion rather than reactivation of Mesozoic features as active faults. Broader, higher lineament expression in older alluvial surfaces indicate that whatever processes are responsible for lineament development are likely ongoing.

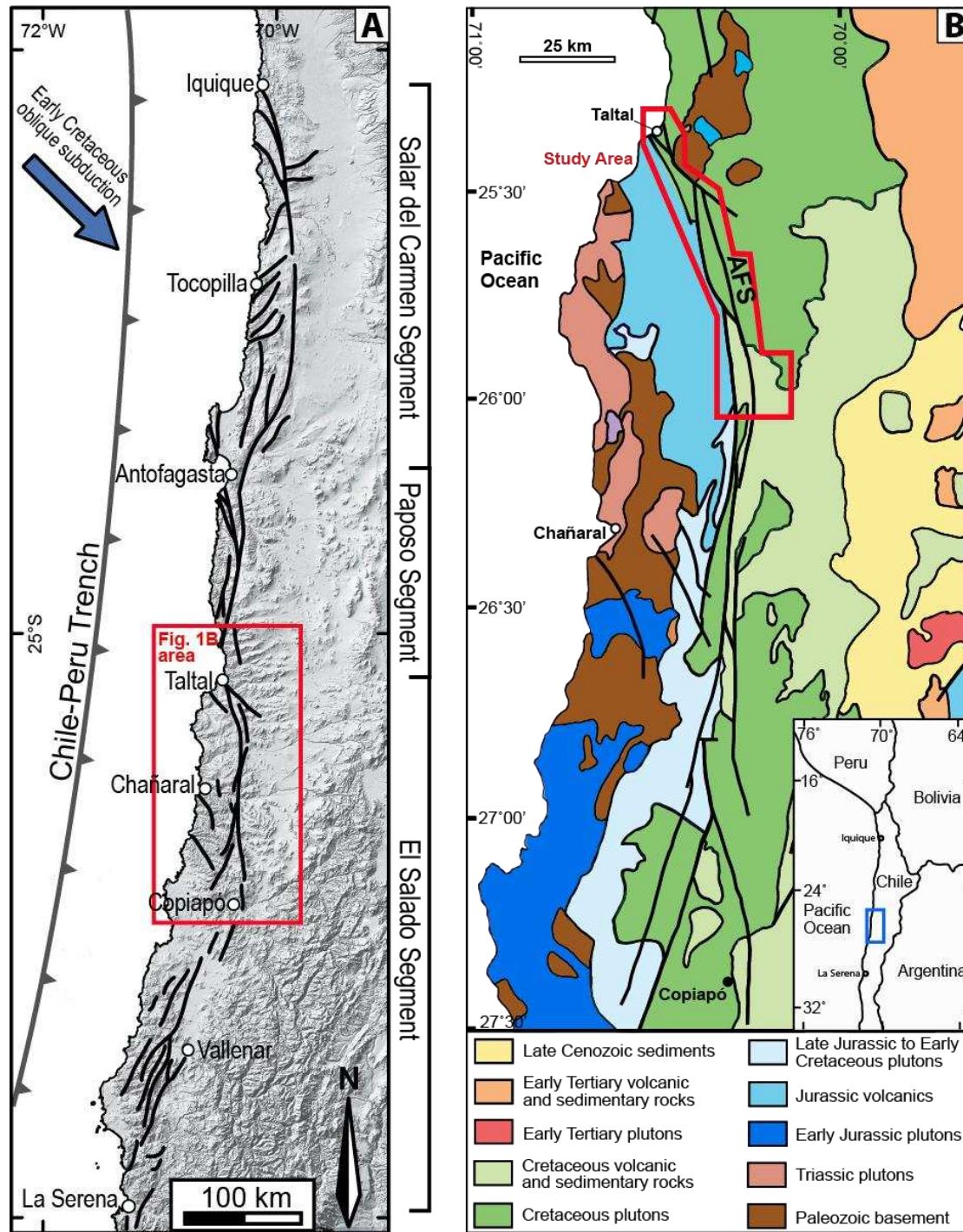


Figure 4.1. A) Digital elevation map of northern Chile, with simplified major faults of the Coastal Cordillera. The Early Cretaceous oblique convergence direction from the north is plotted after Angermann et al. (1999). B) Simplified geologic provinces of the El Salado segment of the AFS (after Dallmeyer et al., 1996), showing an eastwards migration of magmatism through the Mesozoic and Cenozoic towards the current volcanic arc position at the Chile-Argentina border.

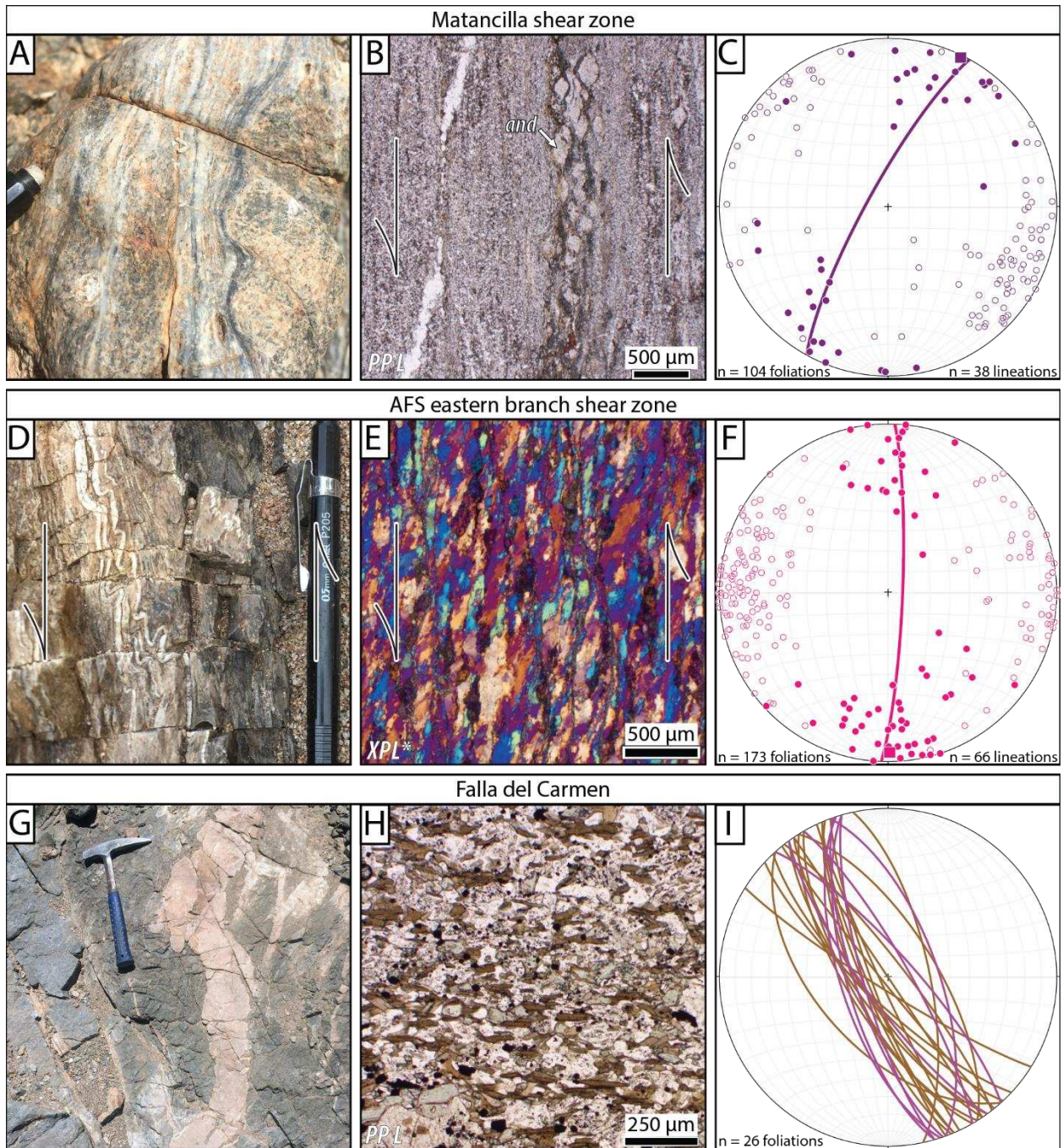


Figure 4.2. A-C) Mylonitic shear in the Matancilla shear zone. A) Discrete shear zone in Matancilla granodiorite. B) Photomicrograph of mylonitic Chañaral Complex phyllite in the Matancilla shear zone with andalusite (and) porphyroblasts. A displaced quartz vein indicates sinistral shear. C) Measurements of mylonitic foliation (poles to planes, hollow circles) and lineation (filled circles) in the Matancilla shear zone across all protoliths and textural domains (data from Chapter 3). Averages shown in bold. D-F) Mylonitic shear along the AFS eastern branch near the Cerro del Pingo tonalite. D) Asymmetric folds in mylonitic Chañaral Complex rocks. E) Oblique recrystallized grain shape fabric in mylonitic quartzite indicating sinistral

shear. F) All mylonitic foliations (poles to planes, hollow circles) and lineations (filled circles) in the Cerro del Pingo mylonitic zones (data from Seymour et al., 2021). Averages shown in bold. A) Intrusive contact with Aeropuerto Formation andesite intruded by Barreal Seco tonalite. B) Thin section of andesite foliation with the fabric formed by aligned biotite. Polygonal quartz grains that lack undulatory extinction provide evidence that the aureole underwent static rather than dynamic recrystallization. D) Measurements of foliation within the Barreal Seco pluton (purple) and andesite in the contact metamorphic aureole (brown).

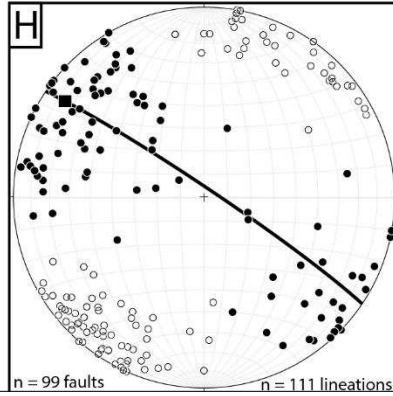
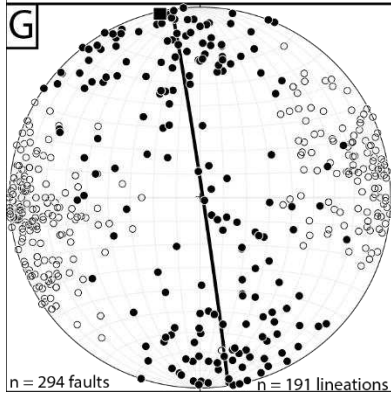
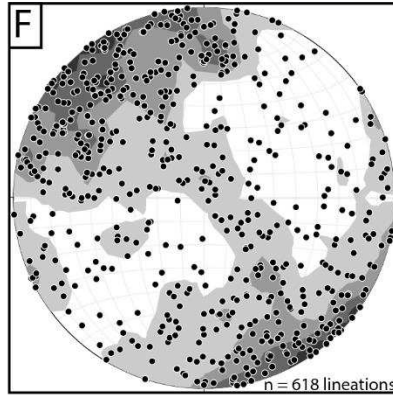
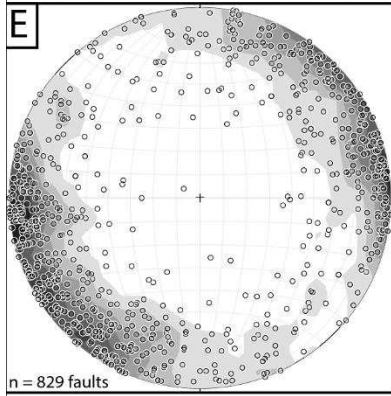
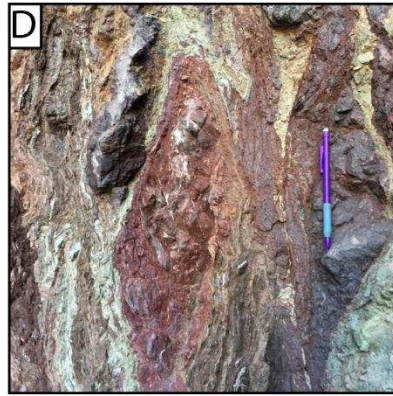
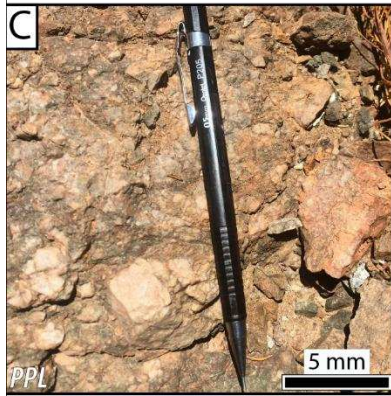
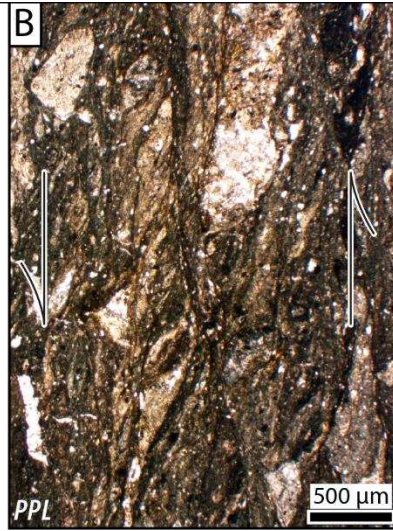


Figure 4.3. Fault rock of the AFS. A) An exposure of the gouge core of the AFS eastern branch. Gouge foliation (white lines) is oblique clockwise to the principal slip surfaces (black outline), a sinistral kinematic indicator. B) Oriented thin section of foliated gouge from Quebrada San Ramón with S-C fabric indicating sinistral shear. C) Cataclasite derived from the Chañaral Complex along the AFS eastern branch. Light colored clasts are relict quartzite fragments. D) Foliated gouge core of the El Muelle Fault (photo taken facing NNW). E) All measured fault planes within the map area. F) All measured slickenline lineations within the map area. G) All measured faults (poles to planes, hollow) and slickenlines (filled) for AFS-associated faults. I) All measured faults (poles to planes, hollow) and slickenlines (filled) for TFS-associated faults.

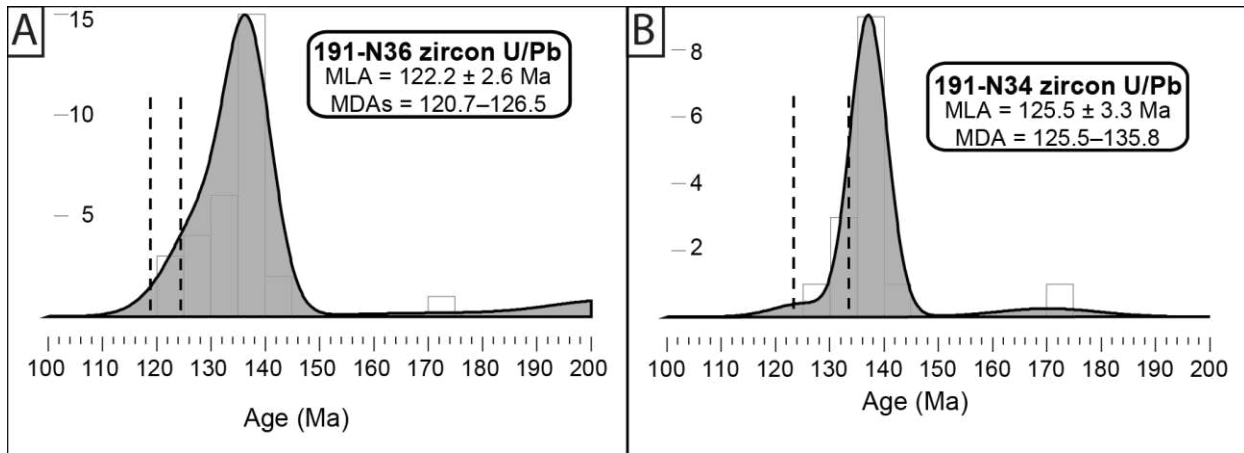


Figure 4.4. Detrital zircon U-Pb analyses of Aeropuerto Formation lithic sandstones filtered for <20% discordance. Only the youngest peak of each sample is shown; analytical data are available in Dataset 2. Dashed lines show the range of calculated MDAs from all methods, excluding the uncertainties of individual MDA estimates. Histograms are plotted with bins of 5 Ma A) KDE diagram of sample 191-N36. B) KDE diagram of sample 191-N34.



Figure 4.5. A) Aerial oblique view (view to the south) of overturned folding in a fault-bounded block of Late Jurassic to Early Cretaceous carbonate of the Aeropuerto Formation (unit *Km*). Note pickup truck for scale. B) Photo of outcrop scale folding in unit *Km* carbonate from outcrops in the southeast corner of the map area. C) Moderately inclined volcaniclastic sandstone southeast of the Taltal fault near cross section B-B'.

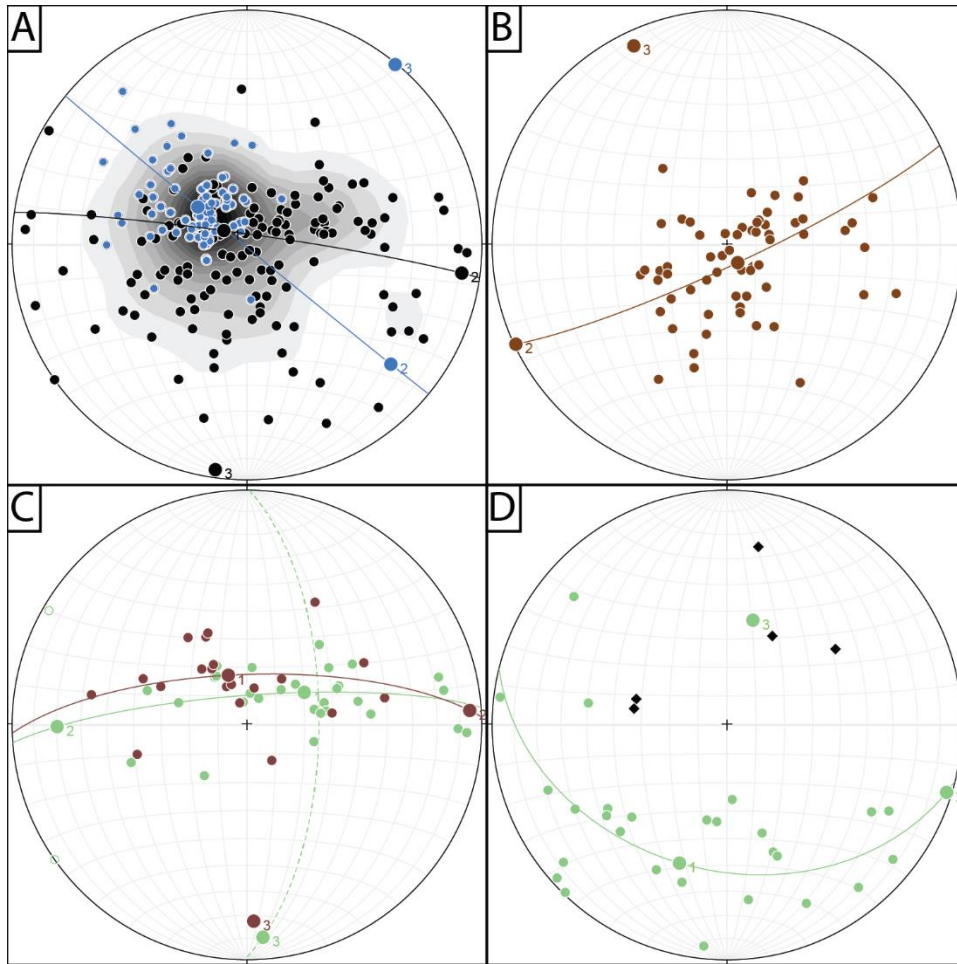


Figure 4.6. Stereoplots of poles to bedding in Mesozoic stratified rocks. Eigenvectors are labeled and shown with bold circles. A) Poles to all bedding measurements of all Mesozoic volcanic and sedimentary rocks west of the AFS eastern branch ($n = 222$, black) and poles to bedding in unit Jv west of the El Muelle fault ($n = 83$, blue). These data include measurements up to 12 km west of the present map area digitized from existing 1:100,000-scale geologic maps (Arabasz, 1971; Escibano et al., 2013; Espinoza et al., 2014). B) Poles to bedding measurements ($n = 60$) within unit JKv in the northern part of the map area, north of cross section line B-B' (Plate 1). C) Poles to bedding in unit JKv (brown) and unit Km (green, hollow where overturned) within 2 km of cross section line C-C'. D) Measurements within carbonate outcrops in the southeast portion of the mapped area (Plate 3). Black diamonds are fold axes of centimeter to meter-scale folds measured in outcrop.

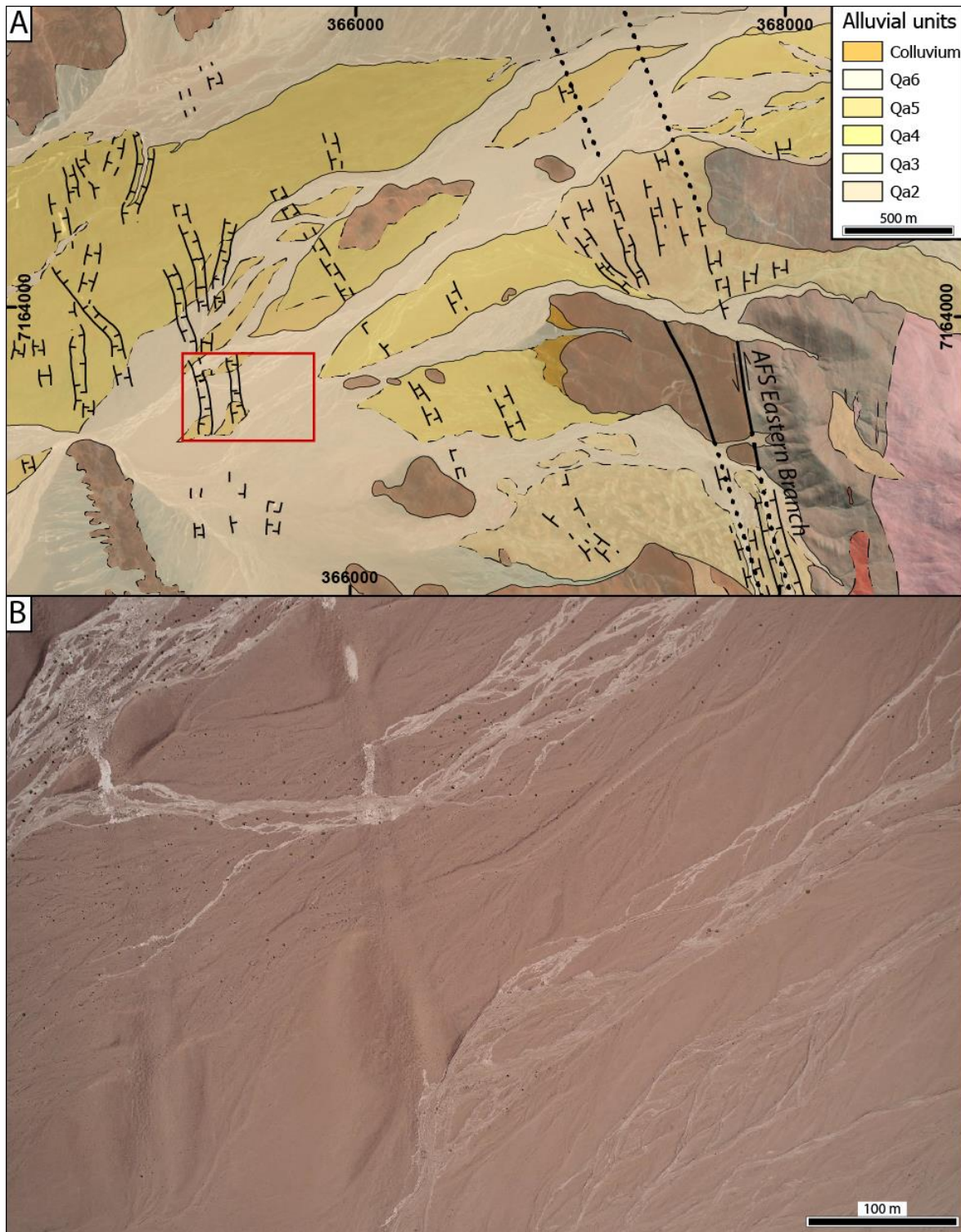


Figure 4.7. A) Alluvial lineaments west of Cerro Del Pingo with detailed mapping of alluvial surface generations (with higher numbers indicating younger relative age). B) Drone imagery of lineaments crossing surfaces of differing age. Lineament morphology is variable; ridges are narrower and have lower amplitude where the lineament crosses the youngest (Holocene?) alluvium.

5. MIOCENE NORMAL AND DEXTRAL FAULTING IN THE LOWER COLORADO RIVER CORRIDOR NEAR BLYTHE, CALIFORNIA⁴

5.1. INTRODUCTION

Deformation connected to the Pacific-North American transform plate margin is distributed in the continent interior east of the San Andreas fault, where strain is accommodated by NW-striking dextral faults. Geodetic studies demonstrate that the Eastern California Shear Zone (ECSZ) accommodates as much as ~29% of the modern relative plate motion (Miller et al., 2001). Inception of the ECSZ began as early as ~10 Ma (Dokka and Travis, 1990b; Nuriel et al., 2019), but the spatial distribution of deformation at this time is not well known. Block reconstructions suggest that plate-margin connected dextral shear may have jumped inland from the plate boundary at 10–12 Ma (McQuarrie and Wernicke, 2005). Transform plate margin-connected deformation extended well inboard of the plate boundary with late Miocene and younger dextral slip documented on NW-striking faults in southern Nevada (Guest et al., 2007) and in western Arizona where NW-striking dextral faults overprint shallowly-dipping detachment faults in the lower Colorado River extensional corridor (Singleton, 2015). A better understanding of the spatial extent and temporal evolution of the early ECSZ and fault interactions with precursor structures is essential to constrain the evolution of the Neogene Pacific-North American plate margin and connected strain in the continent interior.

The hypothesized bounds of a paleo-ECSZ include right-separation faults near the California-Arizona border surrounding Blythe, California (e.g., Richard, 1993; Bennett et al., 2016; Dorsey et al., 2021; Figure 5.1), but it is unclear if these faults are temporally and

⁴Chapter in preparation for submission to a *Geosphere* special volume.

kinematically compatible with ECSZ deformation. In the regions northwest and southwest of the lower Colorado River corridor near Blythe, the structural grain is defined by NW-striking dextral faults. Northeast of Blythe, large-magnitude extension was accommodated by NE-directed detachment faulting and development of metamorphic core complexes in the early to middle Miocene. NW-striking brittle faults with kilometer-scale displacement of Mesozoic and Cenozoic rocks are prevalent in the region surrounding Blythe and may have driven Neogene structural control of landscape evolution (e.g., Bennett et al., 2016; Dorsey et al., 2017, 2021). However, the timing and kinematics of these faults are poorly constrained, and they have been variably interpreted to record early Miocene extension as dip-slip faults (Rotstein et al., 1976; Hamilton, 1982, 1984) or late Miocene and Pliocene dextral strike-slip (Richard, 1993; Salem, 2009). Some faults have trace lengths up to 25 km and as much as 2 km right separation of Mesozoic markers (Hamilton, 1984). Compilation of the cumulative dextral separation of faults across southeastern California and western Arizona by Bennett et al. (2016) indicates that the known magnitude of dextral shear in the lower Colorado River corridor is 30–35 km less than the required amount for coherent block model reconstruction, suggesting that dextral shear may be significantly undercounted or decreases along strike. Here, we use structural analysis and geochronology to evaluate the kinematics, timing, and cumulative shear magnitude of NW-striking fault near Blythe and assess connections of these faults to the evolving regional strain regime during the Miocene.

5.2. GEOLOGY OF THE BLYTHE REGION

Geologic mapping of the mountain ranges northwest of Blythe has identified numerous NW-striking faults, many with 100 m to km-scale right separation of Mesozoic markers (Emerson, 1981; Hamilton, 1984; Stone and Pelka, 1989; Ballard, 1990; Stone et al., in press;

Figure 5.2). These faults cut ductile folds and thrusts of the south-vergent Maria fold-and-thrust belt (Reynolds et al., 1986), and for most faults, brittle slip can only be bracketed to post-date these Late Cretaceous structures and predate the Quaternary fan surfaces that overlap fault traces. A mapped fault previously interpreted to curve from a NW strike in the central Big Maria Mountains to NE-strike across the northeastern Big Marias (Hamilton, 1984) cuts a chain of intermediate to felsic intrusions dated to 21.7 ± 2.8 Ma (hornblende K-Ar; Martin et al., 1982), indicating this fault is early Miocene or younger. Cenozoic rocks are also faulted at Palen Pass, where the Packard Well fault zone cuts an undated presumably Miocene conglomerate (Stone and Kelly, 1989), and clockwise paleomagnetic rotations in a nearby late Miocene basalt record localized deformation of the fault zone (Richard, 1993). For most other faults northwest of Blythe, no such interactions with Cenozoic rocks are exposed, and the timing of fault slip is poorly constrained. Southeast of the Blythe basin, Oligocene to middle Miocene volcanic and clastic rocks are exposed in the hanging wall of a shallowly W-dipping fault on the west side of the Dome Rock Mountains. In the footwall, Mesozoic metasedimentary and metavolcanic rocks are cut and displaced by NW-striking faults with both right- and left-separation of tilted bedding (Stone, 1990; Richard et al., 1992). With poor timing constraints, and unknown fault dip directions and slip vectors, it is unclear if right- and left-separation faults are compatible as opposing normal faults (e.g., Johnson et al., 2021), or are strike-slip faults with different slip sense formed during different deformation episodes.

An elliptical gravity low centered on the Blythe basin indicates a 2–3 km depths to higher-density basement rocks, and the basin may be the deepest the region (Rotstein et al., 1976). Reported sharp linear gradients in both gravity and electromagnetic data (Rotstein et al., 1976; Hamilton, 1984) on the flanks of mountain ranges bound the gravity low and suggest

structural control of basin geometry and perhaps structurally controlled deposition patterns of Miocene and younger basin-fill strata. Subsurface records indicate that the base of the 3.5–4.5 Ma Bullhead Alluvium locally lies at least 62 m to as much as >100 m below sea level, well below a river profile graded to Pliocene sea levels (Howard et al., 2015; Crow et al., 2019). Compaction of underlying basin fill is insufficient to explain the elevation discrepancy (Thacker et al., 2020), suggesting Pliocene or younger faulting down-dropped Colorado River deposits in the basin axis. Low-displacement (decameter to centimeter scale) faults locally cut the early Pliocene Bouse Formation (e.g., Busing, 1992; Gootee et al., 2016; Thacker et al., 2020). Growth strata in the hanging wall of a W-dipping normal fault near Cibola indicate syndepositional tectonism near the time of Colorado River integration (Cassidy et al., 2017; Dorsey et al., 2017, 2021), but the role of NW-striking faults in controlling nascent Colorado River sedimentation is unclear. Here we present structural data and geochronology to constrain the timing, kinematics, and tectonic significance of these faults and find evidence that these faults were active in the late Miocene, which supports suggestions that Colorado River sedimentation was influenced by deformation prior to, or possibly during, river integration to the Gulf of California. We also compile fault-slip magnitude estimates from geologic mapping to demonstrate that cumulative amount of dextral shear is more significant than previous studies have recognized.

5.3. METHODS

5.3.1. Fault kinematic data collection

To determine the geometry, kinematics, and strain fields of faulting in the Blythe region we present a fault dataset targeting mapped NW-striking faults that likely record Cenozoic slip. Fault sense of slip was determined in outcrop using the fracture geometry and surface texture

criteria of Petit (1987) and Doblas (1998). For some measurements where outcrop-scale kinematic indicators are not observed, we assume slip sense from offset of geologic features along the trace of a mapped fault or parallelism to faults of known slip sense. Fault data analysis use Stereonet 10.2.9 and FaultKin 7.5 software (Marrett and Allmendinger, 1990; Allmendinger et al., 2011) to determine incremental strain axes (P- and T-axes) and evaluate kinematic compatibility. Averages are computed using maximum eigenvectors or linked Bingham axes. Stereoplot Kamb contours to linear features and poles to planes are calculated with interval = 2σ , significance level = 3σ , grid nodes = 20, and using an exponential smoothing algorithm, except where these parameters produced anomalous contouring patterns (in which case other settings are noted). Fault measurements are separated as principal slip surface measurements to mapped faults or subsidiary fault surfaces. Additional fault orientations are determined using PlanarOrientationsTools Python scripts (Haugerud, 2020) extracted from 1 meter LIDAR for faults northwest of Blythe, and a photogrammetry-derived DEM from 2017 NAIP imagery for faults in Arizona (<https://libguides.library.arizona.edu/GIS/ImageryandLidar>).

5.3.2. Calcite U/Pb geochronology

Faults in the study area are commonly coated with synkinematic calcite, and we use laser ablation inductively-coupled mass spectrometry (LA-ICP-MS) U-Pb geochronology to determine the timing of this mineralization. Oriented samples collected from fault surfaces were cut into thin (30 μm) or thick (120 μm) sections and analyzed in-situ to preserve textural context. Using a petrographic microscope we identified textural generations of calcite, timing context relative to brittle deformation, and microscopic slip sense indicators. Analyses were performed at the UTChron laboratory at the University of Texas at Austin using a 110 μm laser spot size and the NIST 614 glass standard (Jochum et al., 2011) for Pb isotope normalization and calcite standard

WC-1 (Roberts et al., 2017) for U-Pb normalization. Some ablation spots exhibited down-hole isotopic differences and are presented with multiple integrations (Dataset 5; analyses with duplicate spot numbers indicate multiple integrations from the same analytical spot). Analyses are filtered for $<1 \text{ Pb}^{207}/\text{Pb}^{206}$ and $<0.2 \text{ Pb}^{207}/\text{Pb}^{206} 2\sigma$ error, which removes high-uncertainty analyses that may have ablated phases other than calcite. Dates are calculated from a Tera-Wasserburg discordia lower intercept and reported with 2σ uncertainty.

5.3.3 Sanidine $^{40}\text{Ar}/^{39}\text{Ar}$ geochronology

Sanidine from ash bed sample 1912-SM167 was packaged in Al foil along with Bodie Hills sanidine monitor minerals ($9.7946 \pm 0.0031 \text{ Ma}$; Fleck et al., 2019) and encapsulated in quartz vials. The quartz vials were wrapped in 0.5 mm thick Cd foil to shield samples from thermal neutrons during irradiation. Samples were irradiated for 2.5 hour in the central thimble of the U.S. Geological Survey TRIGA reactor in Denver, CO (Dalrymple et al., 1981) at a power level of 1 MW.

Following irradiation, monitor minerals and sanidine from sample 1912-SM167 were analyzed by total fusion using a CO_2 laser and NGX-600 mass spectrometer at the U.S. Geological Survey in Menlo Park, California. The U.S. Geological Survey NGX-600 mass spectrometer is a 10-collector instrument outfitted with nine Faraday detectors and one electron multiplier, which allows for simultaneous measurement of all Ar isotopes and half-mass baselines. This system is fitted with an ATONA amplifier that significantly reduces amplifier noise and improves baseline and calibration stability, which allows for reproducible measurements of small quantities of Ar. Measurement of monitor minerals and unknown sanidines were made using Faraday detectors for ^{40}Ar , ^{39}Ar , ^{38}Ar , and ^{37}Ar , whereas ^{36}Ar was measured on the electron multiplier. For all experiments, extracted Ar was exposed to a 4 A

tungsten filament, 125K cold finger, and two SAES ST-175 getters (one operated at 300°C and one at room temperature) to remove active gasses. Instrumental mass discrimination was calculated by repeated measurement of atmospheric argon, assuming $^{40}\text{Ar}/^{36}\text{Ar}_{\text{atmosphere}} = 298.56 \pm 0.31$ (Lee et al., 2006). Intercalibration of Faraday detectors with the electron multiplier was performed using an in-house mix gas that contains ^{40}Ar , ^{39}Ar , ^{38}Ar , and ^{36}Ar . $^{40}\text{Ar}/^{39}\text{Ar}$ ages are calculated using the decay constants recommended by Steiger and Jäger (1977). Uncertainties in reported $^{40}\text{Ar}/^{39}\text{Ar}$ ages include propagated uncertainties in counting statistics and J values.

5.4. FAULTS IN THE BIG MARIA MOUNTAINS

5.4.1. Eagle's Nest, Maria Wilderness, and Slaughter Tree Wash faults

5.4.1.1. Map relations

Several NW-striking faults are exposed within or along the margins of the Big Maria Mountains. The Eagle's Nest fault (Salem, 2009) is a NW-striking brittle fault that transects the Big Maria Mountains with a ~24 km long, discontinuously-exposed fault trace. In the central and northwest parts of the range, the fault is marked by recessive topography and a well-defined lineament. The fault cuts Proterozoic through Mesozoic rocks and has no interactions with mapped Cenozoic units. A NW-trending topographic lineament in isolated outcrops in the west-central Big Maria Mountains expose NE-dipping fault surfaces that are either the Eagle's Nest fault or a parallel structure to the SW of the concealed Eagle's Nest fault trace.

Existing geologic maps of the Big Maria Mountains depict a separate E-side down normal fault with a trace that curves from NE-striking in the northeastern part of the range to NW-striking in the central and southeastern part of the range (Hamilton, 1984). In contrast to a sharply curved fault, we instead find that the NE-striking fault is truncated against a throughgoing NW-striking fault (Figure 5.3). We propose the name 'Slaughter Tree Wash fault'

for the NE-striking striking fault that extends to the NE of the Big Maria Mountains in the drainage of the same name. The Slaughter Tree Wash fault cuts a chain of rhyolite and dacite outcrops with a hornblende K-Ar date of 21.7 ± 2.8 Ma. We use the name 'Maria Wilderness fault' to describe the younger NW-striking fault that truncates the Slaughter Tree Wash fault in the central Big Maria Mountains. From the intersection with the Slaughter Tree Wash fault, the Maria Wilderness fault traces northwestward along the western toe of the range (Figure 5.3). The fault has not been identified in the northwestern Big Maria Mountains, and we postulate that it merges with the Eagle's Nest fault. We use the right separation of the Big Maria syncline to infer that the offset equivalent of the Slaughter Tree Wash fault on the southwest is concealed by alluvium on the southwest side of the Maria Wilderness fault. Additional NW-trending topographic lineaments in the north-central Big Maria Mountains are visible in digital elevation data and could partly explain sharp curves in the mapped trace of the NE-striking Slaughter Tree Wash fault, though geologic mapping of the area has not depicted faults in these lineaments.

In the northeastern Big Maria Mountains, west of Quién Sabe point, NW- and NNW-striking faults cut crystalline rocks and project towards the NE-striking Slaughter Tree Wash fault. The NW-striking Quién Sabe fault (QS on Figure 5.2, Richard, 1993; Dembosky and Anderson, 2005) cuts an undated Oligocene-Miocene breccia with volcanic and metamorphic clasts. The intersections between these structures are concealed by alluvium, and the Slaughter Tree Wash fault is shown either cutting (Hamilton, 1984) or displaced by (Hamilton, 1964; Carr, 1991) the NW-striking fault. Additional concealed NW-striking right-separation faults are postulated between the Big Maria and Riverside Mountains (the Big Wash fault) and between the Riverside and Whipple Mountains and are interpreted to connect to exposed right-separation faults that cut the Miocene Whipple detachment (Carr, 1991).

The southeastern Big Maria Mountains has a more complicated fault architecture, and several faults branch between the Eagle's Nest fault and the Maria Wilderness fault (Figure 5.4). The southwestern most of these faults strikes NNW and likely splays from the Eagle's Nest fault, though the intersection is concealed by alluvium. As mapped, the Eagle's Nest fault does not continue to the southeasternmost outcrops of the Big Maria Mountains, but the fault connections between the Eagle's Nest fault and the Maria Wilderness fault may suggest that strain is partitioned to the latter in this part of the range.

5.4.1.2. Kinematics

The principal slip plane of the Slaughter Tree Wash fault crops out in the eastern Big Maria Mountains (ST on Figure 5.2) and is steeply SE-dipping with NE-raking slickenlines (Figure 5.5A). Map relations suggest southeast-down displacement, and slickenlines indicate normal-sinistral oblique slip. Slickenlines on subsidiary fault surfaces with similarly oriented fault planes likewise have SE-raking slickenlines on average. P-axes (incremental shortening axes) plunge moderately N, and T-axes (incremental extension axes) plunge SE.

Several outcrops of the principal slip plane of the Maria Wilderness fault both southeast and northwest of the intersection with the Slaughter Tree Wash fault expose similar fault plane measurements with steeply SE-raking slickenlines (Figure 5.5B, C). The core of the fault is marked by several meters of foliated gouge and brecciated wall rock. In one location gouge foliation is systematically oblique to the principal slip plane exposed in a nearby outcrop and serves as a dextral-normal oblique slip kinematic indicator (Figure 5.5B); a calculated slip vector from the gouge and fault orientation using the graphical method of Moore (1978) is 127/07, more shallowly SE-plunging than the average slickenline at that locality (093/41, Figure 5.5B). In the northwestern part of the Big Maria Mountains, the principal slip surface of the Eagle's Nest fault

dips steeply northeast with variable slickenlines that rake steeply SE on average (Figure 5.6A). Subsidiary fault surfaces are variably oriented but are largely parallel to principal slip surface exposures, with more shallowly-raking slickenlines on average. In the lineament valley north of Black Hill, fault surface measurements are NE-dipping with steeply SE-raking (near down-dip) slickenlines (Figure 5.6B). The Maria Wilderness and Eagle's Nest faults strike similarly in the southeastern Big Maria Mountains. Faults that splay from or connect between the Maria Wilderness and Eagle's Nest faults are largely steeply NNE- to ENE-dipping (Figure 5.4). Overall, faults in the southeastern Big Maria Mountains have slickenlines that are steeply SE-raking, with lesser down-dip or subhorizontal lineations and rare NW-raking oblique lineations. Some faults dip steeply SW (e.g., Figure 5.4A) and have left separation, opposite the main trend of NE-dipping fault planes. Similar steep SE oblique slickenline rakes on these faults suggest they may have originated as conjugate normal faults to NE-dipping fault planes. Where visible, the faults that splay from or connect between the Eagle's Nest and Maria Wilderness faults have right separation of map features, and we use this relation to assume slip sense for faults without textural slip sense indicators.

Some faults have multiple orientations of slickenlines. In most cases, overprinting relations are not visible between slickenline sets, but an exposure of the principal slip surface of a splay to the Maria Wilderness fault has shallowly-raking lineations that appear to truncate steeply-plunging lineations, suggesting that dextral strike-slip followed normal and normal-dextral oblique slip. Subsidiary fault surfaces to the Maria Wilderness fault in the southeastern Big Maria Mountains have largely down-dip slickenlines, while exposures of the principal slip surface have subhorizontal slickenlines with dextral slip sense indicators (Figure 5.4B). T-axes vary from gently NE-SW-trending for normal faults to subhorizontal E-W-trending for domains

with dominantly dextral slickenlines. P-axes are more variable and range from subhorizontal N-S to steeply S- or SW-plunging. Together these axes fit an overall transtensional kinematic regime with NE-SW to E-W T-axes and P-axes varying from N-S subhorizontal to steeply plunging. If normal and slightly oblique normal-dextral kinematics predate dextral strike-slip kinematics, as suggested by slickenline overprinting relations, it suggests that the kinematic shift progressed from NE-SW extension to E-W extension, and from vertical to N-S subhorizontal shortening.

5.4.1.3. Displacement magnitudes

Estimates of fault slip offset in the Big Maria Mountains are confounded by the lack of suitable piercing points and previously unknown fault kinematics. Cenozoic rocks are sparse in the Big Maria Mountains and do not offer any suitable linear offset marker. Several lines of evidence from geologic mapping suggest a significant component of NE-down vertical displacement on the Maria Wilderness fault. Jurassic metavolcanic rocks are in the core of the Big Maria syncline NE of the fault trace, but lower Paleozoic rocks are in contact with the SW side of the fault, which suggests the exposure level is deeper on the SW side. No such relations requiring dip-slip displacement are apparent for the Eagle's Nest fault, and Mesozoic structural features have comparable exposure levels on either side of this fault.

Salem (2009) describes an estimated 1.5 km of dextral separation of the Eagle's Nest fault by aligning traces of Late Cretaceous folds (designated F3) and 104 m of NE-down separation of the Eagle's Nest fault on a cross section that reconstructs the Big Maria syncline (Salem's F2). By these measurements, the calculated overall slip vector rake in the fault plane would be 4° SE, significantly shallower than many of the steeply-raking slickenline measurements from the principal slip surface. Using the Eagle's Nest fault average principal slip plane measurement of 313, 62 NE (Figure 5.4E, 6A) and the 148, 66 W average orientation of S3

cleavage (Salem, 2009), which rakes 17° NW on the fault plane, 1.5 km of horizontal right separation could be explained by 400 m of purely dip-slip displacement. A similar estimate using the 290, 40 N approximate orientation of the Big Maria syncline axial plane (Salem, 2009) indicates that the ~1.5 km of right separation could be explained by 1.0 km of pure dip-slip displacement. By using a slip vector from measured slickenlines on the Eagle's Nest fault principal slip surface that rakes 83° SE (average of 11 principal slip plane slickenline measurements that are steeply-raking or SE-raking from stereoplots 6A and 4E), 900 m of NE-down oblique normal-dextral displacement would be required to generate 1.5 km of horizontal right displacement of a planar marker dipping 290, 40 NE, and 800 m of true displacement would be needed for a marker oriented 148, 66 W. In both cases, this translates to approximately 100 m top-NE heave and 800 m normal throw.

For the Maria Wilderness fault, 2.3 km right separation of the Big Maria syncline axial plane oriented 290, 40 N (Salem, 2009) could be explained by 1.39 km of normal displacement on the Maria Wilderness fault oriented 307, 57 NE (average of 22 principal slip plane measurements from stereoplots 4A, 5A, and 5B). However, for a more extreme example of a marker plane dipping 15° N like some measurements on geologic maps (Hamilton, 1981), 2.3 km of right separation could be explained by as little as 500 m of normal displacement. By using a slip vector from measured slickenlines on the Maria Wilderness fault principal slip surface with an average rake of 50° SE (average of 19 principal slip plane slickenline measurements from stereoplots 4A, 5A, and 5B), 1.2 km of NE-down oblique normal-dextral displacement along this vector (0.8 km dextral and 0.9 km normal components) would generate the 2.3 km of horizontal right displacement of a planar marker dipping 290, 40 NE.

The range of measured slickenline rakes from NW-striking faults in the Big Maria Mountains suggests a multistage slip history and that the true magnitude of displacement is a composite of dip-slip, oblique, and strike-slip deformation. Given that the Big Maria syncline is significantly refolded around NW-tracing folds (F3 of Salem, 2009), the assumption in the above calculations that the syncline axial surface is a suitable planar offset marker is demonstrably not met, but such calculations illustrate the likely range of possibilities for the magnitude of slip on these faults. A discrepancy of right separation of the Maria Wilderness fault is evident in the SE Big Maria Mountains where the ~2.3 km separation of the Big Maria syncline is greater than that observed using the top of Paleozoic strata on the SE limb of the fold as a marker with ~200 m right separation (unit *JTrs* on Figure 5.4 at the locality of stereoplot A). The noted discrepancy is not readily explained by the differing dip orientations, as both the axial surface and the Mesozoic metasedimentary marker units broadly dip to the N or NE. It is possible that these differing displacement estimates are the product of complex map patterns from polyphase folding of these markers, or that the mapped position of the syncline axial trace is not well constrained. As such, the lack of an accurately located linear piercing point precludes better estimations of the true magnitude and vector of fault displacement, but between the two faults there could be as much as ~3.8 km of dextral shear, or the mapped separation could be primarily an artifact of dip-slip displacement of dipping markers. If the average measured slickenlines for each fault is taken to represent the true slip vectors, total dextral slip in the Big Maria Mountains would be ~1.0 km.

5.4.1.4. Calcite U-Pb geochronology

Calcite along the Eagle's Nest fault in the northwestern part of the Big Maria Mountains is mineralized in a banded vein on the principal slip surface (Figure 5.7A; sample 1912-SM215), and slickenlines on the vein margins indicate veining occurred before fault slip had terminated.

Two sets of slickenlines are present on opposing vein margins, raking 77° SE and 62° NW. In a thin section perpendicular to the vein, calcite has syntaxial growth textures with coarse-zoned dogtooth calcite terminating inwards from an outer margin of fine-grained calcite, and we targeted both textural domains for LA-ICP-MS analysis (Figure 5.7B). The overall regression age for the sample 191-SM215 is 7.9 ± 1.0 Ma, (MSWD = 1.6, Figure 5.7C). Calcite from the coarse growth zone domain have the highest U concentrations (up to 20 ppm) and regressions of individual transects across zonation boundaries yield late Miocene ages (Dataset 5). Calcite from the finer-grained textural domain has lower U concentrations (< 6 ppm) and a high uncertainty regressed age of 1.5 ± 7.4 Ma (MSWD = 1.4). The regressed age for analyses from only the coarse zoned textural domain ($n = 125$) has the same age and uncertainty as to the whole-sample age (with MSWD = 1.7), indicating that the coarse calcite is late Miocene and the dominant signal in the whole-sample age.

5.4.2. *Maria fault*

Several studies have suggested that a syncline of metamorphosed Paleozoic rocks in the southern Little Maria Mountains is a continuation of the Big Maria syncline that is either continuous along trace (Stone, 2006; Salem, 2009) or truncated by a concealed NW-striking fault between the ranges (Ellis, 1981; Richard, 1993). Citing gravity and telluric surveys, Hamilton (1982, 1984) infers a concealed SW-dipping normal fault on the west side of the Big Maria Mountains that traces towards but does not reach the saddle between the Big Maria and Little Maria Mountains (location MF on Figure 5.2). A chain of low-lying hills composed of Cenozoic boulder breccia lies southeast of this proposed fault and forms a topographic lineament with a similar trend to the geophysical lineament. A stronger gravity gradient is present southwest of these hills and bounds the deep gravity low of the Blythe Basin (Rotstein et al., 1976; Hamilton,

1984). Stone (2006) suggested that the aligned breccia hills may be controlled by a structure that splays from a larger basin-bounding fault. Bedrock exposure in the topographic low between the Big Maria and Little Maria Mountains is concealed by deposits of the boulder breccia in subdued hills. The eastern contact of the breccia with crystalline bedrock is marked by a subtle NNW lineament visible in lidar and aerial imagery (locality MF on Figure 5.2), and fault surfaces and cataclasite are present at the west margin of the bedrock exposures. Fault surfaces exclusively dip moderately west, oblique to the adjacent topographic lineament. Slickenlines are largely down-dip, though one observed set rakes shallowly from SSE (Figure 5.8A). Riedel shears on fault planes with dip-slip slickenlines suggest W-down normal sense slip. Incremental strain axes for these fault measurements suggest E-W subhorizontal extension and vertical shortening. Where exposed, the breccia is cut by NW- and NNW-striking, steeply-dipping faults marked by several centimeters of gouge, indicating at least some tectonism postdates deposition of the breccia. No faults are present at the breccia-bedrock interface in the easternmost Little Maria Mountains, but NNW-striking faults are mapped in the bedrock to the west (locality MD on Figure 5.3). These faults have both right- and left- map separation of Paleozoic units in the overturned northern syncline limb (Emerson, 1981; Ballard, 1990). Measured fault planes are steeply W-dipping or NE-dipping with steeply NW-plunging slickenlines (Figure 5.8).

From the topographic lineament, bedrock fault surfaces, and faults internal to the breccia, we infer that the low pass between the Big Maria and Little Maria Mountains is a structural depression that may be controlled by a NW-or N- striking fault that continues to the southeast following the fault trace depicted by Hamilton (1984). We follow the nomenclature of Richard (1993) and refer to this structure as the Maria fault. The available bedrock exposure allows but does not require significant right separation along this fault. The 4.5 km (Richard, 1993) or 5 km

(Richard and Dokka, 1992) estimates of right separation of the Maria fault are likely near the upper end of permissible dextral separation magnitudes that align map units in the north limb of the Big Maria syncline between the two mountain ranges. Fault slip may be entirely W-down normal sense, as suggested by brittle fault kinematics. If this is the case, the magnitude of slip is probably small as this would impart apparent left separation of the N-dipping Paleozoic markers. We concur with Stone (2006) that this structure is likely of lesser significance than faults with stronger horizontal gravity gradients to the southwest.

5.4.3. Blythe graben

The Blythe graben (locality BG on Figure 5.2) is notable as the only evidence in the region for surface rupture of faulting through Quaternary alluvial fan deposits. Trench logs (Fugro Inc., 1975) report fault and fracture planes that cut and displace older alluvial deposits but are overlapped by the youngest alluvium. The largest displacement on any individual fault is 1.5 m on a fault oriented 116, 77 SW on the northeast side of the graben (Figure 5.8C). Reported fault and fracture surfaces in trench logs strike NW-, E-, or NE-, and smaller-displacement surfaces that with strikes outside of the 100–120° surface trace of the graben likely do not reflect the trace of the larger structure. No slickenlines are reported, but oblique dextral-normal slip would be compatible with regional Pliocene-Pleistocene E-W extension and the modern geodetic strain field (Thacker et al., 2020). The Blythe graben surface lineament is not parallel to, and does not project towards the Maria fault, and gravity gradients suggest that the along-strike projection of the Blythe graben instead lies south of the Little Maria Mountains.

5.5. FAULTS IN THE LITTLE MARIA MOUNTAINS

5.5.1. *Valley fault*

5.5.1.1. *Map relations and kinematics*

Two NW-striking right-separation faults transect the northern Little Maria Mountains with linear valleys tracing each fault for 5-8 km. We follow the nomenclature of Emerson (1981) and refer to the western fault as the ‘Valley fault’ and the eastern as the ‘Border fault’ (Figure 5.2). Mapping by Emerson (1981) shows the SE termination of the Valley fault splay into a horsetail of NNW-striking faults. Both faults displace Paleozoic and Mesozoic rocks with Late Cretaceous metamorphic fabrics, and do not affect Quaternary fan surfaces. Using Paleozoic carbonates in the northern Little Maria Mountains as a marker, mapped horizontal right-separation is ~150 m and ~100 m for the Valley fault and Border fault, respectively (Emerson, 1981).

The steeply NE-dipping principal slip plane of the Valley fault is exposed in several places where eroded gullies expose the fault core. Slickenlines are subhorizontal to shallowly NW-raking, indicating dextral and dextral-reverse oblique deformation with an average slickenline orientation of 324/12. Unlike faults in the Big Maria Mountains, no dip-slip slickenlines are recognized on the large NW-striking faults in the Little Maria Mountains, which supports the inference that right separation of Paleozoic units is the result of strike-slip rather than dip-slip faulting (Emerson, 1981). Subsidiary fault surfaces that merge with the principal slip plane are consistent with a dextral Riedel shear orientation (Figure 5.9).

5.5.1.2. *Calcite U-Pb geochronology*

Faults along the mapped central splay fault are mineralized with calcite; slickenfiber steps and calcite veins with T-fracture orientations to the main fault surface indicate syn-

kinematic calcite precipitation during dextral slip (Figure 5.7 D, G). Two samples of calcite collected from this fault are shown in Figure 5.7. Sample 1912-SM183 is cut perpendicular to the fault plane and parallel to slickenlines on dextral oblique slickenfiber steps. A ~5 mm-thick zone of fine- to medium-grained calcite coats the fault surface. Discrete shear fractures within this sample trace parallel to the exposed surface and are associated with cataclasis. Presence of calcite slickenfibers, calcite along shear- and T-fractures, and involvement of calcite in brecciation clearly indicate that that calcite is synkinematic to faulting. Laser ablation spots were targeted along both the fine- to medium-grained calcite as well as the mineralized shear fractures. A regressed age for the whole sample of 6.8 ± 2.9 Ma (MSWD = 1.5) indicates faulting in the late Miocene or early Pliocene.

Sample 1912-SM184, collected from the same fault, has calcite slickenfiber steps on an exposed fault surface. In thin section, calcite is present in several textural domains. Much of the sample is composed of fine-grained patchy calcite with some wall rock material. Sub-mm thick en-echelon T-fracture veins mineralized with colorless calcite cut the fine-grained calcite (Figure 5.7G–H). Calcite slickenfibers coat parts of the exposed fault surface. T-fractures and Riedel shears observed in both outcrop and thin section support interpretations of dextral kinematics. LA-ICP-MS ablation spots targeting the slickenfiber textural domain have low U (<0.5 ppm, n = 58) and do not yield a negatively sloped regression age. Calcite from the T-fracture textural domain (n = 72) yields a well constrained intercept age of 9.8 ± 0.8 Ma (MSWD = 1.4). Analyses from the fine-grained calcite matrix (n = 35) yield a low-precision age of 9.7 ± 7.9 Ma (MSWD = 0.9), which is compatible with the late Miocene age from T- fracture calcite.

5.6. PACKARD WELL FAULT ZONE

The Packard Well fault zone is a system of NNE-dipping faults that crosses Palen Pass, which separates the Palen Mountains from the Granite Mountains to the north. Richard and Dokka (1992) suggest that the Packard well fault zone connects northwestward to faults of the ECSZ at Cadiz Lake, and southeastward to faults of the Cibola Pass fault zone. At Palen Pass, the Packard Well fault traces $\sim 294^{\circ}$ – 277° , while the trace of the fault required to pass between the Little Maria and McCoy Mountains is $\sim 304^{\circ}$ – 321° . Richard (1993) recognized this geometry and suggested oblique dextral-reverse kinematics with an estimated minimum 2.3 km of right separation and 0.9 km of reverse slip on this fault system required to restore the southern contact of the Cretaceous Cadiz Valley batholith.

At Palen Pass, two NE-dipping faults bound an alluvial fan conglomerate (fanglomerate) that consists primarily of gravelly sand or interbedded sand and gravel with subangular to angular clasts. Crudely-defined bedding is visible in most outcrops, though massive intervals and well-sorted sandstone beds with ripple marks are locally present. On the north side of Palen Pass, several ravines provide good exposures of the northernmost fault that bounds the fanglomerate. The fault is moderately NNE-dipping with NW-raking slickenlines (Figure 5.10), indicating that dextral/reverse oblique slip juxtaposed the Mesozoic plutonic rocks of the Granite Mountains over the fanglomerate. The fault is overlapped by Quaternary alluvium (unit *Qa2* of Stone and Kelley, 1989; Figures 5.10C, 5.11). P-axes record N-S shortening. Bedding within the fanglomerate is folded asymmetrically against the bounding faults, and in places bedding is slightly overturned with a SSW-vergent tight anticline bound by synclines (cross section A-A', Figure 5.11). Further east the fanglomerate bedding defines a single syncline between fault exposures with the steepest bedding dipping SSW. Poles to bedding (Figure 5.10B) define a

scattered girdle distribution with a NNE-striking profile plane and a shallowly- NW-plunging fold axis. Based on cross sections (Figure 5.11), folding accommodated ~110 m of shortening, or ~23% shortening between the bounding faults. The axial plane strike is 9° counterclockwise of the measured fault, which is compatible with fold-fault obliquity expected for a dextral restraining bend (e.g., Sylvester, 1988). The 145° slip vector azimuth predicted by the average strike of faults used in regional palinspastic reconstructions matches the 326° average trend of slickenlines on the principal slip plane of the Packard Well fault, supporting suggestions that the Packard Well fault is linked to regional structures with a localized restraining bend at Palen Pass (Richard, 1993).

Numerous small faults cut and displace bedding within the fanglomerate with gouge zones up to 3 cm thick. Where visible, many of these faults have separation on the order of a few meters or less, though one fault juxtaposes fanglomerate of different bedding orientations and likely has displacement of tens of meters or greater. Orientations of these minor faults are scattered but are dominantly NW-striking and steeply dipping with an average orientation of 133, 88 SW (Figure 5.10C). Most faults within the fanglomerate do not have a visible slickenlines or determined slip sense, but of those measured the average slickenline plunges shallowly NW with predominantly N-plunging P-axes and shallowly ENE-WSW plunging T-axes (Figure 5.10C).

Sparse outcrops of relatively flat-lying olivine basalt are present in the Palen Pass area ~4 km SSE of the fault-bounded fanglomerate (Figure 5.2). Stone and Kelley (1989) suggest that this basalt postdates faulting at Palen Pass and associated folding of the fanglomerate. However, paleomagnetic data from these outcrops indicate $31.4 \pm 11.5^\circ$ clockwise rotation (Carter et al., 1987) and are interpreted to reflect localized deformation of the Packard Well fault zone (Richard, 1993). In outcrop, the basalt is largely undeformed, however in the northeast part of

the exposure an incipient shear fracture fabric cuts and displaces basalt flow horizons. Shear fractures are steeply dipping and strike either SSE or WSW as apparent conjugates (Figure 5.12). Where visible, slickenlines have shallow rakes and are consistent with a conjugate strike-slip relation. The overall shortening direction recorded by kinematic data (199/05) corroborates the shortening direction indicated by the acute conjugate bisector. These shear fractures indicate that at least some deformation continued after eruption of the basalt, most likely recording the later stages slip on the Packard Well fault zone.

A lightly reworked ~75-cm-thick ash horizon is interbedded in steeply S-dipping Palen Pass fanglomerate. Sanidine separates dated by $^{40}\text{Ar}/^{39}\text{Ar}$ yield ages from 10.9 to 260 Ma (35 grains, Dataset 6), with a distinct young population of mid- to late-Miocene grains that likely reflect the eruptive age. A weighted mean age of the youngest 14 grains is 11.707 ± 0.069 (1 σ), and the MSWD of 1.4 is below the critical value of 1.78. Given the abundance of young grains and textures inconsistent with extensive reworking, we suggest that there was not a prolonged hiatus between eruption and final deposition of the ash bed, and that the 11.7 Ma weighted mean age is a good approximation of the age of the deposit.

From field relations, Packard Well fault zone slip can be bracketed to post-date deposition of the Palen Pass fanglomerate and predate deposition of undeformed alluvial fan gravels (Figure 5.10D). Conflicting ages have been reported for the basalt southwest of Palen Pass. Stone and Kelley (1989) present whole rock K-Ar ages of three samples, two from basalt flows and one from a dike of similar lithology, that overlap between 6.2–6.4 Ma. However, a 13.7 ± 1.6 Ma K-Ar date (Carter et al., 1987) suggests that the flow could be significantly older. Assuming the younger ages are correct, and that the minor faults and paleomagnetic rotation of reflect Packard Well fault zone deformation imparted on the basalt, these constraints indicate that

at least some deformation on the Packard Well fault zone continued into the latest Miocene and perhaps the Pliocene, if this fault displaces the Bullhead alluvium in the Blythe basin.

Other WNW- and W-striking faults cut Paleozoic and Mesozoic bedrock at Palen Pass and may have been involved in Packard Well fault zone deformation. The frontal thrust of the Maria fold-and-thrust belt traces between the McCoy and Little Maria Mountains and through Palen Pass (Salem, 2009). N-dipping overturned strata and reverse faults with Late Cretaceous slip juxtapose Paleozoic and Mesozoic map units. Some of these faults are overprinted by Cenozoic brittle faults with breccia zones (Salem, 2009), while other structures lack brittle deformation and instead are marked by thin zones of ductile shear recording Mesozoic strain. We interpret Neogene faulting at Palen Pass to have preferentially localized into the WNW-striking Mesozoic discontinuity, which introduced a rightward bend in the otherwise NW-striking fault system and imparted the localized transpressional deformation.

5.7. FAULTS IN THE PALEN AND MCCOY MOUNTAINS

The Palen and McCoy Mountains expose a thick package of mostly SSE-dipping Mesozoic volcanic and clastic rocks. In the center of the Palen Mountains, these rocks are cut by several NNW-striking, right-separation faults with pronounced topographic lineaments along fault traces (Stone and Pelka, 1989; Fackler-Adams et al., 1997). Extracted planar feature orientations from digitized fault traces on 1 m lidar are NNW-striking and steeply NE-dipping to vertical. An outcrop of the principal slip surface of a mapped fault has subhorizontal slickenlines and oblique gouge foliation indicating dextral strike-slip kinematics (bold line and square in Figure 5.13A). Additional measured faults in the central Palen Mountains are variable but most commonly parallel to this orientation (Figure 5.13B). Slickenline measurements from all fault measurements are near horizontal on average, and faults with shallow slickenlines have dextral

kinematic indicators. Few outcrop observations of slip sense are available for dip-slip slickenlines, but ENE-down normal slip is expected for kinematic compatibility with NE-SE extensional dip-slip faults in the McCoy and Big Maria Mountains. Since bedding in the central Palen Mountains is S-dipping and faults dip ENE, normal sense slip would impart apparent left separation, and thus dextral strike-slip must be dominant to explain the observed right separation unless reverse sense slip is invoked for down-dip lineations. Faults in the Palen Mountains have 0.2–1.6 km right separation of Mesozoic strata on individual slip surfaces, and an estimated 2.1–3.4 km of cumulative dextral displacement. Marker horizons present in the central Palen Mountains are not recognized to the west (Stone and Pelka, 1989), and no displacement magnitudes are estimated for mapped faults in the southeastern Palen Mountains, so the true amount of distributed slip presented here may be significantly greater than estimates presented here.

In the McCoy Mountains, NW-striking faults are mapped as NE- and SW-down normal faults. Sparse outcrop exposures of these faults have predominantly dip-slip slickenlines, though shallowly plunging and subhorizontal lineations are also observed on subsidiary fault surfaces. We suggest that Cenozoic landslide breccia may overlap the fault trace in the center of the range rather than be restricted to the hanging wall of the fault. If true, this unit may postdate SW-down normal slip, but the depositional age of the breccia is not presently known.

The base of the McCoy Mountains Formation does not align along strike between the Palen and McCoy Mountains, and is apparently offset with ~4 km dextral separation (Stone and Pelka, 1989). A NNW-striking gravity gradient on the west side of the McCoy Mountains likely marks the location of a concealed structure, and has been interpreted as a WSW-down normal fault. (Rotstein et al., 1976; Stone, 2006). A concealed fault with dip-slip kinematics would be

compatible with the steeply-raking lineations on NW-striking normal faults in the McCoy Mountains. However, to generate 4 km of apparent right separation of the 35° SSE dipping McCoy Mountains Formation, a dip-slip fault perpendicular to bedding and dipping 60° WSW would need 2.8 km vertical throw. This amount is unlikely for a Miocene fault given the ~0.5–0.7 km depths to pre-Cenozoic bedrock between the ranges suggested by gravity inversions (Saltus and Jachens, 1995), and thus we suggest that this fault likely has a significant dextral slip component. A fault with 0.7 km of WSW-down throw would generate only 0.9 km of map right separation of the McCoy Mountains Formation, so we suggest that a rough minimum dextral slip component is ~3.1 km.

5.8. NORTHWEST-STRIKING FAULTS SOUTHEAST OF BLYTHE

The Dome Rock Mountains expose SE-dipping Mesozoic clastic and volcanic rocks that are cut on the west flank of the mountains by a shallowly W-dipping normal fault with tilted early to middle Miocene conglomerates and volcanic rocks in its hanging wall. A series of NW-striking faults cut the Dome Rock Mountains and are marked by sharply recessive topographic lineaments. At Ehrenberg Wash, Mesozoic metasedimentary rocks are faulted with ~4 km right separation across system of interconnected faults and ~3 km on the main Ehrenberg Wash fault (Johnson et al., 2021). North of Ehrenberg Wash, a ~10 km-wide zone of NW- to NNW-striking faults have a cumulative ~5 km left separation of these same markers, the largest of which is at Copper Bottom Pass with 1–2 km separation. South of Ehrenberg Wash, in the Trigo Peaks and Trigo Mountains, a ~3 km wide zone of NW-striking faults of the Cibola Pass fault zone displace the shallowly dipping Miocene fault with ~7 km cumulative displacement (Richard et al., 1992).

While no principal slip surface of the Ehrenberg Wash fault has been found, an exposure of predominantly steeply SW-dipping subsidiary fault surfaces and fault gouge along the fault

trace may approximate its orientation (Figure 5.14A). Slickenlines rake shallowly, with an average orientation of 120/01. Along the southernmost splay fault to the Ehrenberg Wash fault system, brittle fault surfaces strike NW with subvertical dips, shallowly NW-raking slickenlines, and dextral kinematic indicators (Figure 5.14B). Together, the slickenlines of the Ehrenberg Wash fault system are subhorizontal to shallowly NW-raking, indicating that this fault system had at least some deformation with dextral strike-slip rather than dip-slip kinematics. Fault surfaces of left-separation faults near Copper Bottom Pass are less well exposed; one fault south of Cunningham Mountain has a small exposure of the principal slip surface, and other mapped faults have measurable subsidiary fault surfaces that trace NW or NNE with steep dips (Figure 5.14C). Calculated orientations of faults using the 3-point solutions based on well-defined topographic lineaments yield planes dipping $>58^\circ$ to the NE and SW. Measured slickenlines on these fault surfaces are variable and most commonly obliquely SE- or NW-raking. Some strike-slip slickenlines are present along with very sparse dip-slip lineations, suggesting that these faults may have a polykinematic slip history. Faults of the Cibola Pass fault zone generally do not crop out in the Trigo Mountains, but reported shallowly-plunging slickenlines in fault exposures along strike to the southeast in the Middle Mountains (Richard et al., 1992) suggest that the right map separation is a product of dextral strike-slip rather than dip-slip faulting.

Richard et al. (1992) interpret the Ehrenberg Wash fault to predate slip on the gently W-dipping Miocene fault on the west side of the Dome Rock Mountains (the Dome Rock Mountains fault) and argue that the deeper exposure levels of Jurassic metavolcanics to the north indicate that Ehrenberg Wash fault slip predated the shallowly-dipping fault. Neither the Dome Rock Mountains fault nor the conglomerate in its hanging wall are recognized north of the Ehrenberg Wash fault, as would be expected if the ~4 km of dextral separation of the Mesozoic

bedrock was due to dextral strike-slip displacement. Right separation of SE-dipping Mesozoic markers could be explained by normal-sense displacement on the Ehrenberg Wash fault if the fault dips SW, as some fault plane measurements indicate, and the Copper Bottom fault and Ehrenberg Wash fault zones could be kinematically compatible as oppositely dipping conjugate normal faults (Johnson et al., 2021). SW-down normal slip of the Ehrenberg Wash fault would impart apparent left separation of the Dome Rock Mountains fault and could explain why it does not crop out north of Ehrenberg Wash. However, shallowly-raking slickenlines with dextral slip sense indicate that the Ehrenberg Wash fault has at least some Miocene dextral slip history. Shallowly-raking slickenlines for left-separation faults north of Ehrenberg Wash could also record a minor amount of dextral strike-slip with displacement insufficient to exceed previous left separation. The apparent dip of Mesozoic bedding on the average Ehrenberg Wash fault plane (oriented 120, 80 SW) rakes 27° SE, and 3 km of dextral separation of bedding on the Ehrenberg Wash fault system could be produced by 1.5 km of dip-slip displacement. The Dome Rock Mountains fault is folded south of Ehrenberg Wash, but the calculated orientation of the northernmost fault trace is 219, 05 W, which rakes 5° W on the average Ehrenberg Wash fault. Approximately 1.5 km dip-slip displacement on the Ehrenberg Wash fault would produce >17 km horizontal left separation of the shallowly dipping fault, an amount more than sufficient to have shifted the fault northwestward to be concealed by younger alluvial fans and unlikely to have been restored by later dextral strike-slip. This example shows that the apparent deeper exposure levels and missing Dome Rock Mountains fault trace north of Ehrenberg Wash do not preclude Cenozoic slip on the Ehrenberg Wash fault zone, but neither do our observations confidently prove late Cenozoic strike-slip kinematics of NW-striking faults in the Dome Rock Mountains. Faults in Ehrenberg Wash do not cut overlying Pliocene fanglomerate, indicating that

Cenozoic deformation on this structure had ceased by that time. If the 306, 67 NE fault plane exposure of a left-separation fault is taken to reflect the orientations of all left-separation faults, the 1.5–2 km left separation of Cretaceous markers across the Copper Bottom fault could be generated by 730–980 m NE-down dip-slip displacement, and the cumulative ~5 km of all left-separation faults could reflect ~2.4 km NE-down displacement.

5.9. DISCUSSION

5.9.1. Overall fault kinematic patterns

To evaluate overall patterns of brittle fault kinematics, we separate faults by type using slip sense and slickenline rake. Faults with acute rake ($\leq 45^\circ$) and dextral slip sense indicators (Figure 5.15 A1–A2) or assumed dextral slip sense (Figure 5.15 A2–A3) have N-S shallowly-plunging to subhorizontal P-axes and E-W shallowly-plunging T axes. Faults with slickenline rake $> 45^\circ$ and normal slip sense have near vertical P-axes and NE-SW shallowly-plunging T-axes (Figure 5.15 B1–B4). Faults with either dextral (39%) or normal slip sense (36%) are 77% of all measured faults with slickenlines and slip sense indicators and 96% of faults including those with slip sense assumed (43% dextral, 53% normal). Slickenlines of normal faults are on average slightly oblique SE, imparting a minor dextral component of oblique slip. Faults with left-lateral slip sense are uncommon and make up only 5% of all measured faults with observed slip sense. Some of these faults are NW-striking and steeply NE dipping, and from the similar geometry to the population of dextral faults it is possible that these faults are either pre-Neogene, or have slip sense misinterpreted, in which case the WNW-ESE P-axes and NNE-SSW T-axes may not accurately depict Neogene strain regime patterns (Figure 5.15C). Conflicting incremental strain axis orientations suggest the latter for at least some faults with assumed sinistral sense (Fig 15 C4), and left separation of a dextral fault is possible where a planar marker

dips more shallowly than the slip vector obliquity. Other faults with left-lateral slip sense assumed from map left separation of contacts are NE-SW striking and near vertical, with P-axes shallowly plunging N-S and T-axes shallowly E-W plunging. These faults have similar orientations to the Slaughter Tree Wash fault but with shallow slickenlines, and some geometric similarities to late Neogene left-lateral faults in the Mesquite and northern Plomosa Mountains (Thacker et al., 2020). Faults with indicated or assumed reverse sense slip are 18% of measured faults with slip sense indicators and have shallowly NNE-SSW plunging P-axes. T-axes are more scattered with steeply-plunging axes with a range of trends and averages near vertical (Fig 15D). The shallowly NNE-SSW plunging P-axes of reverse sense faults are broadly compatible with P-axes for dextral faults, but not with those for normal-sense faults.

Across the entire dataset, faults are most commonly NW-striking and steeply dipping (82% of fault planes strike in the NW or SE quadrants, and 96% dip 45° or greater), and the average fault surface is oriented $318, 77$ NE (Figure 5.16A). Few NE-striking faults are measured in this dataset and shallowly-dipping fault planes are near-absent. Only 6 of 642 (0.9%) planes dip $<30^\circ$, while 491 (76.5%) are 60° or steeper. Slickenlines broadly fit a scattered girdle distribution around the average fault surface; shallowly NE-plunging and horizontal to steeply SW-plunging lineations are rare. Within the range of slickenline orientations, steeply E-plunging lineations are the most common orientation as depicted by stereoplot contours and the overall average lineation of $094/68$ (Figure 5.16B). Slickenlines measured from principal slip plane surfaces have a crude bimodal distribution with steeply SE-raking or shallowly-raking populations, and significantly fewer steeply NW-raking slickenlines. Faults with outcrop sense of slip indicators have an overall pattern of NE-SW to E-W shallowly plunging T-axes and N-S shallowly to steeply plunging P-axes, with an oblique normal-dextral transtensional fault-plane

solution (Figure 5.16D). These patterns are strengthened when including faults with the criteria for assumed slip sense (Figure 5.16E); T-axis contours show a continuum from NE-SW to E-W, while P-axes are slightly bimodal with subhorizontal N-S and steeply S-plunging populations. An incremental strain axes plot with measurements only from mapped fault principal slip surfaces has the same overall pattern with fewer points that are incompatible with an overall dextral-normal oblique fault-plane solution (Figure 5.16F). A P-axis compatibility determination using FaultKin finds that 300 of 367 (82%) of these fault surfaces could have been compatible in the same strain regime, with the caveat that such solutions are non-unique. Incremental strain axes that plot in fields incompatible with the fault-plane solution could be from older episodes of faulting, have misinterpreted slip sense, or could reflect strain partitioning or localized strain fields influenced by bends or interactions between faults. The bimodal distributions of steeply SE-raking and subhorizontal principal slip surface slickenlines and of N-S subhorizontal and steeply S-plunging P-axes could suggest punctuated brittle deformation with oblique normal-dextral and dextral strike-slip episodes rather than a smooth transition between the styles. However, a histogram of acute slickenline rakes has a near even distribution across the range between dip-slip and strike-slip, with a slight prevalence of steeply oblique and strike-slip lineations (Figure 5.16H), and the overall data better support a continuous range of fault styles from normal, oblique dextral-normal transtensional, dextral strike-slip, and oblique dextral-reverse on NE-dipping faults. Fault surfaces with more than one set of slickenlines are not uncommon, but textural clues to determine timing relations between slickenline sets are rare. The best examples encountered in the southeastern Big Maria Mountains suggest that shallowly SE-raking slickenlines overprint down dip-slickenlines, and in another outcrop subhorizontal dextral sense slickenlines are overprinted by dextral reverse oblique lineations. However, such textural

relations are scant, and it is not possible to draw conclusive interpretations. Oblique gouge foliation predicted dextral slip vector on the Maria Wilderness fault (Figure 5.5B) is shallower than many of the slickenlines, which could reflect the kinematics of the youngest fault slip. Dextral slickenlines on fault principal slip surfaces may record a longer-lived slip history than subsidiary fault surfaces with normal-sense slickenlines more prevalent.

5.9.2. Fault timing

Timing constraints presented in this study indicate that NW-striking faults surrounding the Blythe Basin were active in the Late Miocene and possibly into the early Pliocene. The $\sim 21.7 \pm 2.8$ Ma dacite that is cut by the Slaughter Tree Wash fault and the subsequent Maria Wilderness fault indicates that both of these faults are early Miocene or younger. Two calcite U-Pb dates from the Valley Fault in the Little Maria Mountains with shallowly NW-raking slickenlines overlap at ~ 9 Ma and could indicate that strike-slip deformation, dextral or dextral-reverse oblique, was active at that time. Alternatively, these two samples could reflect multiple periods of fault activity, one 9.0–10.6 Ma and another 9.7–3.9 Ma. Kinematic context for the sample from the Eagle's Nest fault is less clear, as there are both NW- and SE-raking slickenlines on the sample margin and both dip-slip and strike-slip slickenlines elsewhere on the fault. Intact calcite growth domains may indicate late synkinematic slip, but the lineated vein margins preclude a postkinematic interpretation and indicate that deformation on this fault occurred between 8.9–6.9 Ma. The youngest age of the three calcite dates has the largest 2σ uncertainty, and deformation in this sample could be as young as ~ 4 Ma. The Packard Well fault, potentially the largest in the Blythe region, was active after 11.7 Ma deposition of the Palen Pass fanglomerate with sufficient deformation to deform that unit into overturned folds. If the three ~ 6.3 Ma K-Ar dates of the olivine basalt at Palen Pass better represent the true age of that unit

rather than the $\sim 13.7 \pm 1.6$ Ma K-Ar date, and if the paleomagnetic rotation and weak brittle deformation in that rock do indeed reflect activity of the nearby Packard Well fault, then Neogene brittle deformation at Palen Pass must have continued into the latest Miocene or early Pliocene.

Together, these timing constraints suggest that NW-striking faults in the region were active, at least some with dextral strike-slip or oblique-slip kinematics, by 9.8 ± 0.8 Ma and at least some brittle deformation continued until after ~ 6.3 Ma. If faults of this network displace Bullhead alluvium in the Blythe Basin as has been suggested (e.g., Howard et al., 2015; Crow et al., 2019; Thacker et al., 2020) then deformation continued at least beyond the early Pliocene deposition of that unit. The onset of faulting has few constraints, and it is likely that some of these faults were active before the middle Miocene. Most faults have no indications of deformation in the later Pliocene or Quaternary, with exception of the Blythe graben that displaces Pleistocene to Holocene alluvium (Fugro Inc., 1975). Epicenters of recorded seismicity are sparse in the region, but a vague NW-trend aligned near the trace of the Blythe graben could suggest historical activity (Thacker et al., 2017). The Blythe graben could be the southeasternmost fault of the ECSZ as defined by Miller (2017) that meets the criteria of recent activity.

Fault surfaces with a range of normal, oblique dextral-normal, and oblique dextral-reverse kinematics suggest that these faults were persistent structural weaknesses that record a transition between extensional and oblique dextral faulting. The predominance of steeply NE-dipping fault planes, with few E-W or N-S striking planes and a near complete absence of shallowly-dipping fault surfaces in this dataset suggests a common origin for these faults, even for faults with differing slickenline rakes and incremental strain axes. NE-dips of dextral faults

may be inherited from earlier formed normal faults that accommodated NE-SW extension. Multiple orientations of slickenlines on similarly-oriented faults suggests that these faults were active across changing kinematic regimes, and the documented shift in the regional strain regime from middle Miocene NE-SW extension to late Neogene E-W extension and N-S shortening (Singleton, 2015; Singleton et al., 2019; Thacker et al., 2020) could explain the observed patterns. Few constraints exist to estimate the onset of faulting in the present study area, but NE-down normal faulting is kinematically compatible with early to middle Miocene NE-SW extension, while shallowly-raking slickenlines and E-W-trending T-axes are best compatible with the known late Miocene and younger strain regime.

NE-directed extensional detachment faulting in the nearest parts of the Lower Colorado River Extensional Corridor initiated ~22–20 Ma, and slip on most detachment faults ceased ~14–12 Ma (Foster and John, 1999; Stockli et al., 2006; Singleton et al., 2014), so the NE-SW extensional strain regime predates the calcite U-Pb dates presented here that are synkinematic to oblique dextral faulting. Overprinting relations between steeply- and shallowly-plunging slickenlines are not unequivocal, but sparse indications suggest that more steeply-plunging slickenlines are overprinted by shallowly-plunging slickenlines, and we favor a model where normal faulting in an early to middle Miocene NE-SW extensional strain regime is overprinted by dextral and oblique dextral slip in a late Miocene to Pliocene E-W extensional strain regime. Oblique normal-dextral slip may record transitional kinematics between these regimes.

Timing relations show that the ENE-striking, steeply SSE-dipping Slaughter Tree Wash fault was active in the early- to middle Miocene. The steeply NE-raking slickenlines, combined with the limited outcrop textural and map indicators for NE-down slip, would impart oblique normal-sinistral kinematics. The kinematic connection of this fault to the early-middle Miocene

NE-SW extensional strain regime is not readily apparent, and with the steep dip and steeply-raking slickenlines this fault appears somewhat incompatible with deformation at that time. ENE-striking faults are present in the Colorado River extensional corridor belt of metamorphic core complexes, where they parallel the extension direction accommodate discrepancies in slip magnitude or polarity between extensional domains as transfer faults (e.g., Spencer and Reynolds, 1989; Beratan, 1991). The steeply ENE-oblique slickenlines on the Slaughter Tree Wash fault could be compatible with a transfer fault model between steeply NE-dipping faults. Within the limits of the time constraints, it is also possible that this fault was active into the late Miocene near the end of or shortly after detachment fault slip. The incremental strain axes for the Slaughter Tree Wash fault may suggest compatibility with the N-S shortening strain regime that postdated earlier NE-SW extensional strain. NNE to ENE-striking postdetachment sinistral-normal oblique faults are present in the northern Plomosa Mountains (Strickland et al., 2017), though these faults have more shallowly-raking slickenlines than the Slaughter Tree Wash fault. In the Mesquite Mountains, a NNE-striking sinistral strike-slip fault was likely coeval with deposition of basal Bouse carbonates (Thacker et al., 2020). ENE- to NNE-striking left-separation faults with late Neogene slip are likewise recognized to the south of the present study area in the Chocolate Mountains anticlinorium (Beard et al., 2016), and to the northeast at the oblique sinistral-normal Nipton Mountains fault (Mahan et al., 2009).

5.9.3. Structural inheritance

Several lines of evidence indicate that fault reactivation that may have played a significant role in fault localization across the region. Thickness changes of Jurassic strata across NW-striking left-separation faults in the northern Dome Rock Mountains provide strong evidence for syndepositional slip on these faults and subsequent reactivation (Crowl, 1979).

Restoration of the 069, 30 SW average bedding of 140 measurements within Jurassic units on the Cunningham Mountain quadrangle (Johnson et al., 2021) to horizontal changes the 306, 67 NE fault planes to 300, 85 NE, an approximation of the orientation at the time of deposition. While the timing of fault slip for the NW-striking faults in the Dome Rock Mountains is not well constrained, these relations demonstrate that faults in this region may be long-lived structural features.

Neogene deformation on the Packard Well fault zone at Palen Pass most likely reactivated strands of a Mesozoic fault system. N-dipping faults that bound the fanlomerate also align with significant discontinuities in the Mesozoic bedrock units that mark the boundary between the Maria fold-and-thrust belt and the McCoy basin (Stone and Kelly, 1989; Salem, 2009). Our transpressional kinematic data support the suggestion that the E-W curve in the trace of the Packard Well fault zone through Palen Pass imparts a restraining bend in the dextral system (Richard and Dokka, 1992), and we argue that a major Mesozoic weak zone guided this bend. Slip magnitude estimates for the Packard Well fault zone of 12–16 km, or as much as 24 km northwest of Palen Pass (Powell, 1981; Richard and Dokka, 1992), likely include pre-Miocene deformation that displaces Mesozoic markers (Richard, 1993). Salem (2009) hypothesized that the concealed frontal fault between the Maria and McCoy Mountains could have been a Jurassic–Early Cretaceous normal fault bounding the McCoy rift basin that was reactivated as a Maria fold-and-thrust belt accommodation zone for SE-directed thrusting. If true, this suggests that faults with late Miocene slip could in places be reactivating long-lived structures with previous episodes of early Miocene, Cretaceous, and Jurassic slip. The Mule Mountains thrust system is reportedly reactivated as a brittle fault in the southeastern Dome Rock Mountains, southern Palen Mountains, and the southern Coxcomb Mountains (Tosdal,

1990), and dextral restraining bends in the central ECSZ may have localized on early Miocene structures (Singleton and Gans, 2008).

5.9.4. Cumulative dextral shear of NW-striking faults

Palinspastic reconstructions and existing estimates of the cumulative magnitude of fault slip in the Blythe region do not include widespread right-separation faults within the Big Maria, Little Maria, and Palen Mountains. To estimate the possible range of cumulative dextral slip in a ~55 km transect from the Palen to Riverside Mountains, we compile literature descriptions of fault slip magnitudes and measure magnitudes of dextral separation for other faults without published offset estimates (Dataset 4). Our tabulated estimates indicate a minimum of 10 km and maximum of 38 km of dextral shear between the Palen and Riverside Mountains. These estimates are complicated by the lack of suitable Cenozoic piercing points, and largely rely on sub-planar Mesozoic markers. Estimating true displacement is not possible with these markers, and separation estimates are dependent on the true slip vector that we argue changed through the displacement history. Dextral separation of some faults in Big Maria and McCoy mountains could be purely a product of dip-slip motion that generates apparent map separation, and we use a lower bound input with no dextral shear for these faults. However, most faults have slickenlines indicating at least some oblique or strike-slip deformation and we consider the minimum estimates a likely undercount. Faults within the Palen and Little Maria Mountains have slickenlines suggesting mostly strike-slip deformation, and right separation of SE-dipping markers cannot be explained by normal-sense displacement on NE-dipping faults, so we approximate the magnitude of dextral shear using the map strike separation.

The greatest uncertainties with the cumulative slip magnitude are from the Packard Well fault and the Maria fault. We use Richard's estimate of 2.3 km minimum dextral slip for the

Packard Well fault as a lower bound of slip between the northern Palen Mountains and Little Maria Mountains. Estimates of ~12 km (Richard and Dokka, 1992) or ~16 km (Powell, 1981) to align rocks in the Little Maria Mountains to Palen Pass may be greater in part due to combined displacement through the Ford Lake North fault (3–4 km of dextral slip) and the Iron Mountains fault (~5.5 km dextral or 1 km normal slip; Miller and Howard, 1985; not included in Dataset 4) that likely merge with the Packard Well fault east of Palen Pass. Even if dextral shear of the Packard Well fault is held to the minimum value of 2.3 km, an upper estimate of 25 km of dextral slip is allowable on the recognized structures in the present study area. These estimates demonstrate that the cumulative dextral shear is possibly greater than the maximum value of 16 km proposed northeast of the Sheep Hole fault (Richard, 1993), or the 17.5 km estimated for the lower Colorado River region (Bennett et al, 2016; excluding dextral shear in the Buckskin Mountains that is further northeast). Recognition of late Miocene faulting in the Blythe region with higher cumulative displacement than previously noted may in part fill the gaps identified by reconstructions that require higher magnitudes of Miocene dextral shear than are known from offset marker constraints (McQuarrie and Wernicke, 2005; Bennett et al., 2016). We estimate a minimum of 2.3 km and maximum of 9.4 km dextral shear on structures that have not previously been included in published reconstructions. Additional dextral shear unaccounted for here may be accommodated by sub-map scale distributed faulting, or by faults that lie entirely concealed in valleys between mountain ranges. Significant dextral shear along minor faults is recognized in the Coxcomb Mountains west of the present study area (~10 km; Richard and Dokka, 1992) and across a the belt of metamorphic core complexes in western and central Arizona (~7–8 km, decreasing southeastward; Singleton et al., 2019). Descriptions of numerous small-scale faults in the Little Maria Mountains (Emerson, 1981) suggest that diffuse dextral shear may be significant

within the present study area. Future palinspastic reconstructions must be careful to allow for this cumulatively significant shear as intra-block deformation. Displaced geophysical anomalies suggest ~7 km of concealed dextral faulting between the Riverside Mountains and eastern Buckskin Mountains (Carr, 1991), suggesting that regionally consistent but difficult-to-constrain dextral shear is likely present across a wider region. The strong geophysical lineaments and deep gravity low in the Blythe Basin could indicate even more unrecognized dextral shear – perhaps as much as 30–35 km suggested to close the geophysically-defined elongate Blythe Basin (Umhoefer et al., 2020) or up to 50 km required to align the McCoy Mountains Formation between the McCoy and Dome Rock mountains (Stone et al., in press). However, our kinematic data suggest that the gravity low in the Blythe basin is likely in part due to the normal component of oblique faulting, and shear estimates made by restoring a geophysical pull-apart basin with only strike-slip shear on NW-striking faults may not be accurate. If the potential ~7 km of dextral shear along concealed faults near Parker is accounted for, only 23–28 km of dextral shear in the region surrounding Blythe is required to resolve the 30–35 km slip magnitude discrepancy identified by Bennett et al. (2016) between the Lower Colorado and surrounding regions, and this amount of shear is permissible by our estimates.

5.9.5. Fault connections to other regional structures

While some Miocene dextral shear is possible along NW-striking faults in the Dome Rock Mountains, the permissible amounts are relatively small and cannot match the amounts of dextral shear in the transect to the northwest. In contrast to the hypothesized connections across the basin of aligned fault lineaments (Hamilton and Myers, 1966; Powell, 1981), most of the dextral shear along NW-striking faults in the Big Maria Mountains and in the Blythe Basin apparently does not continue along strike into the NW-striking faults in the Dome Rock

Mountains, and may instead step south into the Cibola fault system, where ~7 km of dextral shear is permissible, and the releasing stepover geometry could allow down-dropping of the Blythe Basin.

Sharp NW-SE gravity gradients between the McCoy and Big Maria Mountains are suggestive of concealed faults that bound the Blythe Basin, and the magnitude of these gradients suggests dip-slip faults juxtaposing low-density basin fill against more dense crystalline bedrock (Rotstein et al., 1976). The kinematic model proposed here suggests that early to middle Miocene normal movement of these concealed faults formed the apparent vertical displacements evident in geophysical data, but also that normal faulting was later overprinted by dextral oblique-slip and strike-slip by the end of the Miocene. Continued basin down-dropping in releasing stepovers between dextral faults into the Pliocene could explain the downdropping of Bullhead deposits in the Blythe Basin by about 100 m. The data presented here are consistent with hypotheses of strike-slip pull-apart basin deformation near the time of Colorado River integration (Cassidy et al., 2017; Dorsey et al., 2021), but also suggest that earlier basin history may have been controlled by normal and oblique dextral-normal deformation on the same faults. Small-scale N-striking normal faults are recognized in the Bouse Formation and record late Miocene to Pliocene E-W extension (Thacker et al., 2020). Our fault kinematic dataset from bedrock mountain ranges does not identify a significant population of faults in this orientation, but neither do our data preclude the existence of such faults concealed in the subsurface. Such faults may not be recognized in the bedrock owing to the preexisting anisotropy of NW-striking surfaces that localized strain. NNE-striking normal faults control the path of the Colorado River south of Cibola (Beard et al., 2016), and are suggested to underlie La Posa Plain (Strickland et al., 2018; Thacker et al., 2020), Castle Dome and Indian Wash basins (Richard et al., 1992;

Richard, 1993), and the valley between the Moon and Big Maria Mountains (Bennett et al., 2016). Further north, extensional basins in Ivanpah and Mojave valley are suggested to accommodate strain in the gap between the Stateline and Buckskin dextral systems (Mahan et al., 2009; Bennett et al., 2016; Thacker et al., 2020). If the NW-striking geophysical anomalies that bound the northeastern side of the Blythe Basin do not connect to Copper Bottom or Ehrenberg Wash and instead step south to NW-striking faults of the Cibola fault system in the northern Trigo Peaks, a W-dipping normal fault would be expected on the east margin of the basin. With timing constraints presented here that NW-striking faults were active by 9–10 Ma and may be responsible for downdropping the early Pliocene Bullhead Alluvium, it seems likely that an interconnected fault system across the California-Arizona was active both before and during the early Pliocene integration of the Colorado River system. Future work is warranted to better constrain the subsurface architecture of the Blythe Basin and influence of faulting on the evolution of the Colorado River system.

5.9.6. Connections to regional tectonics

The kinematic shift to E-W extension and dextral to oblique dextral faulting may have shortly followed the ~14–12 Ma cessation of high-magnitude extension in the lower Colorado River extensional corridor. The timing of faulting and the continuum of kinematic data from normal to oblique normal-dextral to dextral we have documented in the Blythe region are consistent with a progressive clockwise rotation from NE-SW to E-W extension at the end of detachment faulting in the corridor (Singleton, 2015), and we favor the interpretation of a continuous rather than punctuated transition between strain regimes. Our observations that the same structures were active in both regimes and locally reactivated Mesozoic anisotropies

suggest that fault localization onto preexisting weaknesses may be an underappreciated factor for initiation and localization of paleo-ECSZ deformation.

Our timing constraints are consistent with hypotheses of a wide zone of late Miocene paleo-ECSZ spanning from the Gulf of California to southeastern Nevada. Dextral shear in the Blythe region recorded by our oldest synkinematic calcite date of 9–10 Ma supports hypotheses of ECSZ initiation by ~10 Ma (Dokka and Travis, 1990a; Nuriel et al., 2019), and demonstrates that such dextral shear strain was more widespread than the present extent of the ECSZ.

Transitional fault kinematics in the Blythe region may coincide with widespread observations of a kinematic shift across a broad zone of Pacific-North American plate margin associated deformation. Deformation in the Blythe region is seemingly concurrent with the initiation of the southern San Andreas fault system in the northern Salton Trough at ~8 Ma (Mason et al., 2017), a shift to rapid transtensional faulting in the Gulf of California (e.g., Seiler et al., 2010; Bennett et al., 2017), clockwise rotations in the eastern Transverse ranges (Carter et al., 1987), initiation of NW-striking dextral faults in Death Valley where the southern Death Valley fault zone with ~40 km dextral slip was active during regional extension between 6–12 Ma (Pavlis and Trullenque, 2021), or western Nevada where dextral slip on NW-striking faults initiated at ~10 Ma. (Reheis and Sawyer, 1997). These events could all relate to increasing relative plate velocities and a steady clockwise rotation of decreasingly divergent oblique relative vectors between the Pacific and North American plates through the mid-Miocene (DeMets and Merkouriev, 2016) or eastward strain partitioning due to development of the Big Bend in the San Andreas fault between 5–12 Ma (Liu et al., 2010).

With exception of the Blythe graben, there is little evidence to suggest that significant dextral faulting continued into the later Pliocene in this region, and the wide footprint of late

Miocene dextral shear waned in the Pliocene to Quaternary. Strain transfer out of the Blythe region in the Pliocene was likely taken up by the San Andreas-ECSZ systems, and is consistent with relatively low rates of dextral shear on the San Andreas fault between 12.6–6.3 Ma that rapidly increased by 4.7 Ma (Oskin et al., 2001). Decreasing fault activity in the Blythe region by the Quaternary is also consistent with a westward shift in dextral shear identified by some block model reconstructions of southeastern California (McQuarrie and Wernicke, 2005) and within the ECSZ (Dokka and Travis, 1990a).

5.10. CONCLUSIONS

Faults surrounding the Blythe region in southeastern California dominantly dip steeply NE with multiple orientations of slickenlines that indicate polyphase kinematics ranging from normal-slip in a NE-SW extensional regime to dextral-oblique and dextral slip during N-S shortening and E-W extension. Calcite U-Pb dates indicate that faults were active with dextral oblique kinematics between 7–10 Ma and perhaps as late as ~4 Ma. Together with the timing constraints, transitional kinematics are best explained as recording a shift from the well documented early to middle Miocene NE-SW extension of the lower Colorado River extensional corridor to late Miocene dextral transtension connected to the proto–Eastern California shear zone. The kinematic shift from normal to oblique dextral faulting in the Blythe region followed the end of extensional detachment faulting and appears to coincide with a widespread shift in the style and kinematics of Pacific-North American plate margin-connected deformation in the late Miocene. Faulting in the Blythe region was precursor to, and perhaps contemporaneous with, integration of the Colorado River to the Gulf of California, and this deformation likely influenced the river course and geometry of depocenters. Limited faulting affects Quaternary surfaces in the region, but most strain ended in the late Miocene or Pliocene as dextral shear

localized into the San Andreas and ECSZ systems. Oblique dextral-reverse slip and overturned folds in Neogene conglomerate at Palen Pass record localized transpression of the Packard Well Fault in a restraining bend. Collocation of the Packard Well fault with a major Mesozoic structural boundary and differing offset estimates for Cenozoic and Mesozoic markers suggests the geometries of Neogene structures are at least locally influenced by inherited anisotropy.

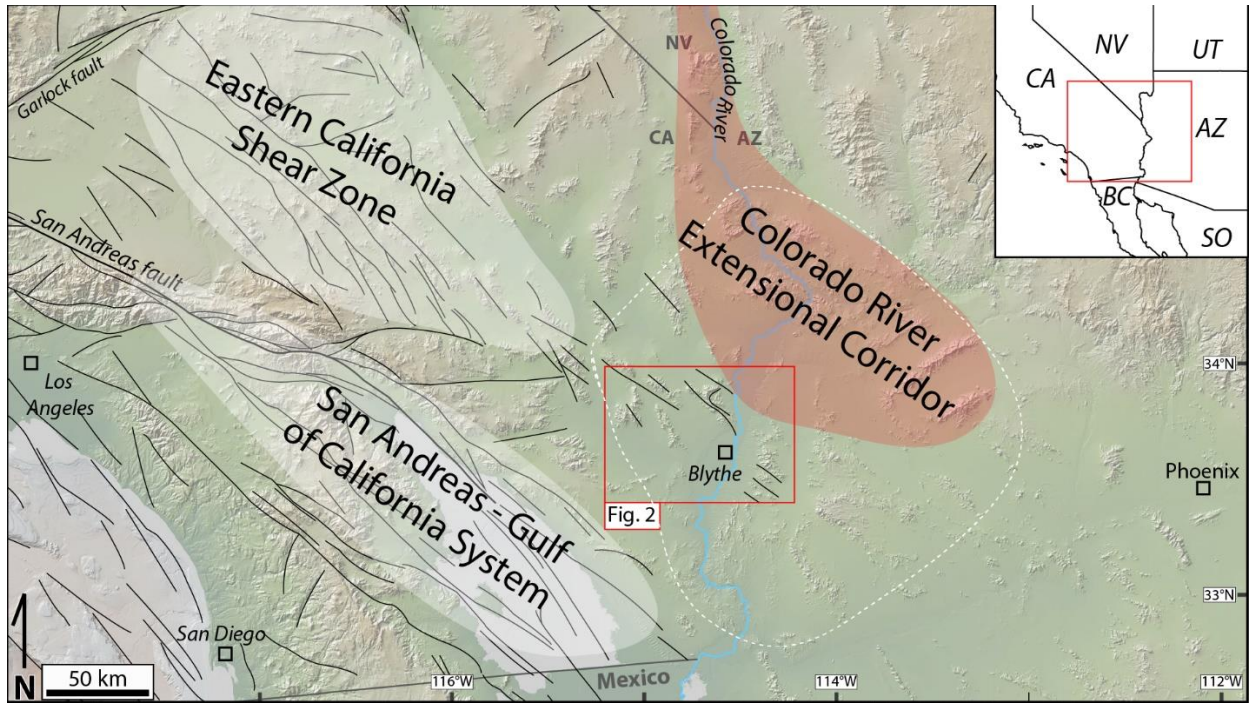


Figure 5.1. Neogene tectonic provinces and major faults in southern California and western Arizona (modified from Singleton et al. (2019)). White dashed line is the outline of the lower Colorado River region from Bennett et al., (2016) with 30–35 km less cumulative dextral shear than adjacent regions to the northwest and southwest.

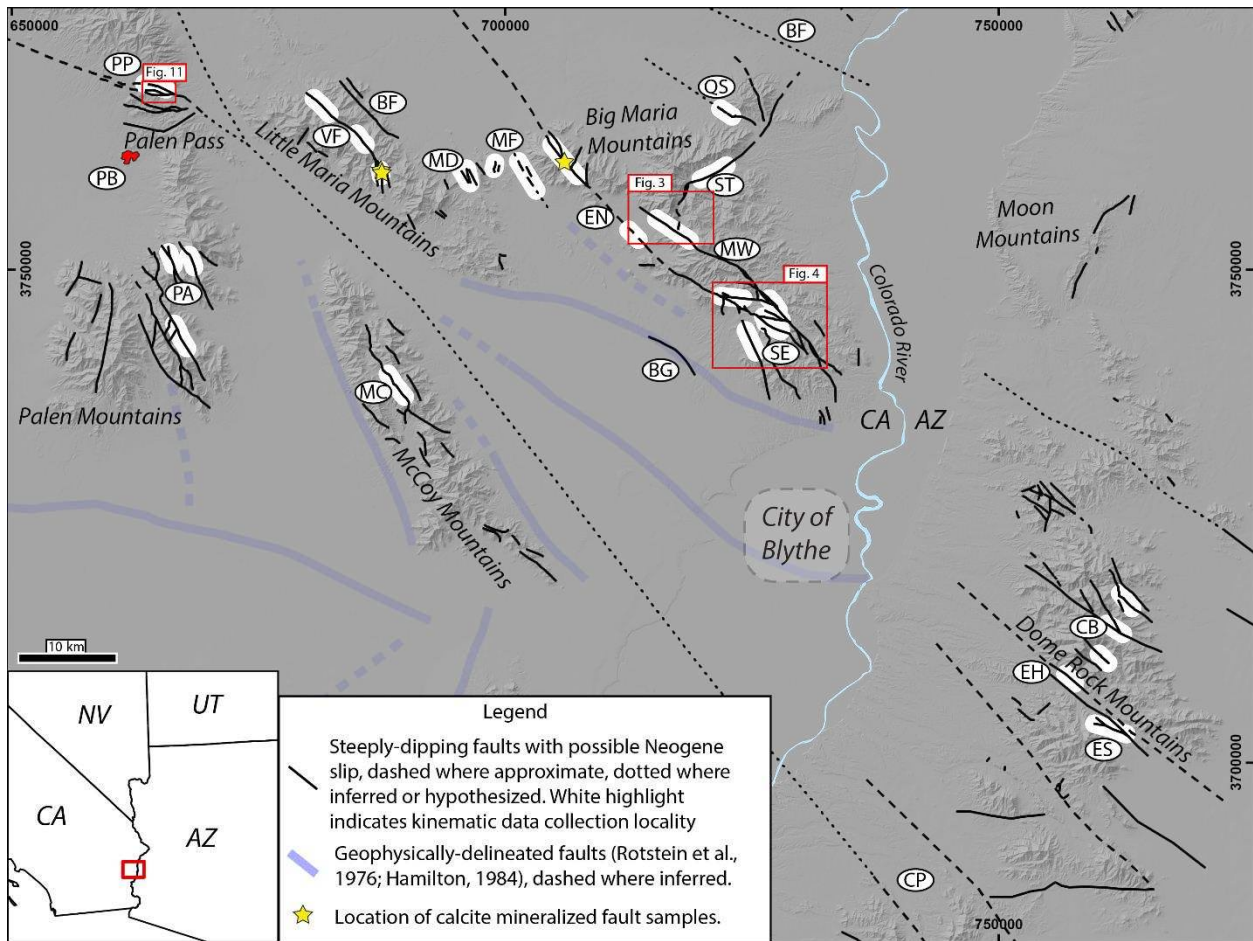


Figure 5.2. Map of simplified regional geology highlighting steeply-dipping faults with possible Neogene motion. Labels refer to places and structures described in the text: PP–Palen Pass; PB–Palen Pass basalt; VF–Valley fault; BF–Border fault; PA–Palen Mountains faults; MC– McCoy Mountains faults; MF–Maria fault; EN–Eagle’s Nest fault; QS– Quién Sabe fault; ST–Slaughter Tree Wash fault; MW–Maria Wilderness fault; SE–Faults in the southeastern Big Marias (Figure KK); CB–Copper Bottom pass; EH–Ehrenberg Wash fault; ES–Ehrenberg Wash fault splay; CP–Cibola Pass. Known and inferred faults in this figure are modified from Hamilton (1984), Emerson (1985), Stone and Pelka (1989), Stone and Kelley (1989), Ballard (1990), Richard and Dokka (1992), Richard (1993), Stone (2006), Bennett et al. (2016), and Stone et al. (in review).

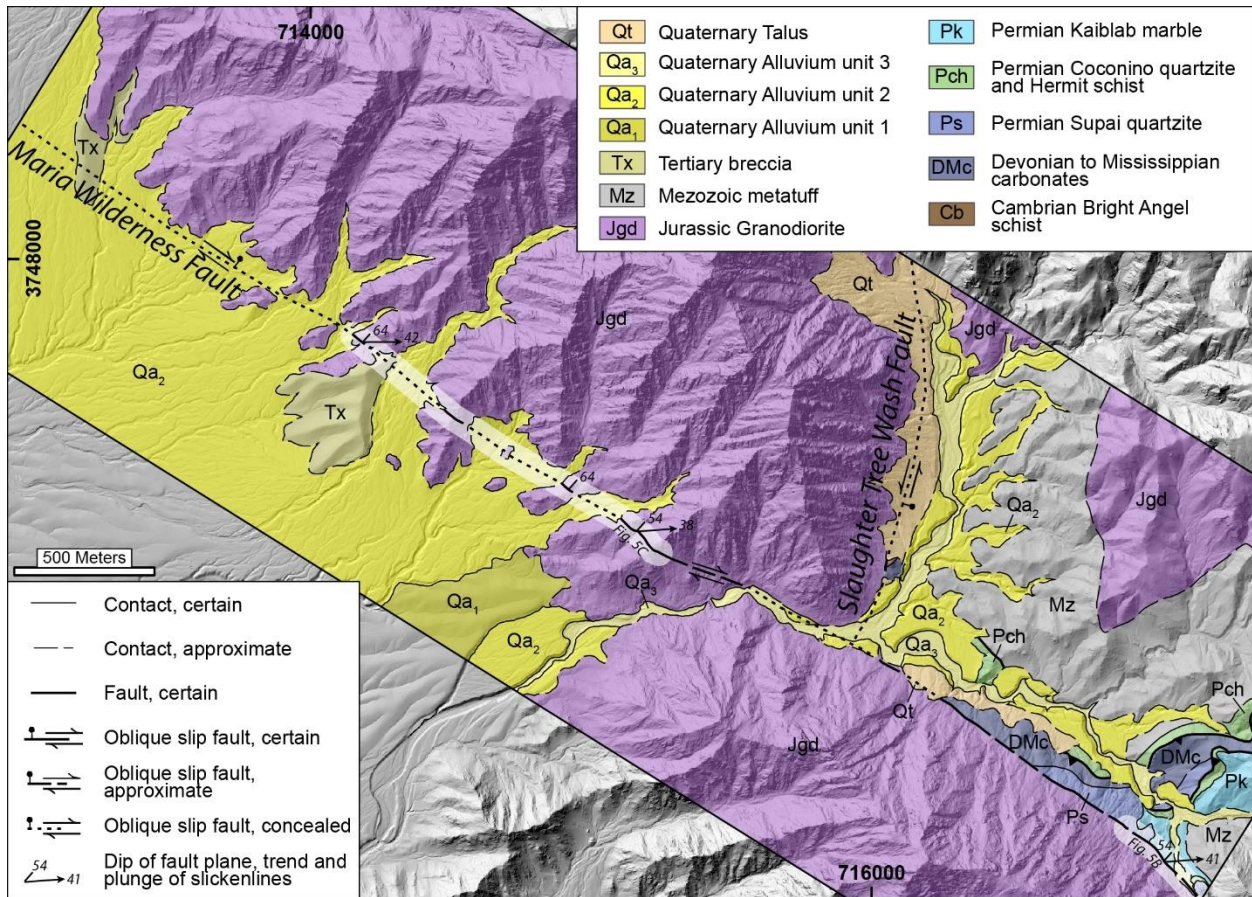


Figure 5.3. Geologic map of the central Big Maria Mountains, showing the NNE-striking sinistral oblique Slaughter Tree Wash fault truncated by the NW-striking Maria Wilderness fault. Modified from Hamilton (1981, 1984). Highlighted fault traces show the localities of kinematic data collection for stereoplots in Figure 5.5.

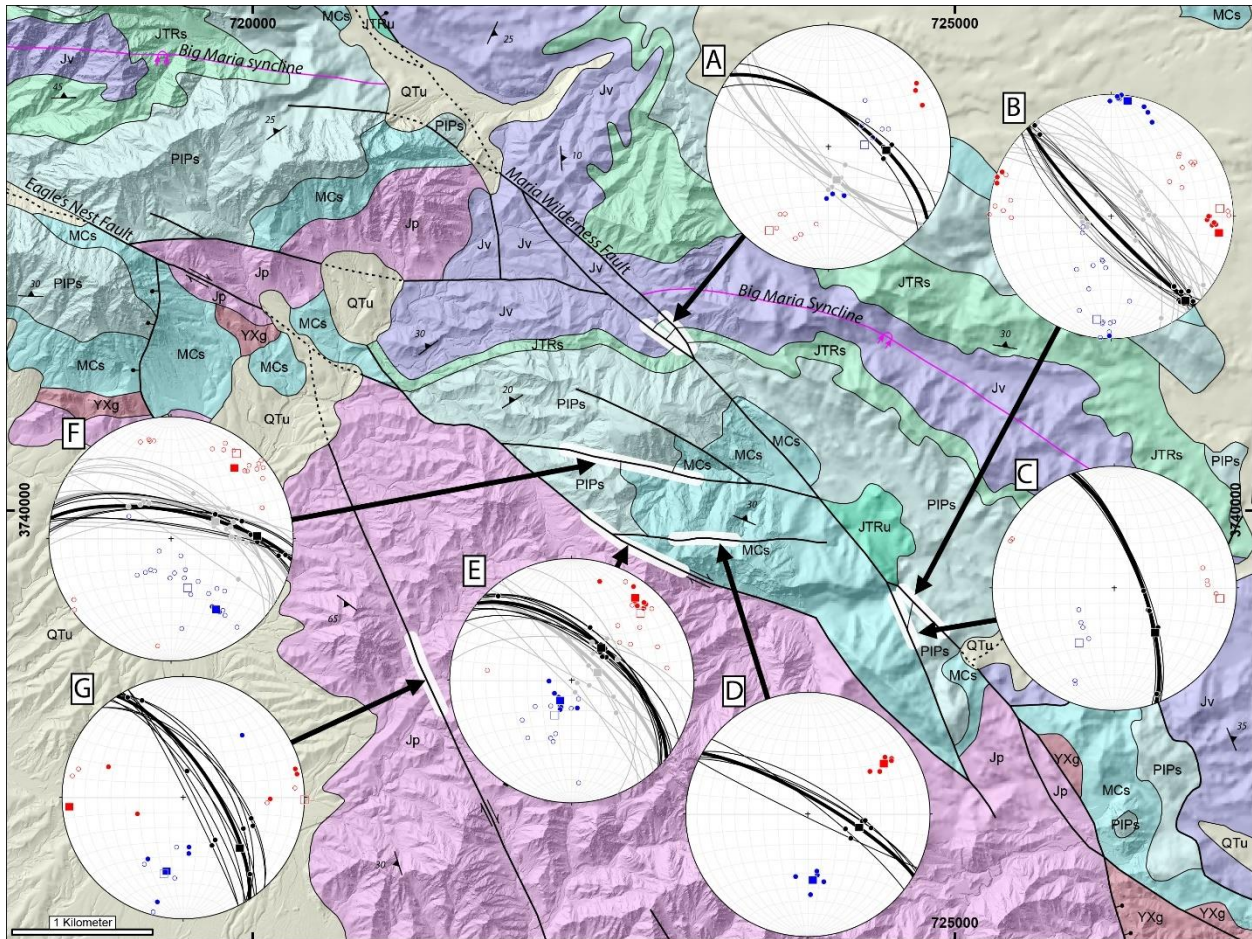


Figure 5.4. Faults in the southeastern Big Maria Mountains. Geologic mapping is modified from Stone et al. (in review) to show additional faults mapped by Hamilton (1981, 1984). Stereoplots show measurements of fault principal slip surfaces in black and subsidiary surfaces in gray. P- (blue) and T- (red) axes are given for faults with observed (filled symbols) or assumed (hollow symbols) slip sense. Average planes are shown with bold great circles, and average linear features with box symbols.

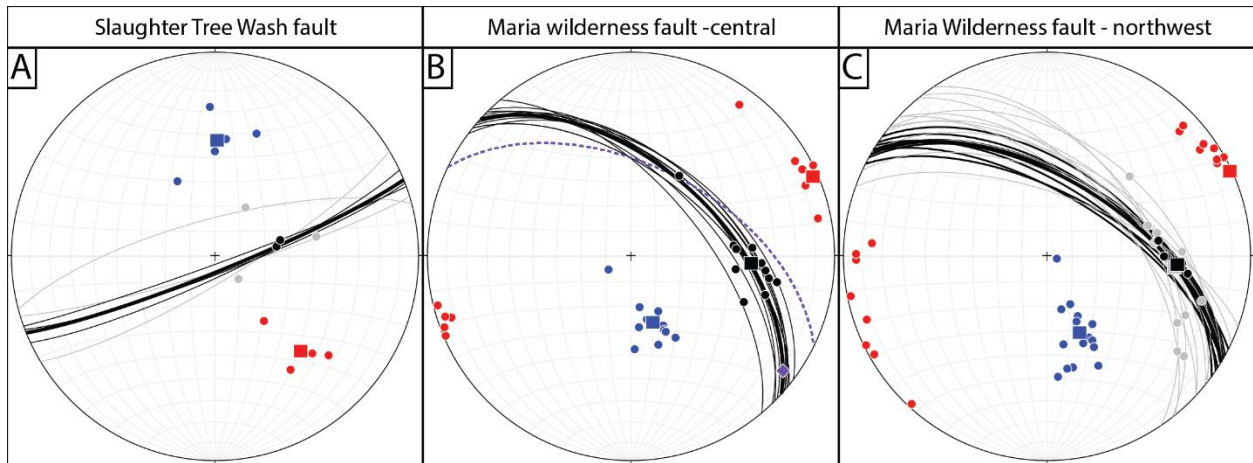


Figure 5.5. A: Fault kinematic measurements from the Maria Wilderness fault southeast of the intersection with the Slaughter Tree Wash fault with the average gouge foliation (purple dashed line, an average of 9 measurements) and the calculated slip vector (purple diamond). Other stereoplot symbols are the same as Figure 5.4) B: Stereoplot of fault surface measurements of the newly-mapped portion of the Maria Wilderness fault. Bold black lines and points indicate measurements of the principal slip plane, while gray lines and points indicate measurements of fault surfaces within the fault damage zone. C: Fault measurements from the NE-striking segment of the Slaughter Tree Wash fault with oblique normal-sinistral kinematics.

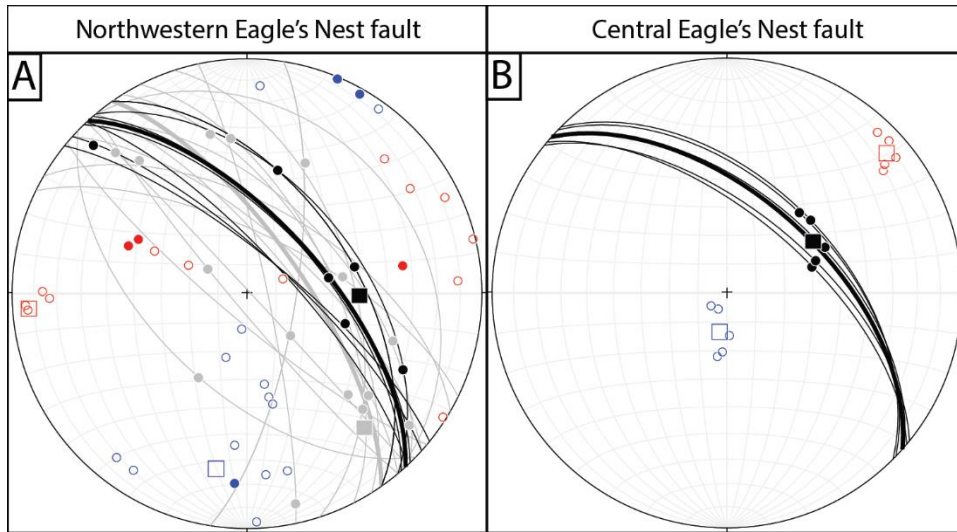


Figure 5.6. Measurements of the Eagle's Nest fault in the northwestern and central Big Maria Mountains. A: Stereoplot of measurements of the Eagle's Nest fault in the northwesternmost Big Maria Mountains. Symbols as for Figure 5.4. B: Fault measurements from the center of the Big Maria Mountains. These fault surfaces are along either the trace of the Eagle's Nest fault or parallel associated faults. The average fault plane dips more shallowly than elsewhere in the range, and the average slickenline lineation is more steeply raking and indicates dip-slip kinematics with only a slight southeast obliquity. Incremental strain axes are shown for an assumed NE-down slip sense, as no unequivocal outcrop slip sense indicators were found in the field.

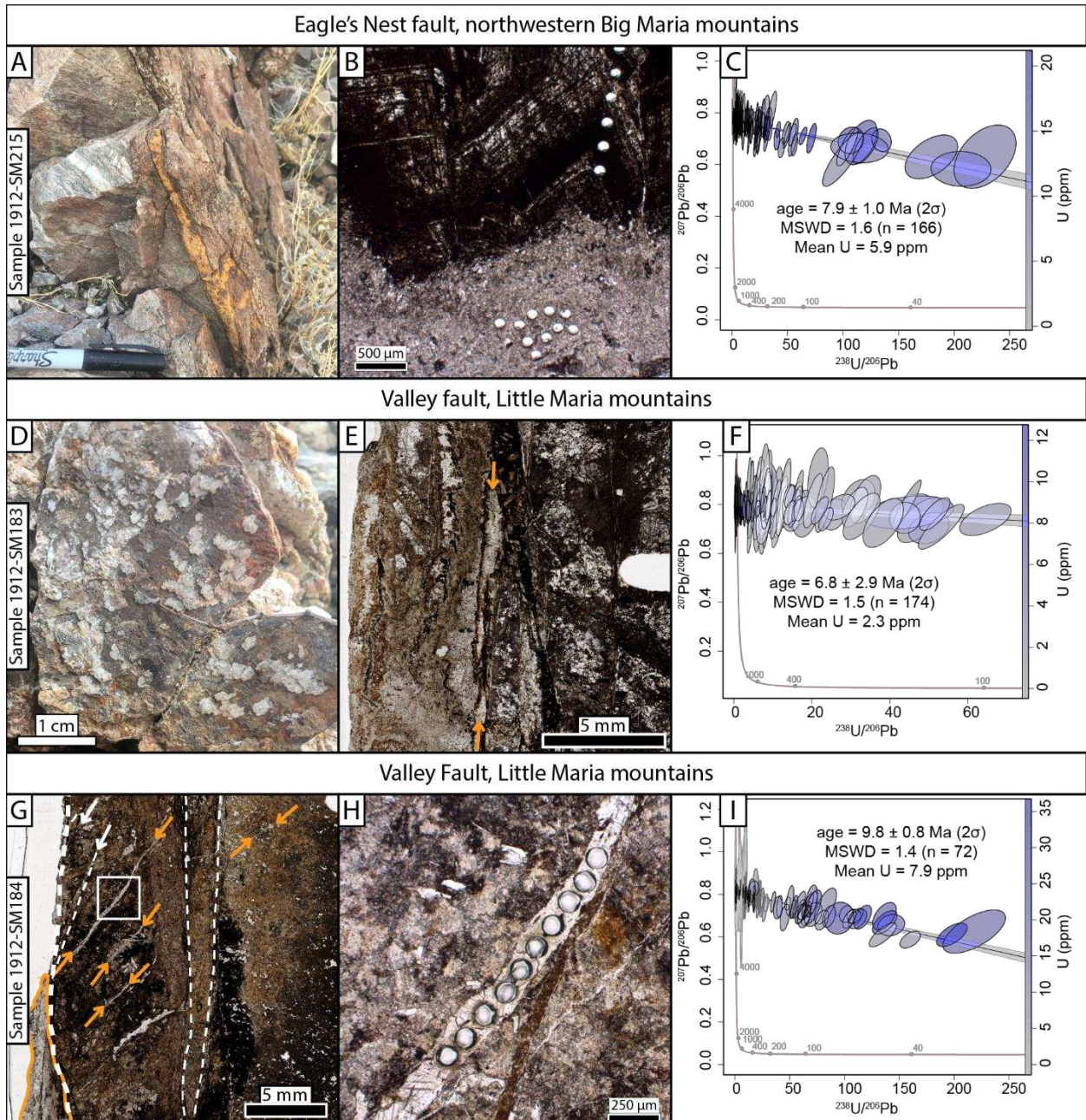


Figure 5.7. A: Field photograph of sample 1912-SM215 from the principal slip plane of the Eagle’s Nest fault. A calcite + siderite vein cuts Proterozoic gneiss, separating these rocks from Mesozoic rocks northeast of the fault. B: Photomicrograph of sample 1912-SM215 with laser ablation pits in a transect across a domain of coarse zoned calcite. C: Tera-Wasserburg diagram of sample 1912-SM215 analyses; coarse-grained calcite analyses are in dark gray outline and fine-grained calcite in light gray. The calculated age is for the entire sample. D: Overhanging fault surface exposure of sample 1912-SM183 collected from a NNW-striking fault at the horsetail splay termination of the Valley fault in the Little Maria Mountains. Calcite slickenfiber steps mineralized on the steeply NE-dipping fault surface indicate dextral-reverse oblique slip of the Valley fault during calcite precipitation. E: Thin section scan of sample 1912-SM183; the left

edge of the scan is the fault surface exposed in outcrop. Discrete internal fault surfaces that run parallel to the exposed fault surface are visible in the center of the sample, and some are mineralized with calcite (orange arrows), and calcite is involved in brecciation along these surfaces. F: Tera-Wasserburg diagram of sample 1912-SM183 with a lower intercept age of 6.8 ± 2.9 Ma. G: Thin section scan of sample 1912-SM184. The sample is cut perpendicular to the fault surface and parallel to the slickenline lineation, such that the fault surface exposed in outcrop is the left edge of the image. White dashed lines demarcate fault surfaces, and those with white arrows are in Riedel shear orientations for dextral shear. Orange arrows mark tension fractures mineralized with calcite, which also indicate dextral shear and syn-faulting calcite precipitation. H: Photomicrograph of calcite mineralized tension fracture (area outlined in white in D), with LA-ICP-MS ablation spots. I: Tera-Wasserburg U-Pb plot of sample 1912-SM184. Analyses from T-fracture calcite are outlined in black, analyses from the calcite matrix textural domain are dark gray, and slickenfiber step calcite are light gray. Lower intercept regression age is for the T-fracture textural domain only, additional regression ages are reported in Dataset 5.

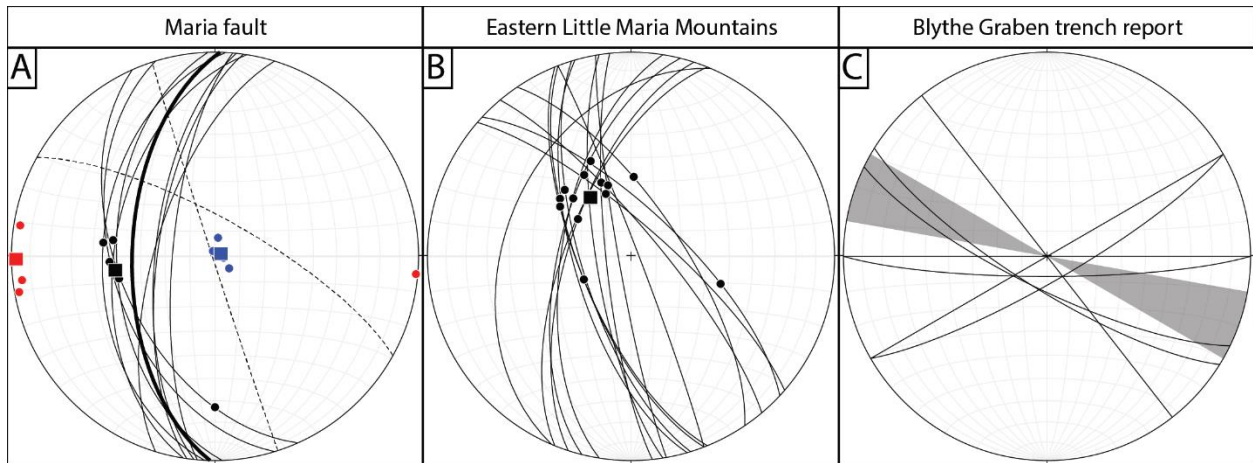


Figure 5.8. A: Measurements from fault surfaces at the Mesozoic-Cenozoic interface in the northwestern Big Maria Mountains (locality MF on figure LL). Fault surfaces in bedrock ($n = 9$) dip moderately to steeply west with mostly down-dip slickenlines ($n = 5$; average 262/49) and one slickenline shallowly plunging south. Incremental strain axes are shown for measurements with down-dip slickenlines based on normal-sense Riedel shears observed in outcrop (average 066/87 and 269/03 for P- and T-axes, respectively). Two NW-striking and steeply-dipping faults cut bedding within the breccia (dashed lines); no lineation or slip sense indicators were observed. B: Fault planes ($n=17$) and slickenlines ($n=14$) from faults northwest of Midland (MD on Figure 1) mapped by Ballard (1990). C: Stereoplot of fault planes reported in trenches at the Blythe graben (citation to trench logs, 197X), (locality BG on Figure 5.2). Rose diagram shows the 280–300° range of surface trace of the Blythe graben as observed in 1 m lidar.

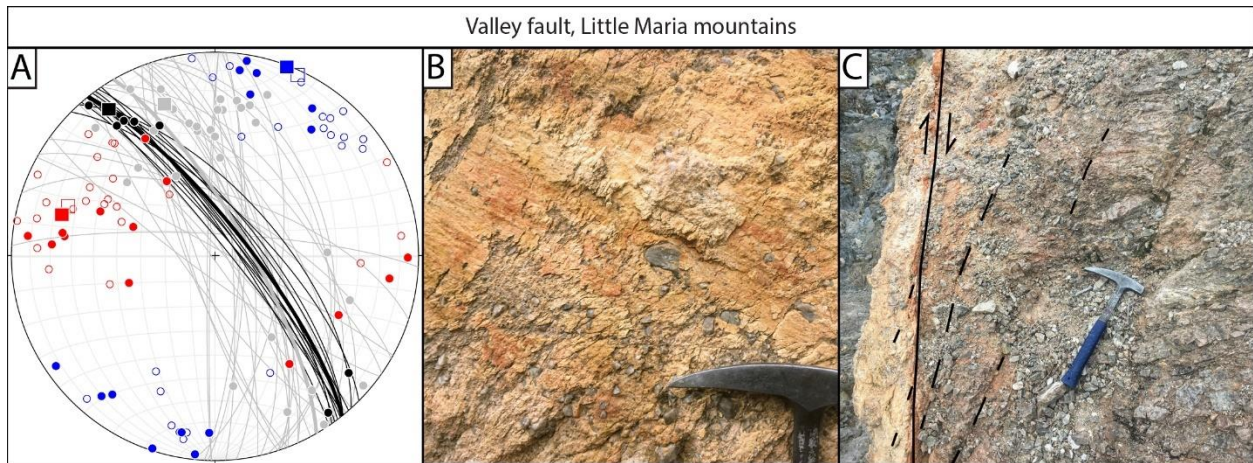


Figure 5.9. A: Stereoplot of measurements along the Valley fault in the Little Maria Mountains that record dominantly dextral slip with a minor reverse-oblique component. Symbols as for figure 4. B: Shallowly NW-raking slickenline lineation on the principal slip plane of the Valley fault (photograph facing SW). C: Plan view photograph of the Valley fault principal slip plane from the top of the outcrop (top of photograph is to the SE), showing Riedel shears for dextral slip (black dashed lines parallel to hammer handle).

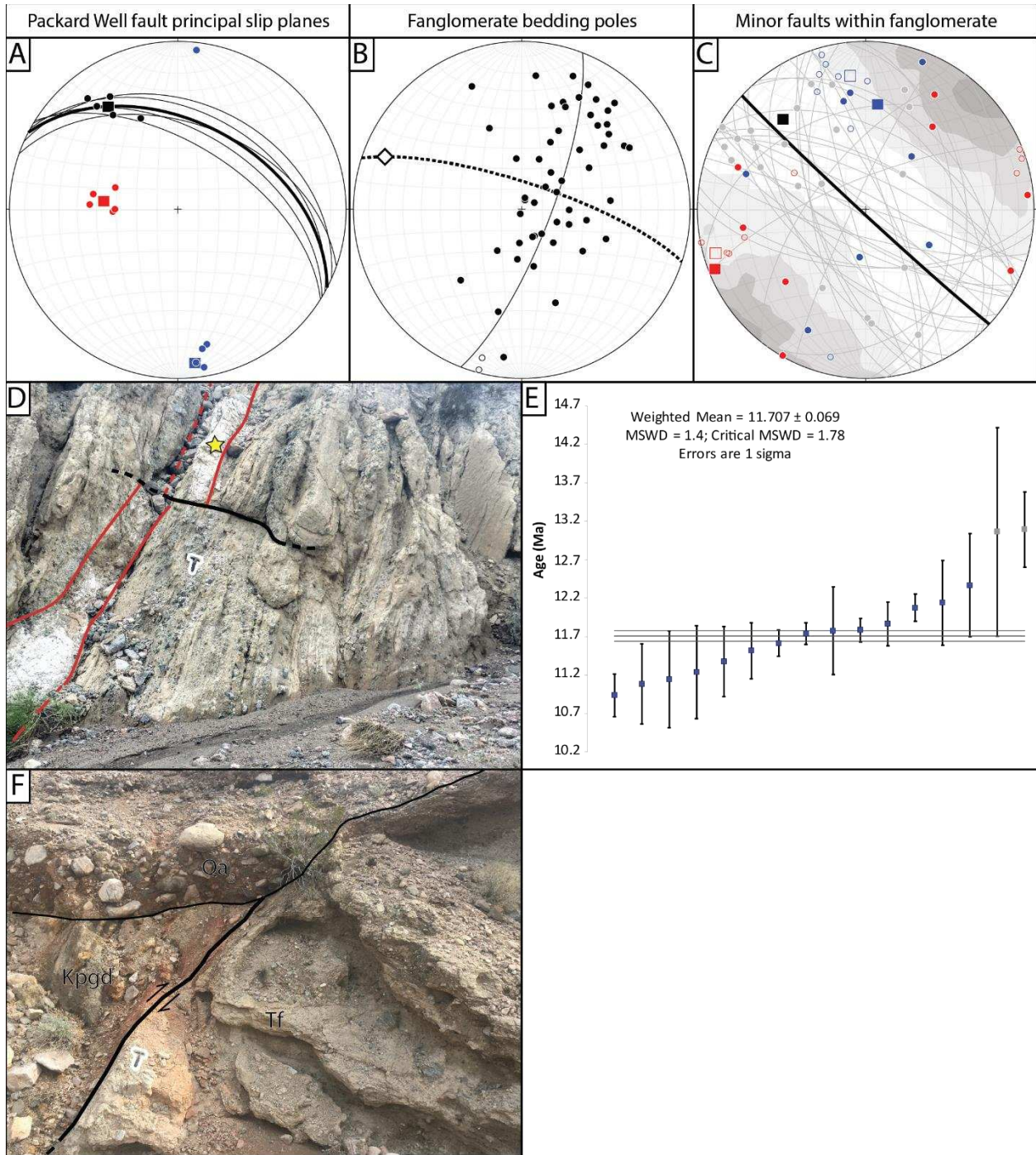


Figure 5.10. Structural measurements from the Palen Pass area. A: Measurements of the principal slip plane of the northernmost strand of the Packard Well fault zone that juxtaposes Mesozoic plutonic rocks over the undated fanglomerate. B: Poles to bedding in the undated Palen Pass fanglomerate, hollow poles signify measurements from overturned bedding. The calculated fold axis (hollow diamond) from the cylindrical best fit to bedding poles (solid great circle) plunges WNW (291/14). An approximate axial plane, calculated as the bisecting surface to the most tightly folded limbs, is oriented 288, 77 NE (dashed great circle). Bedding measurements that deviate from the cylindrical best fit plane in some cases reflect localized

rotation near faults internal to the fanglomerate. C: Measurements of minor faults within the Palen Pass fanglomerate. Fault planes and slickenlines (light gray) show considerable scatter, but contours of fault poles (poles not shown) reveal a predominance of NW-striking planes (average fault plane and slickenline shown in black). D: Ash horizon (red outline) interbedded with steeply SSE-dipping Palen Pass fanglomerate. A small fault (black line) cuts and displaces the bedding. Ripple marks in a sand horizon (right side of photo) show a younging direction to the SE (left). Hammer in center of photo for scale (white outline). E: Age distribution of sanidine grains analyzed by $^{40}\text{Ar}/^{39}\text{Ar}$. An additional 21 inherited grains with older ages are not shown and available in Dataset 6. F: Exposure of the principal slip surface of the Packard Well fault that bounds the north side of the Palen Pass fanglomerate. Fault rock derived from a Cretaceous granodiorite is in the hanging wall, bedded fanglomerate is in the footwall, and the fault is overlapped by Quaternary alluvium (unit *Qa2*, Fig 5.11).

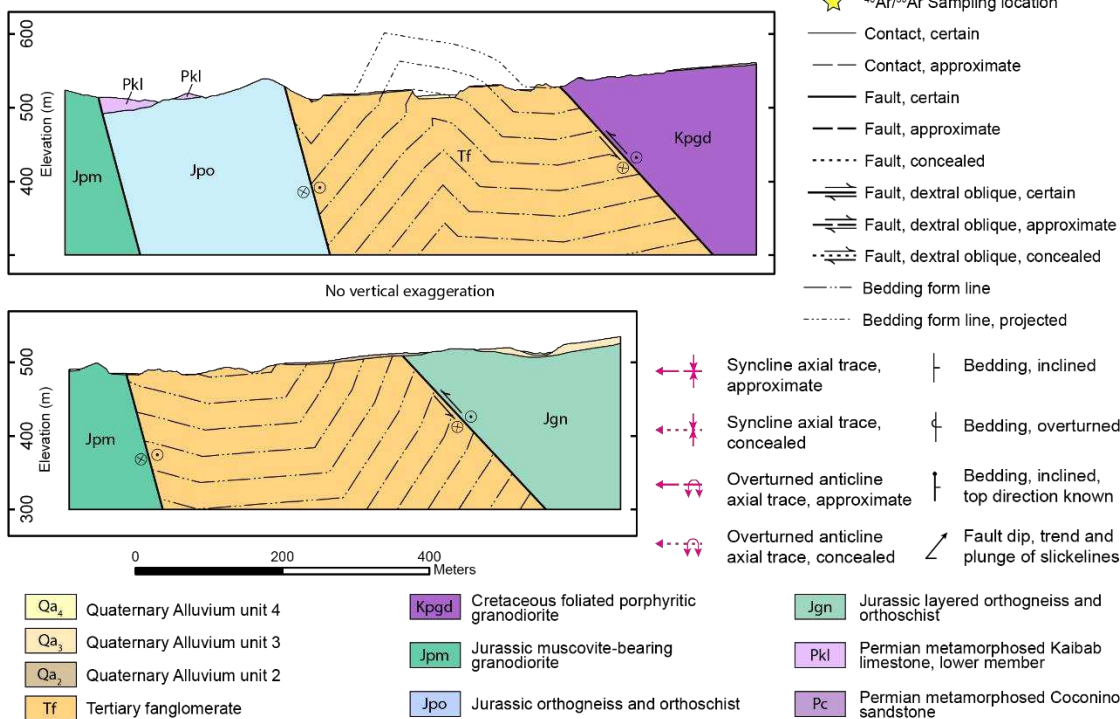
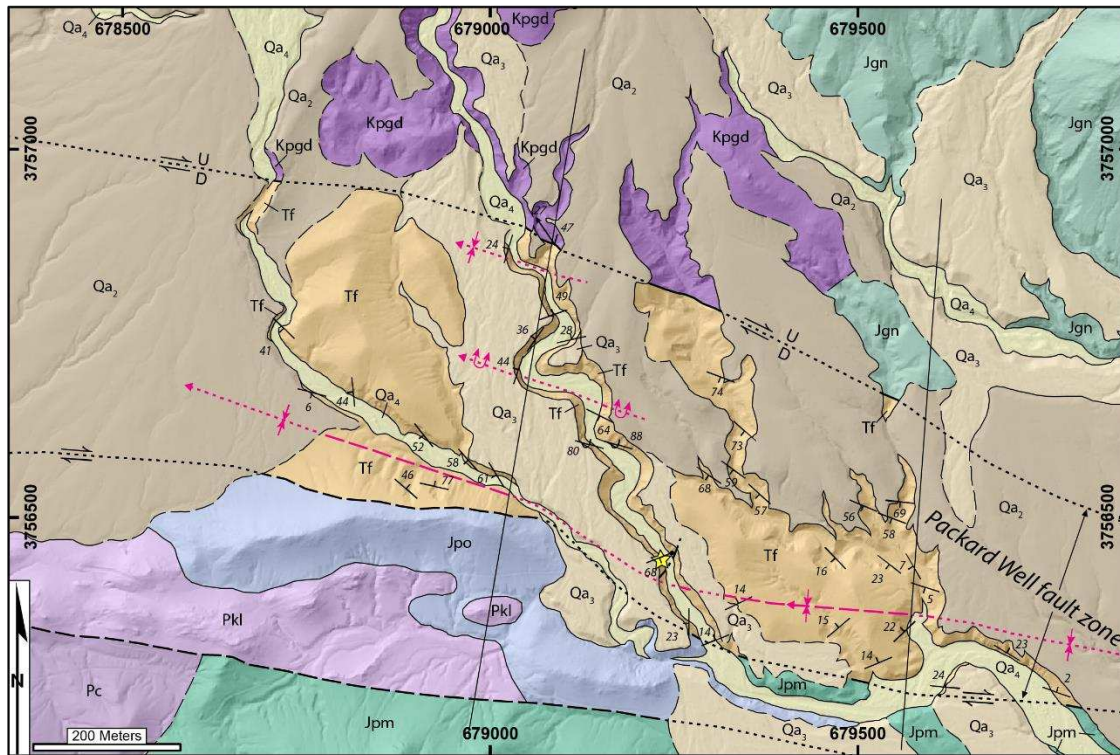


Figure 5.11. Geologic map and cross sections of the Packard Well fault zone at Palen Pass (map units after Stone and Kelly, 1989). N-dipping faults bound the Tertiary fanglomerate (unit *Tf*), with SSW-vergent folding of the fanglomerate locally overturned.

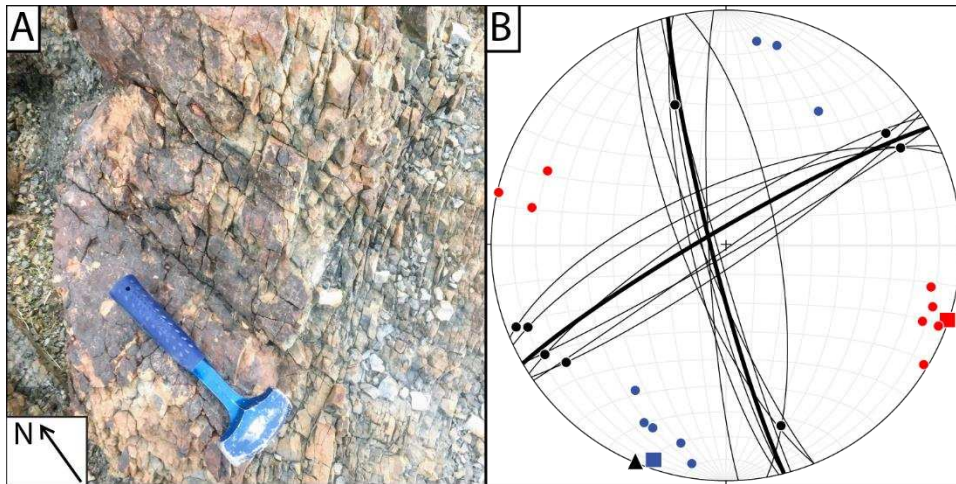


Figure 5.12. A: Incipient brittle conjugate fault fabric cutting the olivine basalt at Palen Pass. B: Stereonet of measured faults in the basalt; averages of each conjugate population are plotted with bold dashed lines, and the acute bisecting line (black triangle, 203/01) shows the shortening direction indicated by the conjugate pairs. Slickenline and incremental strain axis symbols as for Figure 5.4.

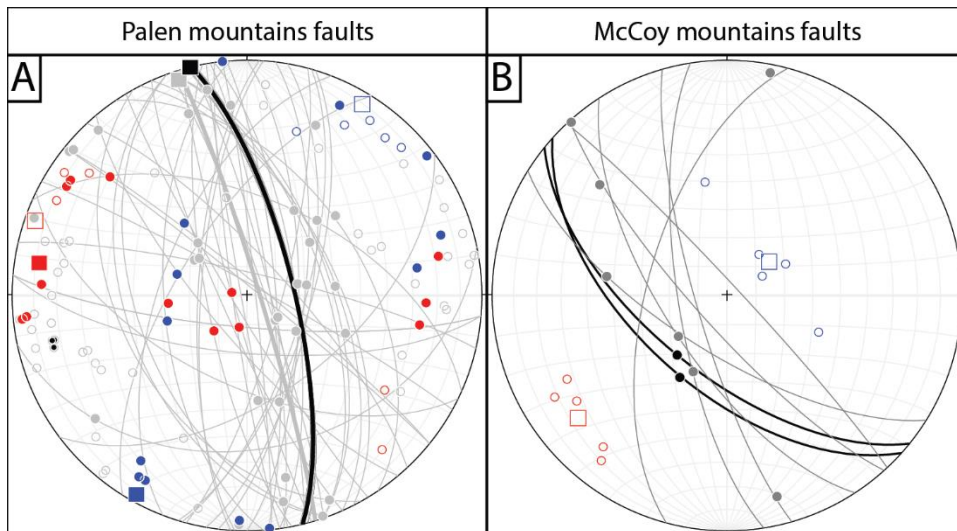


Figure 5.13. A: Measurements of fault principal slip surfaces (black) and subsidiary surfaces (gray) from the Palen Mountains (symbols as for Figure 5.4). Both subhorizontal and steeply-raking slickenlines are observed, but principal slip surfaces have only strike-slip slickenlines. Kinematic axes for faults with textural slip sense indicators (filled symbols) and assumed slip sense (hollow symbols) indicate a broad pattern of NNW-SSE shortening and WNW-ESE extensional strain. B: Measurements from the fault in the center of the McCoy Mountains. Incremental strain axes are plotted for measurements with steeply-raking slickenline lineations ($n = 5$) with W-down normal slip sense assumed based on map relations.

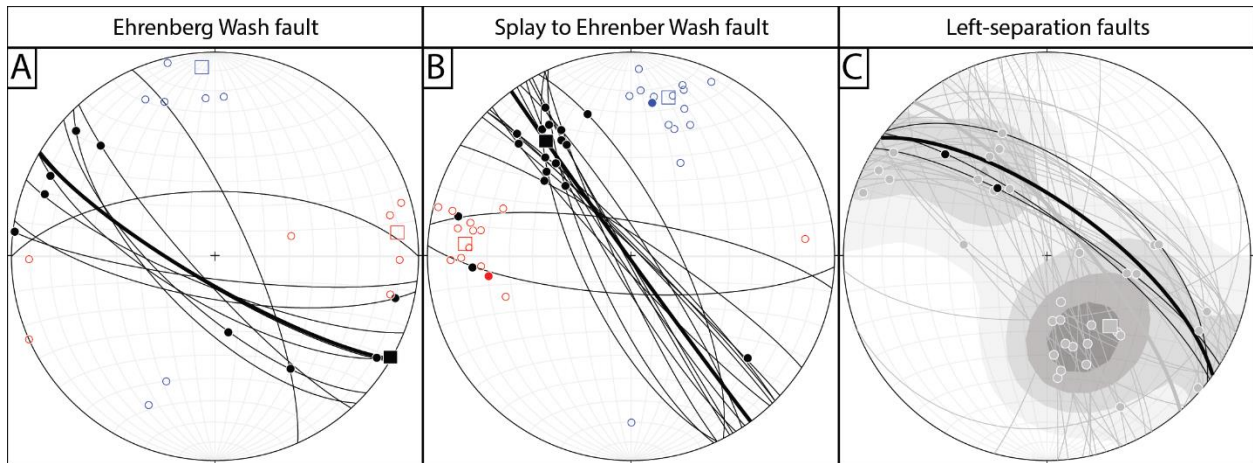


Figure 5.14. A: Measurements of faults in the damage zone of the Ehrenberg Wash fault (locality EH on Figure 5.2). Kinematic axes are shown for NW-SE striking faults with dextral slip sense assumed. On average, slickenline lineations are shallow and fault planes are steeply dipping. B: Fault measurements from a mapped splay to the southeastern part of the Ehrenberg Wash fault (locality ES on Figure 5.2). One measurement has calcite mineralization filling a cm-scale releasing bend as a dextral slip sense indicator, and the slip sense of other faults are assumed from this and the map right separation of the Ehrenberg Wash fault. The average fault plane, slickenline lineation, and incremental strain axes are shown for NW-striking measurements and exclude E-W striking fault surfaces with uncertain kinematics. C: Measurements of left-separation faults in the Dome Rock Mountains north of Ehrenberg Wash. Measurements of fault principal slip surfaces are shown in black and measurements of subsidiary fault surfaces are shown in gray. Measured faults are most commonly NW-striking, parallel to the Copper Bottom Pass fault, or NNW-striking and parallel to faults that splay from the Copper Bottom Pass fault. The average slickenline measurement rakes moderately SE, though contours indicate that lineation orientations span from horizontal to moderately NW-raking.

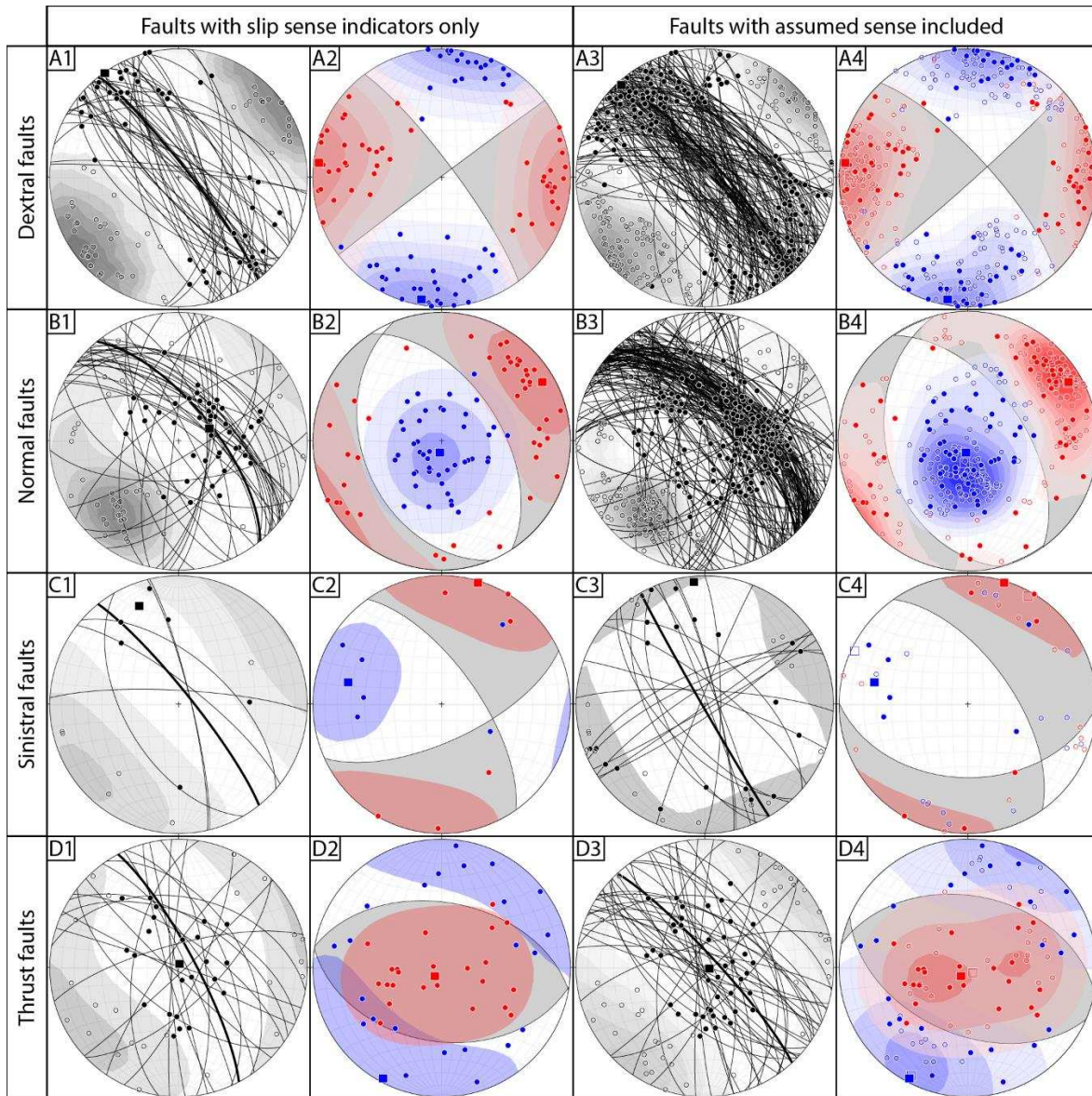


Figure 5.15. All measured faults, separated by slickenline rake and fault type. Row A: Dextral faults with slickenline rake $\leq 45^\circ$. Row B: Normal faults with slickenline rake $> 45^\circ$. Row C: Sinistral faults with slickenline rake $\leq 45^\circ$. Row D: Reverse faults with slickenline rake $> 45^\circ$. For each row: Column 1 displays fault planes and slickenline lineations (filled circles) for faults with outcrop slip sense indicators; contours show the poles to fault planes (hollow circles) with the average fault plane plotted in bold and the average slickenline plotted as a square. Column 2 shows incremental strain axes with contours and averages, and a fault-plane solution for the same data as column 1. Column 3 has the same symbology as column 1 but includes faults with slip sense assumed from geometry or location relative to mapped faults. Column 4 shows incremental strain axes for the faults with slip sense indicators (filled symbols) and for faults with slip sense assumed (hollow symbols). The number of analyses and orientations of average measurements are available in Dataset 3. Plots B2, C2, and D2 have Kamb contours with interval 3σ and significance level 3σ . Plots C3 and C4 have Kamb contours with interval 4σ and significance level 3σ .

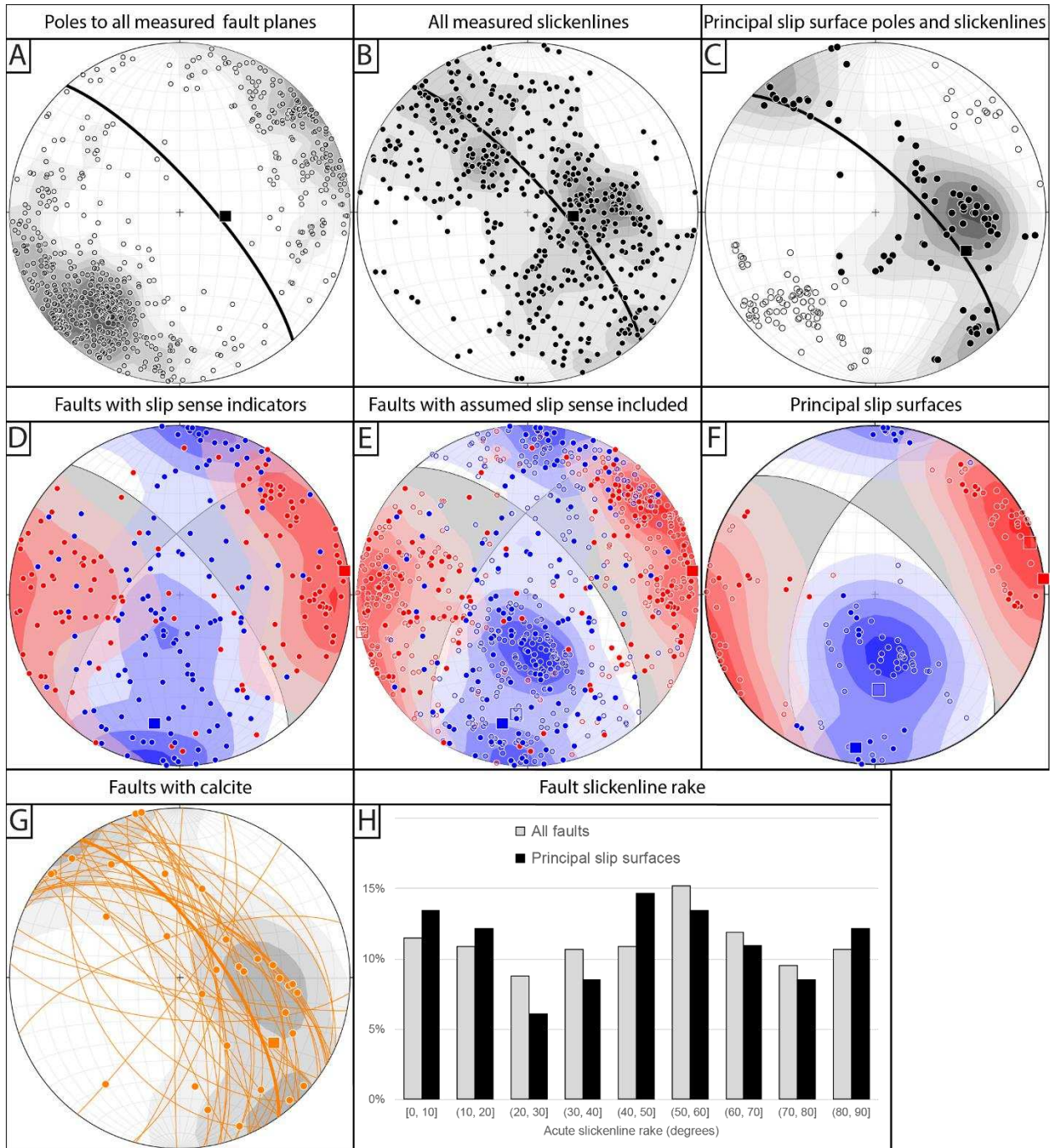


Figure 5.16. A: Poles to all brittle fault plane measurements (n = 642) with the average fault plane (318, 77 NE) and average slickenline (094/68). B: All measured slickenline lineations (n = 512). C: Measurements of the principal slip surfaces of mapped faults. Smoothed Kamb contours show a range of slickenline orientations with steeply E-plunging and NW-SE subhorizontal orientations predominant. D: Incremental strain axes for all measured faults with slip sense indicators observed in outcrop (n = 126). E: Incremental strain axes for all measured faults with slip sense observed (filled circles) or assumed (hollow circles, n = 367 total). F: Incremental strain axes for measurements of mapped fault principal slip planes with outcrop sense-of-slip

indicators (n = 22, solid symbols) and assumed slip sense (n = 69 total, hollow symbols). G: Measurements of all calcite-mineralized fault surfaces. The average calcite fault surface (324, 70 NE) closely parallels the average of all measured fault planes, and the average lineation (125/33), is more shallowly SE raking. H: Histogram of slickenline rake for all slickensided fault surfaces and principal slip plane measurements only (dark gray), showing relatively even distribution of dip-slip, strike-slip, and oblique-slip faults.

6. CONCLUSIONS

6.1. LOCALIZATION OF INTRA-ARC FAULTS

A chief goal of Chapters 2, 3, and 4 is to assess the major controlling factors of intra-arc fault systems. Chapter 4 provides a detailed view into the distribution of brittle and ductile deformation in the intra-arc Atacama fault system and provides insight to the requisite factors that facilitate ductile shear. Chapter 2 documents a kinematic shift in the Early Cretaceous Andean margin that contributed to abandonment of AFS intra-arc shear. Chapter 3 examines the nature of intra-arc deformation that did not localize into a coherent fault system and instead remained an apparently isolated shear zone. While it remains possible that a significant portion of the Mesozoic magmatic arc has been removed by subsequent subduction erosion, the paucity of Middle Jurassic magmatism, as noted in histograms of compiled geochronology (e.g., Seymour et al., 2020; Jara et al., 2021b), could suggest that there was insufficient magmatism, and thus insufficient thermal weakening and reaction softening from magmatic fluids to localize strain into a regional-scale intra-arc deformation zone. Alternatively, Middle Jurassic convergence may have had less of a margin-parallel oblique component than along the Early Cretaceous margin during AFS deformation, leading to the absence of a Jurassic intra-arc shear zone. Regardless, the map relations presented here demonstrate that the pre-existing anisotropy of the Matancilla shear zone did not appear to influence the geometry of the Early Cretaceous AFS that cuts oblique to the Jurassic fabric.

The lack of an interconnected shear zone in Jurassic arc rocks (Chapter 3), combined with the timing constraints that record a transition from slip on the AFS to the TFS near-contemporaneous with a migration of magmatism out of the area (Chapter 2), suggests that the

AFS, and perhaps intra-arc fault systems in general, are not long-lived features of oblique plate boundaries. Our mapping (Chapter 4) demonstrates that ductile shear zones only developed along the AFS eastern branch where magmatism was in close spatial and temporal proximity to the AFS and at emplacement depths deep enough that the thermal influence of magmatism could enable a shift to plastic deformation, and that these conditions were met in only one location along ~75 km of the AFS trace. While AFS-connected, magmatism-enabled ductile shear is documented along the southern Paposo, northern El Salado, and central El Salado segments of the AFS (Ruthven et al., 2020; Seymour et al., 2020), several earlier pluton-connected shear zones (e.g., the Matancilla and Flamenco shear zones) apparently record isolated shear that cannot be connected along a single intra-arc structure at the exposed crustal levels.

In places where ductile shear was associated with pluton intrusion, solid-state deformation fabrics are most strongly developed in quartzose and micaceous rocks surrounding plutons rather than the plutons themselves, where shear fabrics are low-strain protomylonite. This pattern suggests that the weakest part of intra-arc fault systems may depend not only on magmatic patterns but also the lithologies that are intruded, which may be spatially variable. Our findings from geologic mapping that ~59% of the AFS eastern branch is in contact with Chañaral Complex metasedimentary rocks and only ~1% is in direct contact with Early Cretaceous plutons demonstrates the potential importance of lithologic control. Localization of the highest-strain deformation near pluton margins suggests that screens and pendants of pluton country rock are important features for intra-arc shear, especially where shear zones parallel these lithologic boundaries. For modern intra-arc systems, it may not be possible to infer country rock lithology at depths near the brittle-plastic transition, and thus there may be significant uncertainty of the rheology and strength. Strain localization at pluton margins introduces an additional challenge to

recognizing offset markers and quantifying strain magnitudes and rates, since there may not be offset equivalents of plutonic bodies on both sides of an intra-arc fault system.

Textural evidence presented in Chapter 3 demonstrates that ultramylonitic fabric in discrete shear zones are associated with alteration and breakdown of strong phases, suggesting that reaction softening and hydrolytic weakening may drastically reduce the strength of otherwise strong lithologies such as granodiorite. However textural evidence for alteration is not pervasive in the Matancilla aureole or AFS ductile shear zones, suggesting that rheologically weaker lithologies, and not widespread alteration, were the most important at the scale and exposed structural levels of these shear zones.

Previous studies have suggested that abandonment of the AFS occurred as the magmatic arc migrated eastwards towards the present day high Andes (e.g., Dallmeyer et al., 1996). Our data that indicate a transition from slip on the AFS to the TFS occurred between 114–107 Ma broadly support that notion, as this timing overlaps with the last magmatic pulse in the Coastal Cordillera between 120–105 Ma along the AFS corridor (Seymour et al., 2020) and 117–99 Ma across the more broad Coastal Cordillera (Jara et al., 2021b). However, lingering magmatism is present in the Taltal region, marked by the ~110 Ma Tropezón and 106–101 Ma Librillo plutons 5–15 km east of the AFS, and regional studies identify a 103–94 Ma final phase of plutonism east of the AFS before a magmatic hiatus (Jara et al., 2021a). Abandonment of the AFS broadly coincides with the eastward shift of magmatism, but in detail appears to shortly precede the final phase of Coastal Cordilleran Cretaceous plutonism. Chapter 2 argues that the shift from AFS to TFS is contemporaneous with changes in Andean plate boundary dynamics and perhaps with a global plate reconstruction, and the final phases of Coastal Cordilleran magmatism may have lagged behind the shifting plate dynamics. While the localization of the AFS was clearly

influenced by the location of the magmatic arc axis, abandonment of the fault system may have been driven as much by a changing stress regime that allowed the pre-existing TFS crustal weaknesses to be reactivated as by a decrease in magmatic activity in the Coastal Cordillera.

Timing constraints presented in Seymour et al. (2020, 2021) demonstrate that the AFS was active from ~132 Ma to ~119 Ma with localized ductile deformation, and as late as 114–107 Ma with brittle-only deformation. The timeframe of AFS activity spans only 10–13% of the lifetime of the Andean margin that began at ~210 Ma (Jara et al. 2021b) and has continued to the present. In addition to the AFS, pluton-connected ductile shear zones are also recognized in the Coastal Cordillera along the Triassic to Jurassic Tigrillo fault system and the Early to Late Cretaceous Chivato fault system (Grocott and Taylor, 2002). These additional margin-parallel faults, which are located ~30 km on either side of the AFS, suggest that strain migrates between multiple intra-arc systems through the lifespan of a plate margin to wherever magmatism facilitates crustal weakening. These findings potentially contrast with descriptions of long-lived shear on the Liquiñe-Ofqui fault in the southern Andes (Cembrano et al., 1996), though the ‘long-lived’ timeframe described for this fault may be comparable to the ~25 Myr upper estimate for AFS activity, and is relatively short compared to the lifespan of the Andean margin.

6.2. SIGNIFICANCE OF DISTRIBUTED DEFORMATION

Distributed deformation may be an underrecognized mode of plate boundary strain accommodation and may be challenging to quantify where suitable offset markers are not present. Chapters 2, 4, and 5 document fault systems that involve numerous parallel faults that were active contemporaneously, and in both cases the estimated cumulative shear across the distributed system as a whole is significantly greater than estimates using only the largest faults in the system. Displacement of the AFS and TFS is dominantly accommodated by the largest

single fault in those systems, as the AFS eastern branch and Taltal fault are responsible for ~63–70% and ~70% of the total cumulative shear. These results are consistent with findings that relatively minor faults accommodate significant amounts of strain in extensional systems, potentially representing 25–60% of total extension, but are easily overlooked by studies that consider only the largest faults (Marrett and Allmendinger, 1992). However, our estimates of cumulative dextral slip along faults near Blythe indicate that only ~31–42% of the total system slip is accommodated by the largest single fault, while faults with < 5 km and > 1 km of slip (excluding the largest single fault) are responsible for 86–53%, and faults with < 1 km slip accommodate only 11–5% of slip in the system (percentages estimated using both high and low estimates for faults in the system, respectively). Cumulative displacement estimates provided here may yet undercount the true magnitude of strain, as they rely on geologic mapping at a scale that cannot document faults with meter-scale or smaller displacement.

6.3. METHODOLOGY FOR STUDYING STRIKE-SLIP FAULTS

6.3.1. Estimating offset

For strike-slip faults without suitable piercing points, three-dimensional displacement can be approximated by using separation markers in conjunction with fault-surface slickenline lineations. However, this approach must be used with caution, as faults may have undergone polyphase deformation histories with multiple kinematic styles, and slickenlines may provide conflicting indications of slip vectors or only record the most recent episodes of slip. Chapter 5 documents faults that were active through a changing kinematic regime, but planar and curvilinear displacement markers provide some constraints on the total strain magnitude. Chapter 2 documents relatively uniform kinematics for the TFS, and the near-vertical AFS makes an ideal marker for strike separation. Kinematic data for the AFS consistently indicate that

deformation was dominantly strike-slip during both brittle and ductile shear, yet map relations of geologic units require at least some component of dip-slip across the system.

6.3.2. Methods to constrain deformation timing

Geochronology of map units with cross-cutting relations remains an ideal method of constraining the timing history of strike-slip fault systems, but this method may be challenged by the relative scarcity of datable map units with both pre- and post- kinematic relations required to bracket deformation timing of a fault system. Zircon U-Pb geochronology is a proven, robust method to date igneous units with relative timing relations to strike-slip fault systems but is only suitable where there is a datable unit with cross-cutting relations relevant to the structural system. Chapters 2 and 5 demonstrate the utility of calcite U-Pb geochronology as a tool to directly constrain timing of brittle faulting. LA-ICP-MS analysis of calcite allows dating material in-situ, with textural context preserved. This can be immensely valuable, as is the case for samples discussed in Chapter 5 that have multiple generations of calcite that are petrographically differentiable. The method is not without challenges, perhaps the greatest of which are finding material with suitable textural context and sufficient isotopic spread of U for determination of common- and radiogenic Pb. Of the 18 calcite samples analyzed via U-Pb LA-ICP-MS in this dissertation, only 5 had sufficient isotopic spread to yield a robust regression age. Some of the successful analyses in Chapter 5 are from samples with up to three generations of calcite identified petrographically, and only one or two of these generations had sufficient U for a useful age determination.

REFERENCES

- Abels, A., and Bischoff, L., 1999, Clockwise block rotations in northern Chile: Indications for a large-scale domino mechanism during the middle-late Eocene: *Geology*, v. 27, p. 751–754, doi:10.1130/0091-7613(1999)027<0751:CBRINC>2.3.CO;2.
- Allmendinger, R.W., Cardozo, N., and Fisher, D.M., 2011, *Structural Geology Algorithms*: Cambridge, Cambridge University Press, v. 9781107012, 1–289 p., doi:10.1017/CBO9780511920202.
- Álvarez, J., Jorquera, R., Miralles, C., Padel, M., and Martínez, P., 2016, *Cartas Punta Posallaves y Sierra Vicuña Mackenna, Región de Antofagasta*. Servicio Nacional de Geología y Minería: Carta Geológica de Chile, Geología Básica (1: 100.000),.
- Anderson, E.M., 1951, *The dynamics of faulting and dyke formation with applications to Britain*: Edinburgh, Oliver and Boyd.
- Angermann, D., Klotz, J., and Reigber, C., 1999, Space-geodetic estimation of the Nazca-South America Euler vector: *Earth and Planetary Science Letters*, v. 171, p. 329–334, doi:https://doi.org/10.1016/S0012-821X(99)00173-9.
- Arabasz, W., 1968, Geologic structure of the Taltal Area, Northern Chile, in relation to the earthquake of December 28, 1966: *Bulletin of the Seismological Society of America*, v. 58, p. 835–842.
- Arabasz, W.J.J., 1971, *Geological and Geophysical studies of the Atacama fault zone in northern Chile*: California Institute of Technology, 264 p.
- Arancibia, G., 2004, Mid-Cretaceous crustal shortening: Evidence from a regional-scale ductile shear zone in the Coastal Range of central Chile (32° S): *Journal of South American Earth*

- Sciences, v. 17, p. 209–226, doi:10.1016/j.jsames.2004.06.001.
- Arévalo, C., 2005, Carta Copiapó, Región de Atacama: Servicio Nacional de Geología y Minería, Carta Geológica de Chile, Serie Geología Básica, v. 91, p. 54.
- Arriagada, C., Roperch, P., Mpodozis, C., and Fernandez, R., 2006, Paleomagnetism and tectonics of the southern Atacama Desert (25–28°S), northern Chile: *Tectonics*, v. 25, p. 1–26, doi:10.1029/2005TC001923.
- Bahlburg, H., Vervoort, J.D., Du Frane, S.A., Bock, B., Augustsson, C., and Reimann, C., 2009, Timing of crust formation and recycling in accretionary orogens: Insights learned from the western margin of South America: *Earth-Science Reviews*, v. 97, p. 215–241, doi:10.1016/j.earscirev.2009.10.006.
- Ballard, S.N., 1990, The Mesozoic structural evolution of the Little Maria Mountains, Riverside County, California: Santa Barbara, University of California:
- Bascuñán, S., Arriagada, C., Le Roux, J., and Deckart, K., 2016, Unraveling the Peruvian Phase of the Central Andes: stratigraphy, sedimentology and geochronology of the Salar de Atacama Basin (22°30–23°S), northern Chile: *Basin Research*, v. 28, p. 365–392, doi:10.1111/bre.12114.
- Beard, S., Haxel, G.B., Dorsey, R.J., McDougall, K.A., and Jacobsen, C.E., 2016, Late Neogene deformation of the Chocolate Mountains Anticlinorium: Implications for deposition of the Bouse Formation and early evolution of the Lower Colorado River, *in* *Going LOCO: Investigations along the Lower Colorado River: California State University Desert Studies Center 2016 Desert Symposium Field Guide and Proceedings*, <http://pubs.er.usgs.gov/publication/70169150>.
- Bell, C.M., 1984, Deformation produced by the subduction of a Palaeozoic turbidite sequence in

- northern Chile: *Journal of the Geological Society*, v. 141, p. 339–347,
doi:10.1144/gsjgs.141.2.0339.
- Bell, C.M., 1982, The Lower Paleozoic metasedimentary basement of the Coastal Ranges of Chile between 25° 30' and 27° S: *Revista geológica de Chile*, p. 21–24.
- Bell, C.M., 1987, The origin of the Upper Palaeozoic Chañaral melange of N Chile: *Journal of the Geological Society*, v. 144, p. 599–610.
- Bennett, S.E.K., Darin, M.H., Dorsey, R.J., Skinner, L.A., Umhoefer, P.J., and Oskin, M.E., 2016, Animated tectonic reconstruction of the Lower Colorado River region: Implications for Late Miocene to Present deformation: <http://pubs.er.usgs.gov/publication/70194032>.
- Bennett, S.E.K., Oskin, M.E., and Iriondo, A., 2017, Latest Miocene transtensional rifting of northeast Isla Tiburón, eastern margin of the Gulf of California: *Tectonophysics*, v. 719–720, doi:10.1016/j.tecto.2017.05.030.
- Beratan, K.K., 1991, Miocene synextension sedimentation patterns, Whipple Mountains, southeastern California: implications for the geometry of the Whipple detachment system: *Journal of Geophysical Research*, v. 96, doi:10.1029/91jb00596.
- Bonson, C.G., 1998, Fracturing, fluid processes and mineralisation in the Cretaceous continental magmatic arc of Northern Chile (25° 15'–27° 15'S): Kingston University.
- Brown, M., Diaz, F., and Grocott, J., 1993, Displacement history of the Atacama fault system 25°00'S–27°00'S, northern Chile: *Geological Society of America Bulletin*, v. 105, doi:10.1130/0016-7606(1993)105<1165:DHOTAF>2.3.CO;2.
- Buising, A. V., 1992, Small-scale late Cenozoic faulting in the Colorado River extensional corridor, western Arizona and southeastern California, *in* Richard, S.M. ed., *Deformation associated with the Neogene Eastern California Shear Zone, southeastern California and*

- southwestern Arizona, Redlands, California, San Bernardino County Museums Special Publication 92-1, p. 11–15.
- Byerlee, J., 1978, Friction of rocks: pure and applied geophysics, v. 116, p. 615–626, doi:10.1007/BF00876528.
- Calais, E., Mazabraud, Y., Mercier de Lépinay, B., Mann, P., Mattioli, G., and Jansma, P., 2002, Strain partitioning and fault slip rates in the northeastern Caribbean from GPS measurements: *Geophysical Research Letters*, v. 29, p. 3–4, doi:10.1029/2002GL015397.
- Cardozo, N., and Allmendinger, R.W., 2013, Spherical projections with OSXStereonet: *Computers and Geosciences*, doi:10.1016/j.cageo.2012.07.021.
- Carr, W.J., 1991, A contribution to the structural history of the Vidal-Parker region, California and Arizona: US Geological Survey Professional Paper, v. 1430, doi:10.3133/pp1430.
- Carter, J.N., Luyendyk, B.P., and Terres, R.R., 1987, Neogene clockwise tectonic rotation of the eastern Transverse Ranges, California, suggested by paleomagnetic vectors: *Bulletin of the Geological Society of America*, doi:10.1130/0016-7606(1987)98<199:NCTROT>2.0.CO;2.
- Cassidy, C.E., Crow, R.S., Cohen, A.S., Beard, L.S., Thacker, J.O., Felger, T.J., Pearthree, P.A., Howard, K.A., and Gootee, B.F., 2017, The subsurface extent of the Bouse Formation in the lower Colorado River corridor and possible tectonic implications, *in* GSA Annual Meeting in Seattle, Washington, USA-2017, GSA.
- Cembrano, J., González, G., Arancibia, G., Ahumada, I., Olivares, V., and Herrera, V., 2005, Fault zone development and strain partitioning in an extensional strike-slip duplex: A case study from the Mesozoic Atacama fault system, Northern Chile: *Tectonophysics*, v. 400, p. 105–125, doi:10.1016/j.tecto.2005.02.012.
- Cembrano, J., Hervé, F., and Lavenue, A., 1996, The Liquiñe Ofqui fault zone: A long-lived intra-

- arc fault system in southern Chile: *Tectonophysics*, v. 259, doi:10.1016/0040-1951(95)00066-6.
- Charrier, R., Pinto, L., and Rodríguez, M.P., 2007, Tectonostratigraphic evolution of the Andean Orogen in Chile, *in* *The geology of Chile*, doi:10.1144/GOCH.3.
- Clark, R.M., and Cox, S.J.D., 1996, A modern regression approach to determining fault displacement-length scaling relationships: *Journal of Structural Geology*, v. 18, p. 147–152, doi:[https://doi.org/10.1016/S0191-8141\(96\)80040-X](https://doi.org/10.1016/S0191-8141(96)80040-X).
- Coira, B., Davidson, J., Mpodozis, C., and Ramos, V., 1982, Tectonic and magmatic evolution of the Andes of northern Argentina and Chile: *Earth Science Reviews*, v. 18, p. 303–332, doi:10.1016/0012-8252(82)90042-3.
- Contreras, J.P., 2018, Segmentación de patrones de rotación tectónica delimitados por la falla Taltal: Cordillera de la Costa del Norte de Chile (25°-26° Latitud Sur): Universidad de Chile, <http://repositorio.uchile.cl/handle/2250/159307>.
- Contreras, J.P., Espinoza, M., De la Cruz, R., Jorquera, R., Kraus, S., Ramírez, C., Naranjo, J.A., Escribano, J., and Martínez, P., 2013, Carta Cifuncho, Regiones de Antofagasta y Atacama. Servicio Nacional de Geología y Minería: Carta Geológica de Chile, Serie Geología Básica, v. 161, p. 0–100.
- Cortés Aranda, J., 2012, Activité des failles de la plaque supérieure dans l'avant-arc côtier du nord du Chili (~23°30'S) : paléosismologie, implications néotectoniques et relation avec le cycle de subduction: 1 vol. (279-[32] p.) p., <http://www.theses.fr/2012TOU30284/document>.
- Coutts, D.S., Matthews, W.A., and Hubbard, S.M., 2019, Assessment of widely used methods to derive depositional ages from detrital zircon populations: *Geoscience Frontiers*, v. 10,

doi:10.1016/j.gsf.2018.11.002.

- Cox, S.F., 2005, Coupling between Deformation, Fluid Pressures, and Fluid Flow in Ore-Producing Hydrothermal Systems at Depth in the Crust (J. W. Hedenquist, J. F. H. Thompson, R. J. Goldfarb, & J. P. Richards, Eds.): One Hundredth Anniversary Volume, p. 0, doi:10.5382/AV100.04.
- Crow, R.S. et al., 2019, Insights into post-Miocene uplift of the western margin of the Colorado plateau from the stratigraphic record of the lower Colorado river: *Geosphere*, v. 15, p. 1826–1845, doi:10.1130/GES02020.1.
- Crowl, W.J., 1979, Geology of the central Dome Rock Mountains, Yuma County, Arizona:, https://repository.arizona.edu/bitstream/10150/555159/1/AZU_TD_BOX290_E9791_1979_5.pdf.
- Curren, I.S., and Bird, P., 2014, Formation and Suppression of Strike–Slip Fault Systems: Pure and Applied Geophysics, v. 171, p. 2899–2918, doi:10.1007/s00024-014-0826-7.
- Dallmeyer, D., Brown, M., Grocott, J., Taylor, G.K., and Treloar, P., 1996, Mesozoic magmatic and tectonic events within the Andean plate boundary zone, north Chile: *Journal of Geology*, v. 104, p. 19–40.
- Dembosky, J.A., and Anderson, T.H., 2005, A reconstruction of late Miocene to Recent transtension in the southwestern United States and northwesternmost Mexico: Special Paper of the Geological Society of America, doi:10.1130/0-8137-2393-0.523.
- DeMets, C., and Merkouriev, S., 2016, High-resolution reconstructions of Pacific-North America plate motion: 20 Ma to present: *Geophysical Journal International*, v. 207, doi:10.1093/gji/ggw305.
- Doblas, M., 1998, Slickenside kinematic indicators: *Tectonophysics*, doi:10.1016/S0040-

1951(98)00120-6.

- Dokka, R.K., and Travis, C.J., 1990a, Late Cenozoic strike-slip faulting in the Mojave Desert, California: *Tectonics*, v. 9, p. 311–340, doi:<https://doi.org/10.1029/TC009i002p00311>.
- Dokka, R.K., and Travis, C.J., 1990b, Role of the Eastern California Shear Zone in accommodating Pacific-North American Plate motion: *Geophysical Research Letters*, v. 17, doi:[10.1029/GL017i009p01323](https://doi.org/10.1029/GL017i009p01323).
- Dorsey, R.J., O’Connell, B., Gardner, K.K., Homan, M.B., Bennett, S.E.K., Thacker, J.O., and Darin, M.H., 2021, Tectonostratigraphic record of late Miocene–early Pliocene transtensional faulting in the Eastern California shear zone, southwestern USA: *Geosphere* (Boulder, Colo.), doi:[10.1130/GES02337.1](https://doi.org/10.1130/GES02337.1).
- Dorsey, R.J., O’Connell, B., Homan, M.B., and Bennett, S.E.K., 2017, Influence of the Eastern California Shear Zone on deposition of the Mio-Pliocene Bouse Formation: Insights from the Cibola area, Arizona., <http://pubs.er.usgs.gov/publication/70194036>.
- Ellis, M.J., 1981, Structural analysis and regional significance of complex deformational events in the Big Maria Mountains, Riverside County, California:
- Emerson, W.S., 1981, Geological and deformational characteristics of the Little Maria Mountains, Riverside County, California:
- Escribano, J., Martínez, P., Domagala, J., Padel, M., Espinoza, M., Jorquera, R., Contreras, J., De la Cruz, R., and Calderón, M., 2013, Cartas Bahía Isla Blanca y Taltal, Región de Antofagasta. Servicio Nacional de Geología y Minería: Carta Geológica de Chile, Serie Geología Básica, p. 164–165.
- Espinoza, M., Contreras, J.P., Jorquera, R., De La Cruz, R., Kraus, S., and Ramírez, C., 2014, Carta Cerro del Pingo, Regiones de Antofagasta y Atacama: Servicio Nacional de Geología

- y Minería, Carta Geológica de Chile, Serie Geología Básica 169, 1 mapa escala 1:100.000. Santiago, p. 109.
- Fackler-Adams, B.N., Busby, C.J., and Mattinson, J.M., 1997, Jurassic magmatism and sedimentation in the Palen Mountains, southeastern California: Implications for regional tectonic controls on the Mesozoic continental arc: *Bulletin of the Geological Society of America*, v. 109, doi:10.1130/0016-7606(1997)109<1464:JMASIT>2.3.CO;2.
- Fossen, H., 2010, *Structural geology*: Cambridge, Cambridge University Press.
- Foster, D.A., and John, B.E., 1999, Quantifying tectonic exhumation in an extensional orogen with thermochronology: examples from the southern Basin and Range Province: *Geological Society Special Publication*, v. 154, doi:10.1144/GSL.SP.1999.154.01.16.
- Fuentes, P., Díaz-Alvarado, J., Fernández, C., Díaz-Azpiroz, M., and Rodríguez, N., 2016, Structural analysis and shape-preferred orientation determination of the mélangé facies in the Chañaral mélangé, Las Tórtolas Formation, Coastal Cordillera, northern Chile: *Journal of South American Earth Sciences*, v. 67, p. 40–56, doi:10.1016/j.jsames.2016.02.001.
- Fuentes, P., Díaz-Alvarado, J., Rodríguez, N., Fernández, C., Breikreuz, C., and Contreras, A.A., 2017, Geochemistry, petrogenesis and tectonic significance of the volcanic rocks of the Las Tortolas Formation, Coastal Cordillera, northern Chile: *Journal of South American Earth Sciences*, doi:10.1016/j.jsames.2017.11.006.
- Fugro Inc., 1975, Sundesert Nuclear Plant Units 1 & 2 Early Site Review Report, v. 2, sec. 2.5—Geology and Seismology.:
- Garfunkel, Z., 1989, Regional Deformation by Block Translation and Rotation, *in* *Paleomagnetic Rotations and Continental Deformation*, doi:10.1007/978-94-009-0869-7_13.
- Godoy, E., and Lara, L., 1999, Hoja Puerto Flamenco, Región de Atacama: Servicio nacional de

geología y minería.

Godoy, E., and Lara, L., 1998, Hojas Chañaral y Diego de Almagro, Región de Atacama:

Servicio nacional de geología y minería.

Godoy, E., Marquardt, C., and Blanco, N., 2003, Carta Caldera, Región de Atacama: Servicio

Nacional de Geología y Minería, Carta Geológica de Chile, Serie Geología Básica, v. 76, p. 38.

Gootee, B.F., Pearthree, P.A., House, P.K., Youberg, A., Spencer, J.E., and O'Connell, B., 2016,

Geologic Map and report of the Cibola Area, La Paz County, Arizona, and Imperial County, California.; https://repository.arizona.edu/bitstream/10150/630735/1/cibola_dgm-112_layout_final.pdf.

Grocott, J., Brown, M., Dallmeyer, R.D., Taylor, G.K., and Treloar, P.J., 1994, Mechanisms of

continental growth in extensional arcs: An example from the Andean plate-boundary zone: *Geology*, v. 22, p. 391–394, doi:10.1130/0091-7613(1994)022<0391:MOCGIE>2.3.CO;2.

Grocott, J., and Taylor, G.K., 2002, Magmatic arc fault systems, deformation partitioning and

emplacement of granitic complexes in the Coastal Cordillera, north Chilean Andes (25°30'S to 27°00'S): *Journal of the Geological Society*, v. 159, p. 425–443, doi:10.1144/0016-764901-124.

Groome, W.G., Johnson, S.E., and Koons, P.O., 2006, The effects of porphyroblast growth on

the effective viscosity of metapelitic rocks: Implications for the strength of the middle crust: *Journal of Metamorphic Geology*, v. 24, doi:10.1111/j.1525-1314.2006.00644.x.

Guest, B., Niemi, N., and Wernicke, B., 2007, Stateline fault system: A new component of the

Miocene-Quaternary Eastern California shear zone: *Bulletin of the Geological Society of America*, doi:10.1130/0016-7606(2007)119[1337:SFSANC]2.0.CO.

- Guynn, J., and Gehrels, G., 2010, Comparison of Detrital Zircon Age Distributions Using the K-S Test: Manual, p. 1–16.
- Hamilton, W.B., 1984, Generalized geologic map of the Big Maria Mountains region, northeastern Riverside County, southeastern California:, doi:10.3133/ofr84407.
- Hamilton, W.B., 1964, Geologic map of the Big Maria Mountains NE quadrangle, Riverside County, California, and Yuma County, Arizona:, doi:10.3133/gq350.
- Hamilton, W.B., 1982, Mesozoic-Cenozoic Tectonic Evolution of the Colorado River Region, California, Arizona and Nevada:
- Hamilton, W., 1981, Preliminary geologic map of the Big Maria Mountains Southeastern California: Unpublished mapping, scale 1:24,000, 1 sheet, 12p text.
- Hamilton, W., and Myers, W.B., 1966, Cenozoic tectonics of the western United States: Reviews of Geophysics, v. 4, doi:10.1029/RG004i004p00509.
- Haschke, M.R., Scheuber, E., Günther, A., and Reutter, K.-J., 2002, Evolutionary cycles during the Andean orogeny: repeated slab breakoff and flat subduction? Terra Nova, v. 14, p. 49–55, doi:10.1046/j.1365-3121.2002.00387.x.
- Haugerud, R., 2020, Planar Orientation Tools: an ArcMap toolbox for working with planar orientations in GeMS:, <https://github.com/rhaugerud/PlanarOrientationsTools>.
- Herve, M., 1987, Movimiento normal de la Falla Paposo, Zona de Falla Atacama, en el Mioceno, Chile: Andean Geology, v. 0, p. 31–36, doi:10.5027/andgeov14n2-a04.
- Hill, C.A., Polyak, V.J., Asmerom, Y., and P. Provencio, P., 2016, Constraints on a Late Cretaceous uplift, denudation, and incision of the Grand Canyon region, southwestern Colorado Plateau, USA, from U-Pb dating of lacustrine limestone: Tectonics, v. 35, p. 896–906, doi:10.1002/2016TC004166.

- Holdsworth, R.E., Butler, C.A., and Roberts, A.M., 1997, The recognition of reactivation during continental deformation: *Journal of the Geological Society*, v. 154, p. 73–78, doi:10.1144/gsjgs.154.1.0073.
- Howard, K.A., House, P.K., Dorsey, R.J., and Pearthree, P.A., 2015, River-evolution and tectonic implications of a major Pliocene aggradation on the lower Colorado river: The bullhead alluvium: *Geosphere*, doi:10.1130/GES01059.1.
- Jaimes, E., and de Freitas, M., 2006, An Albian-Cenomanian unconformity in the northern Andes: Evidence and tectonic significance: *Journal of South American Earth Sciences*, v. 21, doi:10.1016/j.jsames.2006.07.011.
- Jara, J.J., Barra, F., Reich, M., Leisen, M., Romero, R., and Morata, D., 2021a, Episodic construction of the early Andean Cordillera unravelled by zircon petrochronology: *Nature Communications*, v. 12, p. 4930, doi:10.1038/s41467-021-25232-z.
- Jara, J.J., Barra, F., Reich, M., Morata, D., Leisen, M., and Romero, R., 2021b, Geochronology and petrogenesis of intrusive rocks in the Coastal Cordillera of northern Chile: Insights from zircon U-Pb dating and trace element geochemistry: *Gondwana Research*, v. 93, p. 48–72, doi:https://doi.org/10.1016/j.gr.2021.01.007.
- Jensen, E., Cembrano, J., Faulkner, D., Veloso, E., and Arancibia, G., 2011, Development of a self-similar strike-slip duplex system in the Atacama Fault system, Chile: *Journal of Structural Geology*, v. 33, p. 1611–1626, doi:10.1016/j.jsg.2011.09.002.
- Jochum, K.P. et al., 2011, Determination of reference values for NIST SRM 610-617 glasses following ISO guidelines: *Geostandards and Geoanalytical Research*, v. 35, doi:10.1111/j.1751-908X.2011.00120.x.
- Johnson, S.Y., Blakely, R.J., Stephenson, W.J., Dadisman, S. V., and Fisher, M.A., 2004, Active

- shortening of the Cascadia forearc and implications for seismic hazards of the Puget Lowland: *Tectonics*, doi:10.1029/2003TC001507.
- Johnson, B.J., Ferguson, C.A., Pearthree, P.A., and Richardson, C.A., 2021, Geologic map of the Cunningham Mountain Quadrangle, La Paz County, Arizona:, https://repository.arizona.edu/bitstream/10150/656726/12/DGM-135_CunninghamMtn.pdf.
- Kim, Y.-S., and Sanderson, D.J., 2005, The relationship between displacement and length of faults: a review: *Earth-Science Reviews*, v. 68, p. 317–334, doi:<https://doi.org/10.1016/j.earscirev.2004.06.003>.
- Kociánová, L., and Melichar, R., 2016, OATools: An ArcMap add-in for the orientation analysis of geological structures: *Computers and Geosciences*, v. 87, doi:10.1016/j.cageo.2015.12.005.
- Kurth, D., 2000, Die nordchilenische Küstenkordillere bei Taltal: Scherzonen und Forearc-Sliver im jurassischen und unterkretazischen magmatischen Bogen: Freie Universität Berlin, Universitätsbibliothek.
- Kylander-Clark, A.R.C., Hacker, B.R., and Cottle, J.M., 2013, Laser-ablation split-stream ICP petrochronology: *Chemical Geology*, v. 345, p. 99–112, doi:<https://doi.org/10.1016/j.chemgeo.2013.02.019>.
- Lallemant, H.G.A., and Oldow, J.S., 2000, Active displacement partitioning and arc-parallel extension of the Aleutian volcanic arc based on Global Positioning System geodesy and kinematic analysis: *Geology*, v. 28, p. 739–742, doi:10.1130/0091-7613(2000)28<739:ADPAAE>2.0.CO;2.
- Langenheim, V.E., Beard, L.S., and Faulds, J.E., 2010a, Implications of geophysical analysis on basin geometry and fault offsets in the northern Colorado River extensional corridor and

- adjoining Lake Mead region, Nevada and Arizona: Special Paper of the Geological Society of America, doi:10.1130/2010.2463(03).
- Langenheim, V., Graymer, R., Jachens, R., McLaughlin, R., Wagner, D., and Sweetkind, D., 2010b, Geophysical framework of the northern San Francisco Bay region, California (V. Langenheim, Ed.): *Geosphere*, v. 6, p. 594–620, doi:10.1130/GES00510.1.
- Langenheim, V., and Miller, D.M., 2017, Connecting the Soda–Avawatz and Bristol–Granite Mountains faults with gravity and aeromagnetic data, Mojave Desert, California; <http://pubs.er.usgs.gov/publication/70192105>.
- Lara, L., and Godoy, E., 1998, Hoja Quebrada Salitrosa, Región de Atacama: Servicio nacional de geología y minería.
- Law, R.D., 2014, Deformation thermometry based on quartz c-axis fabrics and recrystallization microstructures: A review: *Journal of Structural Geology*, v. 66, doi:10.1016/j.jsg.2014.05.023.
- Lettis, W.R., and Hanson, K.L., 1991, Crustal strain partitioning: Implications for seismic-hazard assessment in western California: *Geology*, v. 19, p. 559–562, doi:10.1130/0091-7613(1991)019<0559:CSPIFS>2.3.CO;2.
- Liu, M., Wang, H., and Li, Q., 2010, Inception of the eastern California shear zone and evolution of the Pacific–North American plate boundary: From kinematics to geodynamics: *Journal of Geophysical Research*, v. 115, doi:10.1029/2009jb007055.
- Loveless, J.P., Allmendinger, R.W., Pritchard, M.E., Garroway, J.L., and González, G., 2009, Surface cracks record long-term seismic segmentation of the Andean margin: *Geology*, v. 37, p. 23–26, doi:10.1130/G25170A.1.
- Loveless, J.P., Hoke, G.D., Allmendinger, R.W., González, G., Isacks, B.L., and Carrizo, D.A.,

- 2005, Pervasive cracking of the northern Chilean Coastal Cordillera: New evidence for forearc extension: *Geology*, v. 33, doi:10.1130/G22004.1.
- Ludwig, K.R., 2003, User's Manual for Isoplot 3.00 : a Geochronological Toolkit for Microsoft Excel:, <http://books.google.com/books?id=OutNAQAAIAAJ>.
- Ma, X., Wang, G., Hu, D., Liu, Y., Zhou, H., and Liu, F., 2020, Mechanical properties of granite under real-time high temperature and three-dimensional stress: *International Journal of Rock Mechanics and Mining Sciences*, v. 136, doi:10.1016/j.ijrmms.2020.104521.
- Mahan, K.H., Guest, B., Wernicke, B., and Niemi, N.A., 2009, Low-temperature thermochronologic constraints on the kinematic history and spatial extent of the Eastern California shear zone: *Geosphere*, doi:10.1130/GES00226.1.
- Marrett, R., and Allmendinger, R.W., 1992, Amount of extension on “small” faults: an example from the Viking graben”: *Geology*, v. 20, p. 47–50, doi:10.1130/0091-7613(1992)020<0047:AOEOSF>2.3.CO;2.
- Marrett, R., and Allmendinger, R.W., 1990, Kinematic analysis of fault-slip data: *Journal of Structural Geology*, v. 12, p. 973–986, doi:10.1016/0191-8141(90)90093-E.
- Marsh, J.H., and Stockli, D.F., 2015, Zircon U–Pb and trace element zoning characteristics in an anatectic granulite domain: Insights from LASS-ICP-MS depth profiling: *Lithos*, v. 239, p. 170–185, doi:<https://doi.org/10.1016/j.lithos.2015.10.017>.
- Martin, D., Krummenacher, D., and Frost, E., 1982, K/Ar geochronologic record of Mesozoic and Tertiary tectonics of the Big Maria- Little Maria-Riverside mountains terrane, *in* Mesozoic-Cenozoic tectonic evolution of the Colorado River region, California, Arizona, and Nevada,.
- Mason, A.J., Henderson, G.M., and Vaks, A., 2013, An Acetic Acid-Based Extraction Protocol

- for the Recovery of U, Th and Pb from Calcium Carbonates for U-(Th)-Pb Geochronology: *Geostandards and Geoanalytical Research*, v. 37, p. 261–275, doi:10.1111/j.1751-908X.2013.00219.x.
- Mason, C.C., Spotila, J.A., Axen, G., Dorsey, R.J., Luther, A., and Stockli, D.F., 2017, Two-Phase Exhumation of the Santa Rosa Mountains: Low- and High-Angle Normal Faulting During Initiation and Evolution of the Southern San Andreas Fault System: *Tectonics*, v. 36, doi:10.1002/2017TC004498.
- Matthews, K.J., Maloney, K.T., Zahirovic, S., Williams, S.E., Seton, M., and Müller, R.D., 2016, Global plate boundary evolution and kinematics since the late Paleozoic: *Global and Planetary Change*, v. 146, doi:10.1016/j.gloplacha.2016.10.002.
- Matthews, K.J., Seton, M., and Müller, R.D., 2012, A global-scale plate reorganization event at 105–100Ma: *Earth and Planetary Science Letters*, v. 355–356, p. 283–298, doi:https://doi.org/10.1016/j.epsl.2012.08.023.
- Mavor, S.P., Singleton, J.S., Gomila, R., Heuser, G., Seymour, N.M., Williams, S.A., Arancibia, G., Johnston, S.M., Kylander-Clark, A.R.C., and Stockli, D.F., 2020, Timing, Kinematics, and Displacement of the Taltal Fault System, Northern Chile: Implications for the Cretaceous Tectonic Evolution of the Andean Margin: *Tectonics*, doi:10.1029/2019TC005832.
- McCaffrey, R., Zwick, P.C., Bock, Y., Prawirodirdjo, L., Genrich, J.F., Stevens, C.W., Puntodewo, S.S.O., and Subarya, C., 2000, Strain partitioning during oblique plate convergence in northern Sumatra: Geodetic and seismologic constraints and numerical modeling: *Journal of Geophysical Research: Solid Earth*, v. 105, p. 28363–28376, doi:10.1029/1999JB900362.

- McQuarrie, N., and Wernicke, B.P., 2005, An animated tectonic reconstruction of southwestern north america since 36 Ma: *Geosphere*, doi:10.1130/GES00016.1.
- Miller, D.M., 2017, The late Cenozoic Eastern California Shear Zone after 25 years of study, *in* ECSZ Does It: Revisiting the Eastern California Shear Zone: California State University Desert Studies Center 2017 Desert Symposium Field Guide and Proceedings, p. 45–54.
- Miller, D.M., and Howard, K.A., 1985, Geologic map of the Iron Mountains Quadrangle, San Bernardino and Riverside counties, California:, doi:10.3133/mf1736.
- Miller, M.M., Johnson, D.J., Dixon, T.H., and Dokka, R.K., 2001, Refined kinematics of the Eastern California shear zone from GPS observations, 1993-1998: *Journal of Geophysical Research: Solid Earth*, v. 106, doi:10.1029/2000jb900328.
- Moore, J.C., 1978, Orientation of underthrusting during latest Cretaceous and earliest Tertiary time, Kodiak Islands, Alaska: *Geology*, v. 6, p. 209–213, doi:10.1130/0091-7613(1978)6<209:OOUDLC>2.0.CO;2.
- Mpodosis, C., and Allmendinger, R.W., 1993, Extensional tectonics, Cretaceous Andes, northern Chile (27°S): *GSA Bulletin*, v. 105, p. 1462–1477, doi:10.1130/0016-7606(1993)105<1462:ETCANC>2.3.CO;2.
- Mpodosis, C., Arriagada, C., Basso, M., Roperch, P., Cobbold, P., and Reich, M., 2005, Late Mesozoic to Paleogene stratigraphy of the Salar de Atacama Basin, Antofagasta, Northern Chile: Implications for the tectonic evolution of the Central Andes: *Tectonophysics*, v. 399, doi:10.1016/j.tecto.2004.12.019.
- Naranjo, J.A., and Puig, A., 1984, Hojas Taltal y Chanaral, *Cartas geológicas de Chile*; 1: 250 000: Serv. Nac. Geol. Min. Chile, p. 62–63.
- Nur, A., Ron, H., and Scotti, O., 1986, Fault mechanics and the kinematics of block rotations:

- Geology, v. 14, p. 746–749, doi:10.1130/0091-7613(1986)14<746:FMATKO>2.0.CO;2.
- Nuriel, P., Miller, D.M., Schmidt, K.M., Coble, M.A., and Maher, K., 2019, Ten-million years of activity within the Eastern California Shear Zone from U–Pb dating of fault-zone opal: Earth and Planetary Science Letters, doi:10.1016/j.epsl.2019.05.047.
- Nuriel, P., Weinberger, R., Kylander-Clark, A.R.C., Hacker, B.R., and Craddock, J.P., 2017, The onset of the Dead Sea transform based on calcite age-strain analyses: Geology, v. 45, p. 587–590, doi:10.1130/G38903.1.
- Oliveros, V. et al., 2020, Lithospheric evolution of the Pre- and Early Andean convergent margin, Chile: Gondwana Research, v. 80, doi:10.1016/j.gr.2019.11.002.
- Oliveros, V., Féraud, G., Aguirre, L., Fornari, M., and Morata, D., 2006, The Early Andean Magmatic Province (EAMP): $^{40}\text{Ar}/^{39}\text{Ar}$ dating on Mesozoic volcanic and plutonic rocks from the Coastal Cordillera, northern Chile: Journal of Volcanology and Geothermal Research, v. 157, p. 311–330.
- Oliveros, V., Morata, D., Féraud, G., and Fornari, M., 2007, Jurassic to Early Cretaceous subduction-related magmatism in the Coastal Cordillera of northern Chile ($18^{\circ} 30' -24^{\circ} \text{S}$): geochemistry and petrogenesis: Revista geológica de Chile, v. 34, p. 1–24, doi:10.4067/S0716-02082007000200003.
- Oskin, M., Stock, J., and Martín-Barajas, A., 2001, Rapid localization of Pacific–North America plate motion in the Gulf of California: Geology, v. 29, p. 459–462, doi:10.1130/0091-7613(2001)029<0459:RLOPNA>2.0.CO;2.
- Parada, M.A. et al., 2007, Andean magmatism, in Moreno, T. and Gibbons, W. eds., The Geology of Chile, Geological Society of London, p. 115–146, doi:10.1144/GOCH.4.
- Passchier, C.W., and Trouw, R.A.J., 2005, Microtectonics: Springer Berlin Heidelberg, 1–366 p.,

doi:10.1007/3-540-29359-0.

Paterson, S.R., Vernon, R.H., and Tobisch, O.T., 1989, A review of criteria for the identification of magmatic and tectonic foliations in granitoids: *Journal of Structural Geology*, v. 11, doi:10.1016/0191-8141(89)90074-6.

Pattison, D.R.M., and Spear, F.S., 2018, Kinetic control of staurolite–Al₂SiO₅ mineral assemblages: Implications for Barrovian and Buchan metamorphism: *Journal of Metamorphic Geology*, v. 36, doi:10.1111/jmg.12302.

Pavlis, T.L., and Trullenque, G., 2021, Evidence for 40–41 km of dextral slip on the southern Death Valley fault: Implications for the Eastern California shear zone and extensional tectonics: *Geology*, v. 49, doi:10.1130/g48528.1.

Petit, J.P., 1987, Criteria for the sense of movement on fault surfaces in brittle rocks: *Journal of Structural Geology*, v. 9, p. 597–608, doi:[https://doi.org/10.1016/0191-8141\(87\)90145-3](https://doi.org/10.1016/0191-8141(87)90145-3).

Philippon, M., and Corti, G., 2016, Obliquity along plate boundaries: *Tectonophysics*, doi:10.1016/j.tecto.2016.05.033.

Powell, R.E., 1981, Geology of the crystalline basement complex, eastern Transverse Ranges, southern California : constraints on regional tectonic interpretation:, doi:10.7907/F22F-YX04.

Prinz, P., Wilke, H.-G., and von Hillebrandt, A., 1994, Sediment Accumulation and Subsidence History in the Mesozoic Marginal Basin of Northern Chile, *in* Reutter, K.-J., Scheuber, E., and Wigger, P.J. eds., *Tectonics of the Southern Central Andes*, Berlin, Heidelberg, Springer Berlin Heidelberg, p. 219–232, doi:10.1007/978-3-642-77353-2_15.

Randall, D.E., Taylor, G.K., and Grocott, J., 1996, Major crustal rotations in the Andean margin: Paleomagnetic results from the Coastal Cordillera of northern Chile: *Journal of Geophysical*

- Research: Solid Earth, v. 101, p. 15783–15798, doi:10.1029/96JB00817.
- Reheis, M.C., and Sawyer, T.L., 1997, Late Cenozoic history and slip rates of the Fish Lake Valley, Emigrant Peak, and Deep Springs fault zones, Nevada and California: GSA Bulletin, v. 109, p. 280–299, doi:10.1130/0016-7606(1997)109<0280:LCHASR>2.3.CO;2.
- Reiners, P.W., Farley, K.A., and Hickey, H.J., 2002, He diffusion and (U–Th)/He thermochronometry of zircon: initial results from Fish Canyon Tuff and Gold Butte: Tectonophysics, v. 349, p. 297–308, doi:https://doi.org/10.1016/S0040-1951(02)00058-6.
- Reiners, P.W., Spell, T.L., Nicolescu, S., and Zanetti, K.A., 2004, Zircon (U–Th)/He thermochronometry: He diffusion and comparisons with $^{40}\text{Ar}/^{39}\text{Ar}$ dating: Geochimica et Cosmochimica Acta, v. 68, p. 1857–1887, doi:https://doi.org/10.1016/j.gca.2003.10.021.
- del Rey, A., Deckart, K., Arriagada, C., and Martínez, F., 2016, Resolving the paradigm of the late Paleozoic–Triassic Chilean magmatism: Isotopic approach: Gondwana Research, v. 37, p. 172–181, doi:https://doi.org/10.1016/j.gr.2016.06.008.
- Reynolds, S.J., Spencer, J.E., Richard, S.M., and Laubach, S.E., 1986, Mesozoic structures in west-central Arizona: Frontiers in geology and ore deposits of Arizona and the Southwest: Arizona Geological Society Digest, v. 16, p. 35–51.
- Richard, S.M., 1993, Palinspastic reconstruction of southeastern California and southwestern Arizona for the Middle Miocene: Tectonics, v. 12, p. 830–854, doi:10.1029/92TC02951.
- Richard, S.M., and Dokka, R.K., 1992, Geology of the Packard Well fault zone, southeastern California, *in* Richard, S.M. ed., Richard, S.M., ed., Deformation associated with the Neogene, eastern California shear zone, southeastern California and southwestern Arizona, Redlands, California, San Bernardino County Museums Special Publication 92-1, p. 71–74.
- Richard, S.M., Sherrod, D.R., and Tosdal, R.M., 1992, Cibola Pass fault, southwestern Arizona,

- in* Deformation associated with the Neogene, eastern California shear zone, southeastern California and southwestern Arizona, Redlands, California, San Bernardino County Museums Special Publication 92-1, p. 66–70.
- Roberts, N.M.W., Rasbury, E.T., Parrish, R.R., Smith, C.J., Horstwood, M.S.A., and Condon, D.J., 2017, A calcite reference material for LA-ICP-MS U-Pb geochronology: *Geochemistry, Geophysics, Geosystems*, v. 18, p. 2807–2814, doi:10.1002/2016GC006784.
- Rodríguez, N., Díaz-Alvarado, J., Fernández, C., Breikreuz, C., Fuentes, P., and Merida, G., 2021, Relation between intrusive and deformational processes in oblique subductive margins. The case of the zoned Flamenco pluton in northern Chile: *Journal of South American Earth Sciences*, v. 112, doi:10.1016/j.jsames.2021.103553.
- Rotstein, Y., Combs, J., and Biehler, S., 1976, Gravity investigation in the southeastern Mojave Desert, California: *Bulletin of the Geological Society of America*, doi:10.1130/0016-7606(1976)87<981:GIITSM>2.0.CO;2.
- Ruthven, R., Singleton, J., Seymour, N., Gomila, R., Arancibia, G., Stockli, D.F., Ridley, J., and Magloughlin, J., 2020, The geometry, kinematics, and timing of deformation along the southern segment of the Paposo fault zone, Atacama fault system, northern Chile: *Journal of South American Earth Sciences*, doi:10.1016/j.jsames.2019.102355.
- Saldías, J., 2015, Origen de la fábrica magnética del plutón granodiorita Cerro del Pingo (25°40'S - 70°15'O): Implicancias en relación a su mecanismo de emplazamiento: Universidad de Chile, 92 p.
- Salem, A.C., 2009, Mesozoic tectonics of the Maria Fold and Thrust Belt and McCoy Basin, southeastern California: An examination of polyphase deformation and synorogenic response:

- Salfity, J., 1985, Lineamientos transversales al rumbo andino en el noroeste argentino, *in* IV Congreso Geologico Chileno, v. 2, p. 119–137.
- Saltus, R.W., and Jachens, R.C., 1995, Gravity and basin-depth maps of the Basin and Range Province, Western United States:, doi:10.3133/gp1012.
- Sanderson, D.J., and Marchini, W.R.D., 1984, Transpression: *Journal of Structural Geology*, v. 6, doi:10.1016/0191-8141(84)90058-0.
- Scheuber, E., and Andriessen, P.A.M., 1990, The kinematic and geodynamic significance of the Atacama fault zone, northern Chile: *Journal of Structural Geology*, v. 12, p. 243–257, doi:10.1016/0191-8141(90)90008-M.
- Scheuber, E., Bogdanic, T., Jensen, A., and Reutter, K.-J., 1994a, Tectonic Development of the North Chilean Andes in Relation to Plate Convergence and Magmatism Since the Jurassic, *in* Reutter, K.-J., Scheuber, E., and Wigger, P.J. eds., *Tectonics of the Southern Central Andes*, Berlin, Heidelberg, Springer Berlin Heidelberg, p. 121–139, doi:10.1007/978-3-642-77353-2_9.
- Scheuber, E., Bogdanic, T., Jensen, A., and Reutter, K.-J., 1994b, Tectonic Development of the North Chilean Andes in Relation to Plate Convergence and Magmatism Since the Jurassic BT - Tectonics of the Southern Central Andes: Structure and Evolution of an Active Continental Margin, *in* Reutter, K.-J., Scheuber, E., and Wigger, P.J. eds., Berlin, Heidelberg, Springer Berlin Heidelberg, p. 121–139, doi:10.1007/978-3-642-77353-2_9.
- Scheuber, E., and Gonzalez, G., 1999, Tectonics of the Jurassic-Early Cretaceous magmatic arc of the north Chilean Coastal Cordillera (22°-26°S): A story of crustal deformation along a convergent plate boundary: *Tectonics*, v. 18, p. 895–910, doi:10.1029/1999TC900024.
- Scheuber, E., Hammerschmidt, K., and Friedrichsen, H., 1995, 40Ar/39Ar and Rb_Sr analyses

- from ductile shear zones from the Atacama Fault Zone, northern Chile: the age of deformation: *Tectonophysics*, v. 250, p. 61–87, doi:10.1016/0040-1951(95)00044-8.
- Scheuber, E., and Reutter, K.J., 1992, Magmatic arc tectonics in the Central Andes between 21° and 25°S: *Tectonophysics*, v. 205, p. 127–140, doi:10.1016/0040-1951(92)90422-3.
- Seiler, C., Fletcher, J.M., Quigley, M.C., Gleadow, A.J.W., and Kohn, B.P., 2010, Neogene structural evolution of the Sierra San Felipe, Baja California: Evidence for proto-gulf transtension in the Gulf Extensional Province? *Tectonophysics*, v. 488, doi:10.1016/j.tecto.2009.09.026.
- Seton, M. et al., 2012, Global continental and ocean basin reconstructions since 200Ma: *Earth-Science Reviews*, v. 113, doi:10.1016/j.earscirev.2012.03.002.
- Seymour, N.M., Singleton, J.S., Gomila, R., Mavor, S.P., Heuser, G., Arancibia, G., Williams, S., and Stockli, D.F., 2021, Magnitude, timing, and rate of slip along the Atacama fault system, northern Chile: implications for Early Cretaceous slip partitioning and plate convergence: *Journal of the Geological Society*, v. 178, p. jgs2020-142, doi:10.1144/jgs2020-142.
- Seymour, N.M., Singleton, J.S., Mavor, S.P., Gomila, R., Stockli, D.F., Heuser, G., and Arancibia, G., 2020, The relationship between magmatism and deformation along the intra-arc strike-slip Atacama fault system, northern Chile: *Tectonics*, doi:10.1029/2019tc005702.
- Seymour, N.M., Stockli, D.F., Beltrando, M., and Smye, A.J., 2016, Tracing the thermal evolution of the Corsican lower crust during Tethyan rifting: *Tectonics*, v. 35, p. 2439–2466, doi:10.1002/2016TC004178.
- Singleton, J.S., 2015, The transition from large-magnitude extension to distributed dextral faulting in the Buckskin-Rawhide metamorphic core complex, west-central Arizona:

- Tectonics, doi:10.1002/2014TC003786.
- Singleton, J.S., and Gans, P.B., 2008, Structural and stratigraphic evolution of the Calico Mountains: Implications for early Miocene extension and Neogene transpression in the central Mojave Desert, California: *Geosphere*, v. 4, doi:10.1130/GES00143.1.
- Singleton, J.S., Seymour, N.M., Reynolds, S.J., Vomocil, T., and Wong, M.S., 2019, Distributed Neogene faulting across the western to central Arizona metamorphic core complex belt: Synextensional constriction and superposition of the Pacific-North America plate boundary on the southern Basin and Range: *Geosphere*, doi:10.1130/GES02036.1.
- Singleton, J.S., Stockli, D.F., Gans, P.B., and Prior, M.G., 2014, Timing, rate, and magnitude of slip on the Buckskin-Rawhide detachment fault, west central Arizona: *Tectonics*, v. 33, doi:10.1002/2013TC003517.
- Spencer, J.E., and Reynolds, S.J., 1989, Tertiary structure, stratigraphy, and tectonics of the Buckskin Mountains, *in* *Geology and mineral resources of the Buckskin and Rawhide Mountains, west-central Arizona: Arizona Geological Survey Bulletin 198*,.
- Stenvall, C.A., Fagereng, Å., and Diener, J.F.A., 2019, Weaker Than Weakest: On the Strength of Shear Zones: *Geophysical Research Letters*, v. 46, doi:10.1029/2019GL083388.
- Stipp, M., Stünitz, H., Heilbronner, R., and Schmid, S.M., 2002, Dynamic recrystallization of quartz: Correlation between natural and experimental conditions: *Geological Society Special Publication*, v. 200, doi:10.1144/GSL.SP.2001.200.01.11.
- Stipp, M., and Tullis, J., 2003, The recrystallized grain size piezometer for quartz: *Geophysical Research Letters*, v. 30, p. n/a-n/a, doi:10.1029/2003GL018444.
- Stockli, D.F., Brichau, S., Dewane, T.J., Hager, C., and Schroeder, J., 2006, Dynamics of large-magnitude extension in the Whipple Mountains metamorphic core complex: *Geochimica et*

- Cosmochimica Acta, v. 70, p. A616, doi:<https://doi.org/10.1016/j.gca.2006.06.1143>.
- Stone, P., 2006, Geologic map of the west half of the Blythe 30' by 60' quadrangle, Riverside County, California and La Paz County, Arizona:
- Stone, P., 1990, Preliminary geologic map of the Blythe 30' by 60' quadrangle, California and Arizona., doi:10.3133/ofr90497.
- Stone, P., and Kelly, M.M., 1989, Geologic map of the Palen Pass Quadrangle, Riverside County, California:, doi:10.3133/mf2070.
- Stone, P., and Pelka, G.J., 1989, Geologic map of the Palen-McCoy Wilderness Study Area and vicinity, Riverside County, California:, doi:10.3133/mf2092.
- Streit, J.E., and Cox, S.F., 2001, Fluid pressures at hypocenters of moderate to large earthquakes: Journal of Geophysical Research: Solid Earth, v. 106, doi:10.1029/2000jb900359.
- Strickland, E.D., Singleton, J.S., Griffin, A.T.B., and Seymour, N.M., 2017, Geologic map of the northern Plomosa Mountains metamorphic core complex, Arizona:
- Strickland, E.D., Singleton, J.S., Wyatt, M.R., and Seymour, N.M., 2018, Post–middle Miocene transtension in the Plomosa Mountains and development of the La Posa Plain, west-central Arizona, *in* Geological Society of America Abstracts with Programs, v. 50.
- Suarez, M., and Bell, C.M., 1992, Triassic rift-related sedimentary basins in northern Chile (24°–29°S): Journal of South American Earth Sciences, v. 6, p. 109–121, doi:10.1016/0895-9811(92)90001-F.
- Sylvester, A.G., 1988, Strike-slip faults: Bulletin of the Geological Society of America, v. 100, doi:10.1130/0016-7606(1988)100<1666:SSF>2.3.CO;2.
- Tankard, A.J. et al., 1995, Structural and Tectonic Controls of Basin Evolution in Southwestern Gondwana During the Phanerozoic, *in* Tankard, A.J., Soruco, R.S., and Welsink, H.J. eds.,

- Petroleum Basins of South America, American Association of Petroleum Geologists, v. AAPG Memoir, p. 0, doi:10.1306/M62593C1.
- Taylor, G.K., Grocott, J., Pope, A., and Randall, D.E., 1998, Mesozoic fault systems, deformation and fault block rotation in the Andean forearc: A crustal scale strike-slip duplex in the Coastal Cordillera of northern Chile: *Tectonophysics*, v. 299, p. 93–109, doi:10.1016/S0040-1951(98)00200-5.
- Taylor, G.K., and Randall, D.E., 2000, Structural analysis of dyke emplacement directions as an aid to palaeomagnetic studies: an example from northern Chile: *Geophysical Journal International*, v. 141, p. 252–258, doi:10.1046/j.1365-246x.2000.00064.x.
- Thacker, J.O., Karlstrom, K.E., Crossey, L.J., Crow, R.S., Beard, L.S., and Dorsey, R.J., 2017, Hypothesis for post-Bouse distributed deformation of the Lower Colorado River corridor, *in* ECSZ Does It: Revisiting the Eastern California Shear Zone: California State University Desert Studies Center 2017 Desert Symposium Field Guide and Proceedings, p. 158–164.
- Thacker, J.O., Karlstrom, K.E., Crossey, L.J., Crow, R.S., Cassidy, C.E., Beard, L.S., Singleton, J.S., Strickland, E.D., Seymour, N.M., and Wyatt, M.R., 2020, Post–12 Ma deformation in the lower Colorado River corridor, southwestern USA: Implications for diffuse transtension and the Bouse Formation: *Geosphere*, doi:10.1130/ges02104.1.
- Tornos, F., Velasco, F., Barra, F., and Morata, D., 2010, The Tropezón Cu-Mo-(Au) deposit, Northern Chile: The missing link between IOCG and porphyry copper systems? *Mineralium Deposita*, v. 45, p. 313–321, doi:10.1007/s00126-010-0277-8.
- Tosdal, R.M., 1990, Constraints on the tectonics of the Mule Mountains thrust system, southeast California and southwest Arizona: *Journal of Geophysical Research*, v. 95, doi:10.1029/jb095ib12p20025.

- Ulriksen, C., 1979, Regional geology, geochronology and metallogeny of the Coastal Cordillera of Chile between 25°30' and 26°00' south: Dalhousie University, 221 p . Canadá p.
- Umhoefer, P.J., and Dorsey, R.J., 1997, Translation of terranes: Lessons from central Baja California, Mexico: *Geology*, v. 25, p. 1007–1010, doi:10.1130/0091-7613(1997)025<1007:TOTLFC>2.3.CO;2.
- Umhoefer, P., Mavor, S., Langenheim, V., Beard, L., Bennett, S., Crow, R., Stone, P., and Brickey, T., 2020, Multiple lines of evidence suggest 30-35 km of offset on the Blythe Basin strike-slip faults: part of the missing dextral shear across the Miocene Pacific-North America plate boundary?, doi:10.1130/abs/2020CD-347488.
- Vaks, A., Woodhead, J., Bar-Matthews, M., Ayalon, A., Cliff, R.A., Zilberman, T., Matthews, A., and Frumkin, A., 2013, Pliocene-Pleistocene climate of the northern margin of Saharan-Arabian Desert recorded in speleothems from the Negev Desert, Israel: *Earth and Planetary Science Letters*, doi:10.1016/j.epsl.2013.02.027.
- Veloso, E.E., Gomila, R., Cembrano, J., González, R., Jensen, E., and Arancibia, G., 2015, Stress fields recorded on large-scale strike-slip fault systems: Effects on the tectonic evolution of crustal slivers during oblique subduction: *Tectonophysics*, v. 664, p. 244–255, doi:10.1016/j.tecto.2015.09.022.
- Vermeesch, P., 2018, IsoplotR: A free and open toolbox for geochronology: *Geoscience Frontiers*, v. 9, doi:10.1016/j.gsf.2018.04.001.
- Vermeesch, P., 2021, Maximum depositional age estimation revisited: *Geoscience Frontiers*, doi:10.1016/j.gsf.2020.08.008.
- Vermeesch, P., 2012, On the visualisation of detrital age distributions: *Chemical Geology*, v. 312–313, doi:10.1016/j.chemgeo.2012.04.021.

- Vignerresse, J.L., 2015, Textures and melt-crystal-gas interactions in granites: *Geoscience Frontiers*, v. 6, doi:10.1016/j.gsf.2014.12.004.
- Vivallos, J., and Donoso, C., 2014a, Carta magnética Cerro del Pingo, regiones de Antofagasta y Atacama, Escala 1:100.000.:
- Vivallos, J., and Donoso, C., 2014b, Carta magnética Cifuncho, region de Antofagasta (Carta Geológica de Chile, Serie Geofísica 81) Escala 1:100.000.:
- Vivallos, J., and Donoso, C., 2014c, Cartas magnéticas Bahía Isla Blanca y Taltal, region de Antofagasta, Escala 1:100.000.:
- Vollmer, F.W., 1990, An application of eigenvalue methods to structural domain analysis: *Bulletin of the Geological Society of America*, v. 102, doi:10.1130/0016-7606(1990)102<0786:AAOEMT>2.3.CO;2.
- Wilson, J., Dallmeyer, R.D.R., and Grocott, J., 2000, New $^{40}\text{Ar}/^{39}\text{Ar}$ dates from the Las Tazas complex, northern Chile: Tectonic significance: *Journal of South American Earth Sciences*, v. 13, p. 115–122, doi:[https://doi.org/10.1016/S0895-9811\(00\)00008-0](https://doi.org/10.1016/S0895-9811(00)00008-0).
- Wolfe, M.R., and Stockli, D.F., 2010, Zircon (U–Th)/He thermochronometry in the KTB drill hole, Germany, and its implications for bulk He diffusion kinetics in zircon: *Earth and Planetary Science Letters*, v. 295, p. 69–82, doi:<https://doi.org/10.1016/j.epsl.2010.03.025>.
- Woodcock, N.H., 1986, The role of strike-slip fault systems at plate boundaries.: *Philosophical Transactions - Royal Society of London, Series A*, v. 317, doi:10.1098/rsta.1986.0021.
- Young, A., Flament, N., Maloney, K., Williams, S., Matthews, K., Zahirovic, S., and Müller, R.D., 2019, Global kinematics of tectonic plates and subduction zones since the late Paleozoic Era: *Geoscience Frontiers*, v. 10, doi:10.1016/j.gsf.2018.05.011.

APPENDIX A: FRICTIONAL SLIDING ANALYSIS OF THE ATACAMA AND TALTAL FAULT SYSTEMS

This appendix presents a frictional sliding analysis using the MohrPlotter program (<https://www.rickallmendinger.net/mohrplotter>) to evaluate characteristics of the transition between the Atacama and Taltal fault systems. Figure 9.1 shows a simplified geologic map of the major faults in the study area. The N-S striking eastern (main) branch of the Atacama fault system (AFS) was active with localized ductile deformation until ~119 Ma, with continued brittle deformation until it was crosscut by the NW-striking Taltal fault system between 114–107 Ma (Chapter 2). The El Muelle fault has slightly arcuate geometry that curves from near parallelism with the AFS to near parallelism with the Taltal fault. The age of the El Muelle fault is not tightly constrained, but a ~110 Ma dike that crosscuts the AFS eastern branch is displaced by AFS strands further west, possibly indicating that brittle deformation shifted westwards to the El Muelle fault in the late stages of AFS slip and may have been active during TFS deformation, as the El Muelle fault is not cut by strands of the TFS (Chapter 2). The average principal slip plane of the AFS eastern branch in the area of Figure 9.2 is 352, 88°E. Measurements of the principal slip plane for the El Muelle fault are sparse, but an average of all El Muelle-associated fault measurements is 329, 83°NE, which is reasonable as an estimate of the average fault plane and matches the more northwesterly parts of the fault trace near the town of Taltal. The average principal slip plane of the Taltal fault is oriented 315, 80°NE. Measurements of all faults within the Taltal fault system have an average of 308, 84°NE and are omitted from Mohr diagram plots for clarity.

For the frictional sliding analysis, the following assumptions are made:

- The stress ratio $\phi = 0.5$. This can also be expressed as $\sigma_2 = (\sigma_1 + \sigma_3)/2$. This stress ratio reflects pure strike slip faulting that is neither transpressional nor transtensional. This assumption is justified by kinematic data that suggest that the AFS in this area is nearly pure strike-slip (Seymour et al., 2021). The Taltal fault has a slight component of oblique-normal slip but is close to near pure strike-slip (average slickenline plunge of 11° NW). With the magnitude of σ_2 known, differential stress is increased until critical conditions for Coulomb failure are met.
- An Andersonian strike-slip stress regime where σ_2 is vertical (Anderson, 1951). While the slightly off-vertical dips ($\geq 80^\circ$) of the Atacama and Taltal faults could indicate that this assumption may not be exactly accurate, calculations are significantly simplified when σ_2 is vertical. From this assumption I use the lithostatic stress equation with an assumed overburden density of 2.7 g/cm^3 to determine $\sigma_2 = (2.7 \text{ g/cm}^3)(6 \text{ km})(9.81 \text{ m/s}^2) = 159 \text{ MPa}$.
- Crustal depth = 6 km. Based on hornblende barometry (Dallmeyer et al., 1996; Kurth, 2000) the presently exposed Early Cretaceous plutons are unlikely to have intruded at depths greater than ~6-10 km. A dike that cuts cataclasite of the Atacama fault but is cut by the Taltal fault system has a $106.7 \pm 8.5 \text{ Ma}$ zircon He cooling age; this sample is far from any plutons of similar age that could have perturbed local thermal conditions. The $\sim 180^\circ\text{--}190^\circ\text{C}$ closure temperature of the zircon He system (Reiners et al., 2002, 2004; Wolfe and Stockli, 2010), combined with estimated $\sim 30^\circ\text{C} / \text{km}$ geothermal gradients away from plutons and present across the region by $\sim 100 \text{ Ma}$ (Seymour et al., 2020) indicates that the presently

exposed Taltal fault was at a depth of ~6 km at ~110 Ma. The cooling age reflects either regional cooling as the Cretaceous magmatic arc migrated eastwards of the Taltal fault, or rapid cooling immediately following dike emplacement. No Early Cretaceous ductile deformation is recorded in the immediate area, signifying that depths were never below the BPT.

- Frictional and cohesion values for the Coulomb failure envelope equation: $\sigma_s = (0.6) \sigma_n + 40 \text{ MPa}$. This cohesion value is within the range observed by Ma et al. (2020) for granite samples at variable temperature.
- Fluid density of $\rho = 1 \text{ g/cm}^3$. Hydrostatic pore fluid pressure is calculated using a vertical water column and the assumed depth constraint $p_f = (1 \text{ g/cm}^3)(6 \text{ km})(9.81 \text{ m/s}^2) = 59 \text{ MPa}$.

Mohr circle diagrams are plotted for three dimensions, though this is difficult to resolve on the plots as the fault planes are all very close to parallel with σ_2 . Normal stresses stated for fault planes are corrected for pore fluid pressure and given as effective normal stresses. For the first Mohr circle diagram (Figure 9.1), I use the following assumptions and discuss the effects of varying each of these parameters with subsequent plots:

- Assume that σ_1 is parallel to the trend of the average P-axis (261°) determined from kinematic analysis of Taltal fault system fault slip data, and that the plunge is horizontal, consistent with Andersonian theory of a pure strike-slip regime with vertical σ_2 . σ_3 is likewise horizontal and trends 351° , perpendicular to σ_1 . As discussed above the kinematic approach generates incremental strain axes that do not signify the orientations of the principal stresses. However, comparison of

kinematic strain axes to principal stress axes calculated from stress inversion methods show similar orientations in most cases (Fossen, 2010, p. 197).

- Fluid pressure is hydrostatic.
- The friction coefficient for reactivation of preexisting faults is $\mu \leq 0.85$ (Byerlee, 1978). Assumption of Byerlee friction (0.85) is potentially problematic as the mineral contents and true frictional properties of fault gouge for these faults are unknown and coefficients may be significantly lower than this assumption. Below I discuss the effects of varying this parameter.

The resulting Mohr diagram (Figure 9.2) demonstrates that none of the faults would be reactivated with a Byerlee frictional slip coefficient of 0.85 before new faults are created by Coulomb failure. The system is at the critical threshold for Coulomb failure when the differential stress is 172 MPa. New faults would be created 30° from σ_1 , striking 291° (left-lateral) and 231° (right-lateral) and vertical. This Mohr diagram does not indicate slip on either the Taltal or El Muelle faults, so parameters must be varied from this first approximation to demonstrate conditions favorable for slip on those faults.

REDUCED FRICTION COEFFICIENT

By reducing the coefficient of friction for fault slip reactivation, favorable conditions for slip on major faults is possible. With $\mu = 0.64$ or lower the Taltal fault is favorable for reactivation (Figure 9.3), and the El Muelle fault is favorable for reactivation when $\mu = 0.35$ or lower (Figure 9.4). Both faults have exposures with several meter thicknesses of foliated clayey gouge; it is highly likely that these faults would have lower friction than the Byerlee value of $\mu = 0.85$.

ELEVATED PORE FLUID PRESSURES

Elevated pore fluid pressure could also serve to allow fault slip, and pore fluid pressures above hydrostatic are expected for major strike-slip faults below depths of 3–7 km (Streit and Cox, 2001). With fluid pressure 90% lithostatic (Figure 9.5), the Taltal fault is favorable for reactivation with $\mu = 0.85$, though the El Muelle fault is not. With fluid pressure lithostatic (Figure 9.6) both faults are favorable for reactivation, and the Atacama fault eastern branch is not. Differential stresses are increased for Figures 9.5 and 9.6 until reaching critical conditions for the Griffith envelope, and failure would create vertical joints striking 261° (perpendicular to σ_3).

ORIENTATION OF THE PRINCIPAL STRESS AXES

If σ_1 is a more northwesterly direction the stresses resolved on fault planes are favorable for fault slip when the differential stress is increased to critical Coulomb failure. With σ_1 oriented 306° and horizontal, the Taltal fault and the El Muelle fault are favorable for reactivation with $\mu = 0.85$, but the AFS eastern branch is just below the threshold for slip by frictional sliding.

TRANSITIONS BETWEEN FAULTS AND FAULT STRENGTH

Figures 9.7 and 9.8 represent one possible ‘lock-up’ scenario, where the orientation of σ_1 rotates from a mid- Early Cretaceous northwesterly azimuth counterclockwise and prompts a transition between fault systems. As brittle slip on the AFS eastern branch becomes unfavorable with a σ_1 azimuth of $\sim 306^\circ$ (Figure 9.7), notably similar to a paleo- σ_1 calculated for the Paposo segment of the AFS by stress inversion methods (Veloso et al., 2015). With σ_1 in this orientation, Coulomb failure is primed for generating faults with an orientation similar to that of the northwesternmost striking parts of The El Muelle fault, which could potentially help to explain the curving trace of that fault. With further rotation of σ_1 to $\sim 285^\circ$, the El Muelle fault is at the

threshold of fault reactivation, and Coulomb failure would generate faults in the orientation of the Taltal fault system. While I use several lines of evidence to argue that the Taltal fault reactivated a deep-seated precursor structure, it seems likely that reactivation of the Taltal Fault at ~110 Ma required conditions closer to Coulomb failure instead of the lower stresses required to generate slip for a cohesionless preexisting fracture. It is possible that for conditions like those in Figure 9.7 the Taltal fault was suitable for reactivation under Byerlee frictional slip conditions, but this did not occur until failure at the Coulomb envelope re-initiated a throughgoing cohesionless weakness.

These diagrams depict several possible scenarios for which slip is favored for the Taltal fault (with effective normal stresses 5–126 MPa and shear stresses 19–81 MPa) and the El Muelle fault. I demonstrate that by varying the coefficient of friction, pore fluid pressure, or the orientations of the principal stresses there are multiple configurations that allow fault slip. Depending on parameters, the Taltal fault can be favorable for slip with effective normal stresses 5–126 MPa and shear stresses 19–81 MPa, and the El Muelle fault is favored for slip with effective normal stresses 14–161 MPa and shear stresses 14–85 MPa. If tighter constraints could be found for the stress field orientation or frictional characteristics of these faults, better estimates of fault strength would be possible.

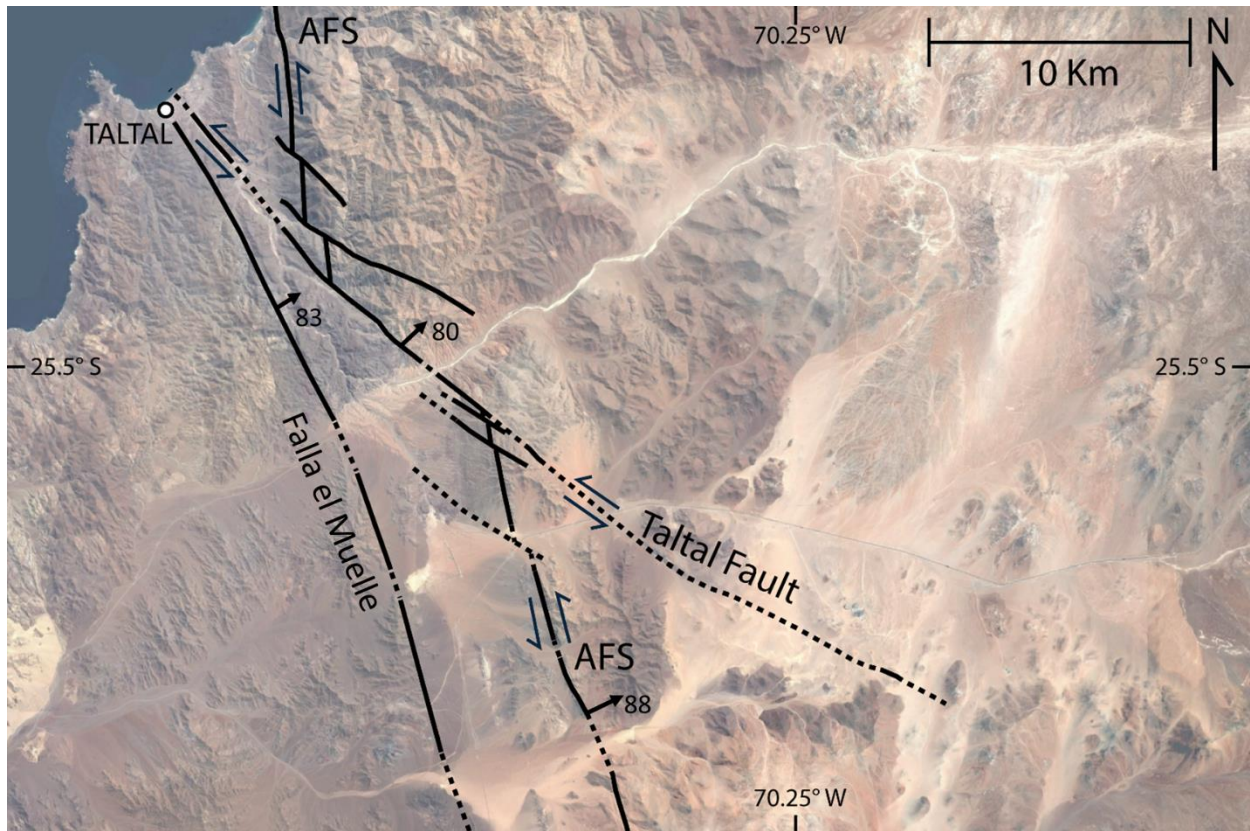


Figure 9.1. Simplified map of major faults near Taltal. Fault plane dip directions are shown with arrows and dip angles labelled.

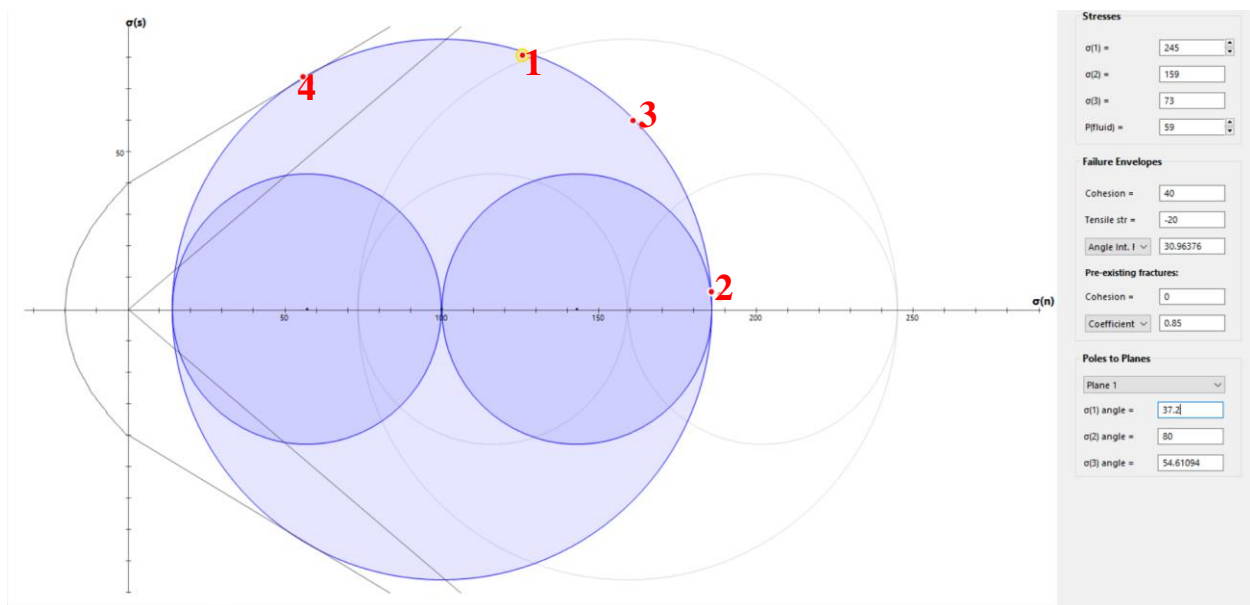


Figure 9.2. Mohr diagram with numbered red dots showing the stresses resolved on planes. The Taltal fault plane (1) is not favorable for reactivation with $\sigma_n = 126$ MPa and $\sigma_s = 81$ MPa. The AFS E branch (2) is not favorable for reactivation with $\sigma_n = 186$ MPa and $\sigma_s = 5$ MPa. The El

Muelle fault (3) is not favorable for reactivation with $\sigma_n = 161$ MPa and $\sigma_s = 60$ MPa. New faults (4) would be formed by Coulomb failure with $\sigma_n = 56$ MPa and $\sigma_s = 74$ MPa.

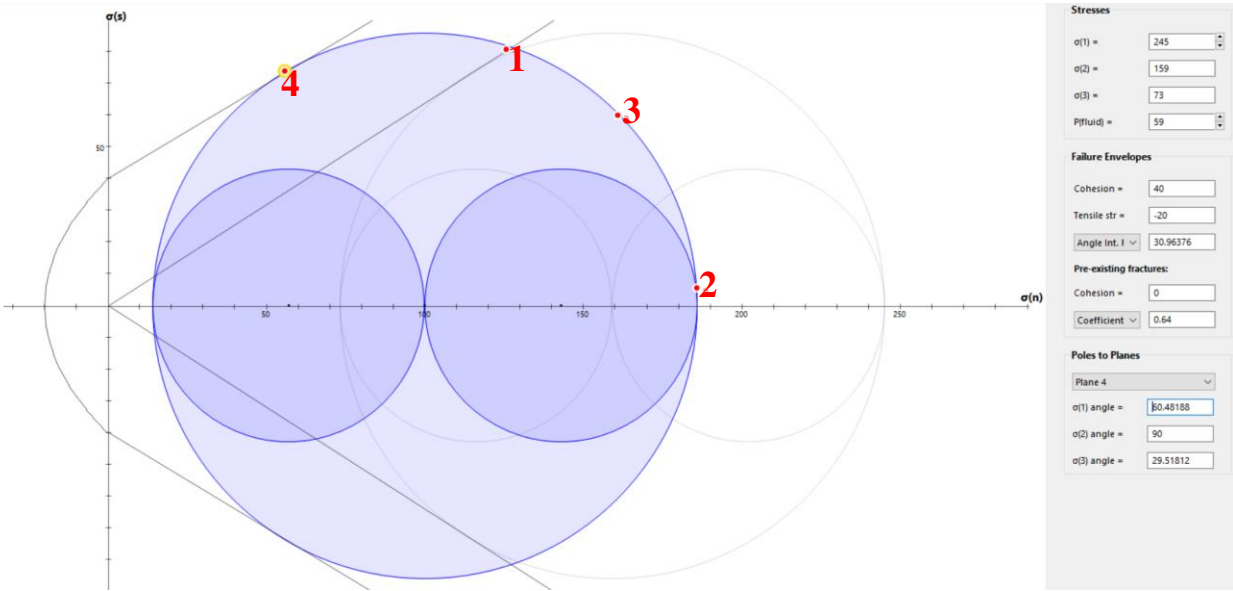


Figure 9.3. A reduced friction to $\mu \leq 0.64$ will favor reactivation of the Taltal fault before new faults are initiated by Coulomb failure criteria. Other input parameters and stresses resolved on fault planes are the same as Figure 9.2. Numbered red dots refer to faults as for Figure 9.2.

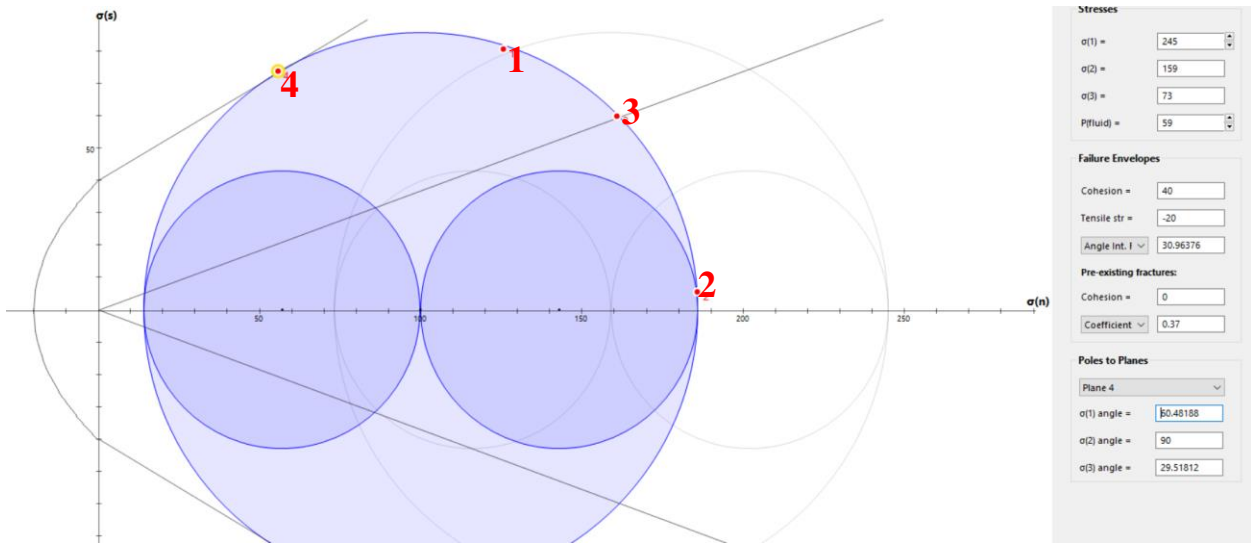


Figure 9.4. A reduced frictional sliding coefficient to $\mu \leq 0.37$ will favor reactivation of both the Taltal Fault and El Muelle faults before new faults are initiated by Coulomb failure criteria. Numbered fault calculations, other parameters, and fault plane stresses are the same as for Figure 9.2.

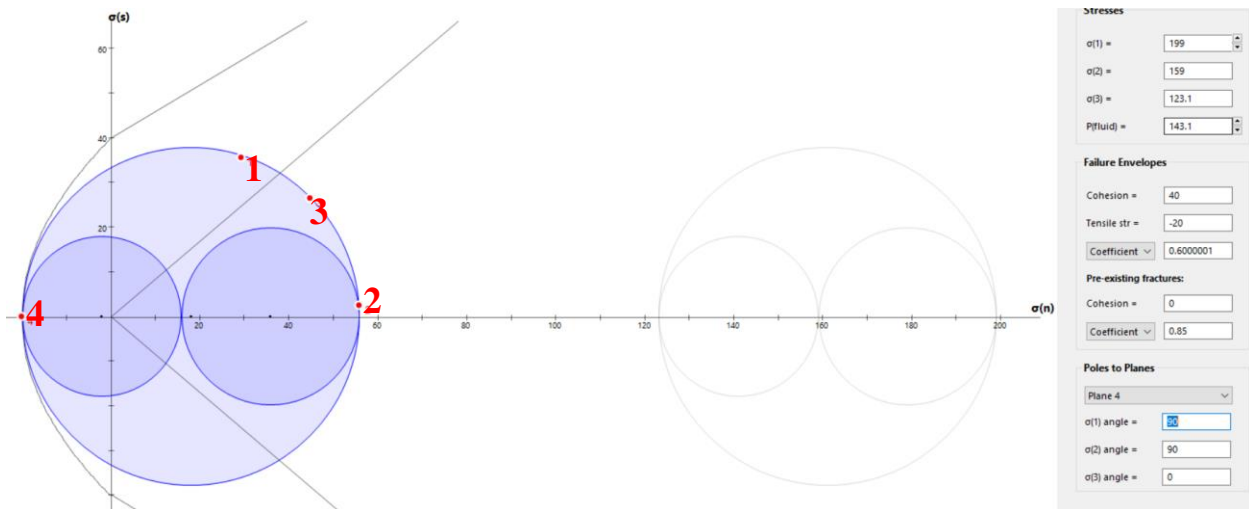


Figure 9.5. Pore fluid pressure elevated to 90% lithostatic, with the differential stress increased to critical Griffith (tensile) failure. Other parameters are as for Figure 9.2. The Taltal fault (1) is favorable for reactivation with $\sigma_n = 29$ MPa and $\sigma_s = 36$ MPa; The AFS eastern branch (2) is not favorable for reactivation with $\sigma_n = 56$ MPa and $\sigma_s = 2$ MPa. The El Muelle fault (3) is favorable for reactivation with $\sigma_n = 45$ MPa and $\sigma_s = 26$ MPa. With any increase of differential stress, joints (4) would form by Griffith failure, with an effective tensile stress of -20 MPa (effective σ_3).

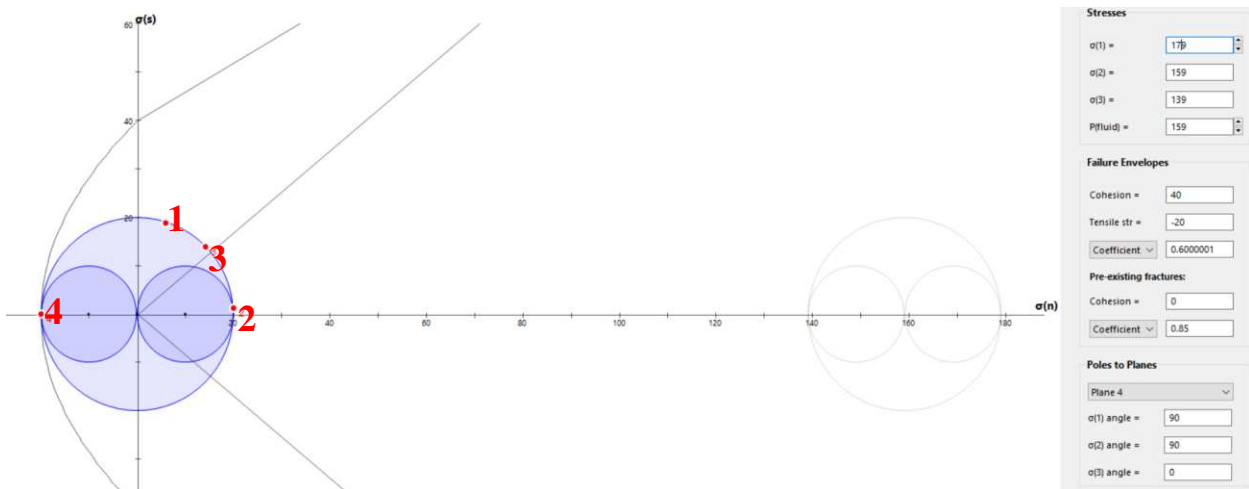


Figure 9.6. Pore fluid pressure elevated to lithostatic, with the differential stress increased to critical Griffith (tensile) failure. Other parameters are as for Figure 9.2. The Taltal fault (1) is favorable for reactivation with $\sigma_n = 5$ MPa and $\sigma_s = 19$ MPa; The AFS E branch (2) is not favorable for reactivation with $\sigma_n = 20$ MPa and $\sigma_s = 1$ MPa. The El Muelle fault (3) is favorable for reactivation with $\sigma_n = 14$ MPa and $\sigma_s = 14$ MPa. With any increase of differential stress, joints (4) would form by Griffith failure, with a tensile stress of 20 MPa.

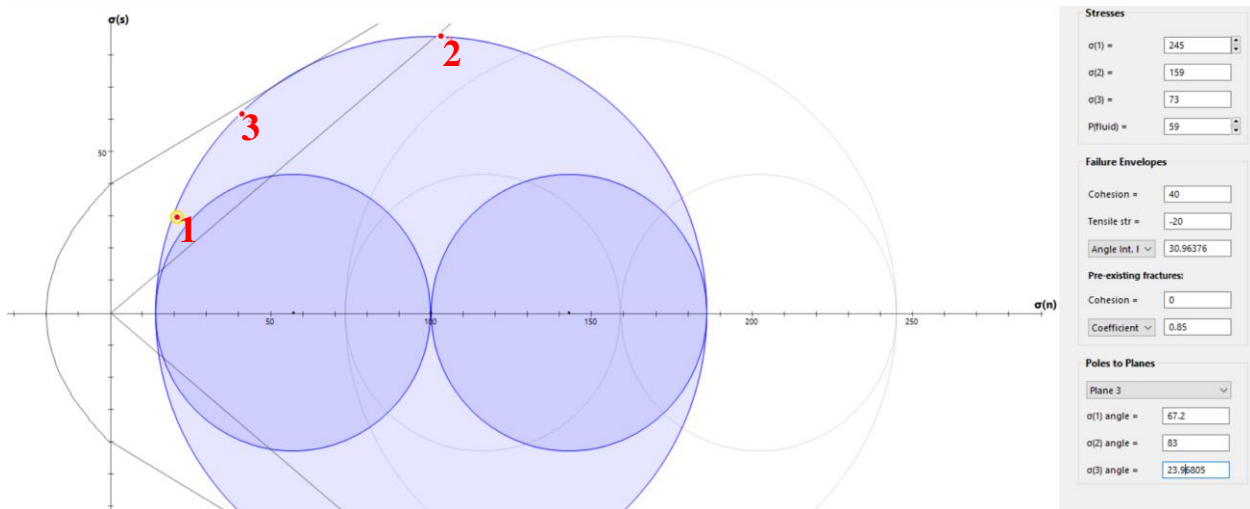


Figure 9.7. Mohr diagram for the major faults with σ_1 oriented 306/0. The AFS (2) is at the threshold for reactivation with $\mu = 0.85$, and the Taltal fault (1; $\sigma_n = 21$ MPa and $\sigma_s = 30$ MPa) and The El Muelle fault (3; $\sigma_n = 40$ MPa and $\sigma_s = 62$ MPa) are both favorable for reactivation.

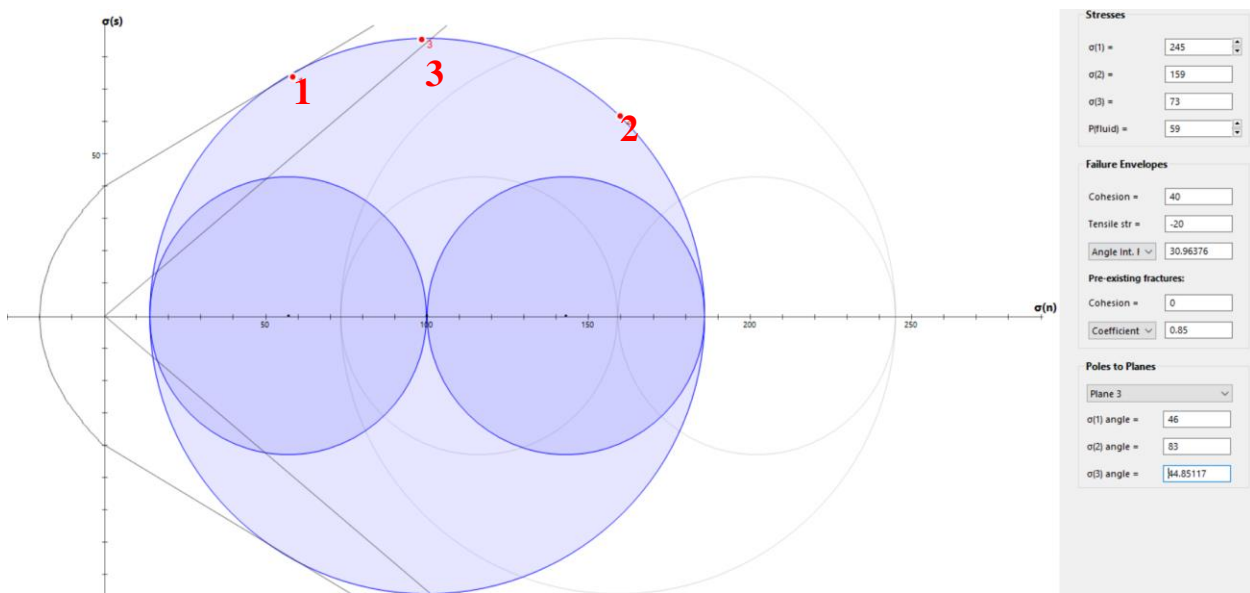


Figure 9.8. Mohr diagram for the major faults with σ_1 oriented 285/0. A fault created by Coulomb failure would form in the orientation of the Taltal fault (1) with $\sigma_n = 58$ MPa and $\sigma_s = 73$ MPa. The AFS (2) is not suitable for slip with $\mu = 0.85$ ($\sigma_n = 160$ MPa and $\sigma_s = 62$ MPa), and The El Muelle fault (3) is near the threshold for reactivation with $\sigma_n = 98$ MPa and $\sigma_s = 85$ MPa.

APPENDIX B: DESCRIPTION OF MAP UNITS

This appendix includes abbreviated descriptions of map units for the geologic maps in Plates 1–3 (Chapter 4). Detailed lithologic descriptions are available in reports by Arabasz (1971), Escribano et al. (2013), and Espinoza et al. (2014). Additional petrographic descriptions of intrusive units are presented in Mavor et al. (2020) and Seymour et al. (2020, 2021).

PALEOZOIC

PZms(c) – Metasedimentary rocks of the Chañaral Complex (Paleozoic)

Tan, gray, and greenish-gray metasilstone, metasandstone and rare metaconglomerate crop out east of the AFS. A distinctive orange weathering color of quartzite-rich intervals is commonly distinguishable in aerial imagery, while phyllite-rich intervals weather to greenish-gray. Lithologies typically alternate at the meter to tens of meter scale between thinly-bedded micaceous metapelite and thick-bedded to massive quartzite. Well-sorted, rounded, medium sand-sized grains are distinguishable in quartzite layers, with variation from well-sorted nearly pure quartzite to poorly-sorted quartz sand in a pelitic matrix. Slaty cleavage is well developed at centimeter to sub-millimeter scales in fine-grained intervals and in most areas is parallel to compositional layering. Quartzite is typically not foliated but in places breaks on fractures parallel to the foliation in adjacent finer-grained intervals. Sedimentary structures other than bedding are typically not preserved. From the rhythmic alternation of sand and mud size layers, previous authors have suggested deepwater turbidite deposition (Arabasz, 1971; Bell, 1987; Espinoza et al., 2014). The interbedded basaltic volcanic rocks reported elsewhere in the Chañaral Complex (Fuentes et al., 2017) were not found in the map area. Polyphase folding and

a general lack of facing direction indicators confound attempts to estimate minimum thickness of the unit.

The Chañaral Complex comprises the oldest recognized rocks in northern Chile and is intruded by Mesozoic plutons, several generations of basaltic to dacitic dikes, and faulted by both the Atacama and Taltal fault systems. Espinoza et al. (2014) report detrital zircon U-Pb analyses from a sample within the map area and suggest a tentative maximum deposition age of 358 ± 13 Ma. Regional paleontology (Bell, 1987) and additional detrital zircon samples (Bahlburg et al., 2009; Escribano et al., 2013) in the Coastal Cordillera give broad Devonian to Carboniferous ages.

TRIASSIC

Trg(c) – Capitana syenogranite (~215–207 Ma)

The oldest pluton in the study area is exposed in the southeast part of the map area and spatially restricted between the AFS eastern branch and a southeastward splay from that fault. The pluton is coarse grained biotite syenogranite with large anhedral quartz and alkali feldspar. Alteration consisting of sericitization of feldspar and chloritization of biotite is pervasive throughout the unit and leads to a chalky outcrop appearance that is distinctive in satellite imagery. The Capitana pluton is pervasively intruded by mafic dikes. Espinoza et al. (2014) present a 207.34 ± 0.96 Ma U-Pb zircon age of the pluton.

JURASSIC

Jgd(cc) – Cerro Concha granodiorite (~195 Ma)

The Cerro Concha granodiorite is adjacent to the AFS mylonitic zone south of the Cerro del Pingo plutonic complex and lacks pervasive ductile strain. Mesocratic in hand sample with 35% mafic minerals, the pluton is a hornblende biotite granodiorite to tonalite composed of 35%

plagioclase, 23% biotite, 21% quartz, 10% hornblende, 7% potassium feldspar, 2% pyroxene, and 1% accessory minerals including zircon, oxides, and apatite. Plagioclase grains are 1–4 mm, preserve oscillatory zoning, and have well developed polysynthetic twinning. Grains are subhedral and have an adcumulate texture. Saussertization is limited and concentrated in cores, and inclusions of hornblende are also common in cores. Quartz grains are 0.5–2 mm, anhedral, and have abundant fluid inclusions. Grains lack a preferred orientation and show only weak undulose extinction or subgrain development. Potassium feldspars are 1–3 mm and dusty in plane-polarized light due to minor sericitization. This Jurassic pluton has a zircon U-Pb dates of 195.6 ± 1.0 Ma, 196.2 ± 2.2 Ma (Seymour et al., 2020), and a biotite $^{40}\text{Ar}/^{39}\text{Ar}$ date of 177.4 ± 0.4 Ma (Espinoza et al., 2014).

EJgd – Early Jurassic Granodiorite (~189 Ma)

In the southern map area, a medium-grained biotite-bearing granodiorite crops out between the southeastern splay to the AFS eastern branch and volcanic rocks of the Aeropuerto Formation further east. This unit is compositionally variable from tonalite to granodiorite. Zoned tabular feldspars are 1–3 mm, subhedral, and commonly altered to sericite. Biotite is 2–3% modal and altered to chlorite. Quartz grains (15%) are anhedral. Seymour et al. (2020) present a zircon U-Pb age of 188.6 ± 0.8 Ma for this unit. Unit *EJgd* is bound on the west by a NW-striking splay fault to the AFS. The eastern contact is intrusive into unit *JKv* andesite and Cerro Concha granodiorite, and the intrusive contact is displaced by additional NW-striking faults subsidiary to the greater AFS.

Jv – La Negra Formation volcanic and volcanoclastic rocks (Jurassic)

This unit is typified by brown, reddish-brown, purplish-brown, or gray andesite and monomict andesite breccia with sparse coarse-grained volcanoclastic sandstone with thin siltstone

interbeds. Most outcrops are massive coarsely porphyritic to glomeroporphyritic andesite with tabular euhedral plagioclase to 1 cm in a brown aphanitic matrix. Breccia is typically pebble to cobble sized angular clasts of brown-gray andesite supported in a matrix of coarse sand-size crystals. Bedding is distinguishable in clastic intervals, or where cm-scale sandstone lenses are intercalated with massive andesite flows. Rare clasts of Chañaral Complex quartzite in conglomerates indicate probable surface exposure of that unit at the time of deposition.

The La Negra Formation represents widespread voluminous magmatism along the Coastal Cordillera of Chile. Geochemically, La Negra volcanics are calc-alkaline and show trace element affinities compatible with subduction zone magmatism (Oliveros et al., 2007). Most magmatism is between 164–150 Ma, with sporadic older magmatism between 177–170 Ma (Oliveros et al., 2006); geochronology of outcrops south of Taltal and west of the AFS coincide with this older pulse of magmatism (Escribano et al., 2013; Espinoza et al., 2014). No stratigraphic base of the unit is observed within the map area, but a conformable contact with the Late Triassic to Early Jurassic Pan de Azúcar Formation is described along the coastline west of the map area (Escribano et al., 2013). The La Negra Formation is cut by crystal-poor porphyritic andesite and basaltic andesite dikes.

Jgd(m) – Matancilla plutonic complex granodiorite (~169 Ma)

Near the Taltal fault, the AFS is bordered on the east by a gray to light gray medium to fine-grained biotite hornblende granodiorite. Moderate pervasive alteration is present in most outcrops, with biotite typically altered to chlorite and feldspar lightly to heavily sericitized, lending pale green to orange hues to the weathered faces. This pluton is distinguished in hand sample from the La Finca granodiorite by the smaller grain size, lower proportion of mafic minerals, lower proportion of biotite relative to amphibole, and generally less fresh appearance.

The Matancilla pluton intrudes Chañaral Complex quartzite and phyllite west of Cerro Breadal and east of Cerro Perales. This contact is irregular, but generally NE-SW or N-S striking. Deflection of the contact over topography (e.g., north of the Quebrada Tipias fault) appears to indicate an overall steep NW dip. The eastern margin of the Matancilla pluton is truncated by the brittle core of the AFS, and this fault contact is displaced by the TFS. Mavor et al. (2020) report 169.0 ± 1.5 Ma U-Pb zircon date of the Matancilla pluton south of the Taltal fault, and Escribano et al. (2013) give an 175–158 Ma age range from samples north of the present map area. Alteration is most strong in discrete mylonitic zones, where concentrated alteration gives a bleached or pinstripe appearance to mylonitic foliation planes. Mylonitic fabric in unit *Jgd(m)* is overprinted by cataclasis and brecciation from both the Atacama and Taltal fault systems.

Jpg(sr) and Jfg(sr) – Quebrada San Ramón intrusive complex

In Quebrada San Ramón NE of the town of Taltal a distinctive coarse to fine-grained granite borders the east side of the AFS eastern branch and intrudes the Matancilla granodiorite. This unit has a distinctive orange-pink weathering color and clots of chloritized amphibole. The unit has variable grain size and modal proportions from the more common coarsely porphyritic variety (unit *Jpg(sr)*) to a fine-grained leucocratic granite (unit *Jfg(sr)*); these units are mapped separately but internal variations between these lithologies are present at meter-scale. From modal proportions the intrusive complex spans from monzogranite to syenogranite, and the grain size and proportions of mafic phases are notably variable between the lithologies. The Quebrada San Ramón intrusives are lithologically similar to intrusives of the Goyenchea complex and could be offset markers across the AFS eastern branch, but zircon U-Pb dates of 160.6 ± 0.8 Ma for coarsely porphyritic granite and 160.1 ± 3.2 Ma for fine-grained leucocratic granite do not support such a correlation to the Cretaceous Goyenchea intrusives (Seymour et al., 2021).

Jgd(q) – Quezada intrusive complex (153 Ma)

At the eastern boundary of the map area, granodiorite of the Quezada intrusive complex intrudes Chañaral Complex quartzite and Cerro Concha granodiorite and is intruded by the Cerro del Pingo plutonic complex. The Quezada intrusive complex within the map area is typified by dark gray medium-grained hornblende biotite. Myrmekitic texture is present in feldspars. The granodiorite is 20–35% mafic minerals, with 2:1 hornblende:biotite most common. Hornblende is partially chloritized and biotite is largely chloritized.

JKgd(lf) – La Finca pluton granodiorite (149–139 Ma)

Outcrops of gray to dark gray medium- to coarse-grained hornblende-biotite granodiorite are present northeast of the Taltal fault and north of Cerro del Pingo. Hypidiomorphic granular texture is present with coarse euhedral zoned plagioclase, euhedral to subhedral biotite and hornblende, subhedral to anhedral quartz, and interstitial anhedral K-feldspar. Biotite is slightly more abundant than amphibole. Biotite is partially to wholly altered to chlorite and plagioclase is lightly mottled by sericite. La Finca granodiorite is coarser than granodiorite of the Matancilla pluton, lacks discrete mylonitic zones, and generally exposes less altered outcrops. The western margin of the La Finca pluton is intrusive into the Chañaral Complex, with biotite-grade contact metamorphism in quartzite. North of the Taltal fault, this intrusive contact is offset 250 m by a sinistral N-S striking brittle fault. $^{40}\text{Ar}/^{39}\text{Ar}$ dates from the La Finca plutonic complex span a range between 149–139 Ma (Espinoza et al., 2014).

CRETACEOUS

JKv(r) – Rhyolite (145–146 Ma)

Near the town of Taltal a resistant north-south elongate ridge exposes a pale pink medium to fine-grained hypocrySTALLINE porphyritic rhyolite flow. These outcrops are distinctive in a

surrounding of brown and dark green andesite, volcanoclastic sandstone, and pebble conglomerate. The upper several meters of the flow are brecciated with rhyolite clasts in a matrix of the same lithology and are interpreted as flow-top autobreccia (Mavor et al., 2020). Rhyolite clasts are present in overlying andesite flows and clastic deposits. The lower contact of the rhyolite flow is sharp against the underlying andesite. Rhyolite outcrops typically exhibit cm to mm-scale pink to brownish-pink flow banding that is defined by concentrations of phenocrysts, fine-grained quartz and spherulitic glass, and banding is accentuated by hematite replacement. A weak flow lineation is rarely visible. Folded flow bands are visible in outcrop and multiple orientations of flow banding is recorded; however, flow banding is often parallel to the upper and lower contacts of the rhyolite and parallel to bedding in clastic strata surrounding the flow (Mavor et al., 2020). Subhedral to euhedral plagioclase phenocrysts range up to 6 mm, and biotite is in places euhedral to 3 mm. Quartz phenocrysts are subhedral and show ameboid embayment textures in thin section, most likely recording melt resorption.

Near Taltal, unit *JKvr* outcrops in an elongate north-south ridge that extends from Caleta el Hueso to a truncation at the Taltal fault. The rhyolite flow is conformable in a west-dipping section of andesite flows and lithic sandstones. Significant thickness changes are observed along strike, ranging from ~150 m at the shoreline to pinchouts along the ridgeline to the south. Abrupt along-strike thickness changes near Caleta el Hueso are likely the result of paleotopography such that the flow thickens across paleovalleys and thins over topographic highs. In places, multiple rhyolite flows are interlayered with finely porphyritic andesite; multiple flows are depicted only where differentiable at map scale near the Taltal fault. Mavor et al. (2020) give U-Pb weighted mean ages of 146.3 ± 0.8 Ma and 143.6 ± 1.2 Ma for outcrops of unit *Jkvr* on either side of the Taltal fault and demonstrate that these samples are not statistically differentiable. They interpret

that the southernmost outcrops are intrusive into the surrounding volcanic rocks and represent deeper exposure levels than the rhyolite flows north of the fault.

JKv – Aeropuerto Formation volcanic and volcanoclastic rocks (~146–122 Ma)

Outcrops east of the AFS eastern branch are largely brown or reddish-brown to gray andesite and dacite with sparse hypabyssal diorite, volcanoclastic sandstone and pebbly sandstone, and rare mudstone. Espinoza et al. (2014) report interbedded rhyolite and lapilli tuff. The dominant lithology is brown to gray porphyritic andesite with concentrically zoned plagioclase euhedral to 1.5 cm. Hematite is prevalent as disseminated sub-mm grains in most samples and along fracture and fault planes in many outcrops and concentrated along flow banding. Volcanoclastic intervals are typified by medium to coarse lithic wacke to lithic arenite with andesite pebbles and in places are interbedded with decimeter-thickness beds of finely-bedded mudstone.

The lower contact of the Aeropuerto Formation is not exposed, but the oldest rocks that crop out east of Taltal are stratigraphically below a 146 Ma rhyolite (unit *JKvr*), and detrital zircon dates presented here demonstrate that clastic strata have maximum depositional ages as young as ~122 Ma.

Km – Marine limestone and carbonate-cemented clastic strata (Early Cretaceous)

South of the Quebrada de la Peineta fault, outcrops of bioclastic limestone and micrite-cemented fine-pebble conglomerate are restricted to a fault sliver between N-S striking AFS faults. Limestone is yellow-tan to dark brown on weathered faces and tan to gray on fresh faces and classified as wackestone to packstone with bivalve fragment bioclasts. A variable component of angular to subrounded andesitic pebbles and disaggregated plagioclase crystals are present in limestone, which grade to interbeds of micrite-cemented pebbly sandstone. Sparse boulders of

andesite are present and supported in a carbonate matrix, suggesting either pyroclastic or olistostromal input to a marine environment. Bedding is crudely visible at the meter scale and often easily distinguished from a distance but difficult to measure in outcrop. Paleontological descriptions of bivalves in these horizons indicate either Late Jurassic or Cretaceous ages (Rubilar, 2012 *in* Espinoza et al., 2014). Barring complications from concealed faults, these limestones should be stratigraphically above the lithic sandstones dated in this study with abundant Early Cretaceous zircons, indicating that the limestones must post-date the ~122 Ma maximum depositional age of the sandstone.

Kcg(g), Kmg(g), Kfg(g), Kr(g) – Goyenchea intrusive complex (142–130 Ma)

Distinctively orange-brown outcrops in the southern map area expose fine- to medium-grained granite with variable sericite and epidote alteration. The Goyenchea complex is divided into textural subunits of coarse-grained granite (unit *Kcg(g)*), medium-grained granite (*Kmg(g)*), and fine-grained leucocratic granite (*Kfg(g)*) as well as rhyolite (unit *Kr(g)*) that is here included as pertaining to the same intrusive episode. The intrusive complex is texturally gradational between these units. Coarse-grained granite has zoned subhedral plagioclase to 7 mm with polysynthetic twinning and minor sericitization. Alkali feldspar is finer-grained (to 1 mm) and subhedral. Hornblende is more common than biotite and typically replaced by chlorite. Quartz is anhedral to feldspars and generally lacks undulatory extinction. Coarse-grained granite is intruded by fine-grained granite and rhyolitic dikes with meter to decameter thicknesses. Epidote-filled miarolitic cavities are present in some outcrops of fine-grained granite and suggestive of epizonal emplacement levels (Vignerresse, 2015). This unit has a notable low proportion of mafic minerals and intrudes andesite of the Aeropuerto Formation, with the best contact relations exposed south of Quebrada Cifuncho. Our mapping of the Goyenchea intrusive complex broadly corresponds to

units JKa₂ and JKa₃ mapped by Arabasz (1971) and includes outcrops previously mapped as the Cerro del Pingo pluton (Espinoza et al., 2014); we revise this mapping to show that Goyenchea intrusive bodies are present between AFS strands while the Cerro del Pingo pluton is present only east of the AFS in the vicinity of Quebrada Cifuncho. The Goyenchea intrusives are in places cut by brittle faults but is not associated with ductile strain. Reported zircon U-Pb ages for Goyenchea fine-grained granite of 140.9 ± 1.1 Ma and 143.0 ± 1.8 Ma (Seymour et al., 2021) as well as a 145 ± 2 Ma date for Goyenchea rhyolite (Espinoza et al., 2014) indicate earliest Cretaceous intrusion.

Kqd – Quartz diorite near Cerro del Pingo (Early Cretaceous)

The western slope of the Cerro del Pingo massif exposes an aerielly small (<0.1 km²) body of quartz diorite. We revise the geologic mapping of Kurth (2000) to show that the quartz diorite (unit *Kqd*) is entirely east of the AFS, rather than between AFS strands. The quartz diorite body is discontinuous and elongated north-south. Geologic mapping shows a boudinaged pattern of the map unit, with a necked shape to the largest mapped body. In aerial imagery, mylonitic fabric of the Las Chañaral Complex is seen to deflect to parallel the margins of the quartz diorite; mylonitic foliation in the metasedimentary rocks parallels the margin boundaries. The core of the quartz diorite body is internally unstrained, whereas the outermost 1–15 m of the body exhibits a mylonitic foliation subparallel to mylonitic foliation in the surrounding metasedimentary rocks. Foliation along the margins and map-scale boudinage of this quartz diorite suggest a syn-kinematic relation between the quartz diorite and AFS ductile deformation that imparted mylonitic foliation in Chañaral Complex metasedimentary rocks. Kurth (2000) provides five K-Ar hornblende cooling ages for unit *Kqd* ranging from 155–132 Ma and overlapping within reported error between 142–141 Ma. While samples collected in this study produced insufficient

zircon for a robust U-Pb crystallization age, a single concordant zircon grain analysis at 136 ± 2.6 Ma is broadly consistent with the Kurth (2000) age range and suggests Early Cretaceous intrusion. Given the uncertainty of the K-Ar data and the insufficient analyses for a robust zircon U-Pb date, a precise age determination of unit *Kqd* remains elusive.

Kgd – Cretaceous granodiorite (~140 Ma)

In the southern part of the map area a gray medium to coarse-grained hornblende granodiorite intrudes andesite of the La Negra Formation. The gray color, coarseness, proportion of mafic minerals, and distinctive weathering pattern of rounded boulders differentiate this unit from granite and rhyolite of the Goyenchea plutonic complex to the west. Unit *Kgd* is restricted to a single occurrence with outcrop area 0.05 km². Espinoza et al. (2014) present a 140.1 ± 6.0 Ma U-Pb zircon date of this outcrop.

Kgd(lt)– Las Tiplas granodiorite (~130 Ma)

The upper slopes of Cerro Perales, the highest peak immediately east of Taltal, expose outcrops of light gray medium-grained amphibole biotite granodiorite and tonalite. A weak foliation defined by aligned amphibole and biotite is locally observed. Quartz is anhedral and interstitial to subhedral zoned plagioclase and subhedral alkali feldspar, and these phases lack textural evidence for dynamic recrystallization. We interpret the fabric defined by aligned mafic minerals as magmatic rather than reflecting tectonic strain. The Las Tiplas pluton clearly cross-cuts the NE-striking mylonitic fabric developed in the Chañaral Complex in the aureole of the Matancilla pluton (Chapter 3). Ductile deformation within this pluton is not observed. Centimeter to decimeter scale fine-grained mafic enclaves are typically present in outcrops of unit *Kgd(lt)*; oblate and prolate mafic enclaves in most outcrops show no orientation pattern. Outcrops of unit *Kgd(lt)* typically expose fresh rocks without the pinstripe alteration bands

present in the Matancilla pluton. U-Pb zircon geochronology indicates a crystallization age of 129.5 ± 1.1 Ma for this unit (Chapter 3). This age is younger than the previously reported 139–134 Ma range for the pluton (Escribano et al., 2013) and the 139 ± 3 Ma K-Ar biotite age (Las Cenizas, 2007 in Escribano et al., 2013) of a sample near the summit of Cerro Perales. On the northern slopes of Cerro Perales unit *Kgd(lt)* is intruded by basaltic dikes of probable Early Cretaceous age.

Kt(cp1) and Kt(cp2) – Cerro del Pingo plutonic complex older (134–132 Ma) and younger (120–119 Ma) intrusions

The Cerro del Pingo plutonic complex is composed of two lithologically similar tonalite intrusions. Both intrusions are typified by light gray medium-grained biotite hornblende tonalite and granodiorite and is orange to pinkish tan on weathered faces. Hypidiomorphic granular texture is dominant with coarse subhedral to euhedral zoned plagioclase, subhedral amphibole and biotite, and fine-grained anhedral quartz and potassium feldspar. The younger intrusive body is distinguished by a finer-grained texture and higher proportions of quartz diorite enclaves and intrudes the older tonalite.

The pluton is generally not foliated, but has a weak protomylonitic fabric along the western margin where the pluton is nearest the AFS (Saldías, 2015; Seymour et al., 2020, 2021). The pluton intrudes metasedimentary rock of the Chañaral Complex and granodiorite of the Quezada intrusive complex in the eastern part of the map area and intrudes Aeropuerto volcanic rocks in the southern map area. Our mapping restricts the Cerro del Pingo pluton purely to the east of the AFS at latitudes 25.6° – 25.8° S and west of the AFS eastern branch between latitudes 25.9° – 26.0° S. Seymour et al. (2020, 2021) present zircon U-Pb ages that restrict the older phase to 134–132 Ma and younger tonalite to 120–119 Ma.

Kt(bs) – Barreal Seco tonalite (125-121 Ma)

The Barreal Seco pluton is exposed in the southeastern corner of the map area where it intrudes andesite of the Aeropuerto Formation (unit *JKv*). Typical lithology is a light gray, tan-gray, or orangeish-gray medium-grained hypidiomorphic granular hornblende biotite tonalite, and sparse outcrops of gray to dark gray hornblende quartz diorite are also present. Outcrops near the intrusive contact with andesite have a weak foliation parallel to the contact trace. Petrographically, this foliation is defined by aligned biotite and/or aligned tabular zoned plagioclase. Quartz is interstitial and generally lacks undulatory extinction or textural evidence for dynamic recrystallization. Espinoza et al. (2014) report zircon U-Pb and $^{40}\text{Ar}/^{39}\text{Ar}$ ages that suggest emplacement at 125–121 Ma.

Kc(u) – Undivided cataclasite (Early Cretaceous)

Unit *Kc(u)* includes black, dark gray, brown, or greenish-gray protocataclasite, cataclasite, and fault breccia. Fault gouge is generally not thick enough to map separately and is included in unit *Kc(u)*. Cataclasite typically has sharply-defined boundaries marked by major fault surfaces, but in places has a gradational contact into the surrounding rock. Cataclasite is most strongly developed near major fault surfaces, where the matrix proportion in places exceeds 65%, and grades to protocataclasite and fault breccia away from these faults. Fault bounded blocks with recognizable protolith lithologies are present in breccia with a range of block sizes, some with surface exposure exceeding ~50 m². Slickensided surfaces, veins, and locally fracture foliation are present in the cataclasite unit. Chlorite, sericite, and calcite are observed petrographically in veinlets and as alteration products of protolith minerals. The greatest thickness of cataclasite and fault rocks (~300 m) is developed along the eastern branch of the AFS, though subsidiary AFS strands have fault cores that locally exceed 50 m thickness.

Undivided unit $Kc(u)$ is mapped where the protolith is unrecognizable or where cataclasite includes recognizable clasts of multiple lithologies. Unit $Kc(u)$ is subdivided into units $Kc(ms)$, $Kc(v)$, and $Kc(p)$ where the cataclasite protolith is recognizable as metasedimentary (Chañaral Complex), volcanic (units Jv or Kv), or plutonic (units $Jgd(m)$ or $Kt(cp)$), respectively. In places the contacts between these subunits are mappable along a single fault surface and distinguishable in multispectral satellite imagery, but more typically a well constrained distinction was not possible, and the contacts between subunits are gradational.

K(d) – Early Cretaceous andesite dike (~110 Ma)

A 7–12 m-wide porphyritic andesite dike cuts the AFS eastern branch south of the Quebrada de la Peineta fault. The dike is pinkish tan to brown on weathered surfaces and speckled gray on fresh faces. Weathered outcrops have characteristic spheroidal weathering at scales up to 50 cm. The andesite is porphyritic with euhedral tabular plagioclase to 6mm and euhedral to subhedral clinopyroxene phenocrysts in a matrix of sub-mm plagioclase. Sparse subhedral quartz grains are present. Clinopyroxene is partially to wholly replaced by chlorite, and plagioclase is mottled by sericite.

This dike cuts the easternmost three strands of the AFS but is offset ~148 m in a sinistral sense by the westernmost of the AFS strands exposed in these outcrops. East of the AFS, the dike cuts quartzite and phyllite of the Chañaral Complex and is truncated by a NW-striking strand of the TFS. The continuation of the dike on the northeast of this fault has not been located but is likely concealed by alluvium of Quebrada de La Peineta. Given that this dike cuts the eastern strands of the AFS but is offset by a strand further west, it most likely intruded during the latest stages of AFS brittle deformation, after deformation ceased on the main eastern strands but shortly before the cessation of slip on the western strands.

NEOGENE

Qoa – Older alluvium (Miocene to Pleistocene)

Older alluvium encompasses abandoned high surfaces without modification from modern drainages. Deposits range from pebble to boulder gravel with sandy matrix. Older alluvium is loose to dense where cemented by caliche, moderately to well sorted, and generally clast supported. Surface clasts are commonly ventifacted and have weathering rinds that approach 1 cm thickness. Alluvial surfaces are faintly channeled and in aerial imagery appear smoother and more red-orange than modern alluvium. Unit *Qoa* was mapped where distinctly older inactive alluvial surfaces are perched above younger drainage alluvium (unit *Qa*) and is only mapped north of 25.69°S. Escribano et al. (2013) present several dates of ash layers interbedded with alluvial fan gravels with ages ranging up to 12 Ma, indicating Miocene sedimentation.

Qa – Alluvium (Pleistocene to Holocene)

Younger alluvium deposits are cobble gravel, pebbly sand, well-sorted sand, and less common boulder gravel in abandoned and modern drainages. Unit *Qa* includes mined and unmined natural nitrate deposits mapped separately by Espinoza et al. (2014). Deposits are orange, tan, gray or brown; color varies with source material. Clast lithologies vary strongly with source material to nearly monomict conglomerates. Ventifacted clasts are present on fan surfaces in the more arid southern and eastern portions of the map area, and weathering rinds are typically < 2 mm thick. Unit *Qa* includes alluvial fans, stream drainage alluvium, talus slopes, and beach deposits. Alluvial surfaces have sharply defined braided and anastomosing stream channels visible in aerial imagery. Unit *Qa* is incised against older alluvium (unit *Qoa*) or bedrock units. South of 25.69°S, unit *Qa* includes older deposits (unit *Qoa*) that may be Pliocene to Miocene.

ml – modified land (Holocene)

Unit *ml* includes anthropogenic artificial fill and material derived from bedrock or alluvial units and is mapped where municipal development and mining activities have obscured the underlying geologic units.